Universidad de Santiago de Compostela

Facultad de Física

Departamento de Física de Partículas

Measurement and study of the residual nuclides produced in fragmentation reactions of ^{238}U at 1 $A \cdot GeV$ with deuterium

Memoria de tesis doctoral presentada por

Enrique Casarejos Ruiz

Santiago de Compostela, Junio 2001

JOSE F. BENLLIURE ANAYA, Profesor del departamento de Física de Partículas de la Universidad de Santiago de Compostela,

CERTIFICA

que la presente memoria, con título ***Measurement and study of the residual nuclides produced in fragmentation reactions of*** ^{238}U ***at 1*** $A \cdot GeV$ ***with deuterium***, realizada por **Enrique Casarejos Ruiz** en la Universidad de Santiago de Compostela, constituye el trabajo de Tesis Doctoral que presenta para optar al Grado de Doctor en Física.

Santiago, 5 de Junio de 2001

Fdo.: J. F. Benlliure Fdo.: E. Casarejos

El tribunal para la defensa de esta tesis, el 29 de Junio de 2001, estuvo integrado por

- **Peter Armbruster**, *Gesellschaft für Schwerionenforschung*, Darmstadt (Germany)
- **Elvira Moya de Guerra**, Instituto de Estructura de la Materia, CSIC, Madrid (Spain)
- **Olivier Lopez**, Laboratoire de Physique Corpusculaire, Caen (France)
- **Jose L. Tain**, Instituto de Física Corpuscular, CSIC, Valencia (Spain)
- **Juan A. Garzón**, Universidad de Santiago de Compostela (Spain)

A todas mis mujeres.
A mi mujer.

Acknowledgements

> One has to abandon his work as Ulysses abandoned Nausicaa: with more gratitude than love[1].

This work is the consequence of a short interview with J.Benlliure, in the fall of 1997. He invited me to join a new subject in my career. I invited him pursue in the development of that subject within our group, in my home-university. After some time, this is the first thesis work presented in that scenario. And the most important, soon there will be more. Many different, trivial and essential conditions and events happened since then till the writing of this page.

I am indebted to the whole collaboration group members, and especially to the welcome at GSI institute by K.-H.Schmidt, where I have spent so many months since 1997. They have introduced me the tuning of FRS electronics, the tuning of the code calculations, the tuning for the correct understanding of the physical processes happening in front of us, . . . I will no mention names, since those involved in this work will recognize their *touch* in the following pages.

I cannot skip a short comment on the starting days at the university. It was already a success, early in 1998, to be able to develop our work with our own resources. Now it seems to be trivial to have a look on the data. But in the beginning it was not so obvious. . . Some people know. Since then, day in day out, our work in the university has grown with the effort of all, and the discussions have become rather exciting.

I am also especially grateful to P. Armbruster and M. Bernas for the carefully reading and correction of this work, as well as their continuous encouragement.

Al margen de los implicados en el trabajo, y ya que antes no hubo tiempo ni ocasión para ello, no quiero dejar de dar las gracias a quienes me han rodeado. Gracias por vuestra infinita paciencia en tantos, casi treinta, años. A mis mujeres, a mi mujer, les dedico este trabajo.

---

[1] Adapted from F.W.Nietzsche, *Beyond good and evil*, 96, where *life* instead of *work* is mentioned.

Contents

List of Figures

List of Tables

Introduction

The subject of this dissertation is the study of the deuteron induced reactions with ^{238}U at a kinetic energy of 1 GeV per nucleon. This reaction belongs to the so called relativistic energy heavy-ion type, processes that allow the study of nuclides under extreme conditions of density and temperature (below the hadronization limit). The impact at relativistic energies of light and heavy ions is interpreted as a two-step process: a fast-one, leading to an excited *pre-fragment*, and a second one where the reaction residues are formed either by particle emission and/or fission. This two different mechanisms lead to the residual production by *fragmentation* and *fission*, respectively. Another reaction mechanism present in heavy ion collisions is *multifragmentation*. This process, enhanced when using heavier targets leading to higher excitation energies and densities, will be a minor contribution to the residual production we observe in the studied reaction. That contribution is well beyond the scope of this work and it will not be investigated. The most of the production of heavy residues in this reaction is by fragmentation. The investigation of that production mechanim is the subject of this work.

The interest on the *spallation* reactions[2] covers very different topics. These reactions allow to investigate excited nuclear matter at normal density and low angular momentum. These conditions are optimal to investigate the onset of thermal multifragmentation, e.g., as well as some fission processes. This kind of reactions also gained in recent years new interest because of their relation to intense neutron sources. These sources become possible by using spallation targets, and are used in a wide range of applications. Either to investigate condensed matter and materials, or in nuclear technologies as those of the *accelerator-driven systems* ADS and their use in transmutation of nuclear waste, the spallation targets are present. Spallation and fragmentation reactions make also possible the production of intense *radioactive ion beams*, which is a very powerful tool to investigate new areas of the chart of nuclides. Different nuclear structure subjects have a new impulse in this scenario. Also nuclear Astrophysics needs results of spallation reactions. Firstly, because of the existing phenomena related to the description of nuclear abundances and fundamental nucleosynthesis processes. Secondly, because the possibility to access to very exotic regions of the chart of nuclides, were fundamental nucleosynthesis processes evolve (*r-process, rp-process, . . .*) depends on the production of those exotic nuclei, and fragmentation seems to be a feasible procedure. These topics we mention cover such a wide

---

[2] Spallation and fragmentation refers to the same reaction but in inverse kinematics. The former is the reaction induced by light particles in heavy targets. The later is the inverse process. Spallation processes were first identified as cosmic rays tracks.

range of different projectile-target combinations and energies, that a dedicated study of all those which are required is not possible. On the other hand, most of the fields involved need very accurate data in order to be able to either schedule experiments with very exotic nuclides production, or to understand basic mechanisms as the nucleosynthesis process, or to design an alternative-energy power plant (ADS). Based on theoretical models, different codes are developed to simulate the processes involved in this kind of reactions. The comparison of the predictions of these models with measured data, allows to refine their performance while understanding the phenomena behind. Different comparisons have concluded that the predictive capabilities of the most common simulation codes available nowadays, are not well adapted to specific uses. The lack of data in wide ranges of energies and nuclides, has made the codes not to be improved in many cases with benchmarking tests.

The reaction $U(1\ A \cdot GeV) + d$ studied in this work, belongs to a systematic study started at the *Gesellschaft für Schwerionenforschung* GSI (Darmstadt, Germany) in 1996, within a collaboration of different EU institutes. The purpose of the project was to study a set of nuclear reactions to obtain a systematic and representative overview in the fission-fragmentation processes involved, and to define a benchmark data collection in order to compare the results of the simulation codes related to the subject. The involved institutes together with the GSI are the *Institute de Physique Nuclèaire* IPN (Orsay, France), *Commissariat à l'Energie Atomique* DAPNIA/SPhN (Saclay, France), *Centre d'Etudes Nuclèaires* CEN-BG (Bordeaux, France), and the *Universidade de Santiago de Compostela* (Spain). The experimental program included, among others, the deuteron and proton induced reactions with $^{238}U(1.0\ A \cdot GeV)$ and $^{208}Pb(1.0, 0.5\ A \cdot GeV)$. The experimental task was accomplished in October, 2000. The results have been partially analysed and published. The results of the present work are a piece to disentangle the peculiarities of the four reactions of ^{238}U and ^{208}Pb with proton and deuteron. On the one hand, all the reactions studied involved the collision of a heavy and a light ion (instead of a heavy ion-ion collision), although they were characterized by very different fissilities. On the other hand, the deuteron induced reactions are compared to those with proton to find differences due to the extra-nucleon and extra-energy deposition in the initial reaction step. The nucleon-nucleus reaction is the basic system that the available models can manage. The additional study of the deuteron reactions will show up the differences between the one and two nucleons processes, the influence of the energy deposition, and will produce data to compare the code-response to the most basic extension of the nucleon-nucleus process.

The experiment we present, was performed at GSI by shooting a $^{238}U(1A \cdot GeV$ beam into a liquid-deuterium target. The produced residual nuclides were fully identified in mass and atomic numbers, while flying forwards, using a magnetic spectrometer and a dedicated detection setup. This is a novel technique, a so called *inverse kinematics* experiment. Nowadays, accelerating ^{238}U ions at that energy and separating the heavy residues with high resolutions $A/\Delta A \sim 400$, is only possible at GSI. This is a very exigent technique, and any of the developed experiments in the program is a challenge itself. The setup peculiarity of this experiment was the use of a cryogenic target that allowed to study of reactions induced in hydrogen and deuterium. The proton and proton-neutron systems as target, were available for this kind of studies for the first time. The overview on the GSI facilities will show the requisites this new type of experiments must fulfill. Being the technique itself a challenge, the experiments have demonstrated the compatibility of the results obtained with previous existing data. Another success of this method is the large amount of high-quality data measured in just a single experiment. Something which is definitely an innovation in this field.

Since the aim of the work is the production cross sections of the residues of the reaction, we have to measure three independent parameters. The production rate of each nucleus has to be normalized to the beam intensity and to the target thickness. Despite the inherent constrains that high precision measurements impose on all the involved magnitudes, the most complicated part is the the definition of the production rates. Mainly because of the separation method needed to identify unambiguously each nucleus is very exigent for heavy products. The spectrometer we have used is the only one existing able to resolve heavy residues at relativistic energies. Different detectors are used to define the particle magnetic rigidity and its atomic number, and by using the procedure described in this work, the identification is fully unambiguous. The method proposed measures the cross sections as function of the longitudinal momentum distribution of the residue, providing additionally that magnitude. The momentum distribution is also a valuable information to constrain the theoretical models, and to define technical parameters in applications of spallation reactions.

The proposal of the project initiated at GSI, aimed at the high-quality of the data measured. The accuracy limit of $\sim 10\%$ for the cross sections down to 0.1 mb, was one of the points. That quality degree involves, together with the dedicated new experimental technique, the deep study of all the necessary corrections to define the cross sections. The production cross sections and momentum distributions of more than 500 residues have been measured for the fragmentation of $^{238}U(1\ A \cdot GeV) + d$. The result itself is an important collection of data in the topic of spallation reactions.

This dissertation opens with a brief review on the application and general understanding of the spallation reactions, and the particular contribution of the results obtained in this work within that scenario. Nuclear structure, nuclear Astrophysics, radioactive-ion beam production, alternative energy production in ADSs, ... are fields where the spallation process understanding is either an important clue or a powerful study tool.

In the following two chapters the experimental method used and the results obtained in this work, are shown. Firstly, the procedure used in this experiment is reviewed. The heavy-ion separation is a very exigent task, and it is worth to explain some points that characterize this technique. A detailed discussion of the identification procedure is given. It will be stated clearly how the produced nuclides can be identified, event by event, without ambiguity. The different corrections involved in the definition of the cross sections are discussed. The aim of measuring the values with high accuracy is an exigent constrain. The corrections are discussed and cross-checked with available and measured data. These cross sections are the main experimental result of this work.

The discussion of the data obtained, comparisons with existing heavy-ion reactions data, and the outline of the main features observed, is done in the following chapter. Both, cross sections and momentum distributions, are discussed together with results measured within the experimental program at GSI. The comparison of heavy-ion reactions where the fissility of the ions is very different, e.g. ^{208}Pb and ^{238}U, allows to discuss the influence of the fission channel. The fragmentation of ^{238}U with proton is also a counterpart to this work, and defines the differences due to the additional nucleon in the system. Already this overview on the results allows to present some guidelines on the possibilities of this experimental technique to produce exotic heavy ion beams.

In the last chapter we compare the data measured with theoretical models and calculations done with simulation codes, showing the *state-of-the-art* of the available descriptions. The large amount of data measured within this experimental program, allows very detailed comparisons. The more striking example is that of the isobaric distributions, where small accumulated differences show up, and test very exigently the codes.

To further investigate some related topics of our ^{238}U system, we propose a simple model to describe the nucleon induced reaction, and formation of the pre-fragments. Assuming the spirit of the Glauber model, a semi-classical impact model with a few and simple approximations, was implemented. This code was tested to perform realistically, reproducing the general trends and results measured in the proton induced reaction with ^{238}U. The alternative description of these complex reactions with simplified models is already a success. It opens the possibility of using fast and reliable code results, instead of the full and long-time consuming complete codes, that sometimes do not reproduce adequately the observed results. Another feature which can be investigated with our simplified code, is the influence in the results, of using a realistic nuclear shape. Since all existing microscopical models propagate the interacting nucleons within the matter distribution of the target, the actual shape of that distribution is implicated in the description. All codes parameterise a symmetric spherical target nucleus, and do not allow to alternatively study that topic. Our simplified model triggers also the discussion of some features of the deuteron induced reactions. The model was extended to a geometrical sequential impact of two nucleons. The results showed up a general good response when compared with the measured data, underlaying again the success of the Glauber concepts in the high-energy domain.

Chapter 1

The quest for spallation reactions

> *Within the large house of nuclear physics, research with relativistic heavy ions represents the department of material science*[1].

Very energetic heavy-ion reactions were studied first as *cosmic-rays* [1]. The observed particle cascades in the atmosphere due to the passage of a cosmic-ray, were interpreted as *spallation* processes. Since the high-energy accelerators became available, relativistic nuclear reactions were investigated under controlled conditions [2]. Starting in the 50's a lot of data have been accumulated on the heavy ion production topic. From the mid of the 70's the amount of data increased by using more sophisticated methods.

Relativistic heavy ions offer the possibility to study the properties of the nuclear matter under extreme values of density and temperature. These are quantities that interplay decisively in the dynamic properties of the nuclear matter. In particular, spallation and fragmentation reactions allow to investigate excited nuclear matter at normal density and low angular momentum. These conditions are optimal to investigate the onset of thermal multifragmentation, e.g., as well as some fission processes.

Relativistic heavy-ion reactions are of interest in nuclear Astrophysics and nuclear structure studies. The spallation is a process probed to influence the observed nuclear abundances in the Universe. It is present in both the *nucleosynthesis* processes and the distribution of the initial abundances due interstellar reactions of the cosmic-rays. Both heavy and light nuclei abundances are definitely influenced by those reactions. In a high-energy nuclear reaction, all particle stable nuclei with lower masses than the target or projectile can be produced. Many nuclei far from the valley of stability appear, and they may be studied before the β-decay chain bring them back to the stability range. In addition, the produced exotic nuclei may be used as *secondary beams*: the Radioactive Ion Beams (RIB, also called Radioactive Nuclear Beams) are an experimental tool since some time ago. Now it exists the possibility of producing intense radioactive beams. A more technical application of these reactions is the intense neutron sources topic, using spallation targets. Neutron sources are of deep interest in solid state studies, nuclear waste transmutation, alternative nuclear energy production and medicine.

---

[1] J.Hüfner, Phys. Rep. 125 4 (1985) 129

In the studies where spallation reactions are needed, many target-projectile combinations are required, in a wide range of energies. Of course, not all of them can be studied. Experiments are usually a lot of time, effort and money consuming, and limited by the experimental possibilities at a certain time. Theory and models must be used to describe the processes involved. In order to dig into general trends and benchmark the simulation codes and parameterisations, experiments provide valuable data.

In this chapter we will review some applications of the spallation reactions, the different approaches to study this process, and the general concepts that propose the models underneath the most widely used simulation codes, applied to describe the reaction.

1.1 Some applications of spallation-reactions

1.1.1 Radioactive Ion Beams

Nowadays it is relatively easy to produce unstable nuclei. The about three-hundred stable nuclei, which have benchmarked the nuclear theories of this century, have been extended to the more than 2900 nuclei known today. This opens the question about the adequacy of the existing theoretical description, developed for the stable matter. New phenomena, predicted and discovered, have arrived to the laboratories: halo nuclei, double and single shell closures far from stability, new deformation regions, ... The *proton drip line*, see figure 1.1, has been reached for elements with $Z < 80$; the *neutron drip line* only for elements with $Z < 10$. The study of exotic nuclei became more exciting since it was possible to use radioactive beams instead of stable ones. That is the *radioactive ion beam* RIB or *nuclear beam* RNB concept, that has changed the Nuclear Physics scenario in the last years. Of course the starting point is to be able to produce such non-stable beams. Several methods allow to produce different regions of the chart of the nuclides, in a variety of experimental conditions. Many experiments have been done to solve different quests accordingly to the mass ranges available in the facilities. New and ambitious projects have grown to extend the range of experiments. Two general methods are discussed nowadays in order to produce intense RIBs: *Isotopic Separation On-Line* (ISOL) and *in-flight separation.* The reaction mechanisms involved in any case are fission and spallation/fragmentation. The fission process populates the neutron-rich side of the medium weight isotopes. Fragmentation produces heavy and light isotopes in the neutron deficient side.

RIBs are produced at a certain rate depending on the reaction mechanism involved and procedure used, but the cross sections implied are often low, down to pb for exotic nuclei [3]. To the low production rates one has to add all those factors related to the separation technique. Some studies [4] dig into the secondary intensities that would be of interest for the near-future physics research, and quite high values are requested. Now the point is to define the most performing mechanisms and techniques to populate the different mass regions of nuclides.

ISOL production is based on spallation reactions induced by high energy protons or low energy neutrons on a heavy-element thick target. The reaction products are extracted by thermal diffusion, and transported to an ion source. Using thermal-chemical properties or laser methods it is possible to select the output nuclei from the target. The ~ 100

KeV ions are separated into a mass spectrometer and then prepared for a second-stage acceleration. This method cover energies around the Coulomb barrier up to a few tens of $A \cdot MeV$. The most representative EU project is EURISOL [5] and in the US the RIA [2] project [6]. The use of charged particle induced reactions means that the primary beam releases a lot of energy within the target (by electromagnetic interactions in addition to nuclear reactions). That energy deposition is crucial since the temperature is a very sensible parameter to control the production rate: the extraction techniques from thick targets are strongly dependent on temperature. Actually that parameter limits the beam intensity in many cases.

Neutrons are advantageous since only nuclear reactions deliver heat to the medium. Neutron induced fission of actinides allows to produce intense beams of isotopes in the region of masses A=80-150. Thermal neutrons from a HFR (High Flux Reactor) were proposed in the abandoned project PIAFE (Grenoble) and inherited by the MAFF project at the FRM-II (Munich) [7], the advantages of using ^{235}U being demonstrated: the only point is the complexity of handling of the source. Note that this proposed RIB techniques are based on fission residues. The Argonne group [8] proposed a different scenario for isotope production in the medium masses region: a high-intensity deuteron beam would hit a *converter target*, producing neutrons. The neutron beam resulting from the reaction would be focused forward and hits into a ^{238}U *production target*. The heat production is then decoupled from isotope production in the reaction. The concept was recovered by the french project SPIRAL-II [9]. The idea to use a deuteron beam and a converter was already pointed out in 1947 by E.O.Lawrence in the initial operating time of the Berkeley 184-inches cyclotron [10, 11]. Here we have the proposal of a neutron source by using a spallation reaction: a subject that is close to the study of neutron sources with spallation targets for transmutation of nuclear waste and the new proposed *accelerator-driven systems* power plants.

The most developed method for in-flight RIB production is the fragmentation of heavy ions, used at GSI, GANIL, MSU and RIKEN. The core of these studies since its origin. A heavy-projectile primary beam impinging into a thin target would produce many nuclei with energies about that of the projectile: in the $^{238}U(1A \cdot GeV) + Pb$ reaction, about 2000 residues would be produced [12]. In this method the kinematics have been reversed relative to the spallation process. This is the reason why *fragmentation*, instead of spallation, is the mentioned process. The separation of the reaction residues is done in-flight by using a magnetic spectrometer. The short times involved in the method (at $1A \cdot GeV$, below 300 ns for paths below 100 m) allow to separate short-lived species that would be difficult to see in ISOL setups. This method provides secondary beams at energies of some tens of $A \cdot MeV$ up to $A \cdot GeV$. For a review on in-flight separation see e.g. ref. [13]. A very interesting application for low energy fission studies has been developed and applied in ref. [14].

The fragmentation process populates mostly the neutron-deficient region, within the so called *fragmentation corridor*. The heavy masses reach the proton-rich limit of existence, the proton drip line. Beyond that limit we have an interesting region where many *proton*

---

[2] The RIA project includes ISOL techniques together with a new hybrid concept of in-flight separation plus re-acceleration after a stopping step.

emitters could be discovered. We are just now in the edge of starting experiments to investigate that new region, using fragmentation processes. The wide region in between the known nuclei and the neutron drip-line is nowadays being investigated by using fission reactions, which produces medium masses with A<170. The so called *cold fragmentation* channels, populated in the fragmentation processes, allow to explore the production of heavy neutron-rich nuclides. Heavy-ion fragmentation and inverse-kinematics is one of the most promising methods to investigate that production of that region [3].

The inverse kinematics technique is the method used in this study of the fragmentation residues in the reaction $^{238}U(1A \cdot GeV) + d$. More than 500 nuclides were identified as fragmentation residues. When the whole residues of the reaction, fission included, be analysed, we will see the large isotopic range that the method can cover. That is also the case of the proton and deuteron induced reactions in $^{208}Pb(1A \cdot GeV)$ [15, 16]. In experiments scheduling the use of exotic nuclides, very low reaction rates are expected, and that is the main drawback. The design of such experiments rely on a realistic evaluation of the production rates involved. In many situations either the needed data are scarce, or the complexity of the whole simulation too high. The models describing the spallation reactions, and the simulation codes where the *state of the art* of the understanding of the processes is applied, must demonstrate their capability. The experimental results allow both, to exigently benchmark the simulation codes, as well as to trigger the understanding and the improvement of the models. Nuclear reaction descriptive codes and transport codes are under test.

1.1.2 Neutron sources and ADS

In solid state and material structure studies, the neutrons are a very interesting tool [17]. Although the idea of using neutrons is not new, only recently powerful neutron-source projects are on the way, mainly triggered by the interest on *nuclear waste transmutation* and *accelerator-driven systems* ADS. Several facilities in Europe are in operation as the continuous source PSI-SINQ [18], or under study as the pulsed source ESS [19]; in the US is also the project SNS [20]. The production of isotopes for medical applications, e.g. ^{99}Tc, is also feasible by this method. Also tritium, being an strategic component in the defense policy of some countries, may be produced by these sources: that is the aim of the US project APT [21] and the french abandoned project TRISPAL [22].

The study of the intense neutron sources is very close to one of the most well known technological applications: the so called *hybrid systems* or *accelerator-driven systems* (ADS). The topic has produced a lot of interest from other scientific communities[3]. These

---

[3] Some numbers: $\sim$ 20000 million tones of CO_2 are emitted annually from the burning of fossil fuels; one third of this fuels are use to produce electricity. To stabilise the CO_2 concentration in the atmosphere at present levels a 50-80 % reduction in the emissions is required. The emissions due to electricity production were reduced by 80% in France in the period 80-87, by increasing the nuclear capacity. In the scenario of substitution of fossil fuels and natural gas by another massive source of energy, only nuclear energy competes at reasonable costs. In 1993 about 17% of worldwide electricity was generated by nuclear technologies: 26% in USA, 38% in Switzerland, 36% in Spain, 31% in Japan, 30% in Germany, 78% in France. Since the 60's, when the nuclear technology expanded, $\sim$ 160000 tons of highly radioactive waste have been produced worldwide. Such waste needs $\sim 10^5$ years to reach natural radioactivity limits. (The

systems are sub-critical reactors. The excess of neutrons they need, can be provided by spallation reactions. In addition, instead of using fissile nuclei in a U-Pu fuel cycle, they can use fertile nuclei and the alternative Th-U cycle. The quantity of effectively used fuel would increase largely, since the burnt fuel of the present reactors can be used in alternative solutions. The spent-fuel residue inventory would be enormously reduced, as well as the long-time potential hazards. The most developed proposals are those reviewed in refs. [23, 24].

In most of the designs of ADSs a proton beam hitting a lead-target would be the neutron source. The direct and compound nucleus reactions within the thick target would produce ~ 30 neutrons per incident proton ($\sim 1\ A \cdot GeV$), peaked in the 1-10 MeV region. Inelastic scattering first and elastic scattering later, shift the spectra to values below 600 KeV. That neutron flux is the bath that reaches the fertile material placed in the surrounding blanket. The fertile nuclei produce fissile nuclei after neutron absorption and radioactive decay, triggering the reaction chain that drives the fission in the system. The fission heat is the energy source. The rest of the technology is the usual one for thermal to electrical power conversion in reactors. The idea of using a deuteron induced spallation system either to produce ^{239}Pu from depleted uranium, or as a neutron source for fission reactors, was early outlined [11].

To face a rigorous study of the feasibility and design of an ADS-based reactor it is essential to optimize the target-blanket assembly. It is necessary to obtain information from spallation reactions relative to (a) the number of neutrons produced according to the target material and geometry, what is related to the ratio of the produced and accelerator-recycled powers; (b) the energy and angular distributions of the spallated particles, needed to optimize the target geometry and to study the structural and target materials damage; (c) the isotopic distribution of the residues, related to structural problems, radioactivity, gas production, ... One of the most important points in an ADS design is to ensure that the residue inventory is certainly improved form the present-technology inventories. Another important point to take care of is the radiation damage of structure materials. Radiation introduces changes in diffusion, composition, phases, micro-structure, ... it may produce chemical corrosion and embrittlement of structural materials. The material mechanical yield stress, have been demonstrated to correlate strongly with the number of the so-called *atomic displacements* (dpa). The possibility to calculate the dpa in a certain material depends on the knowledge of the production cross sections, angular distribution and momentum of the recoil residues. The activation of the materials is also a source of radioactive waste. Additionally the production of gases (like helium and hydrogen in a spallation environment) has strong bearings on the structural damages caused to the target and window materials used at the target station.

Being the global description of an ADS system so complex, the help of simulation codes is essential to successfully describe the processes involved. Realistic nuclear and transport codes are needed. It has been stated that the existing codes need important improvements in order to produce realistic results [25, 26]. Two types of measurements are needed to benchmark the codes, specially above 800 $A \cdot MeV$:

---

data are from the United Nations).

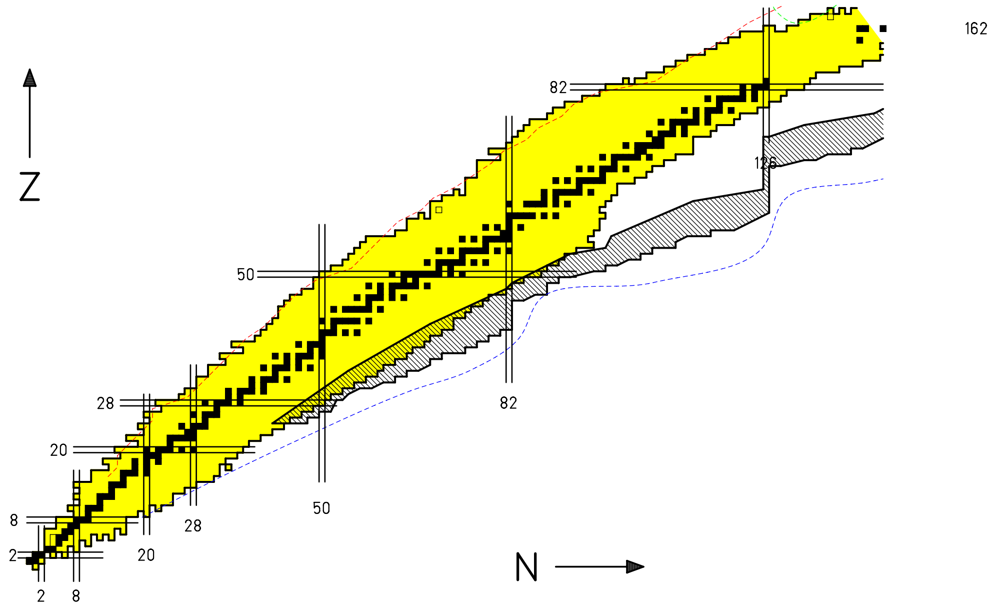

Figure 1.1: Chart of nuclei showing the stable nuclei (squares), the known nuclei (shadowed area) and the magic proton and neutron numbers. The *s-process* path lies on the β-stability line. The *r-process* path is the stripped region below. The proton drip line and neutron drip line are also plotted as dashed lines.

- fundamental cross sections, to further develop the existing nuclear model codes.
- thick target results, to study the transport codes and the target performance.

The present projects of ADSs always consider proton beams impinging into heavy targets as the neutron source. That is the result of a criterion based on the maximisation of the total neutron yield. Nevertheless, a deuteron beam and a light target used as converter to produce the neutron fluxes, could be a very competitive process with different advantages. That can lead to different project criteria. Only by performing realistic calculations it is possible to define the most interesting scenario for that alternative technology.

In the study of the residues of the reaction $^{238}U(\ A \cdot GeV) + d$ we cover several aspects of the discussed topics. In this work we measure the cross sections of most of the residues with productions above 0.01 mb. Also the momentum distribution is measured. The new results are discussed together with other data of heavy-ion reactions. In this way we can outline the differences that can be explained by the characteristics of each system. The large amount of data we have measured allows also to discuss the behaviour of the standard codes that are available to describe different processes involved in the reaction.

1.1.3 Astrophysics: cosmic-ray interactions

Basic questions for nuclear Astrophysics are the origin of the isotopes we find in the Universe (*nucleosynthesis*), and the role of the nuclear processes as sources of energy involved in the astrophysical events. A general review on Astrophysics related topics is e.g. that of Rolfs-Rodney [27], and one dedicated to cosmic-ray extracted information is e.g. that of Shapiro-Silberberg [28].

In the description of the *nucleosynthesis* process, the proposed theories have to correlate with the observed distributions of nuclei. The so-called *local galactic abundances*, are the element and isotopic abundances in the solar system. The cosmic-ray matter observed in the space[4] is a sample of the matter in our Galaxy and also from outside. In the late 40's Gamow and others proposed the *universal synthesis hypothesis*: the elements would have been formed mostly in the early universe. The nucleosynthesis process initiated with the deuterium and other light species formed in the *big-bang*, would continue by successive neutron-capture and β-decay. Working the whole universe as a kind of fusion reactor, the similar abundance distributions observed appear to be natural. But masses five and eight present nuclear stability gaps that make the way beyond ^4He practically impossible. In 1957, a new theory proposed that the elements were actually formed in the interior of the stars. However, in 1964, it was recognised that the amount of light species, as ^4He, could not be provided by the processes in the stars. Nowadays a double hypothesis is accepted. A *primordial nucleosynthesis* accounts for the formation of ^1H (75%) and ^4He (23%) and some other light nuclides (^4He, ^2H, ^3He and ^7Li). Some 10^9 years after the big-bang, galaxies and stars would form from that material, and the cooking of heavier nuclei was possible. The gravitational condensation provides the thermal energy to start the nuclear reactions. That burning will provide energy to stabilize the star. Once a certain fuel is exhausted, a new gravitational contraction make the temperature to raise, and a new reaction chain may start. These different steps would be able to produce nuclides within certain mass ranges. The origin and population of many of the nuclei is possible within that model. The overall similarity between the two element distributions, local and cosmic-ray patterns, reinforces the model for the nucleosynthesis as it is.

The production of nuclei with masses above 60, would be possible by the *s-* and *r-processes*, when the neutron-capture and β-decay channels, compete to produce heavier nuclei[5]. The *s-process* production follows closely the valley of β-stability. The s-models are widely accepted and reproduce many of the relevant aspects of the abundance curves. Nevertheless when there is a mass gap in the isotopic chain, the *s-process* may continue only by β decay, and some nuclei cannot be produced in that way. If the calculated s-abundances are subtracted from the measured abundances, strong peaks appear at char-

---

[4] The energy spectra of the cosmic rays is continuous, reaching 10^{14} MeV, mostly in the range 100-3000 MeV. The composition is about 87% hydrogen, 12% helium and 1% heavier nuclei. There are evidences that most of the cosmic rays below 10^9 MeV have their origin in our Galaxy, and the rest are probably extra-galactic. The abundances of those high-energy cosmic rays are a source of information about the composition outside our Galaxy. It is actually the only sample available. There is no model explaining either the acceleration mechanism, or their cosmic birth-place. The local and cosmic rays abundances comparison is important to test the nucleosynthesis models. In addition the radioactive species, being kind of galaxy-clocks, give information on the acceleration times, and some age-related parameters.

[5] The *slow* s-process is feasible when in between two neutron captures the delayed time allows for any β-decay to happen. The *rapid* r-process happens within high neutron fluxes, allowing for many captures and neutron rich isotopes to be produced. Characteristic of the latter process are the so called *waiting points*, when the capture is delayed. See the references for details and the figures in the chapter.

acteristic masses. Most of those lacks are overcome if the *r-process* is considered. This process is believed to explain the abundances of many trans-iron nuclei, and all of those heavier than ^{209}Bi. The main difficulties to understand the *r-process* are the cosmological sites where the restrictive conditions allowing this process could be possible, e.g. the outburst of Supernovae. The abundances produced by this process are defined by the (n,γ) and (γ,n) reactions, which depend on the neutron shell positions. A third process of interest is the so called rapid proton capture *rp-process*, following the proton-drip line. It is related to Nova, and X-ray bursts and pulsars. A better understanding of this process will help in topics as isotopic anomalies in meteorites, time of the bursts and light curves, population of the neutron-defficient isotopes of the Mo-Ru, ...

The observed abundances are partially modified from those of the original production, since the reaction of the cosmic-rays with the interstellar medium changes the distributions. It is the case of the spallation of the abundant ^{56}Fe, whose interaction with the H and He in the medium produces most of the observed Sc-Mn isotopes. The product abundances are a constrain for the amount of matter traversed by the cosmic rays. Specific nuclides can probe the confinement time in the Galaxy, and the modes of acceleration of the cosmic-rays. Some abundances are a source of discussion, not being fully understood: e.g. the highly-reactive light elements Li-Be-B abundances are orders of magnitude higher in the observed matter outside the solar system. An alternative *l-process* was postulated, requiring low temperature and/or densities, to overcome fast destruction of these highly reactive species. The spallation of cosmic rays is the most probable candidate for this process.

Radioactive beams allow to study sistematically the nuclear structure, reactions, decays, masses, ... necessary to understand the astrophysical scenario, which we have seen happens often in regions of yet unkown nuclides. The study of several key nuclei will allow to stablish the general nuclear trends far from stability: large skins, quenching of shell gaps, (n,γ) and (γ,n) strengths, ... Improved models with detailed treatment of different reaction mechanisms and transport are needed to explain the differences between abundances and the interplay between stellar and primordial nucleosynthesis, as well as many different subjects. Spallation reactions are of interest in Astrophysics for a double reason: because they are one of the processes defining the isotopic abundances; and because they provide a powerful tool, the radioactive beams.

1.2 The spallation data quest

The amount of energy present in relativistic nuclear reactions induces the production of many fragments. Disregarding elastic scattering studies, exclusive experimental results on heavy-ions are scarce, due to its high complexity . In the one-particle inclusive measurement, a projectile nucleus with certain energy strikes a target nucleus; a resulting heavy fragment is identified, and its recoil energy and angle measured. The differential production cross section $d^4\sigma/dAdZdEd\Omega$ is the complete information available. The inclusive results suffer from a partial loss of information: in our experiment the cross sections were measured integrated over angular distribution $d\Omega$. Since the 50's data about the production of heavy fragments have been obtained, especially for proton induced reactions for Astrophysics related topics. In the last years the spallation targets used as neutron sources, have pushed strongly the interest and effort deployed.

The traditional approach to investigate the residual nuclei produced in spallation is by accelerating light particles that hit a target. The resulting target break-up fragments were usually stopped within the material. By using *γ-spectroscopy* methods, the residues are identified. The method consists in measuring the characteristic gamma radiation that appears during a decay chain. The cross section of a certain nucleus appear from the balance of the channels populating and depopulating the isotope. The values are always relative, referred to the production of a monitoring isotope. The spectra is typically very complex, with a strong background to be subtracted. Most of the isotopes produced in the reaction are short-lived and only the beta-decay chain products within the analysis time (from hours to days) are observed. The relative simple setup and short irradiation times involved make the method very attractive to study many material combinations and energy ranges. Wide and systematic studies have been done at the University of Hannover by a group lead by R.Michel [29], and at ITEP-Moscow lead by Y.T.Titarenko [30].

A different method is based in *mass spectrometry* techniques. The ions are extracted from the target and re-accelerated to a certain energy. Using a dipole and a velocity filter, the nuclides can be identified in charge and mass. The technique is possible for stable nuclei but in the case of radioactive ones, it is necessary the use of accelerators and reactors: this method was introduced by R.Bernas at IPN in 1960. In the case of fission products, it is possible to detect the nuclei in direct kinematics if they leave a very thin target. Sometimes the energy they carry is not enough to identify in charge, but they can be identified in mass by measuring the time of flight and energy [31]. Since the 70's, triggered and lead by the Berkeley group, heavy projectiles have been accelerated and different detection setups have been used. The detection in charge is relatively easy for relativistic residues. The experiments performed by Cummings [32] and by Waddington [33], and other groups measured the charge-exchange cross sections for many different heavy projectiles.

At the *Gesellschaft für Schwerionenforschung* GSI (Darmstadt, Germany) together with the spallation process, the fragmentation residues are also investigated in *inverse kinematics*: now the target is a light mass nucleus, and the accelerated nucleus, a heavy one. The resulting reaction fragments will keep the kinematic properties of the projectile, leaving the target, and can be studied in detail by using spectrometers. Note that traditionally the so called *residue* was the final result from the β-decay chain. Now the residues are the direct particle-stable nuclei produced in the reaction, i.e. the primary production of the reaction. From the reaction point of view there are no difference between the spallation and fragmentation processes. Form the experimental point of view only a change of system of reference is done: from laboratory to projectile reference systems, the same physics involved. This experimental technique has only been deployed so far at the BEVALAC [34] and at GSI so far.

One of the most detailed and systematic approaches to study the fragmentation at relativistic energies was initiated by a GSI-patent in 1995 and started in 1996, within a collaboration of different EU institutes. The purpose was to study a set of systems to obtain a systematic and representative overview, and to define a benchmark data collection in order to compare the results of the codes related to the spallation topic. The involved institutes together with GSI are the *Institute de Physique Nuclèaire* IPN (Orsay, France), *Commissariat à l'Energie Atomique* DAPNIA/SPhN (Saclay, France), *Centre d'Etudes Nuclèaires* CEN-BG (Bordeaux, France), and the *Universidade de Santiago de Compostela* (Spain). The experimental program included proton and deuteron induced reaction in heavy ions

- $^{208}Pb(1.0, 0.5A \cdot GeV) + p, d$ [15], [16]
- $^{197}Au(0.8A \cdot GeV + p)$ [35], [36]
- $^{238}U(1.0A \cdot GeV) + p, d$ [37], this work
- $^{56}Fe(1.0, 0.7, 0.5A \cdot GeV) + p, d$ [38]

The experimental task was accomplished in October, 2000. The results have been partially analysed and published elsewhere. The work is focussed in relativistic energies and heavy-ion results. That is the reason for studiying ^{208}Pb and ^{238}U. The strongest difference between both projectiles is their fissility. The ^{197}Au data provided the test of the whole experimental method, and very interesting and new discussions. The ^{56}Fe data will allow to complete the mass range study, as well as to provide data closely related to the material needs within the ADS projects. The heavy-ion systems are studied in reactions with protons and deuterons. The nucleon-nucleus system is the basic reference that the standard simulation codes can manage. The study of the deuteron reactions will show up the differences between the one and two nucleons process, the influence of energy deposition, and will produce data to compare the code-response to the most basic extension of the nucleon-nucleus mechanism.

1.3 Interpretation of the reaction mechanism

Spallation reactions were studied in the laboratory in the late 40's at the Berkeley cyclotron for the first time [39]. The early description of the process given by Serber [40] was that the incident particle collides with several nucleons, losing a large fraction of its energy. The system becomes excited and particle-unstable, and emits nucleons. This *two-step* model, is the image for high-energy fragmentation reactions since then. The model was originally called *cascade-evaporation*, and later referred to as *abrasion-ablation* in ref. [41]. The two names refer nowadays to the microscopic and macroscopic approaches, but many times confused.

The fragmentation is in general a hot process: the *pre-fragment* formed after the initial collision of the nuclides is generally highly-excited. The de-excitation of the *pre-fragment* is mostly by emission of particles (*evaporation*), producing the final residues of the reaction or *primary production*. Many radioactive species are produced, and they decay according their half-life. The resulting products of the α- and β-decay chains are not longer the actual production of the reaction. The two steps in which the reaction is described, occur in two different time scales. The characteristic time for the abrasion stage is that of the participants passing through each other, some 10^{-23} s. During the second step the system de-excites by emission of nucleons or light nuclei, fission and emission of γ-rays. During this step there is a competition between all those processes. The times involved are in a range 10^{-16} s at 10 MeV, till 10^{-21} s at ∼200 MeV.

The models that describe the second step of the reaction, assume that the *pre-fragment* is a *compound nucleus*, becoming thermalyzed [42], as well as the different nuclei populated successively in the de-excitation chain till the excitation energy is dissipated. The thermalization hypothesis is actually an unproven assumption. By looking at the time-energy dependence it is rather difficult to support the thermalization hypothesis in the higher range of the excitation energies of the pre-fragments [43, 44]. If accepted, it allows the use of the statistical model [45] to define the probability of each decay channel and parameterise the process within a standard evaporation-fission model. The thermalization is equivalent to a maximum loss of memory of the initial conditions. In high-energy reactions there exists many direct experimental proofs of such loss of memory: target mass scaling for the mass yields, the isotopic distributions, the maximum production position, and the isotropic angular distributions, ...

In this work we only consider the fission and fragmentation mechanisms in the reaction, being both responsible for most of the production we observe in the reaction of $^{238}U(1A \cdot GeV) + d$. The lighter the residue, the more excitation energy had the original pre-fragment. The higher energies trigger the population of different processes as that of *deep spallation* and *multifragmentation*. Those reactions cover a reduced part of the distribution of the produced residues, and will not be discussed within our results.

1.3.1 Fast initial step

For energies large compared to the Fermi energy, the nucleus-nucleus collisions proceed by nucleon-nucleon interactions instead of mean field interactions. That is a picture valid in the high-energy approximation. The nucleon-nucleus reactions are described microscopically, nevertheless some concepts of the macroscopical description, usually applied to ion-ion collisions, are very useful in further discussions and we review them briefly.

The overlapping areas of target and projectile trajectories contain the nucleons that actually interact in the collision. When the nucleons collide at high energy, little transverse momentum is exchanged. For large longitudinal momenta, it induces small scattering angles, and the collision picture is that of the nucleons moving in straight lines. For a given impact parameter, the nucleons which lie in the geometrical overlap between projectile and target are called *participants*. Outside the interacting region the nucleons are *spectators*. After the abrasion, most of the participants have left the collision region and only the spectators remain. The target spectator is nearly at rest and the projectile spectator moves with almost the projectile velocity. These spectators constitute the *pre-fragments*. The participants constitute the *pre-equilibrium emission*. The spectator matter is then the source of the observed heavy fragments, as it is supported by the measured kinematics of the fragments, that are either slow or move at beam velocity. Here we have the distinction between the *target-like* and *projectile-like* residues. This geometrical picture has been justified by Hüfner [46]. The statistical treatment of the abrasion model has succeeded in the description of nucleus-nucleus reactions [47].

Microscopically, the process is described as a series of nucleon-nucleon interactions: the *intra-nuclear cascade* INC. The description is usually semi-classical, where the nucleons see each other, and quantum effects as e.g. Pauli blocking, are taken into account. Although many approximations are used in those descriptions, the INC models contain the *state-of-the-art* of the knowledge related to the description of the nucleon induced reactions. These models, implemented in simulation codes, are used to estimate the results in a wide range of reaction possibilities. They are exigently tested when compared with the available experimental data. Some of these standard simulation codes will be briefly described and used to discuss the measured data in the last chapter. The possibility to compare the performance of widely used codes with our deuteron induced reaction data, allows to discuss the behavior of the codes in the simplest extension from nucleon-nucleus to nucleus-nucleus interactions. Our interest is focussed in the interplay of the geometrical description of the deuteron impact as a double collisions of nucleons. Also the comparison of the results from heavy-ions reactions with very different nuclear shapes, as ^{208}Pb and ^{238}U, triggers the question of the possible influence of the actual shape.

The standard codes cannot implement alternative studies, and we investigate those topics within a simple semi-classical INC model we propose. Since the overall results of the standard codes are rather poor in some cases, and additionally time consuming, we compare the performance of this fast simplified model, which opens the possibility of alternative description in particular and demanded applications.

1.3.2 Evaporation-fission step

In realistic INC microscopic models, the evolution in time of the excitation energy in nucleon induced reactions, increases fast till reaching a maximum, and then it decreases: fast at the beginning and slowly later on. The different parts are interpreted as the initial energy release by the projectile, the fast energy loss due to pre-equilibrium emission, and finally the slow phase is identified with the evaporation. The INC models support the idea of the second step, the evaporation phase. Nevertheless the model is not well suited for the whole description. Once the pre-fragment, the spectator left over, is formed it undergoes different processes to produce the observed residues. Its excitation energy is distributed in a wide range from some MeV till 1 GeV. The starting assumption is that the processes happen on a *compound nucleus* [42]. That means that the pre-fragment is thermalyzed, the excitation energy distributed among all degrees of freedom, and the entrance-channel memory lost except by the energy, angular momentum and parity, that are conserved in the whole process. Assuming that all open channels are equally likely populated, the statistical method defines the transition rates for the different processes: gamma emission, particle emission, light particle (α, Li, ...) and cluster emission and fission. The method was presented in the work of Weisskopf [45] for neutron evaporation, and there were soon extensions to more channels.

The statistical model describes the emission of particles from the principle of *detailed balance*. The decay rate of a certain channel depends namely on the nuclear level densities of initial and final states, and transmission coefficients of the inverse process of emission. The original treatment of Weisskopf included only the energy conservation, while the right angular momentum coupling was added later in the Hauser-Feshbach formalism [48]. A complete classical description is reviewed e.g. by Ericsson in ref. [49]. The introduction of the basic concepts of the statistical model will be done in the Chapter 5.

Fission is described alternatively with the Bohr-Wheeler *transition-state method* [50]. The transition rate depends for fission on the properties of the compound nucleus at the saddle point (the transition state). Already in the early work by Bohr-Wheeler the nucleon emission and fission were treated separately. The difference is inconsistent, since between fission and evaporation only the relative size of the emitted particle and residual nucleus, change. Moretto [51] and Swiatecki [52] claim the necessity of treating the evaporation in the same manner than fission. For a general review on the method and related discussions see e.g. [53, 54]. Those details are beyond the scope of this work, and will not be discussed.

1.3.3 Pre-equilibrium models

We have described the two-step process by using a two-step model: an overall description does not exist yet for high energies. The second part of the process assumes that the thermalization is reached. The abrasion models switch the treatment directly. The INC-codes include always a finishing condition, so that the cascade is considered terminated, and the new step treatment starts. The switching between the two steps sometimes seems too sharp, and the only solution so far is to couple a third step in between.

The possibility to incorporate a transition process in between the INC and the evaporation-fission, enters the problematics of the thermalization time in high energy regions. It should be a kind of soft-transition, allowing the system to reach the equilibrium, while undergoing some emission process. That is described by the so called *pre-equilibrium models*, see e.g. ref. [54] for a general overview. Some comparisons between the two- and three-step models show not very convincing results till now. The Cugnon model coupled to some transition step, showed no clear advantages while adding the inconvenience of a changing time between the two treatments [55]. Some other recent studies [56] also conclude that the effects of a third-part, seem not to be decisive in the final results. According to these results and to keep the description the simplest, in our work we have decided not to consider the possibility of the pre-equilibrium models contribution in the reaction simulation.

Chapter 2

Experimental procedure

In order to investigate the residual nuclides produced in the reaction $^{238}U(1\ A\cdot GeV)+d$ we propose to measure the isotopic production cross sections and longitudinal momenta. To define the isotopic production cross sections we have to measure three independent magnitudes: the beam current, the target thickness and the isotopic production rates. The latter value is, roughly, the counting observed of a given residual nucleus. The former values normalise the rates. We have measured the production in *inverse kinematics* because the fragments produced in the reaction are projected forwards, and can be analysed with a magnetic spectrometer. The isotopic identification is achieved by measuring both the atomic number, and the mass-over-charge ratio of each nucleus. The measurement in done in a short time, below 300 ns, allowing to observe the primary production prior to any radioactive decay. Additionally the different kinematics involved in the main reaction mechanisms of fission and fragmentation, allow to separate the two contributions from each other.

A brief introduction of the facility where the experiment was done opens the chapter. The possibility to accelerate heavy nuclides like ^{238}U up to an energy of $1\ A\cdot GeV$ is already a challenge, and it can be done nowadays only at the GSI. A second challenge is the necessity of a high resolution detection setup to provide the separation of the produced nuclei, due to the very exigent resolution conditions that heavy-ions at relativistic energies impose. That is possible with the in-flight separator *FRS* at GSI. Since the aim of the experiment is to perform the measurements of cross sections with high precision, the setup was designed to be able to separate the heavy ion residues, and to identify them clearly. The identification will depend on the magnetic separation of the nuclear mass to charge ratio, and the definition of the nuclear charge. The mass resolution becomes a key problem for heavy-ions, since the relative change in magnetic rigidity[1] is drastically reduced: ~6% for $^{16}O-^{17}O$, ~1% for $^{103}Rh-^{104}Rh$, ~0.4% for $^{237}U-^{238}U$. Also the charge definition is problematic since the heavy ions show a certain ionic charge distribution. That means on the one hand, that the resolution obtained from an energy loss measurement is reduced;

---

[1] The magnetic rigidity of an ion is the ratio of the momentum over charge. From equation 2.4 we see that for a given atomic number Z, and supposing negligible the difference and spread in $\beta\gamma$ value, the relative change in rigidity is
$\delta(B\rho)=(B\rho-B\rho|_o)/B\rho|_o=(A-A_o)/A_o$. That is the change solely due to the mass change.

on the other hand, it makes mandatory the measurement of both, the ionic and nuclear charges. Only for that case the isotopic identification is possible without ambiguities. In the chapter it will be discussed how the different magnitudes involved in the definition of the cross section can be measured, and the identification performed unambiguously, event by event. Also the study of the setup performance was necessary in order to describe all the corrections necessary later to define the production rates. Another feature was the use of a cryogenic system for liquefied deuterium as target, also a challenge of this experiment, and necessary for the the precision aimed in the experiment.

At few $A \cdot GeV$ the heaviest elements loose their electrons. The SIS energy was chosen 1 $A \cdot GeV$ to guaranty a high yield of fully stripped U ions. The possibility to define the nuclear charge with enough resolution for high charges and to disentangle the different ionic charge states of the nuclei, is achieved by using a *degrader* and the so called *energy-loss* method, as well as a combined measurement of the energy loss in two ionisation chambers. For elements with nuclear number Z below $\sim$ 70 the two drawbacks are overcome and the *degrader* is not longer necessary. In the experiment the whole charge range of residual production from fragmentation and fission has been measured. Fragmentation production stands down to $Z \sim 55$. In this work the production of residues with $Z > 64$ are presented. For $Z > 68$ the two procedures, with and without degrader, were used. The comparison of the results obtained will show additionally the full compatibility of the corrections applied to the measured yields, and discussed in the next chapter.

2.1 The experimental facilities

2.1.1 The GSI accelerator system

The GSI (Darmstadt, Germany) is presently one of the most representative facilities for relativistic heavy-ion nuclear research. Since 1992 the SIS synchrotron [57] can accelerate ions from hydrogen till uranium. In 1993 it was achieved the first spatial separation of uranium isotopes [58]. The limiting magnetic rigidity of the synchrotron is 18 Tm, corresponding to energies of 1.0 to 4.5 $A \cdot GeV$ depending on the ion. No other facility nowadays achieves that range of energies for heavy ions. Typical maximum intensities delivered by the accelerator vary from 10^{11}, for Ne, to 10^{9}, for Au or U, particles/spill in 2001. The available intensities depend mostly on the operation of the ion sources[2]. The extracted ions are then injected into the linear accelerator UNILAC, providing energies about 11.5 $A \cdot MeV$ at the exit, see figure 2.1. The ions are then injected into the SIS, with four bunches for U, achieving the working energy: 1.0 $A \cdot GeV$ for the $^{238}U^{+73}$ ion in the present experiment. The beam momentum spread $\delta p = \Delta p/p$ is kept below 10^{-3}.

The beam can be driven to different experimental areas. In our experiment it was injected into the *FRagment Separator* (FRS) area. The *slow extraction* procedure used

---

[2] Different ion sources are used (CHORDIS, PENNING, MEVVA and high-charge-state-injectors, ...). The different treatment on extraction profits from selective properties of the elements that are required. Typically different charge states pass to the acceleration stages. There they are identified and the most populated state is selected for tuning the beam.

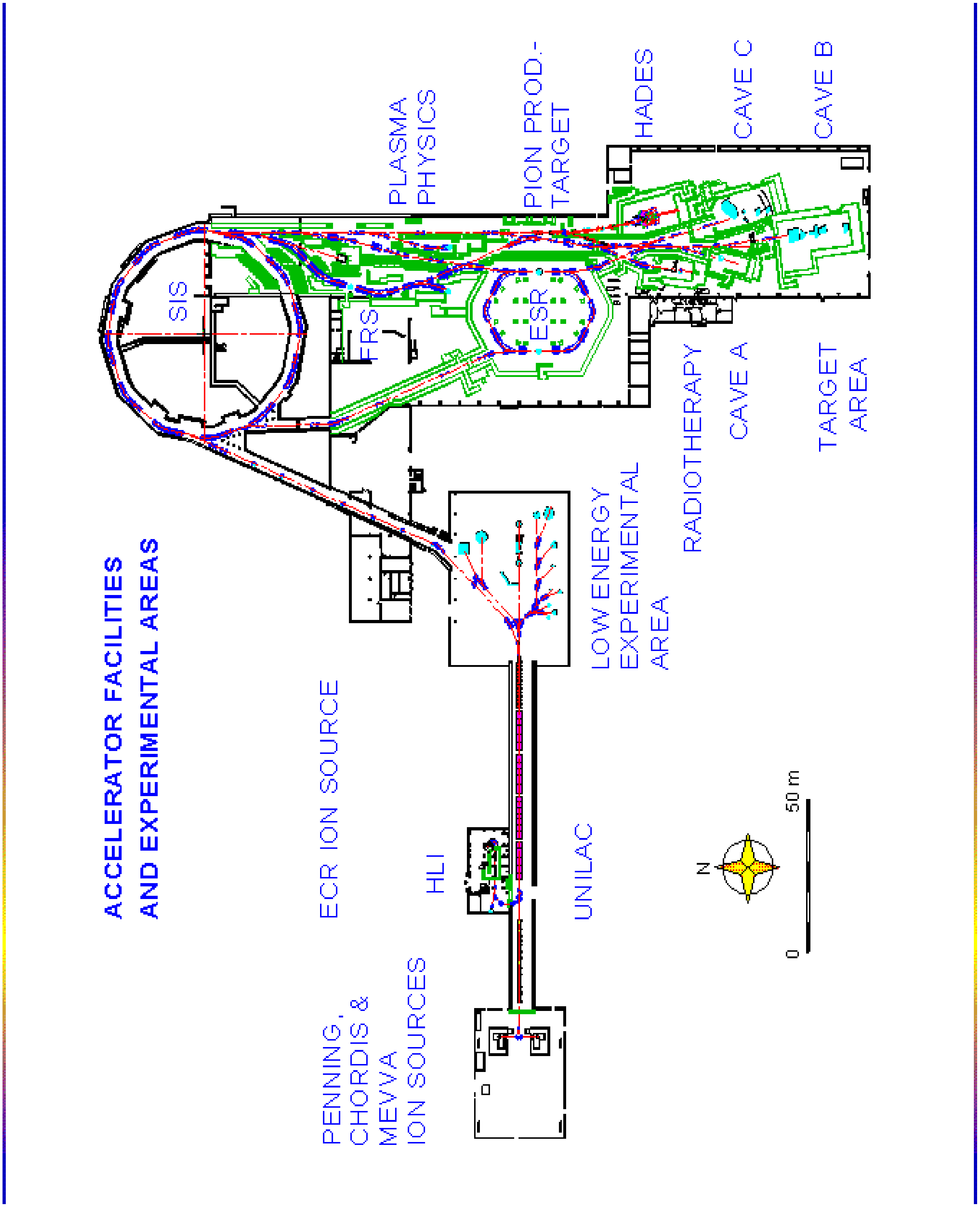

Figure 2.1: Schematic view of the GSI facilities. From the ion sources (left) the ions accelerated in the UNILAC, are injected into the SIS synchrotron. The beam is accelerated and then shaped during the extraction, being driven till the different experimental areas. The FRS is the S-shaped structure in between the SIS and ESR. It is ∼ 70 m long, and the key piece in the separation of heavy ions.

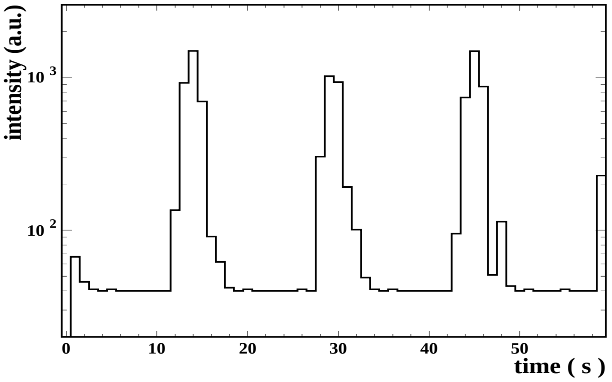

Figure 2.2: SEETRAM-counting as a function of time, for a certain time interval during the experiment. The beam spills have a length ~ 6 s and are repeated each ~ 15 s. We can also see the base line due to black-currents in the monitor. See the text for details.

keeps low beam emittance values and a time structure of few seconds. The *spills* delivered to the experimental areas are actually feed by the bunches in many turns, and after a cycle the SIS is refilled by the LINAC, repeating the sequence. Both processes result in the spill time-pattern. During the experiment the usual spill time-pattern was a 6 s spill every 15 s. In figure 2.2, a plot of the beam monitor SEETRAM (see below) as a function of time, shows the typical spill structure. The Gaussian-like profile provides the beam current, as explained later.

2.1.2 Beam current monitor

A *SEcondary Electron TRAnsmission Monitor* (SEETRAM) is used in order to determine the beam intensity impinging into the target [59]. The SEETRAM consists of three Al-foils, placed in vacuum in front of the target. The outer layers are both connected to a positive voltage and the inner one to ground. The secondary-electron emission induced by a relativistic ion beam passing through the inner foil is driven to the outer layers due to the potential. The resulting positive current in the central foil, is measured by a *current digitizer*. This device converts the current into a voltage; after passing a filter the voltage in converted into a frequency, which produces the digital output signal, here referred to as *SEETRAM units*. Additionally the black currents in the monitor produce a quasi-constant background, inducing a continuous counting even if no beam is triggering the secondary current, see figure 2.2. That *SEETRAM background* has to be taken away when measuring the number of *SEETRAM units*, to obtain the actual secondary emission:

$$N_{tot} = N_{SEETRAM} - N_{background} \tag{2.1}$$

The absolute calibration of the monitor depends on the ion type, as well as the energies under consideration. The calibration is then performed by comparing the counting with an additional detector system: either plastic scintillator counters or ionisation chambers. A review on the method is found in ref. [60]. In section 3.1 we show the calibration curve obtained in this experiment. The calibration is extended to high intensities since no saturation effects were neither expected nor observed. By using that procedure several times per run, one can ensure an accuracy in the measurement of the beam flux of a few per cent, needed in this experiment.

Due to the different beam intensities that are requested during the experiment to fit the maximum production to the acquisition rate, the SEETRAM range is selected accordingly. The range factor, *sensitivity*, goes from $10^{-4} - to - 10^{-10}$ A, full scale. The full scale current produces an output of 1 V and 10 KHz C: the maximum rate being always 10^4 Hz. The calibration provides the conversion factor between the actual number of counts and the secondary-current units:

$$N_{beam} = N_{tot} \cdot f \cdot 10^{10} \cdot sensitivity \tag{2.2}$$

The *f* factor is the calibration factor and it was measured in our experiment to be 290.3(29.0) counts per SEETRAM-unit [3]. The monitor is designed for high counting rates, when so no single event counting is possible.

2.1.3 The deuterium target

The target thickness wasps about 10% of the projectile range: that is a typical value which meets the conditions of maximum production while keeping low the secondary-reaction rates within the target, and preserving the energy range of the residues, see ref. [61]. By reason of its density, in this experiment we used a liquid target, what includes a cryogenic setup. The cryogenic target station [62], mounted for the experiments of fragmentation and fission of ^{238}U with hydrogen and deuterium, is placed before the FRS. It works at ∼1 atm and ∼20 K. The target element is a double container. The outer one is isolated of the vacuum line by a Ti foil at each side. The inner container, the liquid container itself, about 1 cm thick, is also isolated by a Ti foil and five layers of Al-coated mylar strips at each side, and introduced in the outer element in high vacuum. The double encapsulation preserves the whole vacuum line from accidents due to the pressure differences. That pressure determines the target shape and so its thickness, discussed in the next chapter. The main characteristics of the target layers are listed in Appendix D.

The whole target system contains ∼45 cm^3 of liquid, and the target itself is 7 cm^3. That amounts for ∼40 l (STP) deuterium gas. The gas reservoir has ∼60 l (STP). The cryogenic pump provides an effective cooling power of ∼0.7 W . About 90% of the impinging particles just pass through the target without nuclear interaction, leaving $\sim$ 16 $A \cdot MeV$ per projectile. The beam intensity may reach $\sim 10^9$ particles/spill. Assuming a Gaussian shape with σ ∼2 s, it amounts for a maximum of $\sim 10^8$ Hz. The energy deposition has then a peak of $\sim 10^{-1}$ W. With a cooling power $\sim$ 0.1 W the temperature stabilisation is guaranteed and the thickness dependence in temperature is negligible: that was also experimentally verified, see Chapter 3.

---

[3] This calibration was made by F.Farget (at IPN-Orsay in 2001).

2.1.4 The ***FR***agment ***S***eparator FRS

The *FRS* [63] is an achromatic magnetic zero-degree spectrometer. It is built by four similar magnetic groups, each of which having one H-type 30^o dipole, quadrupoles and sextupoles. The quadrupoles are grouped in doublet and triplet sets at both sides of the dipoles: before the dipole they illuminate the magnetic volume; after the dipole they provide the right optics in the focal planes. The sextupoles in front and behind of the dipoles, are used for high-order corrections. The four magnetic groups are placed in a symmetric *two-stage* setup with four focal planes and an orbit length of $\sim$ 70 m, see figure 2.3. The independent powering of the elements allows for a quite flexible operation of the device. The dipoles are operated up to 1.6 T, covering a magnetic rigidity range from 5 to 18 Tm. The fields are measured on-line by Hall probes with a stability $\sim 10^{-4}$ Tesla.

The FRS can be operated in three different configurations: achromatic, dispersive and high-acceptance modes. Here we are only interested in the achromatic mode, in which point-to-point images are required at the four focal planes F1 to F4[4], in the dispersive axis (horizontal plane). The dispersions of the dipoles[5] in the second FRS stage are such that they compensate those of the first stage, the whole system resulting achromatic from the target till F4. The central focal plane F2 is dispersive, with a momentum dispersion value of -6.81 cm/%, i.e., a 1% relative difference in rigidity from that of the central orbit rigidity[6] will produce a deviation of 6.81 cm from the central position.

The *momentum resolving power* of an optical system can be described at first order as:

$$\frac{p}{\Delta p} = \frac{D}{2 \cdot V \cdot x_o} \tag{2.3}$$

where x_o is the spatial spread of the isotope before the magnetic element, D the dispersion and V the magnification. The D and V values are characteristic of the magnetic system used. This power will define the possibility for isotopic separation. The resolving power of the FRS at F2 has a value of $\sim$1600 for the nominal values V=0.79, D=-6.81 cm/% and a beam spot of 2.7 mm . That power fixes the limiting rigidity resolution of the FRS $\delta(B\rho) = \Delta(B\rho)/B\rho \leq 3 - 4 \cdot 10^{-4}$. The longitudinal-momentum acceptance of the system is $\Delta p/p \sim \pm 0.015$ and the angular acceptance $\sim \pm 15$ mrad. Those acceptances are namely determined by both geometrical restrictions, since the magnetic volume is restricted to the vacuum pipe, and magnetic restrictions. The acceptance is the key parameter to define the transmission of the system [64]. For a more detailed description of the FRS see ref. [65].

---

[4] Usually the areas where the instrumentation is placed are referred to as S0-to-S4 corresponding to the areas before the first magnetic group (S0), between first and second groups (S1), and so on. The focal planes F1-F4, after each magnetic group, lay on the S1-S4 areas.

[5] The dispersion of a system is the coefficient that relates the dependence of the position to a certain change in mass, velocity or charge, i.e. to momentum. Here it is used in a general sense, since the mass (D_m), velocity parameter ($v = \beta\gamma$, D_v) and charge (D_q) dispersions have the same value, but different signs: $D_q = -D_m = -D_v$. That results from the rigidity definition.

[6] The central orbit is that for which the FRS fields are tuned. Together with the curvature they define the magnetic rigidity $B\rho$. It corresponds to a selected ion and energy, so that the ion will be centred in

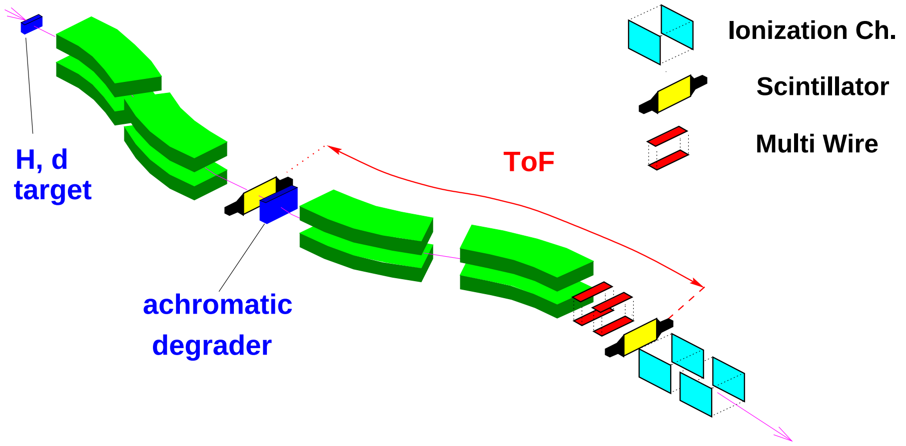

Figure 2.3: Schematic view of the FRS, showing the position of target, degrader and main detectors used. The highly-symmetric lay-out of the spectrometer shows up. Only the pieces of the dipoles are showed, while all the rest of the magnetic elements are missing. The drawing in not on scale. The length of the ToF is about 35 meters, whereas the whole length is $\sim$ 70 m.

The in-flight separation done by the FRS is built on the performance of its magnetic sector fields. They allow to resolve in the momentum over charge value of a given nucleus. Actually the close values of that ratio in heavy ions, determines the necessity of using a high resolving machine, as it is the FRS. Otherwise it would not be feasible to disentangle two nuclides with neighbouring mass to charge values. The separation of the reaction residues at high energies is possible by measuring the magnetic rigidity of the nuclei, as will be described in the following sections.

2.2 The separation procedure

We want to identify the nuclides produced in the reaction of the ^{238}U beam projectiles in the deuterium target. Otherwise, we want to define the mass and nuclear charge values for each event. The beam hits the target placed at the FRS entrance. The projectile-like fragments produced[7] fly forwards reaching the spectrometer entrance. There the fragments are analysed according to their magnetic rigidity.

In our experiment, the magnetic spectrometer separates according to the ratio of mass number A over ionic charge Q, according to the magnetic rigidity

$$B\rho = \frac{p}{Q} = \frac{A}{Q} \cdot \beta\gamma \cdot \frac{u}{c} \tag{2.4}$$

---

all the focal planes: the main or central orbit.

[7] The term *projectile-like* refers to the origin of the residue. The fact that the kinematic characteristics of the residue are those of the projectile, explains the origin of the name. This concepts were introduced in Chapter 1 and are also reviewed at the last chapter.

where B is the deflection field (uniform and transversal to the particle trajectory), ρ is the deflection radius, p the momentum, Q the ionic charge in units of the electron charge , c the speed of light, u the mass unit and $\beta\gamma$ the reduced momentum from the relativistic parameters. By measuring the momentum per nucleon or reduced momentum $\beta\gamma$, and the magnetic rigidity $B\rho$, we can define the A/Q ratio. The nuclear charge of the fragment is determined at the exit of the FRS. Note that the identification will depend on the possibility of defining the nuclear and ionic charges within the FRS, since the separation is sensible to the ionic charge. A set of detectors are used with those different purposes, by measuring the positions and tracking angles at certain points, the energy losses, flight times, counting rates, ... A brief description of the detector setup and the data acquisition used is done in the next section, together with a description of the measuring procedure.

The first magnetic-stage of the FRS takes care of selecting a certain $B\rho$ range, according to the acceptance, around a central value $B\rho|_o$: that is the *first selection*. The accepted range has a positive slope in the space defined by the atomic and neutron numbers , see figure 2.9. In experiments with elements with lower Z values, the ionic charge equals the nuclear charge value, since there are a negligible contribution from other ionic charge states. In those cases it is possible to identify the residues with that *first selection*. Many experiments profit from that one-step separation. The second magnetic stage allows a *second selection*. If a *degrader* is used at S2, the *second selection* concept becomes different from the first, and in fact it will be the clue to provide the identification of the heaver residues. Note also that the beam itself and very intense related channels (one-neutron removal, one-electron ionic charge state, ...) must be taken away before reaching S2, otherwise they would saturate the detectors with the full experimental intensities used. If the magnetic selection is not enough, collimators are used at S0 and S1.

Now we present how the nuclei may be identified according to equation 2.4. On the one hand we can measure the magnetic rigidity $B\rho$ of the nuclei. On the other hand, the measurement of the time-of-flight of the particle allows to obtain its velocity, and to define the *reduced momentum* $\beta\gamma$. Since the former quantities can only provide the ration of mass to ionic charge A/Q, we need to know not only the nuclear charge Z, but additionally the ionic state of the particle, to define Q and to assign the correct mass.

2.2.1 The magnetic rigidity measurement

The magnetic rigidity in the second-stage of the FRS $B\rho|_{24}$ to be measured, demands the position of the ion at intermediate F2 and final F4 image planes. The ion-optic theory [66] provides the relation:

$$B\rho|_{24} = B\rho|_o \cdot \left(1 - \frac{1}{D_{34}} \cdot (x_4 - V_{34} \cdot x_2)\right) \tag{2.5}$$

Here $B\rho|_o$ refers to the main trajectory rigidity, i.e. the rigidity of the central isotope of the setting; the magnetic field applied B and the dipole bending radii ρ provide the value. The *dispersion* values D_{12}, D_{34} at the focal planes F2 and F4 respectively, are calibrated by measuring the position of the projectile ionic charge-states; we have measured the values D_{12}=6.96 cm/% and D_{34}=-8.35 cm/%. The *magnification* in an achromatic system is

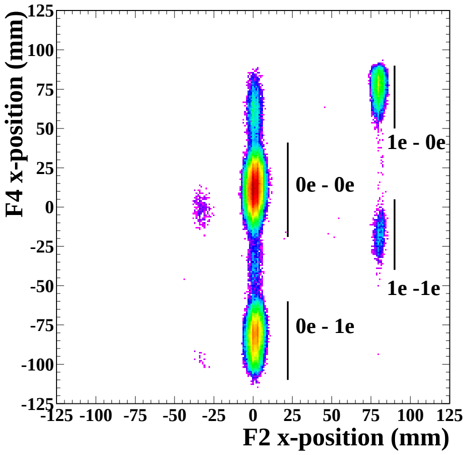

Figure 2.4: Position of the ^{238}U projectiles in the dispersive coordinate of the intermediate F2 and final F4 focal planes. The bare projectiles populate the centred spot. The projectiles carrying one electron have different magnetic rigidity, and lie in different places. The combinations of charges before and after the degrader at F2, define the pattern we observe. A selection by using the positions, can be used to study the charge detection in the chambers. The different sizes of the spots at F2 and F4 are due to the energy spreading at the thick *degrader*. See the text for details.

V_{34}=-D_{34}/D_{12}. The x_2 and x_4 refer to the dispersive coordinates measured at F2 and F4 respectively.

The positions in the dispersive plane at the focal planes F2 and F4 are determined with different detectors. At F2 one plastic scintillator provides the information. At S4 several detectors were used: two multi-wire chambers, a plastic scintillator, and two ionisation chambers, in order to define the position as well as the trajectory exit-angle. The position of the focal plane F4 has to be defined according to its own image properties. In this analysis we used either one ionisation chamber or the two multi-wires together with the plastic. The main characteristic of these detectors are sketched in the following sections.

Multi-wire proportional chambers

Several multi-wire (MW) chambers were used during the experiment [67, 68]. Located at S1, S2 and S3 they were used during the calibration procedure of the experimental setup to guide the beam through the FRS. Their inhomogeneity disturb the measurements, and they are taken away. Only at the exit of the FRS, S4, two MW-chambers are used to measure the position and angle of the transmitted ions..

The MW-chambers are made of Ti and capton windows, filled with a mixture of Ar, CO_2 and alcohol at atmospheric pressure. At S4 they are placed in air, but in the FRS line they are housed and used in vacuum. The tungsten wires are placed in two planes for vertical and horizontal measurements. The MW-chambers have a dedicated CAMAC CFD

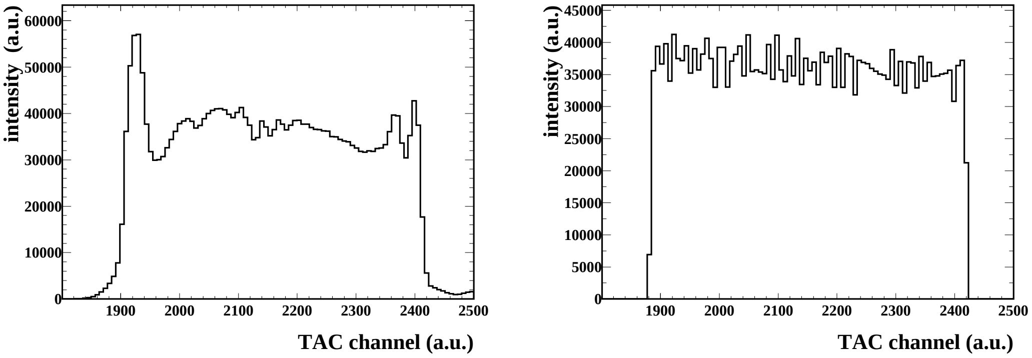

Figure 2.5: Left panel: distribution of the dispersive position coordinate at the intermediate focal plane F2, as recorded by the scintillator plastic at S2. The inhomogeneities observed are due to the non-linearity response of the device.Right panel: corrected distribution. See the text for details.

system (constant-fraction-discriminator, to reject the noise and shape the signals), and the signals from the time-delay lines of the four chamber sides (vertical and horizontal) are read by TDCs (time-to-digital converters): a 4418/T SILENA unit. Independent calibrations made with a radioactive source finger, are used as reference. An accuracy of ∼1 mm is achieved. The MW's do not suffer appreciably of non-linearity effects on the whole range. Some reduced efficiency for the higher charges (up to 98% for Z=92) have to be taken into account. These MW-chambers were used either directly to measure the positions or to calibrate the plastics and ionisation chambers used elsewhere. They were used together with the plastic at S4, so that any efficiency decrease could be corrected for. In fact, the response was about the same than that of the plastic scintillator.

Plastic scintillators

Two plastic scintillators, are placed close to the focal planes at S2 and S4, respectively. The S2 plastic scintillator may be selected from a rack housed in the evacuated beam line. There, UV-transmissive light guides at the sides of the plastic pieces, bring the light pulses till fast response photomultiplier tubes. Typical plastic thicknesses of ∼5mm were used. A detailed description may be found in ref. [69]. The plastics are used to measure both the positions at S2 and S4 (the horizontal coordinate is the one of interest since it is the dispersive one), and the time-of-flight between S2 and S4. The efficiency of the plastic scintillators in the regime of counting ($\leq 10^5$ Hz) is close to 100%.

The positions at the horizontal plane are measured by using each plastic left-and-right signals, as start and stop of a TAC (time-to-amplitude converter) module, via a CFD. The CFDs were set with a noise rejection of ∼10mV, a threshold that cuts very low charge events, which are of no interest in this study.

The analogic output is read by an ADC (analog-to-digital converter): a 4418/V SILENA unit. The positions are calibrated by using either the multi-wire chambers or the physical range of the plastics. The former method uses an independent calibration as reference. The later one compares the signal range with the bounds of the plastic scintillators (218.6 mm at S2 and 200.0 mm at S4). The typical resolution is ∼2 mm.

The position at the focal plane F4 (the F2 position modifies only slightly the result, see equation 2.5) is important to identify the isotopes. Nevertheless the accuracy is not crucial since the isotopic identification is always made by reference to a calculated pattern. However the definition of the position at F2 is crucial to define the longitudinal momentum. An offset is not of importance since the values are relative to that of the central trajectory, but the slope correlates with the width.

An expected effect in the plastic's response is certain non-linearity in two senses: first, at the bounds the signal is not longer linear: we do not suffer of that since the overlapping settings allow to discard the side bounds of each setting if necessary. Secondly, the measured signals correspond to the convoluted behaviour of the light signals and the response of the photomultiplier electronics. The result of that are intensity variations happening at some positions of the output range, see figure 2.5. A first order correction is applied, as discussed in ref. [70]. The method relies in two assumptions: the non-linearities being local, i.e., it affects neighbouring channels only, and a step-like population of the true response output, as it is expected for a homogeneous distribution covering the range; see figure 2.5.

2.2.2 The reduced momentum measurement

The measurement of the reduced momentum $\beta\gamma$ of the ion, is done by measuring the *time-of-flight* ToF and the length of the flight path through the spectrometer. The ToF is obtained in the second magnetic section, by using the S2 and S4 plastic signals as start and stop signals, respectively, for a TAC device; see figure 2.3. The independent right and left signals of the plastic scintillators were measured, and both combined into a single ToF measurement as an average: that helps to correct partially the difference in the length of the flight path of the ions off the central orbit. Typical times involved were ∼150 ns. The calibration of the delay line Δ_{ToF}[8] of the ToF, as well as the length of the central orbit flying-path L_o, is done by measuring the values for the beam velocity after traversing different calibrated thicknesses of the *degrader* at S2. The slowing down of the beam provides β, which is very accurately calculated [71]. A simple relation as

$$\frac{1}{c\beta} = \frac{ToF}{L} = \frac{\Gamma_{ToF} + \Delta_{ToF}}{L} \tag{2.6}$$

where L is the length-of-flight, is used to obtain the velocity. For the central trajectory the *length-of-flight* corresponds to a value L_o. The calibration of the TAC device provides Γ_{ToF}, and the calculation of the slowing down gives β. The fit of several measured points provides both $L_o \sim 35$ m and the Δ_{Tof} values.

---

[8] The delay line is needed since the trigger follows a spatial-reversed structure. The events arriving at the exit of the FRS, trigger the acquisition, and the detector signals at S2 are delayed adequately to be recorded properly.

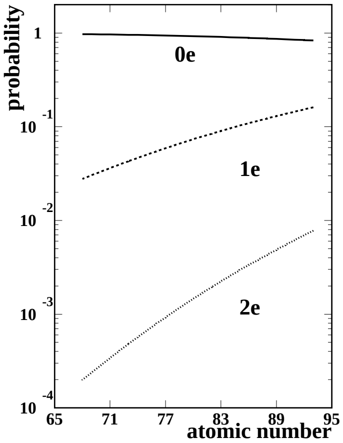

Figure 2.6: Charge states distribution as calculated with the *three states* method, for a bare ion with atomic number Z, after traversing a Nb foil of 60 mg/cm^2: bare ions (full line), hydrogen-like ions (dashed line), and helium-like ions (dotted line).

In general the ions take a path different from that of the central trajectory. The length L is estimated from L_o, and corrected for the dependence on the fragment momentum angle θ. The evaluation of the correction with θ is obtained by studying the dependence of the resolution in mass for different nuclides. A proportionally factor k is determined. The resulting velocity is

$$\beta = \frac{1}{c} \cdot \frac{L}{ToF} \approx \frac{1}{c} \cdot \frac{L_o + k\theta}{ToF} \tag{2.7}$$

Plastic scintillators

The ToF measurement is done by using the plastics at S2 and S4 (see also the previous description). The start and stop signals of a TAC, read out by an ADC of the type 4418/V SILENA. Each side of the plastics, left and right, provides an independent value, both combined in an average. The TAC is calibrated in slope by using a calibrated pulser. The result of a measurement is a certain value Γ_{ToF}. The start-stop have an additional delay line. The right value of it is obtained by calibration with the beam as described above.

2.2.3 Charge measurement

Once we know the A/Q value of the particle, to identify the isotope we need to define the value of the nuclear charge Z, to assign the element, and of the ionic charge Q, to define the mass. An energy loss measurement at the exit of the FRS, with one ionisation chamber, could provide the charge value Q of the ion. The resolution of the chamber allows to separate sharply charges below 80 with a $FWHM \sim 0.3$ charge units. Above that charge value the signal width increases, and the FWHM amounts for ~ 0.6 charge units, not good enough for charge separation, see figure 2.11(a). That loss of resolution comes from the different ionic charge states populated by the heaviest ions. The state can change within the active region of the ionisation chamber, and those changes contribute to the broadening of the energy loss signal. That is a difficulty in the identification of the high charges we want to measure. By using two chambers instead of one, and a stripper Nb foil in between, we can fold the two independent measurements of the energy loss and define an *effective* charge. Additionally the A/Q value is defined within the FRS, so that one has to relate the effective charge value measured in the MUSIC chambers at S4, with the actual value within the FRS.

There is a second possibility to measure the ionic charge within the FRS: the energy loss in the *degrader*. Using the degrader as a passive detector, we can define the ionic charge value according to the change of magnetic rigidity in between the two sections of the FRS, due to energy losses. The difficulty of this method is once again the limited resolution for the heavier elements. However, if the MUSICs and degrader energy losses are combined, it is possible to improve the resolution to a level that allows to separate the charges.

A common problematic to these two methods is the presence of ionic-charge states. At 1 $A \cdot GeV$, the ^{238}U isotopes and neighbours are not fully stripped in general, since the cross sections for electron capture in any layer of matter traversed by the ions, is rather high. The effect influences in different aspects: we commented already that the resolution in the MUSIC chambers is reduced. Since the chambers are sensible to the ionic charge Q, the energy loss will correspond to Q and not, in general to the nuclear charge Z. Due to charge-changing collisions, within the FRS the charge Q can be different to the one we measure with the MUSICs.

In this scenario special care must be taken to preserve the right identification of high Z elements: it is easy to check that the rigidity of the bare nucleus (Z,A) is close to that of the hydrogen-like state of the nucleus (Z-1, A-5), as long as the velocities are not too different. It means that the spectrometer will not separate one from the other, and the charge state will become a *contaminant* of the bare nucleus. Even if the ionic state has a lower probability, the effect may be important when the production of the contaminant is much higher than that of the bare nucleus (see the discussion in section 4.5).

The two difficulties in defining the nuclear and ionic charges, loss of resolution and presence of ionic-charge states, are solved by a common procedure, using the information we get from the two MUSIC chambers and the energy loss in the degrader. Both effects depend strongly on the nuclear charge Z. For Z values below ~ 70, the resolution of the charge identification is enough and moreover most of the ions are bare. It is possible to define Z unambiguously already at the FRS exit with the MUSIC chambers. In our experiment we have measured the reactions production with and without degrader. The *degrader method* limits the selected fragments within a single magnetic setting (see next sections). However, the method guarantees both the required charge resolution and a fully unambiguous identification. Both procedures are used in overlapping the charge regions. The compatibility of both will be discussed and will show the degree of accuracy of the corrections applied in the definition of the cross sections.

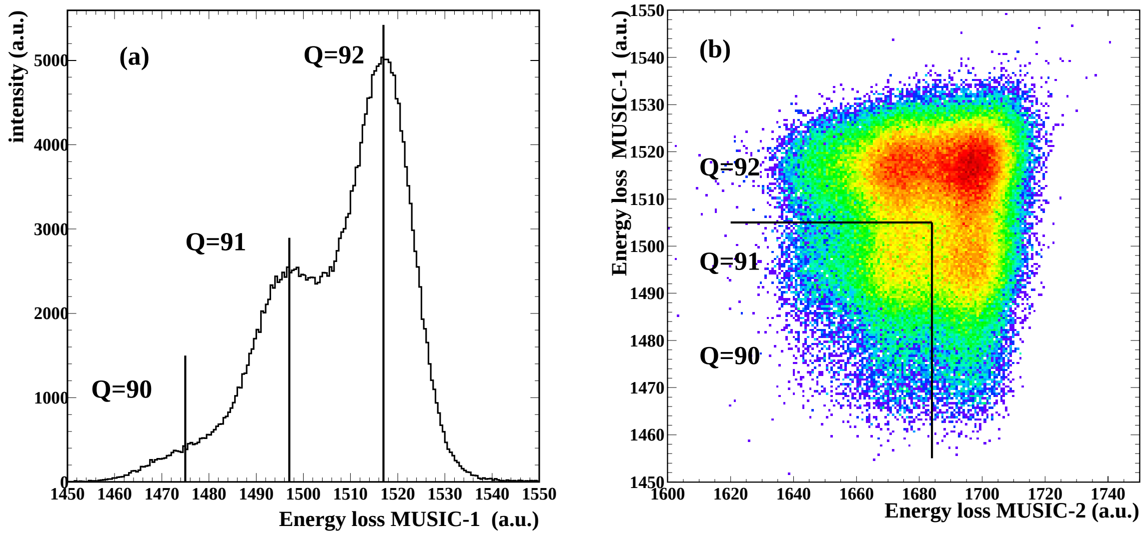

Figure 2.7: Panel (a): signal of the energy loss as measured in the MUSIC chamber-1, for ^{238}U nuclides which are bare within the FRS. They are selected as shown in figure 2.4. Panel (b): the same signal as in (a) but as measured in both MUSIC chambers. We can see the double-wing shapes corresponding to charges 92 and 91. See the text for details.

2.3 The ionic charge states

Any nucleus traversing a layer of matter will undergo charge changing collisions within the medium. At the exit, it may be stripped or not, i.e., it may carry certain number of electrons. Those different ionic charges correspond to the *ionic-charge states* distribution of the isotope. For an ensemble of projectiles it becomes a statistical problem, and the result is a distribution of the charge-states of the ion. The process depends on the electron-capture and ionisation cross sections within the medium. Those cross sections depend on the energy of the projectile, the mass and ionic charge of the projectile and the atomic number of the target, the electronic shell affected, ...According to those dependences, low Z projectiles are fully stripped at energies $\sim 1\ A \cdot GeV$ when traversing some material, but for heavy nuclides like ^{238}U several charge states are populated [72]. At relativistic energies the most of the nuclei are bare, hydrogen-like or helium-like. A simplified description based on the rate of charge exchange between ionic states [73, 74] is enough to provide a solution to the problem of the calculation of the distribution. More details will be given in the next chapter. The main difficulty within the former simplification arises with the evaluation of the electronic exchange cross sections.

In our experiment the projectile was accelerated in the SIS synchrotron with atomic charge +73, i.e. with 19 electrons in its shell. The projectile hits the target after traversing several layers of matter. At that point, the realistic GLOBAL-code estimation [72] shows that many of the electrons would have been taken away, although the distribution includes several charge states. The nuclear reaction is a very fast process compared to the velocities of the electrons in the shells, just by comparing the energies of the two systems. In this picture, the electronic shell stays with the residue. Since light target materials are not good as*stripper*, we used at the exit of the target a *stripper foil* made of Nb (60 mg/cm^2). The stripping effect of that material is optimum for the energies and nuclei involved, and the result is that after that layer only bare, hydrogen-like or helium-like nuclei are present, with the distribution very much peaked on bare ions. In figure 2.6, the distribution probabilities for the three states with zero, one and two electrons are shown, calculated after traversing a Nb foil, 60 mg/cm^2 thick, with an energy $\sim 1A \cdot GeV$, and considering a bare ion as input. Note the strong dependence in the atomic number. The effect of the stripper can be seen with some examples: a hydrogen-like ion of ^{238}U (^{205}At) would come out the stripper as bare with a probability of 0.68 (0.76), and 0.11 (0.23) for one-electron states; a helium-like ion goes out as bare with probability 0.52 (0.63), 0.40 (0.33) for one-electron and 0.08 (0.04) to remain with two electrons. After the thick degrader a new stripping foil of Nb (105 mg/cm^2) is used to ensure again the peaked distribution. If the degrader is not used, at S2 there still remains a plastic scintillator and the stripper.

We see also that the distribution of the ionic charge states depends on the state at the entrance of the layer. One more favourable situation is that of *equilibrium*[9] because the final ionic state proportions are independent of the entrance values. For nuclides with atomic number below 80 we have equilibrium after the stripper next to the target. After the degrader the equilibrium is achieved below 90. The thickness of the stripper is a compromise between the final charge state distribution and the secondary reactions in it.

Due to the effect of the stripper following the target, the charge distribution of the residues at the FRS entrance can be calculated with the *three-states* method [73], resulting in 0.84 (0.89) probability of ^{238}U (^{205}At) to be bare, 0.15 (0.10) to be hydrogen-like (see Chapter 3 for details of the procedure used, based on the results of ref. [74]).

The residue flies through the vacuum of the spectrometer till it reaches the dispersive focal plane F2: a redistribution of the charge states happens due to the matter laying at S2. The second Nb stripper peaks again the charge distributions. The nucleus flies on reaching the achromatic focal plane F4 by traversing again several layers of matter to be identified finally in charge at the MUSIC chambers. In order to uncorrelate the charge distribution between the two MUSIC chambers we also used a thick Nb foil (230 mg/cm^2) placed in between the chambers. Again a redistribution of charge states happens.

The presence of several ionic charges of the nuclides make the identification more complex, due to the effects it produces. On the one hand, the resolution in charge identification is reduced for the heavier particles. On the other hand, we need to measure both the nuclear and ionic charges in order to identify correctly the mass of each nucleus.

---

[9] The ionic charge state equilibrium is that situation in which the distribution after traversing a layer of matter, does not depend any more on the initial ionic charge state. It depends on the rest of parameters, but it looses memory of the initial configuration. The equilibrium is the result of a sufficiently high number of charge changing collisions within the material.

2.4 Charge separation with the MUSIC chambers

The charge of the high energy residues projected forward can be determined by measuring the energy loss in one ionisation chamber. In figure 2.7 panel (a), we show the energy loss measured in the first MUSIC chamber, for ions corresponding to the beam: only nuclides with atomic number Z=92 and bare within the FRS[10] have been selected. We see two effects: firstly, the nuclides appear in different charge states at the MUSIC chambers. Secondly, the charges overlap strongly. Although the probability for a charge changing reaction to happen within the active region of a MUSIC chamber is very low. Nevertheless they contribute to the broadening of the signal[11], and they spoil the resolution for charge values above ~ 80.

In figure 2.7 panel (b), we show the same events as in (a), but as measured in the two MUSIC chambers. Remark the *two-wing* shape that each charge presents in that kind of plot. For each charge we observe in that plot, the energy loss signal in the horizontal wing corresponds to the case in which the ion carries no electrons in the first chamber, i.e. the maximum charge value for that ion. The vertical wing corresponds to those events where the no electrons case happens at the second chamber. The wings overlap in the cases where the ions carry no electrons in both chambers. Here we find a selection criterion based on the electron exchange probabilities. Just before of the second MUSIC, a thick Nb stripper layer is placed[12]. The atomic charge is fluctuating in the path through the chambers. Actually the charge state from the FRS exit till the second MUSIC can be modified in several layers of matter (FRS vacuum window, air, MW chambers, ...). But the result of a plot as that of figure 2.7 panel (b), is mostly the comparison of the charge state in the second half of the FRS, with the states resulting from traversing the Nb foil. Using the values in the two MUSICs, and selecting the highest energy loss between the two, we define an effective charge Q_{EFF}, corresponding to the zero-electron case. Note that the criterion overcomes the problems when the zero-electron case happens at least once between the two chambers, i.e. the combinations between the two chambers 0e-0e, 1e-0e, 0e-1e, 0e-2e and 2e-0e .

In figure 2.8 we show the energy loss signal measured in the two MUSIC chambers, from a setting where ^{217}Ra was centred. The spots correspond to charges 78 to 88 (also 89 appears, but less populated). A tilted line passing through the different cores would correspond to those events for which the same atomic charge was seen by the two chambers. We observe the *two-wing* pattern we have discussed.

The rest of the states (1e-1e, 1e-2e, 2e-1e, 2e-2e) can be understood by looking to the

---

[10] The selection has been done independently of the values seen in the chambers. That is possible for the case of the projectile, when the positions at F2 and F4 give unambiguously the charge states, as can be seen in figure 2.4.

[11] The broadening is easy to explain since the chamber gives a signal proportional to the ionic charge. Since we add up to four signals per chamber, from the four anodes, if the charge Q_1 changes to Q_2 from one anode to the next, the electronic avalanche will be modified, and the final observed value will be a value in between Q_1 and Q_2. We get a broadening effect of the measurement of the value we observe.

[12] The use of a stripper at that place is helpful due to the charge state equilibrium that it is achieved: the output distribution will not longer depend on the input charge state: a memory-loss effect that disentangles the states seen by the two chambers.

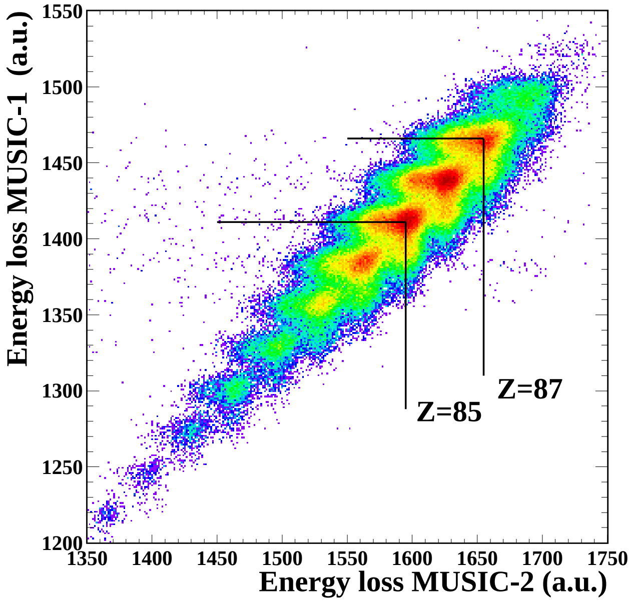

Figure 2.8: Energy loss in the first MUSIC chamber versus the energy loss in the second one. The spots correspond to nuclei with atomic charges 78-88.

figure 2.7 panel (b). We see a second spot lying below the main one, under the lines. The events belong all to the Z=92 case but they lie on the space corresponding to the charge 91. We can understand that the second spot corresponds to the remaining cases: 1e-1e, 1e-2e, 2e-1e, when the Q-1 value would be defined by the Q_{EFF} criterion. Only the 2e-2e case, would appear in a third spot below the second one, corresponding to the Q-2 value, but being the amount negligible it is lost in the plot. We see that for the cases when some electron appears in any of the chambers, the nuclear charge will be wrongly assigned and so $Q_{EFF} \neq Z$. For Z=92 about 18% of the events would be assigned incorrectly to Z=91 by using this procedure. It will be shown how by measuring the so called *degrader energy loss*, it is possible to separate even the latter case.

Note that the selection we apply to define the ionic charge does not improve the charge resolution provided by the MUSIC chambers. The broadening is due to the charge exchange within the chamber, and here we only benefit from the charge exchanges in the Nb foil in between the two chambers. It is by using the value of Q_{EFF} together with the degrader information that we can improve the resolution.

The correlated measurement with two ionisation chambers can be extended to higher order correlations by increasing the number of detectors, and defining better the zero-electron case by correlating the responses in each one. Alternatively by using a higher density filling gas, then increasing the electron exchange probability, it could be used an analogous method comparing the signal among the anodes of a single chamber or even among several chambers. That method has been successfully applied in a recent experiment: it was used by the collaboration to measure the production from proton and deuteron induced reactions in $^{208}Pb(500\ A\cdot MeV)$. The data, under analysis during 2001, has already shown the possibilities of the procedure.

Ionisation chambers

Two *MUlti-Sampling Ionisation Chambers* [75] are used at the exit of the FRS, in S4. The four independent anodes per chamber in the beam line direction, provide a four-fold measurement of the energy loss with a 100% efficiency for the usual counting rates at S4 in our experiment ($\sim 10^3$ Hz). It can be checked that those events lost in one anode are actually lost in all of them, corresponding to particles hitting somewhere outside the active region. The number of those events was measured, resulting negligible.

The MUSIC tank that contains the sensitive parts is 600 mm long and the window area is about 276x150 mm^2. The windows and screening foils are made of Al-coated capton. The P10 filling gas, argon(90%) and methane(10%), is used as active medium at atmospheric pressure. The clouds of electrons generated by an ionisating particle passing through, are driven to the anodes by the electric field created inside. The high voltages applied to the anodes and cathode are those providing the highest electron drift velocities, $\sim 5\ cm/\mu s$, i.e. a maximum drift time of $\sim 5\ \mu s$ in the chambers. The number of electrons generated by the particle is roughly proportional to the square of the atomic number. The charge-sensitive preamplifiers generate a voltage proportional to that charge. The amplifiers shape and increase the signals[13] read out by an AD811-CAEN ADC unit.

The energy loss signals have to be corrected for position and velocity dependences: then a charge resolution of ~0.30 charge units (FWHM) is achieved for charges below ~80. The signal pattern can be calibrated by taking as reference the beam value, as in panel (a) of figure 2.11.

The anode signals may be used also as drift-time measurements: a fast response trigger, the plastic scintillator at S4, is used to start a TAC, whereas the anode signals provide the stop. The four independent drift times provide both the position and angle of the particle at the exit of the FRS. The signals are read now by a TDC C414-CAEN unit. The positions may be obtained by calibrating the signal against either the plastic or the MWs. The resulting calibration have an accuracy of ~2 mm. The angle is obtained by tracking the positions in two different anodes (remember that each chamber has four anodes, so the position calibration of a pair of them will provide the angle). We see that the ionisation chambers provide together with the energy loss, a measurement of the positions and angles at the exit of the FRS. We have used these signals for positioning purposes, as well as to estimate the corrections into the path of the particle to evaluate the ToF, according to equation 2.7.

---

[13] The amplifier output peak voltage generated by a particle with ionic charge Q is roughly given by $V_{AMP} = V_{PREAMP}[mV] \cdot gain = -\frac{0.012283}{C_{PREAMP}} \cdot \frac{Q^2}{\beta^2} \cdot [8.6008 + 2 \cdot ln(\beta\gamma) + \beta^2]$ where C_{PREAMP} is the capacity (pF) of the coupling capacitor of the preamplifier (1 or 2 pF), Q the charge of the ionisating particle and β and γ the relativistic velocity parameters for the particle.

2.5 The energy loss method: the degrader

A very interesting procedure used to separate heavy isotopes is the so called *momentum-loss achromat*, also referred to as $B\rho - \Delta p$ and $B\rho - \Delta p - B\rho$ [61, 76]. At the dispersive focal plane F2 a thick *profiled degrader* is used. There are three notorious effects due to the use of such a thick degrader. Firstly, the energy of the ion changes between the two sections of the spectrometer (for a beam ^{238}U at 1AGeV, an Al thickness producing an energy loss equivalent to reduce the total range to about half the value is $\sim 5.5\ g/cm^2$, the energy decreasing to ~600 AMeV at the exit for that setup). Secondly, the charge state distribution will be different between the two sections (a 100% bare ^{238}U beam would end up with only 55% bare ions at the exit of the degrader). And finally, the total reaction probability is rather important (~42% for the ^{238}U beam).

The energy loss in the degrader depends on the ionic charge Q, the mass number A and the reduced momentum $\beta\gamma$ of the nucleus. Of course the degrader introduces additional changes in the optics of the system. The two-stage spectrometer can be used as a momentum-loss separator: the dispersion matching to preserve the optical conditions can be achieved by setting the dispersions in the second stage in a way that cancel those at the exit of the degrader. See the discussion in the sections below.

The degrader makes a *selection* depending on the degrader thickness and the ratio between the rigidities of the two magnetic stages. The selection bounds cut transversally the selection done by the $B\rho$ on the first stage, when looking to the atomic Z and neutron N numbers. In figure 2.9 we see a typical selection area in the proton-neutron isotopic space, for a tuning of the FRS centered around ^{195}Pb at $\sim 1A \cdot GeV$. The range plotted is the maximum that would be accepted extending the momentum tails of the nuclei. The shape and slope of the second selection can be defined numerically, according to the degrader characteristics.

This degrader acts as a passive energy-loss device. That will help to both define correctly the nuclear and ionic charges, and additionally to improve the resolution in charge, so that the separation of high charges will be feasible. The use of the degrader is discussed to be necessary above Z=70. Below that value, we will see that both the the ionic charge states and the resolution, are no longer a source of ambiguity, and the degrader is no longer necessary.

2.5.1 The achromatic degrader

The possibility of using a passive energy degrader while preserving the ion-optic characteristics of the device is a delicate task. An energy loss element transforms the ion-optics from a Liouvillian system, where the phase space density is preserved, into a non-Liouvillian space. However it is still possible to define a beam transfer matrix with the parameters involved [61, 77]. The achromatic condition of a two-stage ion-optical device relates the dispersions D_i and magnification V_i of the two magnetic steps $i = 1, 2$, according to $D_1 = -D_2 \dot{V}_2$. If the achromatic degrader is in between the stages, the momentum of the ions will change depending on its position at the intermediate plane. The former relation will impose a constraint in the dependences of that change.

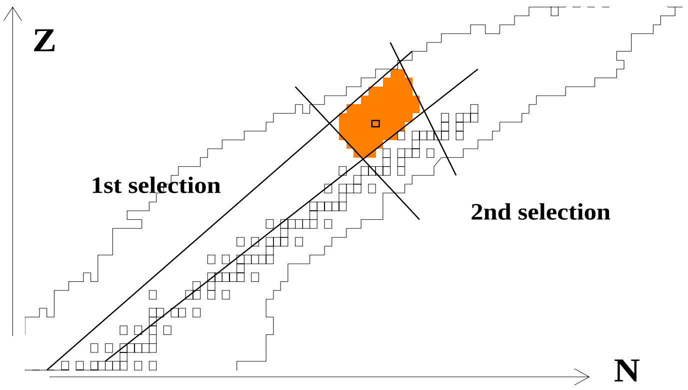

Figure 2.9: Isotopic range that the FRS acceptance selects, for a magnetic setting centred at ^{195}Pb at 1 $A \cdot GeV$ a degrader is used. The stable isotopes as well as the limit for known nuclei are drawn. The small box within the shadowed area is the central isotope of the magnetic FRS setting. The large area corresponds to any isotope that due to kinetic conditions could be included in the setting. Actually the result is a much more restricted area of selection around the selected isotope.

The most representative parameter of the degrader is its *wedge angle* ω, i.e. the dependence of the degrader thickness t on the position in the dispersive plane x_2: $t = t_o + \omega \cdot x_2$, where t_o is the value in the central position. Since the thickness is related to the achromatic condition the wedge must follow certain constraints and ω is defined as[14]

$$\omega = \frac{v_f}{\delta v_f/\delta x} \cdot \frac{\Omega - 1}{D_1} \quad and \quad \Omega = \frac{v_i}{v_f} \cdot \frac{\delta v_f/\delta x}{\delta v_i/\delta x} \tag{2.8}$$

where $v = \beta\gamma$ and i/f refer to the initial and final values, i.e. before and after the degrader. The $\delta v/\delta x$ is closely related to the stopping power [61, 77]. The degrader used at GSI is a several-pieces device that is controlled automatically to fit both mono-energetic and achromatic operation modes The pieces are constructed very precisely in order to keep their homogeneity. Actually the accuracy needed for the definition of ω implies that instead of using values of the stopping powers, the device is calibrated directly.

In the definition of a FRS magnetic setting, with a given nucleus centred through the spectrometer, the ion's energy defines the fields of the first magnetic stage, since the bending radii are calibrated. The degrader thickness of the central trajectory t_o is usually chosen to be $\sim$ 50% of the particle range [61]. The degrader is set to operate as an achromatic device by calculating the ω value. The fields in the second stage are chosen to match the rigidity of the particle at the exit of the degrader. One only has to take care of adjusting the central trajectory, since the degrader is achromatic. While the achromaticity condition holds for just a single selected isotope, it is almost true also

---

[14] It is also often defined as $\omega = \frac{\delta x}{D_1} \cdot \left[\frac{v_i}{\delta v_i} - \frac{v_f}{\delta v_f}\right]$ being both equivalent forms.

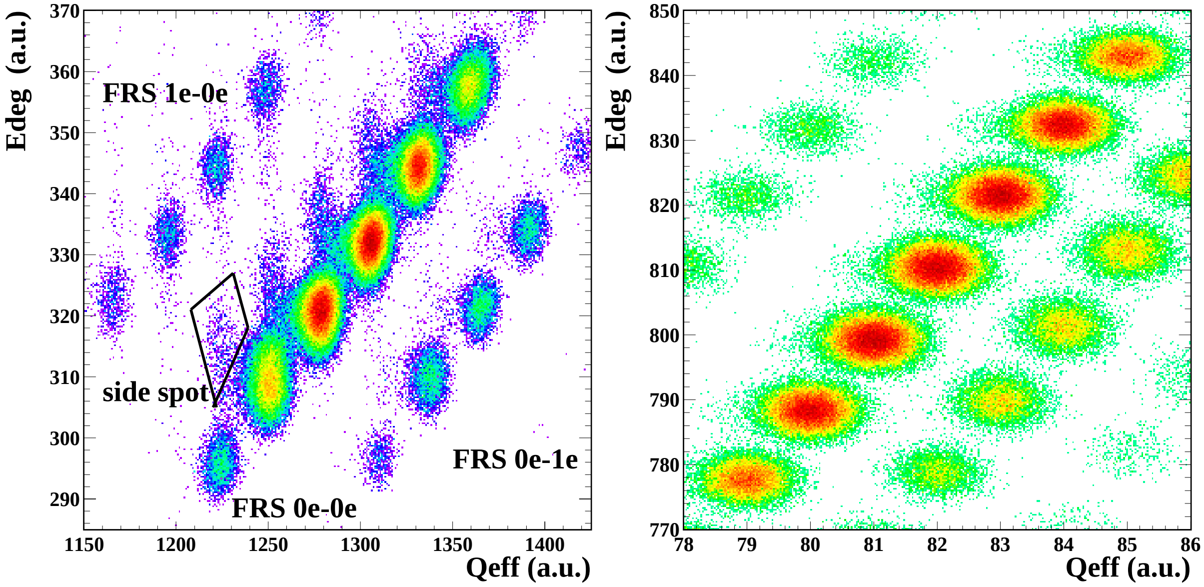

Figure 2.10: Left panel: energy loss measured in the degrader E_{DEG} as a function of the charge as selected by combining the two MUSIC energy losses defining the effective charge Q_{EFF}. See the text for details. The events correspond to a FRS setting where ^{195}Pb is centred: the charges 79-84 appear. Right panel: the same plot as (a) as result of a calculation made with the same setup characteristics. Note that intensities in the simulation are not realistic, being the same for any produced fragment. The difference in shape of the spots is solely due to the scale in the figures.

for the neighbouring nuclei, and so the isotopes passing into the FRS acceptance can be analysed within the same setting.

The degrader makes a *selection* depending on the its thickness and the ratio between the rigidities of the two magnetic stages. The selection bounds cut transversally the selection done by the $B\rho$ in the first stage, when looking to the atomic Z and neutron N numbers, as shown in figure 2.9. The shape and slope of the second selection can be defined numerically.

2.5.2 The degrader energy loss

We have discussed that we can determine the mass to charge ratio of a residue, by measuring its position in the intermediate F2 and final F4 focal planes, and the time of flight, see equation 2.5. The energy loss in the degrader is an electromagnetic effect, depending namely on the atomic charge Q. The measurement of the magnetic rigidity can provide the energy to charge ratio E/Q. Since we have two measurements of that ratio, before and after traversing the degrader, we can define its difference:

$$E_{DEG} = \frac{\Delta E}{Q} = u \cdot (\gamma_1 - \gamma_2) \cdot \frac{A}{Q} \tag{2.9}$$

where we define

$$\gamma_1^2 = 1 + \left(\frac{e_o c}{u}\right)^2 \cdot \left(\frac{B\rho|_1}{A/Q}\right)^2 \tag{2.10}$$

$$B\rho|_1 = \frac{x_2}{D_{12}} \tag{2.11}$$

In these equations the γ_2 is given by the ToF measurement, and $B\rho|_1$ is also measured with x_2 and D_{12} as defined before; u and c are the mass unit and light-velocity respectively, and e_o is the charge unit. Assuming that the value of A/Q we have obtained from the magnetic rigidity $B\rho$ and ToF in the second part of the FRS, was the same in the first section, we can evaluate E_{DEG}. The so called *degrader energy loss* E_{DEG}, is defined as the difference in the E/Q value between the two sections of the FRS. A nucleus flying through the FRS will fall into a Gaussian shaped distribution of E_{DEG} centred in the corresponding Q value, since this energy loss depends mainly on the ionic charge. That value allows to define alternatively the ionic charge within the FRS, since a certain charge will produce a Gaussian distribution around a central characteristic value. If the charge state was different in both FRS sections equations 2.9-2.10, would give a jump in the value E_{DEG} respect to the case of no charge change.

2.6 Charge identification

2.6.1 Degrader method

In this section we show how it is possible to combine the information from the two MUSIC chambers and that of the degrader energy loss, to define the ionic Q and nuclear Z charges of the heavier nuclides with enough resolution, whereas the method allows also to get rid of the contamination from the ionic charge states. In figure 2.10, left panel, we show the measured values of the energy loss at the degrader E_{DEG}, defined in the previous sections, and the combined energy losses at the two MUSIC chambers given by the effective charge Q_{EFF}, defined in section 2.4. They correspond to a FRS setting where the nucleus $^{195}_{82}Pb$ was centred: the elements 79-84 appear in each big spot.

The three sequences we distinguish as tilted lines are those nuclides which have not changed their charge state all along the path within the FRS and later on the MUSIC chambers. We can simulate each component in the plot with the help of a calculation with the same setup characteristics, as we show in the right panel of figure 2.10. In the simulation we can isolate and identify the origin of any spot. Remember that Q_{EFF} has been debugged from most of the charge states present outside the FRS, see section 2.4. The bigger spots correspond to the most probable case: the no change of the ionic charge within the FRS, and assignment $Z = Q_{EFF}$, i.e., the bare ions.

If the ionic charge within the FRS changes between the two FRS sections the E_{DEG} value would be shifted (vertically in the picture), and the spot would be off the main line. Those cases appear as lines parallel to the main one: the upper one corresponds to the events that had one electron in the first stage and zero in the second stage, and the lower line corresponds to the opposite case. If the ion carries some electron and the ionic charge is the same in both FRS stages, the event will lie on the so called *side-spot* in the plot, next to the main-line spots, as can be checked with the calculations. That case has a probability up to 4% for the projectile and strongly decreases with Z, see figure 3.3. Of course the former selection of bare ions stays correct as $Z = Q_{EFF}$ were assigned unambiguously.

In the cases in which the value of Q_{EFF} did not correspond to that of Z, the spot is shifted to lower values of Q_{EFF}=Z-1 or Z-2 for a given Z, while the E_{DEG}-value would remain that corresponding to Z: again the events would lay on the *side-spot* next to the main spot, as we have checked by simulation[15].

In this discussion almost all possible cases have been considered: if the ionic charge does flip between the two sections of the FRS the event is rejected from the main line of the plot, as well as the case when some electron remains in the two FRS sections. If the charge assignment at the MUSICs is $Z = Q_{eff}$, the event lays on the main spots, while if it is not correct it would lay on the side-spot. The only missing events in this discussion are those when the ion carries some electron, and the ionic charge does not change in the whole path from the target till the exit of the second MUSIC. The values for Q_{EFF} as well as E_{DEG} would be assigned to a lower Z than the real one. Fortunately the probability of such events is definitely negligible in the setup: for ^{238}U, the worst case, the probability of having a hydrogen-like ion in the first and second sections of the FRS, and also in the two MUSICS would be below $\sim 0.15 \cdot 0.29 \cdot 0.22 \leq 0.01$.

The method allow to assign both the values of the atomic and ionic charge numbers within the FRS, since we distinguish in a plot as that of figure 2.10, the different electronic combinations. The method additionally increases the resolution in charge separation. In figure 2.7 we can see that the projection of the value measured in the MUSICs as the Q_{EFF} axis is quite poor. By looking to figure 2.10 the separation of Q_{EFF} between two charges is ∼25 units, while the FWHM is ∼18 units: a strong overlapping. Also the separation of E_{DEG} is poor: ∼12 units between the charges, and a FWHM ∼9 units: again a strong overlapping. But in the plane of the two coordinates E_{DEG} and Q_{EFF} the separation is improved: the difference between two spots is $\sim \sqrt{25^2 + 12^2} = 28$, while the FWHM is $\sim \sqrt{14^2 + 6^2} = 15$. The ratio of the values FWHM/separation has moved from the one dimensional values $0.72(Q_{EFF})$ and $0.75(E_{DEG})$ to 0.53. That is the key for separating the higher charges with enough resolution at 1 $A \cdot GeV$, which in charge state equilibrium gives the heaviest isotopes close to ^{238}U not fully stripped, but carrying electrons with ∼ 30% probability.

2.6.2 No degrader method

As already mentioned, the presence of ionic charge states and the charge resolution obtained in the MUSIC chambers, depend both strongly on the nuclear charge Z. The MUSIC allows to separate elements with Z below ∼ 80. In figure 2.11-(a) we show the charge resolution obtained in one of the settings without degrader. The charge values Q_{eff} combined of the two MUSICs still allow to separate the charges of the nuclides with

---

[15] Note also that for charge changing events within the FRS, i.e the upper and lower parallel lines, also the Q_{EFF} value would produce a side-spot, but being of low intensity it is not easy to identify

higher Z values, which now profit from the lower energy spreading caused by the missing degrader. For Z values below $\sim$ 70, the information from one MUSIC is enough to define the Z value. The resolution FWHM/ΔQ we obtain for $_{88}Ra$, $_{60}Nd$ and $_{50}Sn$ is $\sim$0.54, 0.54 and 0.46 respectively.

For Z values below $\sim$ 70, the charge distributions are largely peaked for bare ions, and the presence of the ionic charge states within the FRS can be disentangled in a different way. In figure 2.11, panel (b), we show the x-position at the final focal plane F4 as a function of the charge measured in the MUSICS Q_{EFF}. The events lying off the main band, are those corresponding to the hydrogen-like states in the second half of the FRS: the change in rigidity changes the position, as we can see in the plot, and we can take them away, selecting just the bare ions.

When using the FRS without degrader the selection in both stages is done mainly by the $B\rho$ value, which changes not too much between the two sections since only a plastic scintillator and a stripper remain at S2. The FRS acceptance determines the part of the range of mass to charge values that are transmitted around the central value, modulated by the velocity spread. A large number of elements are transmitted compared with the setups with degrader, which are restricted to $\sim$ 5 elements. That explains that the number of FRS settings needed to cover the same isotopic range as by using the degrader, is greatly reduced. This concept is reviewed and applied in the next chapter.

We see that the no-degrader settings cover the same element range than those obtained with degrader. Despite the restricted range of the charges with the use of the degrader, the method allowed to take away all possible contaminants due to ionic-charge states. When selecting the ionic charge-states in the x_{F4} vs Q_{EFF} plane, only the second half of FRS is included, and only the bare ions are considered.

However, the events can be misidentified if the atomic number Z in the MUSICs is wrongly assigned. The source of identification troubles are (a) those events which are hydrogen-like within the second half of the FRS and and are wrongly assigned in the MUSIC chambers to Q_{EFF}=Z-1, and (b) those events bare in the FRS and wrongly assigned by the MUSICS to Q_{EFF}=Z-1. The case (a) contaminates directly the nuclides with atomic number Z-1, even if the probability is very low. We can calculate the probability for the projectile as $\sim 0.15 \cdot 0.15 = 0.02$. The case (b) spoils the resolution of the Z-1 isotopes with masses A-2 and A-3, having a probability of $\sim 0.85 \cdot 0.15 = 0.13$ for the projectile. These sources of contamination, in a situation in which the ionic charge states cannot be disentangled completely, will produce a difference between the values measured with and without degrader. If the rest of corrections applied in the calculation of the cross sections are correct, the differences in production observed between the two methods will correspond to those described here. That is discussed in the next chapter.

Below a certain threshold in charge $Z \sim 70$ the presented troubles with ionic charge-states are negligible, and the no-degrader treatment is fully correct to a degree within the accuracy limit imposed in the work.

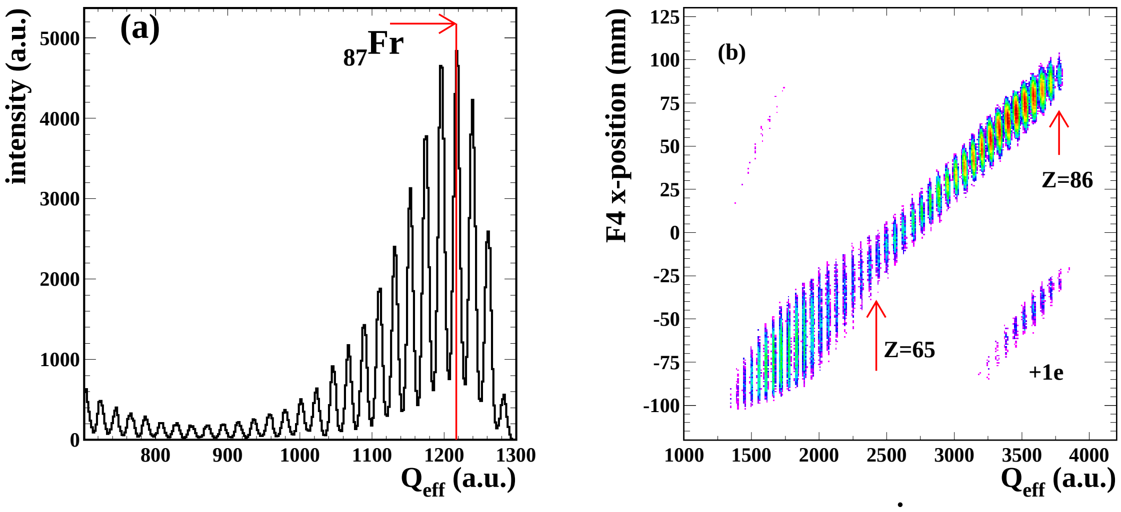

Figure 2.11: Panel (a): charge resolution and identification, obtained for the no-degrader setup. Panel (b): the x-position at F4 vs. the energy loss Q_{EFF} obtained from the combined measures of the two MUSIC chambers, for a setting centred in ^{183}Re. The group below the main band are the ions with one-electron in the second half of the FRS. Note that its intensity decreases with Z. The group above, corresponding to lower charges, is not discussed here.

2.7 Isotopic identification

It has been discussed that we can disentangle the different ionic charge states of the nuclides within both the two FRS stages and the two MUSIC chambers. Additionally, the method provides the resolution we need to separate the higher charges. The procedure presented overcomes these difficulties which appear when dealing with ions neighbouring ^{238}U. We have a criterion to isolate those events for which the nuclear charge Z assignment is without doubt, the atomic charge Q is known, and the mass assignment correct: the identification is fully unambiguous. We achieve that by selecting the events laying in the main spots of the histograms like the one showed in figure 2.10, where we use the combined information of the two MUSIC chambers Q_{EFF} on the one hand, and that of the energy loss in the degrader E_{DEG}, on the other hand.

Once we have the selection in the $E_{DEG}-Q_{EFF}$ plane, the isotopes are separated in the plane of the mass to charge ratio A/Q versus the positions x_2 measured in the dispersive coordinate of the intermediate focal plane F2. In figure 2.12-(a) we show a typical plot where different $_{88}Ra$ isotopes are separated and identified in the plane $A/Z - x_2$. On panel (b) we present a simulated pattern for the same setup characteristics. By using the information from ToF and charge calibrations, and independently the calculation, we can identify the fragments with absolute confidence. The method we used allows the fragment separation and prevents from contamination. On panel (c) we plot the projection on the

A/Z coordinate, showing the mass resolution: typical values for FWHM/ΔA are ~ 0.46 and 0.52 for $_{88}Ra$ and $_{81}Tl$, respectively. Note the reduced production measured in the $^{216}_{88}Ra$ isotope, which has a neutron number N=128: it is due to a fast radioactive decay, to be discussed carefully in Chapter 4. On panel (d) we present the separation of several $_{76}Os$ isotopes. The difference in range of x_2 values in respect to $_{88}Ra$ isotopes is due to the wider spread in momentum of the lighter residues, to be discussed in Chapter 4. Remark that the spots on the bounds are cut: that is related to the FRS acceptance. How to overcome this effect and to cover the whole momentum distributions, is to be showed in the next chapter.

The charge resolution in the MUSIC chambers and the contamination due to ionic-charge states are both depending on the atomic number of the nuclides. To avoid the use of the *degrader* in the identification procedure is possible for fragments with atomic number Z below ~ 70. To calibrate the parameters of ToF and charge, we have used the beam. Both quantities can be accurately calibrated for the full range of masses and charges till the lower values present in the experiment, e.g. those of fission fragments. Moreover the pattern of the 128-neutron isotopes, which suffer a fast radioactive decay, give an alternative mass calibration. The effect is discussed in Chapter 4. The identifications with and without degrader were exactly the same, allowing an additional cross check of the whole identification method.

In figure 2.13-(a) we present a two dimensional histogram of charge values as a function of the mass to charge ratio, for a setting centred in $^{165}_{75}Re$. The selection of the bare ions in the second half of the FRS, as shown in section 2.6.2, is applied. If the degrader is not used, a single magnetic setting includes a large amount of isotopes. In panel (b) we show the projection of the previous plot on the mass to charge ratio axis for $_{70}Y$. The mass resolution values are $FWHM/\Delta A \sim 0.49$, typical of the lower masses.

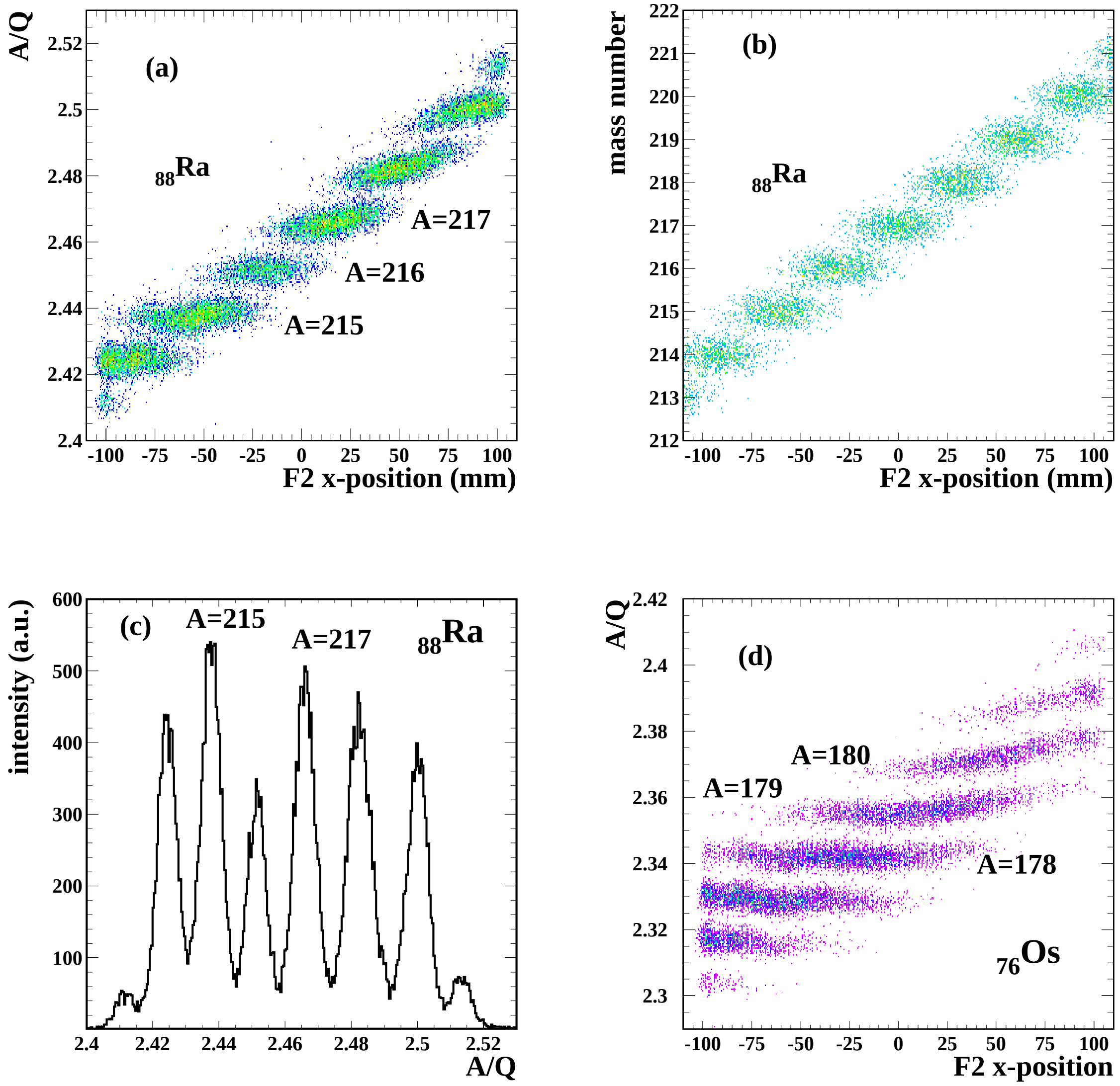

Figure 2.12: Panel (a): A/Z value vs. the x-position at F2, for some $_{88}Ra$ isotopes measured in a FRS setting where $^{217}_{88}Ra$ is centred. Panel (b): same as (a) but showing the result from a simulation using the same setup characteristics. Panel (c): projection of the panel (a) on the A/Z axis. We observe that the mass separation of heavy fragments is quite good. Panel (d): is the same as (a) but now for a setting where $^{179}_{76}Os$ is centred. Remark the wider distribution on positions, as well as that the spots on the bounds are cut, which is related to the reaction kinematics and the FRS acceptance, respectively.

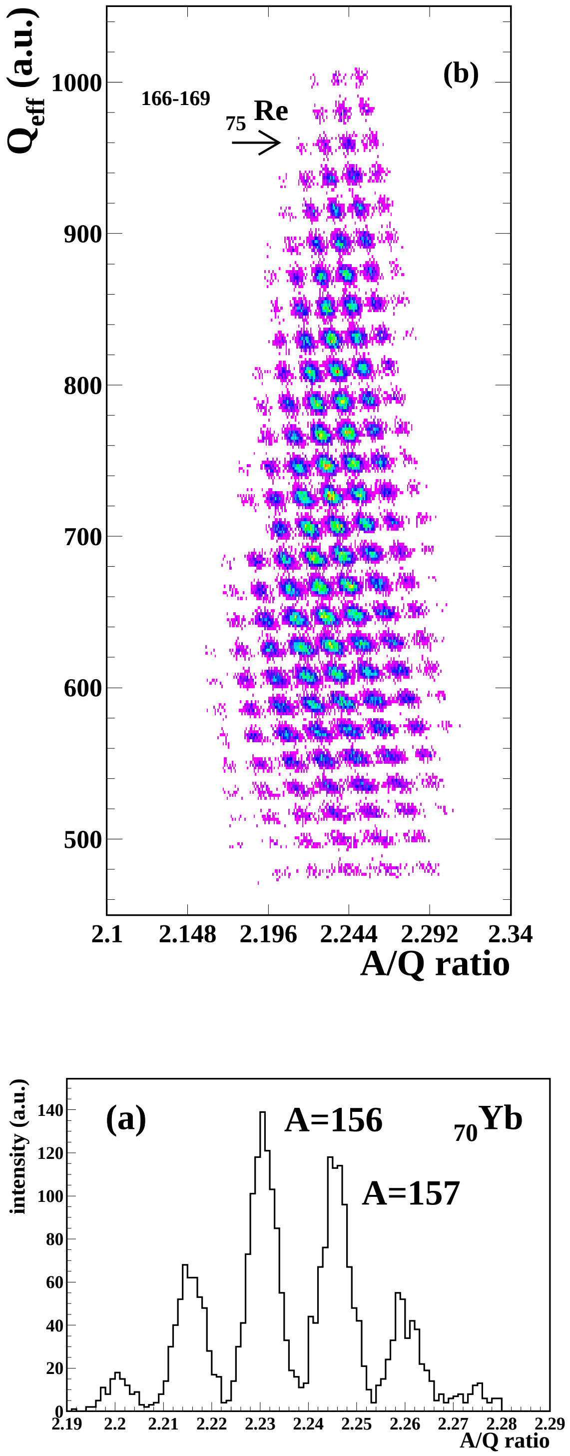

Figure 2.13: Panel (a): histogram with the characteristic identification pattern showing the charges as evaluated with the combined Q_{EFF} value in the two MUSIC chambers as a function of the A/Q ratio, for a FRS setting analysed without the degrader. Panel (b): projection on A/Q values of several isotopes of $_{70}Y$ selected from panel (a).

Chapter 3

Residue production cross sections

In this chapter the main experimental results obtained in this work are presented: the production cross sections and the momentum distributions, of the fragmentation residues of the reaction $^{238}U(1\ A \cdot GeV) + d$. The definition of the cross section will depend on the measurement of three independent magnitudes: the production rate or *yield* of each nucleus, the beam intensity and the number of atoms in the target. A detailed study and calibration of those three values guarantee the quality of the result and defines the final uncertainty of the measured cross sections.

The procedure explained in the previous chapter allows to unambiguously identify the nuclei produced in the reaction, event by event. To obtain the *real yields*, since the setup and analysis make restrictions to the isotopic identification, different corrections have to be applied to the *measured yields* y_{meas}. The discussion of those corrections will take the main part of this chapter. One of the largest corrections we applied is due to the secondary reactions in the intermediate degrader. The comparison of data obtained with and without using the degrader will show the full compatibility of the results and the accuracy of the corrections applied, and will state the necessity of using a degrader in the high-masses range.

The measured quantity in this experiment is actually the differential yield relative to the reaction momentum $dy(Z, A)/dp_{||}$. These measured distributions are characterised by the mean value $\langle p_{||} \rangle$ and width $\sigma(p_{||})$, whose results are presented and discussed in the Chapter4. The integration of the distributions $dy(Z, A)/dp_{||}$ gives the *measured yield* of each nucleus $y_{meas}(Z, A)$. By studying the momentum distributions it is possible, for some elements, to find signatures of the fission contribution besides fragmentation, and to disentangle the two mechanisms.

3.1 Beam current normalisation

In each event readout we get the information on the cumulated number of impinged projectiles into the target N_{beam}. In the previous chapter we showed how N_{beam} is evaluated from the measured quantity $N_{SEETRAM}$. In figure 2.2 we see the shape of the latter parameter as a function of the time, for a certain measurement period. In fact the profile corresponds to the time structure of the spills. We can see the quasi-constant level

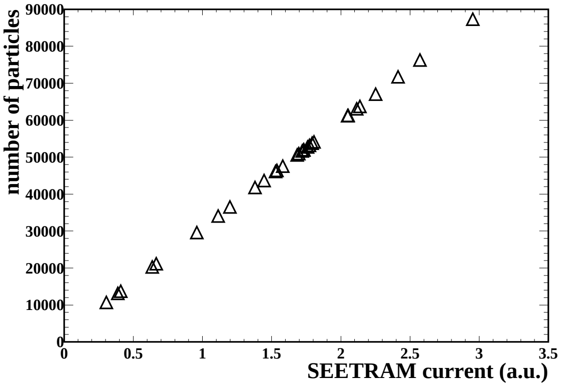

Figure 3.1: Number of particles as function of the SEETRAM current. The counting of the particles is obtained from an independent measure with an ionisation chamber or a plastic scintillator. We can observe the linear behaviour despite the wide range in counting represented.

in between two peaks, that produces the $N_{background}$ counting. The integrated value of $N_{SEETRAM} - N_{background}$ for a particular FRS setting, provides the total target irradiation dose that allows to normalise the production rate. The conversion into the number of impinged projectiles N_{beam} is obtained by calibrating the SEETRAM current with an independent measurement of the number of particles. That is done with an ionisation chamber, as explained in ref. [60]. In figure 3.1 we show the calibration pattern obtained in our experiment. The number of particles is determined with a measurement in an independent detector. The linear relationship of the number of particles with current shows up. The relationship from the calibration provides the factor f to be used within equation 2.1.

3.2 Target normalisation

The reaction target we are interested in is deuterium, but the target itself is a quite complex structure to contain the liquefied deuterium. The container matter contributes to some additional production we have to subtract, and which we review later. To achieve a reasonable production intensity the thickness of the target t must be such that the reaction probability is ∼10% [61]. Therefore if $0.1 \sim N_o/A \cdot t \cdot \sigma$, with N_o the Avogadro's number, $A \sim 2$ for deuterium and the total reaction cross-section σ is $\sim 2 \cdot 10^3$ mb (see section4.1), it results that $t \sim 2 \cdot 10^2 mg/cm^2$. The liquefied deuterium has a density of 162 mg/cm^3, and the target length needed is ∼10 mm. An equivalent deuterium gas target would have a length of ∼ 1 m. Some other experiments go even to solid deuterium targets [78]. Of course one could improve the statistics by increasing the target thickness. But the double reaction probability within the deuterium , also grows. The final thickness is the balanced result of maximum production rate while keeping low the double reaction rate [61].

3.2.1 The target thickness

One of the delicate points for the yield normalisation is the definition of the target thickness. The difference in pressure between the deuterium and the surrounding medium ~ 1 atm, makes the thin Ti windows to curve outwards, keeping a minimum length l_o=10 mm at the bounds. But the active length differs from it. It was necessary a dedicated experiment to determine the actual shape of the target [70]. Important conclusions were obtained:

- Since the surface is curved the spherical shape assumed, as first approximation to the curved target surface, gives a target central axis length value of 12.35 mm. It was also found that the reference scale used was such that the target axis was -2 mm shifted from the beam axis (used as reference of the experiment). The value at the beam axis has a length of 12.32 mm.

- The length dependence in temperature was measured and resulted , at 20 K, less then 0.2 %/K.

Due to the vertical displacement of the axis of the beam and target, and the spherical shape of the surface, the projectiles traverse different thicknesses depending on their position at the beam spot. It is possible to evaluate the part of the projectiles that lie within a thickness which varies less than a given value. The beam spot has a 3-dimensional Gaussian distribution with $\sigma = 1.10$ mm around the beam axis, corresponding to a 2.7 mm beam spot for the typical $\sqrt{6}\sigma$ criterion, i.e. 96% of the particles within the distribution. By integrating numerically the overlap of the beam shape impinging into the spherical target surface, see Appendix F, we found that 82% of the projectiles see a thickness variation of less than 1% of the maximum value, and all of the projectiles see a thickness variation of less than 2%. This value is used to define the uncertainty of the target thickness. The length dependence on temperature results negligible in our experiment, according to the measured value of temperature dependence and the discussion in section 2.1.3.

With the discussed length and thickness the number of target atoms per unit area is obtained as

$$N_{tar} = N_o \cdot \frac{t_{tar}}{A_{tar}} \tag{3.1}$$

where N_o is the Avogadro's number, t_{tar}= 200.1 mg/cm^2, and A_{tar}=2.01 mass units. The thickness value is obtained from the discussed length and the density of deuterium, 162 mg/cm^3. The uncertainty is estimated according to the uncertainty of the energy loss method used in the study of ref. [70] ($\sim$ 1%), the uncertainty due to the position of the beam and the deformed surface of the target we have evaluated ($\sim$ 2%), and the uncertainty in the density and fluctuation due to temperature ($\sim$ 1%). We obtain an uncertainty for the thickness below 3%.

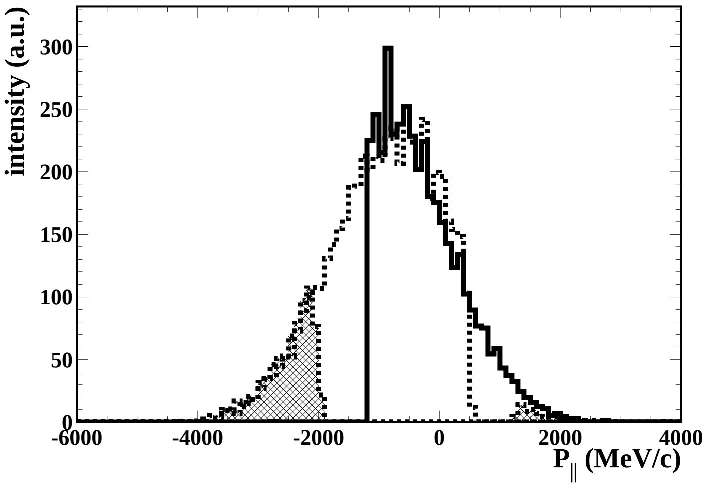

Figure 3.2: Momentum distribution of ${}^{160}_{70}Yb$ obtained in different magnetic settings of the FRS . Several momentum acceptance windows reconstruct the whole distribution.

3.3 Differential and total measured yields

The longitudinal momentum $p_{||}$ of the residues is related to the intermediate focal plane F2 dispersion-coordinate of the spectrometer, see Chapter 4 for details. The measured quantity in our experiment is actually the differential yield relative to the longitudinal momentum $dy(Z,A)/dp_{||}$.

The longitudinal momentum width is expected to vary with the root of the nucleons difference between the projectile and residue [79]. The momentum acceptance of the FRS being limited to $\sim \pm 1.5\%$, the momentum observed of a nucleus will be, in general, a certain window of its total distribution range. For the higher charges $Z \geq 84$ the whole momentum distributions are transmitted in a single *magnetic setting* of the FRS. For lower charges, the distributions have to be re-constructed by overlapping several FRS-settings. In figure 2.12 the spots next to the acceptance-position bounds appear clearly cut. The cut spots have a cut momentum distribution. For the lighter fragments, the distributions occupy most of the position range, most of them being cut.

The residues investigated in this experiment correspond to a wide magnetic rigidity range: between 12.307 and 14.611 Tm. The procedure to map the whole range is to scan the rigidity in overlapping steps, the so called *FRS-settings*, by properly tuning the FRS magnetic stages. Typically the rigidity difference between two settings is 2%: 14 settings for elements Z=92 to Z=55 without degrader; up to 55 settings were necessary in the range of elements Z=70 to Z=92, when the degrader was used, since the degrader setup restricts the transmitted number of charges. The method guarantees that the isotopic momentum distributions are fully scanned and no acceptance windows are missing. The measured quantity is the differential yield, integrated over the transversal angular distribution.

The general procedure is first to obtain the identification in atomic Z and mass A numbers, for those events with well defined ionic charge state. One FRS-setting contains a certain momentum range of a given nucleus: several settings are combined in order to obtain a single momentum spectrum for each nucleus. To compare the yields of a given residue in two different settings, it is necessary to normalise previously all those parameters involved in a particular setting that make a difference in the measured yields. We already point out the necessary corrections for the comparison, described in detail in the following sections.

- number of impinging projectiles, i.e., beam intensity and irradiation time
- dead time correction of the acquisition
- secondary reactions correction in the degrader, since several degrader thicknesses were used during the experiment to preserve the half-range condition in the different FRS settings.

Those corrections are provided by the factors that will be described later in this chapter. The rest of the parameters involved are common to all the FRS-settings, depending only on the nucleus, and can be taken into account at any time as a common correction factor. By using the normalised values, the differential distributions partially seen in different settings can be compared. The overlapping channels are selected by a maximal criterion[1]. The whole momentum distribution is the result as we see in figure 3.2, where one of such overlaps is shown, as done for $^{160}_{70}Yb$. Different FRS settings cover the total range of the momentum distribution. The distribution provides the measured momentum parameters for the width and mean value, and the counting rates as the integral of the channel content.

We see also the reason why only one charge state is selected for the analysis, the bare events. With the method presented in this work, all the combinations of the charge sates can be recognised and the identification would be fully correct, by selecting any spot in figure 2.10. The momentum distributions can be obtained in the same way as described here[2]. Although it is possible to reconstruct the distribution for any charge state combination, a larger number of overlapping settings would be necessary, identifying in each one all the charge states appearing, and combining differently many settings. To optimise both the experimental and analysis effort the ionic distribution should contain mostly bare ions, Only the bare nuclides are selected, and their differential yields reconstructed.

---

[1] The differential distribution is measured with a certain width, so that we obtain $\delta y(Z,A)/\delta p_{||}$as $\Delta y(Z,A)/\Delta p_{||}$. The size of the channels Δy is chosen so that the population of each channel is for the most of the cases well above 30 counts, overriding the possible statistical fluctuations. When comparing one channel $\Delta p_{||}$ from two distributions y_i and y_j, the criterion is to select the more populated. That warrants that the acceptance cut settings are superseded by the full-transmitted ones. The weak point of the criterion is that the statistical fluctuations are also taken always maximised. The effect is mitigated by the size of the channel Δy, containing enough statistics

[2] The momentum distribution is the same independently of the charge state of the ion, since the momentum is not sensible to it: only the rigidity is depending on it.

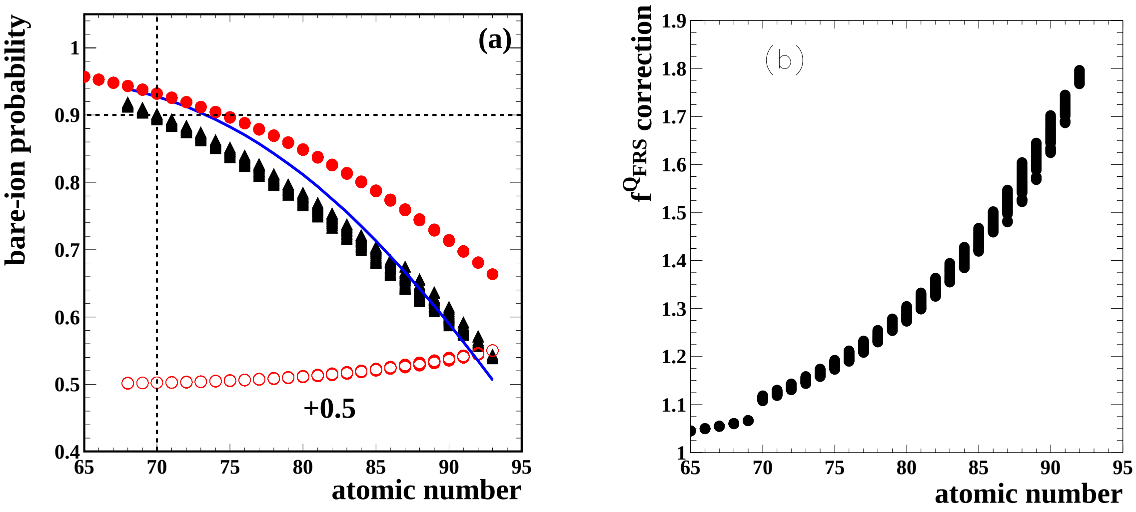

Figure 3.3: Calculated bare ion probability through the whole FRS as a function of the atomic number, panel (a). The solid line shows the GLOBAL result [72] calculated for a setup with degrader. The triangles and dots are the analytical *three-states* solution for the degrader and no-degrader setups respectively. Note the spread of probabilities due to different masses, what also appears in the data measured. The circles are the 1e-1e distribution, with an added offset of 0.5 in the plot. Two reference lines appear at 0.9 probability and Z=70. In panel (b), correction factor f^{Q}_{FRS} as a function of the atomic number. The shift at Z=70 is due to the change between degrader and no-degrader setups as we have used in our analysis. See the text for details.

3.4 Yield corrections

In this section we give a detailed discussion of the corrections needed in order to convert the *measured yields* y_{meas} into *real yields*, partially lost in the setup and analysis[3]. The kind of corrections we apply is defined by the setup we have used. The residue flux produced at the target is attenuated by nuclear and electromagnetic-dissociation reactions, see Appendix B, at the different layers of matter in the setup. These reactions are referred to as *secondary reactions*, with a probability of up to ~40% within the degrader for the heavier nuclides. Also charge changing collisions in those layers can modify the ionic state of the ions. To identify unambiguously in nuclear charge and mass, different ionic charge state combinations are excluded in both the FRS and the two MUSICs. Those rejected events, as well as the attenuation losses, have to be added to define the yields. The acquisition and reaction rates will determine additionally also a certain dead time, which

---

[3] As commented above, only the heavier fragments are measured in a single FRS-setting. The measured values corrected will give the production rates. In the case of overlapping of partial momentum distributions, the corrections are needed previously to the reconstruction of the momentum distributions.

we correct statistically. We will do the correction by calculating the different contributions and defining a factor f_{tot}, so that the yields y will be defined from the measured quantities y_{meas} by the correction factor, and normalised to the projectile current N_{beam}

$$y_{tot}(Z,A) = \frac{1}{N_{beam}} \cdot f_{tot}(Z,A) \cdot y_{meas}(Z,A) \tag{3.2}$$

The different contributions to the correction will be explained in detail in this section. We also review the possible FRS transmission influence.

A further correction is that of the additional production, at the several layers of matter at the target area, which we measure together with the residues produced by the deuterium. This amount of additional production has to be subtracted from the *total yield* to give the deuterium production simply as

$$y(Z,A) = y_{tot}(Z,A) \; - \; y_{dummy}(Z,A) \tag{3.3}$$

Following that procedure, the measured yields give as a result the yield values independently of the setup and analysis procedure. The data available allow us to discuss and evaluate the degree of uncertainty involved in those corrections. Comparing the results we have measured for setups with and without degrader, we can investigate the uncertainty related to one of the main corrections applied, that of the losses due to the thick degrader.

3.4.1 Dead time correction

In each event readout we get the information on the cumulated numbers of *accepted* T_{accep} and *total (free) triggers* T_{free}. The total-trigger number is the counting of those events arriving at the plastic scintillator at the exit of the FRS S4, and then triggering the acquisition. The accepted-trigger number is the counting of events that the acquisition system admits, since an event can be rejected during the processing of a previous one. So far the rate at the plastic scintillator, typically $\sim 10^4$ Hz, is below its maximum response rate, $\sim 10^5$ Hz, the free trigger number will correspond to the actual number of events happening at S4. The number of acquired events will be decreased according to the rate of data processing. Statistically the ratio of both will give the correction applied to the counting of any event.

$$f_{\tau} = \frac{T_{free}}{T_{accep}} \tag{3.4}$$

The dead-time values are given by the acquisition rate, $2 - 3 \cdot 10^3 Hz$, and the number of real events. The latter varies depending on the characteristic production rates of the explored isotopical region. By varying the beam intensity the dead-time values are kept in an optimal range below 20%. Some higher values, till $\sim$ 35%, are possible in regions close to the projectile, when the production rates of some channels are rather high[4]. The

---

[4] Due to the acquisition procedure, a high intensity channel will disturb the read out of lower-rate channels, since the dead time structure will correspond mainly to the overload of the main channel. That will smear off the smaller-intensity effects. It has been tested that to get rid of such *shadowing* effects it is sufficient to keep the dead-time values below 40% .

projectile one-neutron channel and the one- and two-electron ionic charge-states have to be stopped with collimators to avoid them to pass through the FRS: their intensities are too high to measure the rest of the production in that region, due to a large dead time induced. That collimation is the reason for some holes appearing in the isotopic distributions close to the projectile: they correspond to nuclei with magnetic rigidities close to the one of these problematic channels.

3.4.2 Ionic charge states within the FRS

As explained, the measured yields correspond only to ions fully stripped through the FRS. All different electronic combinations but 0e-0e must be included consequently to determine the real yields. That can be done easily if we know the survival probability for the bare ions.

To study the problem of the distribution of charge states we used the results obtained with different models. The GLOBAL model [72] contains a refined parameterisation of charge exchange cross sections depending on the target and projectile, energy and electronic shells. It has demonstrated its adequacy in many applications. The *three states* method [73, 74], considering only bare, hydrogen-like and helium-like ions, a rather good description at relativistic energies, provides an analytical solution to the system. The results are fairly good for heavy ions at relativistic energies, being compatible with those from GLOBAL. The advantage of using the analytical solution, is that the evolution of the distributions of any setup made of different layers may be easily described[5]. By using that procedure, it was possible to calculate the charge state ratios of any nucleus by following the probabilities downstream through the whole set of traversed layers, see Appendix D. That is very advantageous for the correction of charge states within the FRS and also in the MUSIC chambers. In addition we count on measurements of some charge state ratios that can help us to cross-check the results.

A GLOBAL calculation was done for the case of $U(1A \cdot GeV) + p$ reaction [37], in a setup including the degrader. The result was additionally adjusted with the help of a set of points obtained from the measured data. The only difference between the proton and deuteron induced reactions, is the possible different energy that a certain residue carries when flying within the FRS. Since this variation is not too large [6], the result must be compatible with what we obtain in the $U(1A \cdot GeV) + d$ by using the *three states* method. In figure 3.3, panel (a), we can see the results from both the GLOBAL calculation and our calculation. A difference below 5% was found, being both fully compatible in our description.

---

[5] Unless the equilibrium is reached, the output charge distribution after traversing a layer of matter depends on the input charge state. By using the three-states method only the 0-electron, 1-electron and 2-electron cases are considered. Being for a certain layer of matter p_{if} the probability of f-electrons output for i-electrons input, the probability of getting the state q at the exit, r_q is
$r_q = t_0 \cdot p_{0q} + t_1 \cdot p_{1q} + t_2 \cdot p_{2q}$
where $t_{0,1,2}$ is the probability of the input distribution, which is the result of the previous step.

[6] The energy difference will come mostly from energy losses, since the energy transfer does not depend on the reacting system but on the mass difference of residue and projectile; see next chapter.

residue Z	A	1-1 / 0-0	0-1 / 0-0	1-0/ 0-0	calculation
92	238	0.07			0.08
92	237	0.06			0.08
92	235		0.43		0.44
92	234		0.42		0.44
90	227			0.17	0.16
90	226			0.16	0.16
89	225			0.15	0.15

Table 3.1: Probabilities for different ionic charge states combination within the FRS, relative to the 0e-0e case. The 3rd-5th columns are measured data of the residues in the reaction $U(1A \cdot GeV) + d$. The last column represent the values calculated with the *three states model.*

Some results calculated are compared in table 3.1 with measured values in the reaction $U(1A \cdot GeV) + d$. For the higher charges, which present the larger contributions, the absolute differences found are below 2% between the calculations and the measured values, relative to the bare production. From this comparison we can estimate that the accuracy of the correction is ∼5%. It is stated that the analytical solution is suitable for our purposes. Once the bare survival probabilities are known, the measured yields are corrected by the factor f^Q_{FRS}, obtained as the inverse of the former probability. In figure 3.3 the results of the probability of having bare ions through the FRS are shown in the panel (a), for both setups with and without degrader. Also the probability of having an electron in both sections is plotted (here a factor 0.5 was added to zoom the plot). We see how the latter probability decreases strongly when lowering the charge. In panel (b) the f^Q_{FRS} correction values are shown as a function of the Z number.

3.4.3 Ionic charge-states within the MUSIC's

In section 2.4 we discussed that part of the ions arriving to the MUSIC chambers are not correctly assigned to the corresponding atomic number value, and are rejected in the analysis procedure with the degrader, see section 2.6.1. The measurement of the *effective charge* from the combined information of the two MUSIC chambers, allows to define the correct nuclear charge whenever the ion is bare or a charge-exchange process happens in between the two MUSICs. We have to add a posteriori the missing part, corresponding to the probability for the selected bare ions in the FRS, to be correctly assigned to Z in the MUSICs.

The *three-states* method was also used to evaluate such probabilities. The full calculation of the charge population of each residue was performed by considering the layers of matter from the FRS vacuum exit till the second MUSIC chamber, see Appendix D. The main contribution to the final result come from the thick Nb layer set in between the two MUSICs. To benchmark the results we have used the data measured with the projectile beam. In that case, the bare projectiles can be selected by using their positions at the

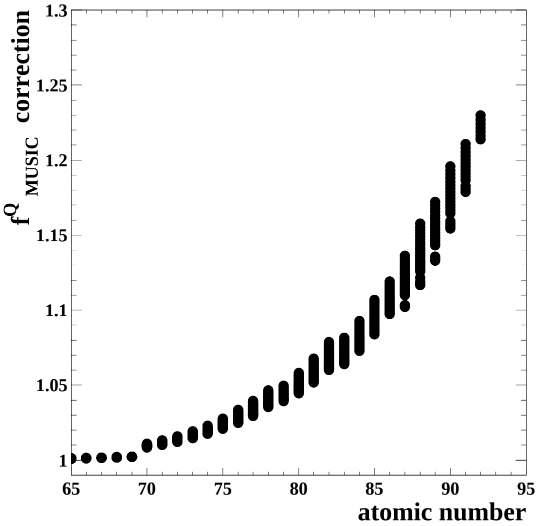

Figure 3.4: The correction f^{Q}_{MUSIC} as a function of the atomic mass number. Up to 22% of events for Z=92 are misidentified using the combined measurement of the two MUSIC chambers and rejected in the selection. See the text for details.

nucleus	degrader	total	correct-Z	ratio	calculation
^{92}U	yes	106400	84000	0.79	0.77
^{92}U	yes	102850	80050	0.78	0.77
^{92}U	no	30750	33950	0.90	0.90

Table 3.2: Evaluation of the events misidentified in nuclear charge with the combined measurement of the two MUSIC chambers. In the 3rd-3rd columns measured data for the beam is given. The 4th column gives the result calculated with the *three-states* model. All the values are restricted to bare ions within the FRS.

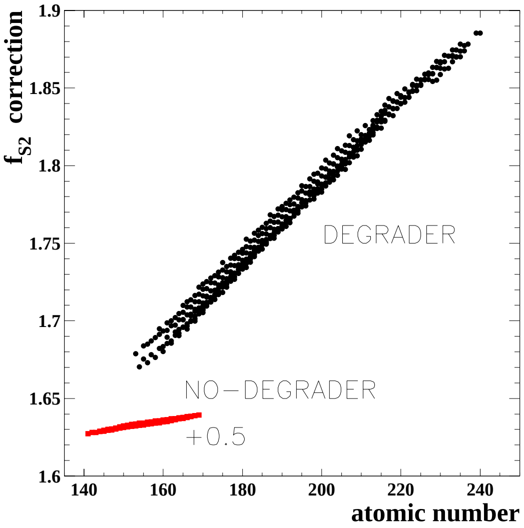

Figure 3.5: Correction values f_{S2} applied for the attenuation losses at the central image plane, as a function of the atomic mass number. They are mostly due to losses at the degrader, but also to the plastic scintillator and the Nb stripper. The lower data correspond to the correction when the degrader is missing: a factor 0.5 was added to zoom the scale. The strong influence of the degrader is clear.

intermediate F2 and final F4 focal planes, see figure 2.4, and the two MUSIC distributions can be studied as in figure 2.8. In table 3.2 we show some results for different setups. The difference between the measured and calculated values are below 2%. From this result we estimate the uncertainty of the correction to be ∼5%, and we state that the correction is suitable. Once the probability for correct atomic number Z assignment of bare ions is known, the measured yields are corrected by the factor f^{Q}_{MUSIC}, which is simply the inverse of the former probability. The values calculated are plotted in figure 3.4: we see the strong dependence of the correction with the atomic number Z. The range of $Z \leq 69$ were measured without degrader and so we distinguish the small shift at that point.

3.4.4 Secondary reactions

The fragments can undergo some reaction, nuclear or electromagnetic dissociation (see Appendix B), when traversing a layer of matter. The result of these *secondary reactions* are products that are no longer the primary reaction residues we are studying.

Any production resulting from a secondary reaction at the target area can be confused with the primary production. We have to correct for that *additional* production. If the reaction occurs within the deuterium we call it a *double reaction*, treated separately. Once the primary residue is produced, it flies forwards traversing several layers of matter before going into the FRS magnets, being attenuated. At the intermediate focal plane area S2, several material layers are used: the plastic scintillator, the Al-degrader and the Nb-stripper. At the FRS exit many materials appear also: air, the isolation and active materials of the different detectors, a Nb-stripper, ..., see the drawings and the list of layers in Appendix D. Also the beam is attenuated before reaching the target and within the target itself.

Attenuation at S2: one-neutron removal channel

If a reaction takes place at the intermediate area S2 the magnetic selection of the second FRS section will reject most of these secondary residues. The lost residues do not contaminate the counting of the the primary production, but they have to be added in order to obtain the *total yields*. We use a factor f_{S2}(Z,A) calculated as the inverse of the survival probability at S2

$$ln\left(\frac{1}{f_{S2}(Z,A)}\right) = \sum_i -\frac{N_o}{A_i} t_i \sigma_i^{tot}(Z,A) \tag{3.5}$$

where the index runs in the different materials present at S2. The σ^{tot}(Z,A) is the total reaction cross section for nuclear and EMD processes of the nucleus (Z,A) within the material, see Appendix B.

If the charge has changed in between the two FRS stages, the degrader method for selecting the isotopes rejects the event, see section 2.6.1. However if the reaction only removes neutrons, the most import channel being that of the one-neutron removal, we have to analyse the effect. Careful calculations, see Appendix, have shown that the one-neutron removal channel production lies exactly in the place of the *side spot* in figure 2.10. The bare ions suffering the removal of one neutron, lie just above the spot corresponding to their parent ions. It means that the identification selection applied already to select the charge state, takes away additionally the one-neutron removal channel. It amounts up to 3% within the thick Al-degrader. If the degrader is not used the neutron removal channel of the isotopes with mass A will contaminate the production of isotopes with mass (A-1). Fortunately the one-neutron channel production is only of importance if the degrader is present, otherwise the value being within the accuracy of the correction.

The values obtained as corrections are shown in figure 3.5. In the lower part of the figure we show the the correction for the no-degrader setup, with an offset of 0.5 to zoom the range. We observe that the largest correction corresponds to losses within the degrader (up to ~ 50%), the rest of layers producing losses below 15%.

Setups with and without degrader

We saw already how the use of the degrader becomes mandatory to overcome the difficulties of charge separation and contamination due to ionic charge-states, for the higher elements. In figure 3.4 we see that below Z ~70 the population of the charge states decreases and the possible contamination becomes negligible. The MUSIC resolution below Z ~80 is sufficient to separate the charges. That criterion is used here to determine the charge range to be investigated in setups with and without degrader.

Nevertheless we have measured the production values of the whole range of elements with atomic number above Z=68 with the two methods. If we neglect the contamination

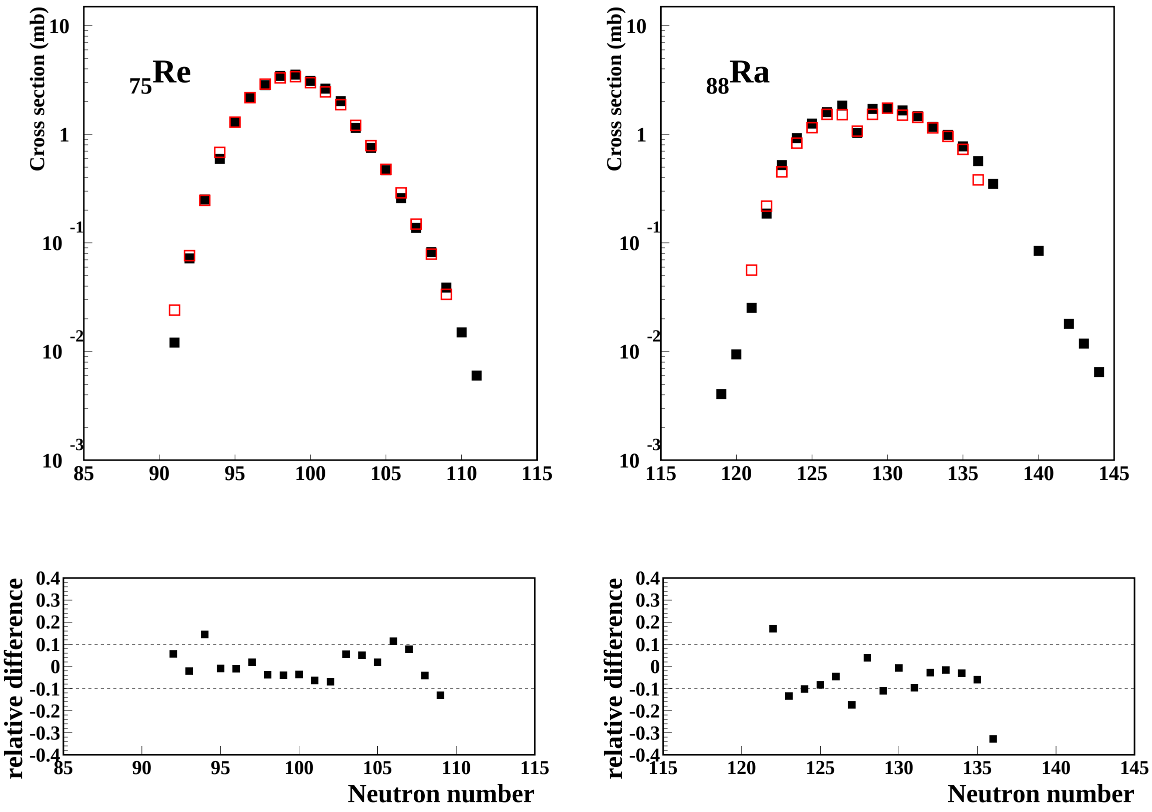

Figure 3.6: Isotopic distribution of the production cross sections of $_{88}Ra$ and $_{75}Re$ measured in this work. The two different data pairs in the upper panels refer to values obtained in a setup with degrader (closed symbols) and without degrader (open symbols). The relative differences of the two measurements, defined as $(\sigma^{no-degrader} - \sigma^{degrader})/\sigma^{degrader}$ are shown in the corresponding lower panels.

due to ionic charge states, the two results differ only in the secondary reactions in the thick degrader[7]. We can use the comparison to investigate the accuracy of the corrections applied. In figure 3.6 the yields and differences of two elements measured with and without degrader are shown. Both values agree with a difference below 10%. If we consider that the no-degrader data contains a certain contamination due to ionic charge-states, see section 2.6.2, we conclude that the accuracy of the correction proposed f_{S2} is better than 10% [8]. These results are very helpful first because the two completely independent procedures give a full compatibility in identification and production cross sections. Second, because it tests the accuracy of the corrections applied, for both secondary reactions and charge states.

Attenuation at S4

We have also to correct for those losses that happen at the exit of the FRS, mostly due to the plastic scintillator and the Nb foils in between the MUSIC chambers. In figure 3.7, left panel, we show the energy loss at the two MUSICs chambers for only ^{238}U projectiles being bare within the FRS. We can distinguish two tails: a horizontal one and a tilted one. If a secondary reaction takes place after leaving the FRS vacuum and before reaching the first MUSIC chamber (probability $\leq$2%), both energy losses measured at the MUSICs will be those of the secondary product, and so the event will lie on the tilted tail, corresponding to a lower charge. If the reactions happens in between the two chambers (probability $\leq$14%) two different energy losses will be measured, one for the primary and a lower one for the secondary product: the event lays on the horizontal tail. Of course the two-reactions case can occur: one before each MUSIC. The possibility becomes negligible for the counting, with probability $\leq 2\% \cdot 14\% \sim 0.3\%$, as it was checked. Nevertheless it explains the spots placed in between the two tails, showing losses that are low in both MUSICs. Note that the trigger at S4, is still produced in any case, since the fragment flies forwards and now we are out of magnetic selections: there are no losses of triggers if a reaction at S4 happens.

The losses at S4 have to be added to the measured yields by a certain factor f_{S4}(Z,A), calculated as the inverse of the survival probability at S4, which is defined as in equation 3.5. One can define that survival for both, before and between the chambers, but since they are independent, they add up. The values we have calculated and measured for the projectile bare ions, using the statistics found in a plot as that of figure 3.7, are shown at table 3.3. Since we observe a difference up to 1% in a correction of ~83 %, the uncertainty of this correction is ~2%.

Note that the attenuation due to all the reactions before and between the chambers are

---

[7] As it was discussed in section 2.4 the measurements made without degrader suffer from the contamination of those events whose nuclear charge is wrongly assigned in the MUSIC chamber. Additionally the charge separation is not so sharp any more for the higher values. The two effects will determine the differences we observe.

[8] Since the corrections for charge states and secondary reactions are mixed up, we can only compare the latter correction. The charge states are evaluated with the same procedure, and the uncertainty is the same for both setups. The difference we observe, up to 10%, is then a limit in the correction for secondary losses.

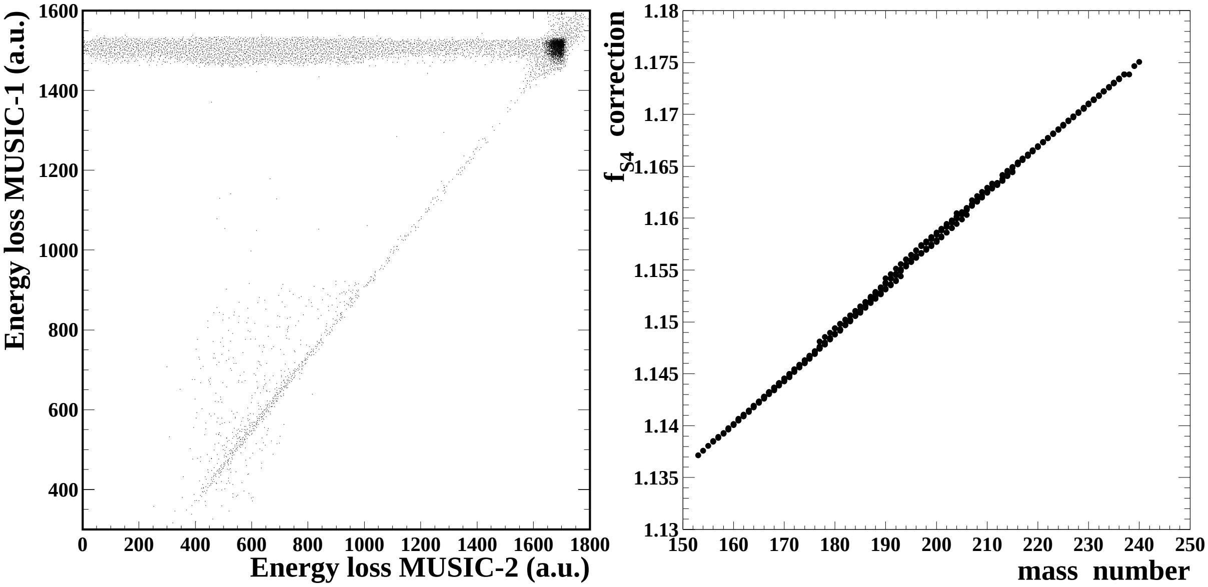

Figure 3.7: Left panel: energy loss at the two MUSIC chambers, for the projectile ^{238}U ions which are bare within the FRS. The horizontal and tilted tails are clearly seen departing from the charge spot in the upper-right corner. They correspond to secondary reactions happening in between or before the MUSIC chambers. Right panel: the correction f_{S4} applied for the losses at S4.

included in the correction factor f_{S4}. Investigating the different possibilities happening at S4, we know that for the reactions at S4 including a change in Z number, the event is rejected (when the degrader is used). If not rejected, i.e., if only some neutrons have been lost, the identification is correctly done, since the Z-value is correct, and the A/Q value will be right (there are no more magnetic deflections). The non rejected values are counted twice, due to the correction applied. Nevertheless they are a tiny fraction of the total nuclear reaction probability. The EMD processes, leading to the loss of neutrons, are not included in the calculation of total reaction probability in equation 3.5. The agreement of the measured and calculated data shows the difference that the channels counted twice introduce in the result, is below our accuracy.

degrader	P_{S4}	P_1	P_1^{cal}	P_2	P_2^{calc}
yes	0.17	0.02	0.02	0.13	0.14
no	0.16	0.01	0.02	0.14	0.15

Table 3.3: Values of the reaction probability of ^{238}U ions at S4: probability till the entrance of the second MUSIC chamber P_{S4}, before the first MUSIC chamber P_1, and in between the two MUSIC chambers P_2. The calculated values are $P_{1,2}^{cal}$.

Residue production in the target area

At the target area S0, we have several layers of matter mixed up downstream, see Appendix D. The observed production of any residue is the result of the production in all of the former layers. Since we want to define the deuterium production, we must take away what is additionally produced at S0: the so called *dummy production*, y_{dummy}[9]. By knowing the additional production, the total measured yields can be corrected to give the deuterium production as shown in equation 3.3. Note that the y_{tot} value is that of the corrected production. Here we refer to the whole target production, independently of the reaction mechanism involved.

The straightforward method to measure this contribution is to use a deuterium-free target: the residues measured will be produced by everything at S0 but the deuterium. Unfortunately a detailed measurement would imply a long time consuming effort, both experimental and of analysis, due to the number of FRS settings needed to fully scan the residues range: for the setup with degrader we would need up to 55 FRS settings, as we discussed above. The strategy used in the experiment was to measure several FRS settings, obtaining a reduced number of dummy yields. The measured data are used to benchmark the results of independent calculations.

The calculation of the residue production in all the S0 layers was made by using the *single reaction approximation*, see Appendix B, the production cross sections of ^{238}U induced reactions in all the different layer materials, and considering both the attenuation of the beam till the reaction point, and that of the residues downstream. The result of the calculation depends decisively on the values of the production cross sections. On the one hand, we had to evaluate those cross sections from existing data of ^{238}U induced reactions. On the other hand, we have to include the reactions and attenuation in all the different layers at S0: the Al-SEETRAM foils, the Ti-windows of the target and the Nb-stripper. The definition of the cross sections is explained in the following section.

In figure 3.8 we show the calculated production rate values of elements ^{90}Th and ^{86}Rn (triangles), compared with those measured directly (circles). Also the total measured productions (squares) are shown for comparison. Typically the dummy production was about 3% of the total measured production. The results showed an overall agreement. Additionally a small scaling factor was applied to the evaluated data to account for the differences due to the presence of Al-coated mylar ($C_5H_4O_2$) mainly, which was difficult to parameterise.

The small contribution resulting from the *dummy production* introduces small uncertainty in the results of the yield calculation, since even a large uncertainty in the evaluation would represent a small change in the correction. As example, consider that a 50% deviation in the evaluation of the dummy yield, would lead to change in the correction up to 4.5%, being 3% the typical value. The induced uncertainty of this correction is below 2%.

---

[9] The name of *dummy production* is due to the way in which the additional production is determined, by measuring the production with a deuterium-empty or *dummy* target

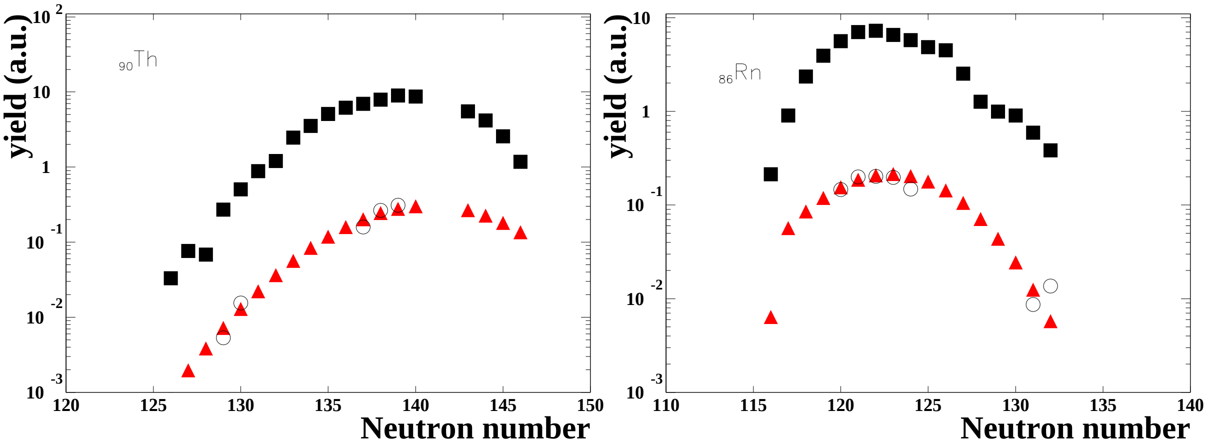

Figure 3.8: Isotopic distributions of the yields of ^{90}Th and ^{86}Rn for ^{238}U induced reactions. The evaluated yields of the different layers of matter but deuterium, at the target area, are plotted (triangles) together the measured values (circles). The typical contribution to the total was ∼3 %. The whole target production (squares) is also shown.

Fragmentation cross sections

To evaluate the production from the matter at S0, we need a large set of production cross sections of ^{238}U induced reactions in different materials: Al, Ti and Nb. Note that we need to evaluate the production for all the measured nuclides. The data is scarce and we were obliged to use calculations and estimations. To crosscheck the results we count on the few data measured with the empty target. To evaluate the cross sections, we have used two alternative procedures: the first, by using measured residue productions and scaling laws; the second, by using model calculations.

The measured residue productions from two different reactions $^{238}U(950A{\cdot}MeV)+Cu$ [80, 81] and $^{238}U(1A{\cdot}GeV)+Pb$ [81, 82] allow to estimate the cross sections of our interest. In the regime of *limiting fragmentation* and *factorisation*, see Appendix C, the shape and position of maximum production of the fragmentation values of different reactions, are about the same, despite the values which are scaled. That is equivalent to a kind of memory loss of the reaction respect to the origin of the process. The production cross sections in different materials σ_i can be estimated from a common cross section σ and a scaling factor depending on the target material γ_i. That scaling can also be seen in the data of proton and deuteron induced reactions on ^{238}U, as shown in figure 4.1. To estimate the scaling factor γ_i for Ti, Al and Nb, from data of Cu and Pb reactions, we use EPAX, since we have tested that the result of the relative value given by EPAX is compatible with the measured data for Cu and Pb[10]. With the data of Cu and Pb as reference, one obtains the different production cross sections: $\sigma_{Cu} \sim 0.956 \cdot \sigma_{Ti}$, $\sigma_{Pb} \sim 0.770 \cdot \sigma_{Ti}$, ...

The possibility of using parameterisations like EPAX [83] is not suitable since the fission channel is not included, and for elements of atomic number above Z=80 the results present a big discrepancy with the data, specially for the neutron deficient side, and in the position of the isotopic maximum production [84]. However more suitable codes as it is ABRABLA, allow the reproduction of cross sections of measured ion-ion collisions [80]. With the help of this code we have calculated the whole set of residual productions of our interest.

Using these cross sections we have evaluated the yields, and we compared the results with the measured data with an empty target. Both methods and the data showed a very good agreement. Additional small scalings factors were applied to the evaluated data to account for the differences due to the presence of Al-coated mylar ($C_5H_4O_2$) mainly, which is difficult to parameterise.

3.4.5 Transmission through the FRS

The design of the FRS allows for a limited acceptance in momentum (±1.5%) and angle (±15 mrad). The longitudinal momentum acceptance is closely related to the physical transversal area of the FRS, the dipole strength and design radius limiting the magnetic rigidities accepted. The nuclei with momentum values $\sim \pm 1.5\%$ of the FRS setting central value, are within the acceptance. The angular acceptance is additionally determined by the aperture and strength of the quadrupoles at the exit of a dipole. That interplay gives an angular acceptance of $\sim \pm 15$ mrad. The transmission of a given nucleus at certain energy is defined by those two limits and the position of the particle at the intermediate and final focal planes of the FRS. A systematic study of the transmission of the spectrometer was performed recently [64]. The transmission of any residue can be accurately determined depending on the reaction mechanism studied and according to the FRS optical characteristics.

The typical angular distribution of fragmentation residues, as we have measured in this experiment, is below ~ 5 mrad. The transmission is close to 100%. Only at the bounds of the focal plane positions, the effect will be important. Since we overlap different FRS settings, as we discussed at section 3.3, the re-construction of the momentum distribution is complete, and the transmission restriction overcome. That is not the case of fission [64, 85], which we discuss later in the chapter. Here we briefly present the result of the transmission of the residues of fissioning heavy ions.

In figure 3.9 we show the result of a calculation of the transmission for fission residues with atomic number Z≥45. If we know the fissioning nucleus, we can estimate the transmission of the fission fragments: the lines in the figure are the results corresponding to ${}_{92}U$, ${}_{86}Rn$, and ${}_{74}W$. The calculation was done by assuming a position at the final focal plane of 80% of the range, what is a conservative estimation. We see that the fission

---

[10] Note that the use of EPAX is to define the relative scaling in the production between two different reactions. Despite the wrong absolute values, the relative value remains correct, as we tested in the comparison of the measured values of production from U induced reactions in Pb and Cu.

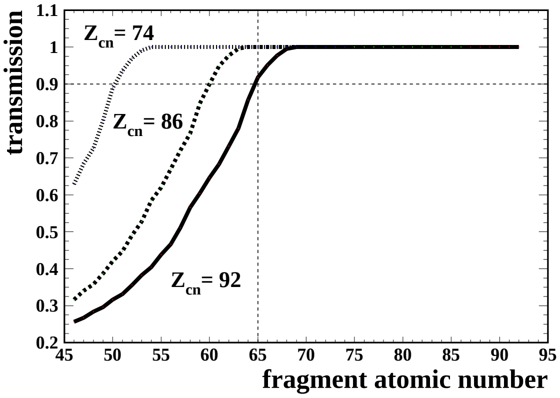

Figure 3.9: Calculated transmission for fission fragments as function of their atomic number. The values were calculated according to ref. [64], selecting the fissioning nucleus and keeping its Z/A ratio for the fission fragments; the position at the final focal plane was chosen 80% of the range. The results correspond to the fissioning nuclides $_{92}U$ (full line), $_{86}Rn$ (dashed line) and $_{74}W$ (dotted line). The two reference lines mark the 90% transmission and the atomic number Z=65.

fragments with atomic number above $\sim$ 65, and produced by nuclei with Z below 92 are transmitted more than 90%. The transmission affects decisively the observation of the momentum distribution of the different reaction mechanisms, as discussed below.

3.5 Yields

It has been described how the number of counts directly measured as production of a certain nucleus has to be corrected to give the actual production rate. According to the former discussion the residue yields are obtained as show in equation 3.2, with the correction factor f_{tot} defined as follows[11]

$$f_{tot}(Z,A) = f_{dead} \cdot f^{Q}_{FRS}(Z,A) \cdot f^{Q}_{MUSIC}(Z,A) \cdot f_{S2}(Z,A) \cdot f_{S4}(Z,A) \tag{3.6}$$

The deuterium yield is obtained by subtracting the measured additional contribution of the materials in the target area, from the total yield as in equation 3.3. The detector efficiency is close to 100% in the counting range of our experiment, introducing no further corrections. If some transmission restriction would exist, the yield should be also corrected with a factor $f_{trans}(Z,A)$. As discussed in section 3.4.5, in the range of fragments with atomic number Z$\geq$65 the transmission is close to 100% for both fragmentation and fission.

Using this prescription, we can calculate the *residue yields*. In this work we present the production of residues with atomic number Z$\geq$65. If the separation of the two underlying

---

[11] It is the same correction we need in order to reconstruct the momentum distributions by overlapping several FRS settings. Additionally it has to be normalised to the irradiation with the factor $\frac{1}{N_{beam}}$.

processes of fission and fragmentation was possible, the yields would be referred to as the fragmentation and fission parts

$$y(Z, A) = y^{frag}(Z, A) + y^{fiss}(Z, A) \tag{3.7}$$

$$y^{frag}(Z, A) = y(Z, A) \cdot \Gamma_{frag}(Z, A) \tag{3.8}$$

where Γ_{frag} is the part of fragmentation found, and obviously $\Gamma_{fiss} = 1 - \Gamma_{frag}$.

3.6 Fission and fragmentation contributions

The initial pre-fragments and neighbouring excited nuclides populated in the de-excitation chains followed in the reaction we study $^{238}U(1\ A \cdot GeV) + d$, are affected strongly by fission, as will be shown in Chapter 4. The production of heavy mass residues is mainly due to the fragmentation reaction mechanism, since fission populates mostly the medium-weight region. Although we have found that the fission contribution is appreciably present in the heavy fragment production. We are not going to discuss the fission process within this work, but we relate the observation of that channel.

We can observe the presence of fission in several quantities that reflect the strong differences between the two mechanism. After a brief discussion on the interplay of the reaction mechanism and the FRS transmission characteristics, we explain how to separate the two components. Unfortunately the method lacks accuracy: we propose a separation which provides an estimation of the contribution of each mechanism. The result is consistent with the systematic behaviour of the cross sections. But the uncertainty in the production cross sections of the separated mechanism increases definitely.

3.6.1 Fission signatures

In this section we are going to show the presence of fission, as it appears in the heavy mass production we have measured.

The pre-fragment distribution keeps the average A/Z value of the projectile, see Chapter 5. It is the same for the fission residues which preserve the A/Z value of the fissioning nucleus. However, in a particle emission chain, during the de-excitation, the Coulomb barrier inhibits the proton emission, and the result is that the A/Z ratio of the residue moves to the neutron-deficient side of the isotopic chains. If a pre-fragment undergoes fission, only a small part of the energy is employed in particle emission, and the resulting fission residues are neutron-rich. That is the result described in experiments as those of refs.[85, 86, 87].

In figure 3.10-(a) we present the production cross sections as measured for $_{65}Tb$, compared with the estimation of EPAX [83]. EPAX provides a rather good description of the fragmentation production slopes within the *fragmentation corridor* (see further discussions in Chapter 4). The code does not include the fission channel. The slopes of the tails of our data and EPAX differ not too much for Z∼70, but below that value, the neutron-rich part changes drastically, and the data over-passes the EPAX predictions. Additionally, the production cross sections values should vary smoothly between nuclides with dependence in the neutron and atomic numbers of type N-Z=constant. In figure 3.10-(b) we show the measured values (dots) of the isotopes following a relation of type N-Z=constant. The expected behaviour of the fragmentation production is that of a constant-slope line (squares).

From a different point of view, the longitudinal momentum of the residues from fission and fragmentation mechanisms are very different, due to their own kinematics. this is discussed in the following section related to the transmission. The momentum distribution is much broader in the fission residues. The momentum of a fragmentation residue depends mostly of the root square of the mass difference relative to the projectile, see section 4.7. It changes very smoothly. If some fission contributes to the production of a certain residue, the momentum width will change very quickly with the mass, increasing for the neutron-rich. In figure 3.10-(c) we show the measured width of the momentum distribution of several elements with atomic numbers 70 to 85 (the measured values for the momentum distributions are presented in Chapter 4). While for higher Z values the width shows no strong correlation with the mass, for $Z \leq 75$ the width increases very much in the neutron-rich side.

All those changes observed in the measured trends, and not expected as a result of the fragmentation process, are understood if we think of a fission contribution. The possibility of disentangling the two processes becomes clearer when looking at the measured momentum distributions of the nuclides.

3.6.2 FRS transmission and the separation of fission

The experimental technique we have used relies in the measurement of the longitudinal momentum distribution of the reaction residues. To understand the observed shapes of these distributions first we have to comment on the kinematic aspects of the two mechanisms of fission and fragmentation, and the role of the FRS acceptance. The longitudinal momentum of a projectile-like residue resulting from a fragmentation reaction is Gaussian shaped in the projectile and laboratory frames, see section 4.7. The fragment distributions can be fully transmitted by the FRS since the angular acceptance (~ 15 mrad) is largely higher than the angular distribution of the heavy fragments measured (~ 5 mrad). The limits in momentum acceptance ($\pm 1.5\%$) are overcome mapping the momentum range with the necessary FRS settings.

When dealing with fission the reaction kinematics are completely different. The fission fragments have isotropic momenta in the centre of mass of the fissioning nucleus. The conversion into the laboratory frame produces a characteristic momentum ellipsoid depending on the ratio of the longitudinal and transversal momentum values. The size of the ellipsoid is defined by the average momentum associated to the process, and its thickness by the width of the momentum associated to the process. This kinematic image is schematically plotted in figure 3.11. The region of the momentum phase space occupied by the fission residue, defined by the angle θ, is collimated by the FRS momentum and angular acceptances, θ_o . That is plotted in the same figure. This briefly outlined concepts are a rather tough topic discussed in refs. [64, 85], and essential in the definition of the fission residues cross sections.

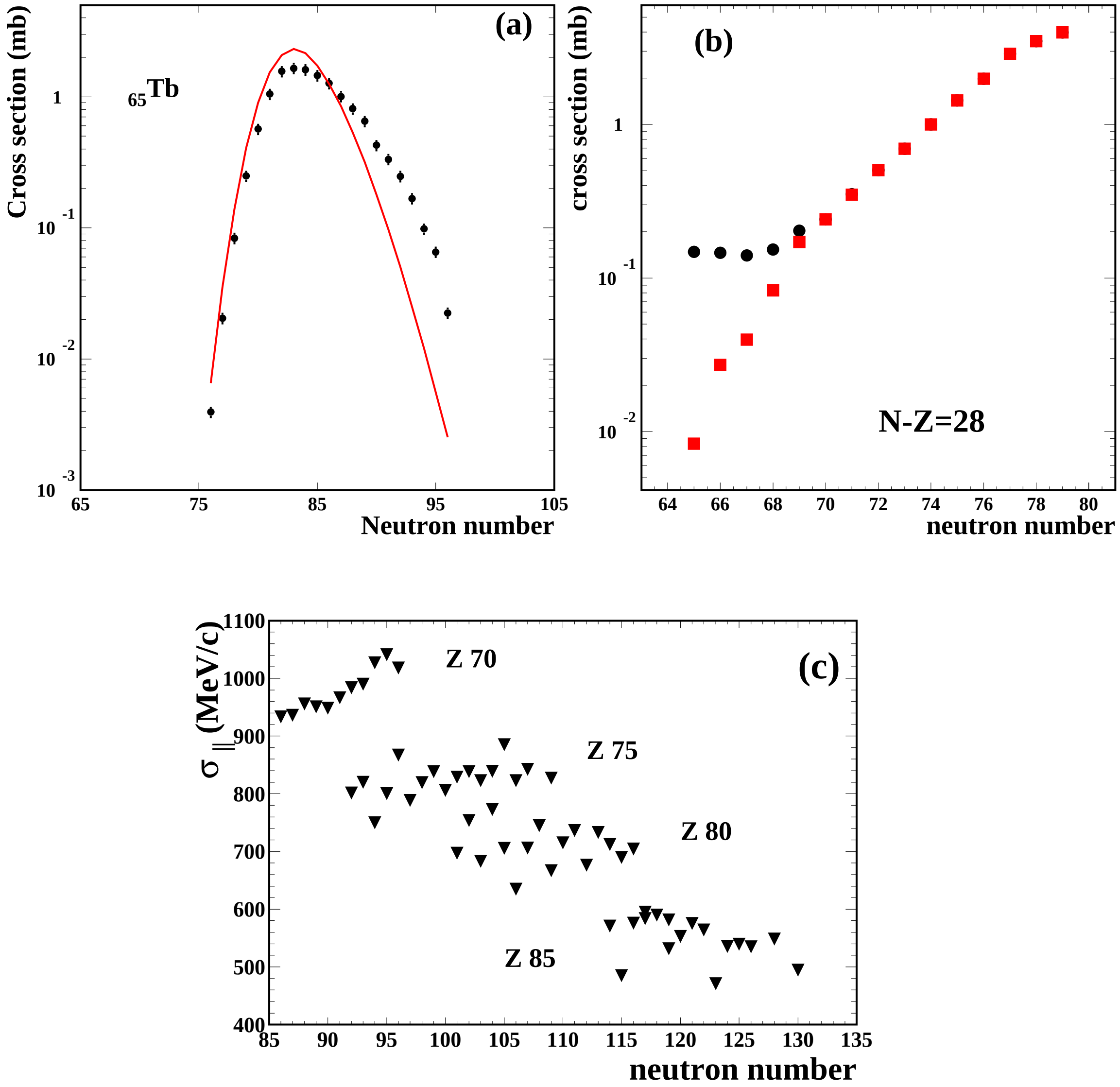

Figure 3.10: Different signatures of fission. Panel (a): measured cross sections of $_{65}Tb$ (dots), compared with EPAX (line) [83]. The change in slope of the data for neutron-rich isotopes cannot be due to fragmentation. Panel (b): measured cross sections of nuclides following the constraint N-Z=constant. The fragmentation production along those lines are expected to follow a constant slope (squares) and we can observe the strong change in the measured data (dots). Panel (c): measured width of the momentum distribution of several elements with atomic numbers 70 to 85. While for higher Z values the width shows no strong correlation with the mass, for Z≤75 the width increases very much in the neutron-rich side.

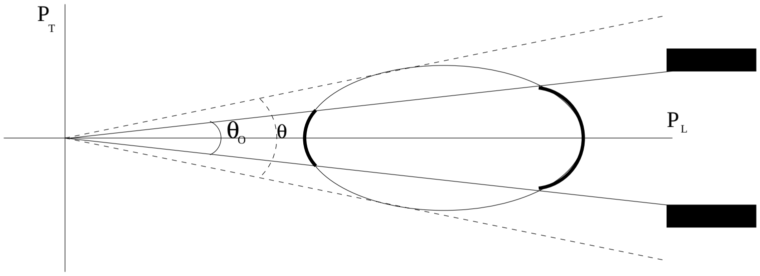

Figure 3.11: Momentum phase space of a fission residue in the laboratory frame. The longitudinal P_L and transversal P_T momentum components are plotted. Note that the distribution covers the *skin* of the ellipsoid. The FRS entrance and subtended angle θ_o defines the accepted part of the residue momentum distribution, subtended in angle θ.

If the transmission was 100% we would observe the full longitudinal momentum distribution by mapping the range again with the necessary FRS-settings. Since the emission is isotropic the resulting distribution is rectangular, with a central value and a spread depending on the fissioning nucleus, typically much wider than those values of fragmentation. In the case of a reduced transmission, the momentum region transmitted is cut for the higher values of the transversal emission. Depending on the size of the momentum region results the missing part of the observed distribution. The projection of the longitudinal coordinate results in a two-piece profile, each one due to the two edges of the ellipsoid: the forward and backward components, the intermediate values being suppressed, cf. figure 3.11

In this work we restrict the study to elements with atomic number $Z \geq 65$. As we discussed in section 3.4.5, we have nearly full transmission for all the residues resulting from any of the two reaction mechanisms. In figure 3.12 we show three measured momentum distributions of nuclides ${}^{205}_{85}At$ (a), ${}^{156}_{66}Dy$ (b), and ${}^{148}_{62}Sm$ (c). The three isotopes belong to the neutron-rich side of the isotopic production. While the distribution in (a) is Gaussian shaped (we have plot a Gaussian fit on top of it), and attributed to fragmentation, the distribution in (c) can be only due to a strong fission contribution, being the fragmentation a smaller part. Panel (b) is a case when both contributions appear: we see how the Gaussian shape is distorted in the base and a wider distribution is underlying in the data. To study the relative contributions of each mechanism we have used the measured momentum distributions, as those plotted in figure 3.12.

We have included several approximations. First, the fragmentation part was assumed to be Gaussian[12]. Second, the width of the neutron-deficient isotopes of each element, where the fission contribution seems to be negligible, is taken as reference to evaluate the width attributed to fragmentation in the rest of the isotopes, according to the Morrisey systematics [79]. Considering a Gaussian distribution for fragmentation, folded with a rectangular distribution for fission, it is possible to fit the measured distributions and

---

[12] In section 4.7 we discuss that additional contributions are included to account for the setup influence. Those contributions are of quite smaller importance in comparison to the contribution of each of the two processes we describe here.

define the main parameters: the mean momenta for fragmentation and fission, the widths and the relative proportions of the two contributions. The latter gives the factor to separate the two contributions from the total yield.

We could not disentangle fission in elements with atomic number above 70. The evaluated fragmentation-to-total ratio is given as a function of the neutron number for each element. It is smoothed by considering the boundary isotopes when the fission contribution is either 0 or 100%, as expected from a systematic behaviour. In figure 3.12, panel (d), we show the corrections applied in this work. The procedure we have used is not completely self-consistent, since different approaches were done, and, e.g., we did not correlate the production between two elements. The method provides an estimation of each contribution to the production. The corrected values are considered realistic, with a higher uncertainty in respect to the whole production cross section, since the resulting values follow consistently the systematic behaviour of the fragmentation cross sections. In figure 3.10, panel (b), the values following the fragmentation systematics (squares) are the result from the proposed evaluation.

3.7 Production cross sections

In this section we discuss the last step to define the residues production cross sections of the reaction $^{238}U(1A\cdot GeV)+d$. The yields have to be normalised according to the target thickness or better, the number of target nuclides N_{tar}, defined in equation 3.1. The beam intensity was already introduced in the definition of the yield, see equation 3.2. Within the *single reaction approximation* the cross sections can be easily given by the yield, the target thickness, and a correction factor for losses within the target itself, see Appendix B. The approximation neglects the possible contribution to the residues of any source but the projectiles. The approximation remains correct as long as such contributions are negligible, i.e. for very thin targets.

Our target was selected with a thickness such that the reaction probability of the ^{238}U projectiles was ~10%. That is also the order of magnitude for the reaction probability for the heavy residues we observe. We cannot neglect the secondary reactions that the residues suffer within the target, inducing a change in the observed residue distribution, respect to the primary distribution. The description of the cross sections has to be done considering that the projectile is not the only source of any observed fragment: also the secondary reactions of the residues will populate lower masses. The effect is referred in the following as *double reactions.*

We are going to discuss a method to effectively correct the cross sections and approximate the values to the corrected cross sections without *double reactions.* This is actually a correction that corresponds to the measured yields. However it is applied directly on the cross sections. In addition we have to include the projectile and fragment attenuation within the target itself.

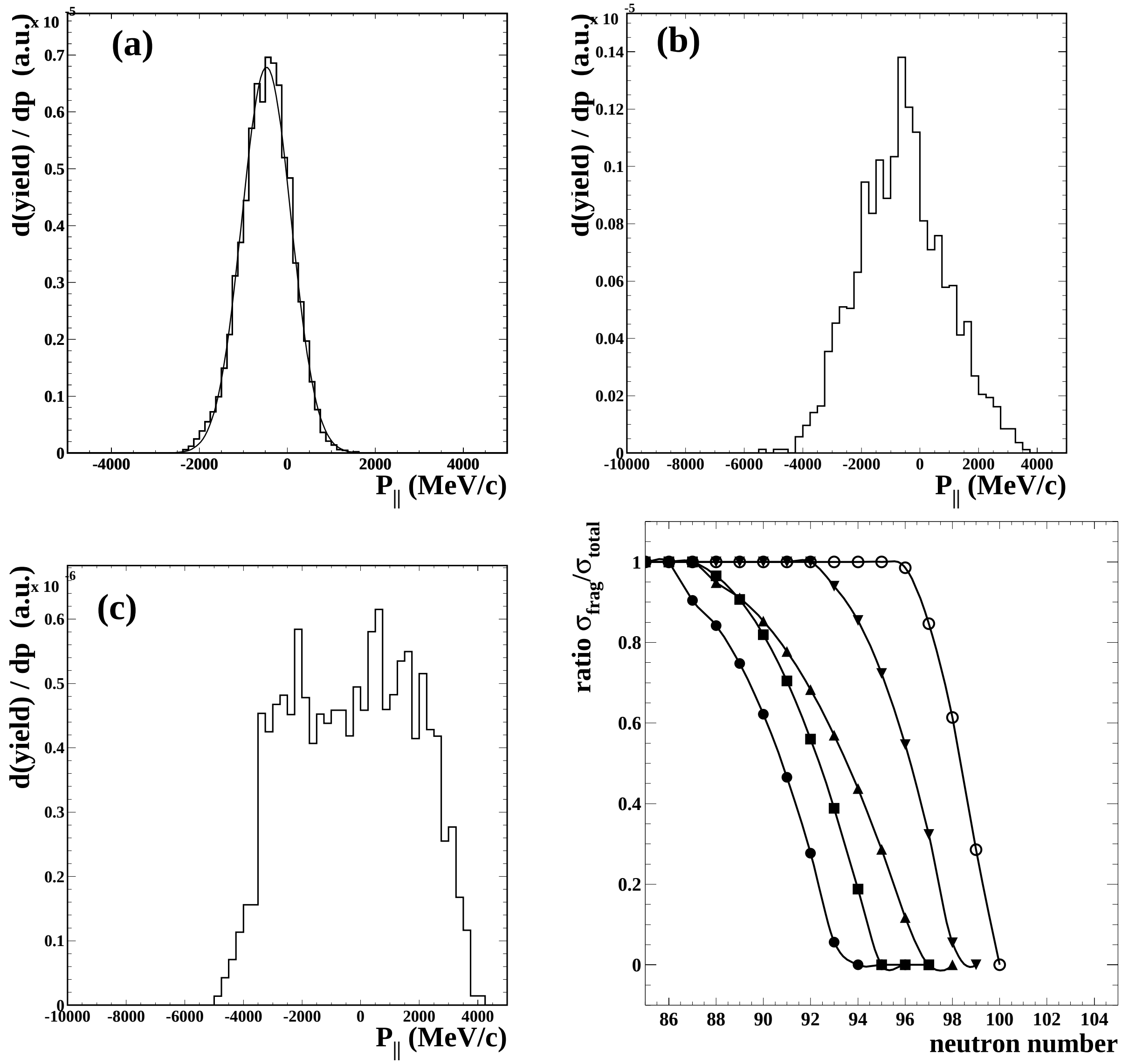

Figure 3.12: Measured momentum distributions of the nuclides $^{205}_{85}At$ (a), $^{156}_{66}Dy$ (b), and $^{148}_{62}Sm$ (c). The three isotopes belong to the neutron-rich side of the production. On top of the distribution (a) we have plotted a Gaussian fit. Panel (d) shows the fragmentation contribution to the production for the elements with atomic number Z=65-69, evaluated as proposed in this work.

3.7.1 Double reactions within the target

The production of a certain fragment (Z,A) is described as the result of the balance of one *populating channel* ,i.e., the primary production by the projectile and the contribution from any other fragment that undergoes some reaction ending into (Z,A), and one *depopulating channel*, i.e., any secondary reaction that can undergo (Z,A). This balance connects the yield $y(Z,A)$ and the number of nuclides in the target N_{tar}. We have a system of equations where all residues are present

$$\frac{dy(Z,A)}{N_{tar}\cdot dl} = \sum_{Z_i,A_i} \sigma(Z_i,A_i \to Z,A) - \sum_{Z_k,A_k} \sigma(Z,A \to Z_k,A_k) \tag{3.9}$$

where l is the target thickness, and $N_{tar}\cdot l$ gives units of number of dispersion centers per surface unit, referred as t in the following. The approximate method to solve the previous system is explained in refs. [15, 35, 36], and it is briefly reviewed here. The method describes the overall production of a fragment (Z,A) within the target as if the projectile production would happen in the first half of the target[13], while in the second half, the fragment could undergo a second reaction (depopulating channel) or some other fragment could become the one we are considering (populating channel).

The first step is to evaluate the data within the *single reaction approximation*, see Appendix B, obtaining certain production cross sections σ_o. Within the prescription proposed above, one considers the relationship between the observed σ_o affected by double reactions, and the actual primary cross section σ. On the other way around, supposing that all the σ values were known, to evaluate the measured production after traversing a target of thickness $t_{target}/2$ we should evaluate

$$\sigma_o(Z,A) = \sigma(Z,A) - \sigma(Z,A)\cdot\sigma^{tot}(Z,A)\cdot\frac{t_{tar}}{2} + \sum_{Z_i,A_i} \sigma(Z_i,A_i)\cdot\sigma(Z_i,A_i \to Z,A)\cdot\frac{t_{tar}}{2} \tag{3.10}$$

The right term contents the measured value σ, the losses by secondary reactions in the second half of the target ($\sigma^{tot}\cdot t/2$ is the reaction probability), and a third term describing the contributions from other residues ($\sigma(Z_i,A_i \to Z,A)\cdot t/2$ is the probability for a formed residue to interact in the second half of the target).

In this equation, the difference $\Delta\sigma = \sigma_o - \sigma$ is the contribution due to the double reactions. One can consider equation 3.10 as an implicit equation, and solve it by iteration. First one inputs the observed values σ_o as if they were the primary production σ [14]. The equation provides a value for $\Delta\sigma$; subtracting that difference from the observed σ_o one gets the first approximation to the actual production. These are the new input values for the second iteration. Obtaining successively a corrected value of σ, the process stops when the result stabilises at some value, below the uncertainty. Otherwise, the obtained values must reproduce the measured values within its uncertainty, according to equation 3.10.

---

[13] This approximation at half the target is not arbitrary, since the production probability has its average at the central plane of the target.

[14] The resulting implicit equation is then equivalent to consider a target of half the thickness, next to the actual one.

The result of the whole calculation is the correction of the measured cross sections by a factor defined from the former procedure

$$\sigma(Z, A) = \sigma_o(Z, A) \cdot f_{double}(Z, A) \tag{3.11}$$

The method would be rather direct, using total reaction cross sections σ^{tot} as described in Appendix B, but it includes a a big drawback: the values $\sigma(Z_i, A_i \rightarrow Z, A)$ are a large collection of data mostly unknown. Only using code calculations providing realistic descriptions of the cross sections it is possible to apply this method. It will be discussed in Chapter 5 the difficulty to determine the code which could be used for reactions happening within a deuterium target. In figure 3.13 we show the value of the correction f_{double}, from a calculation performed considering a simple relation for the production cross sections only depending on the mass difference relative to the projectile. That is a rather good approximation in reactions where the fission is not a very strong component, and it was successfully applied in refs. [15, 36]. Note that the correction describes losses ($f_{double} > 1$) for the heavier masses, and contributions for the lighter ones. We observe also that for masses below $A \approx 150$ the correction is as high as $\sim 40\%$. This result indicates that a large part of the measured residues are coming from the secondary reactions within the target, and not longer from primary production. Since the accuracy associated with the correction decreases with increasing values of f_{double}, the method defines the limit of applicability.

We have decided to skip this correction at this time, since the accuracy needed is not reached by the available code descriptions. Despite the crude approximation to our system, we consider the former calculation as an estimation of the correction in our reaction. Actually one of the main reasons why to restrict the results of fragmentation production to charges above Z=65, is the strong contribution of *double reactions* that we expect for elements below that limit.

3.7.2 Total and fragmentation productions

The total production of residues with atomic number Z≥65 of the reaction $^{238}U(1A \cdot GeV) + d$ have been measured for the two production mechanism involved. For Z≥75 the production is fully attributed to fragmentation, since no fission signature has been found. The neutron-rich residues of elements with Z≤69 are affected by fission and an estimation of that contribution has been obtained. In the range of elements with $70 \leq Z \leq 74$ no disentangling of the two mechanisms is possible. Indications of the presence of fission appears, but neither the yields systematics nor the momentum distributions allow for a clear separation. The fission contribution to the production is estimated to be less than 0.1 mb.

In figure 3.14-3.15 the isotopic total production cross sections results are presented. In figure 3.16 we show the isotopic production cross sections as separated for fragmentation (circles) and fission (squares).

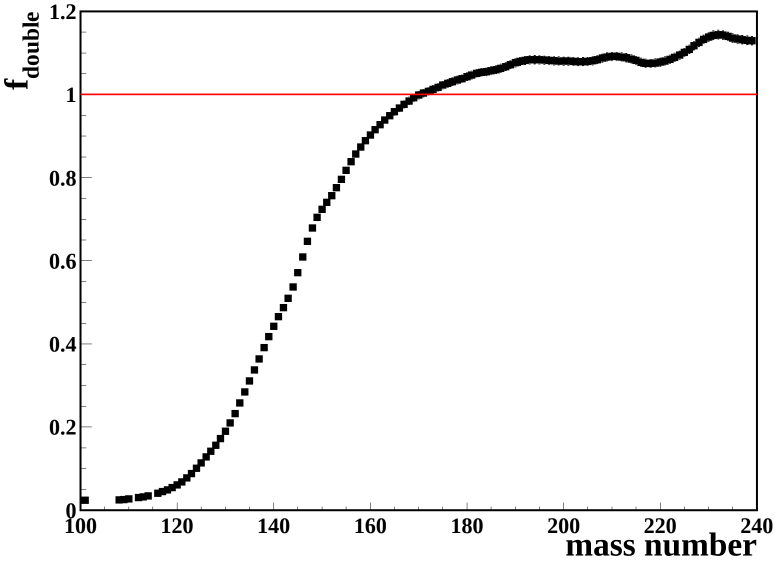

Figure 3.13: Correction for double reactions within the target as a function of the mass number. This result corresponds to a case in which only a dependency associated to the the mass of the isotopes is considered. See the text for details.

3.8 Uncertainties

3.8.1 Statistical uncertainty

The evaluation of the statistical uncertainty was done by adding quadratically the Poissonian error of the accumulated statistics $\sqrt{n}$, and the deviation from a smoothed-trend behaviour. Since the measured data are expected to behave systematically in the lines were the values change slowly, e.g. the $N - Z = constant$ or $N - 2Z = constant$, the data would follow a quite soft trend. By a smooth-interpolating procedure a smoothed curve is fitted to the data. The root-mean-square deviation of the data respect to the fitted value, in a region around the isotope, provides the correction for statistical deviations. Some N-Z=constant data points and the smoothed interpolation-curves are shown in figure 3.17. The statistical uncertainty is kept below 10% down to 0.1 mb, as it was one of the aims in the proposal of this experiment.

3.8.2 Systematic uncertainty

The uncertainty associated to the different corrections applied to the description of the cross sections, have been pointed out through the discussion in this chapter. We review them in table 3.4. We saw that by comparing the values measured in setups with and without degrader, the values were compatible within 10%. That allows to set a uncertainty for the f_{S2} correction, one of the most important factors, below 10%. The uncertainty for f_{S4} is the same. The correction f^{Q}_{FRS}, being important for the highest charge values, was cross checked with available data and we estimate the uncertainty to 5%. The total

Figure 3.14: Total isotopic production cross sections measured for elements Z=77-92. Total uncertainty shown if larger than the symbol.

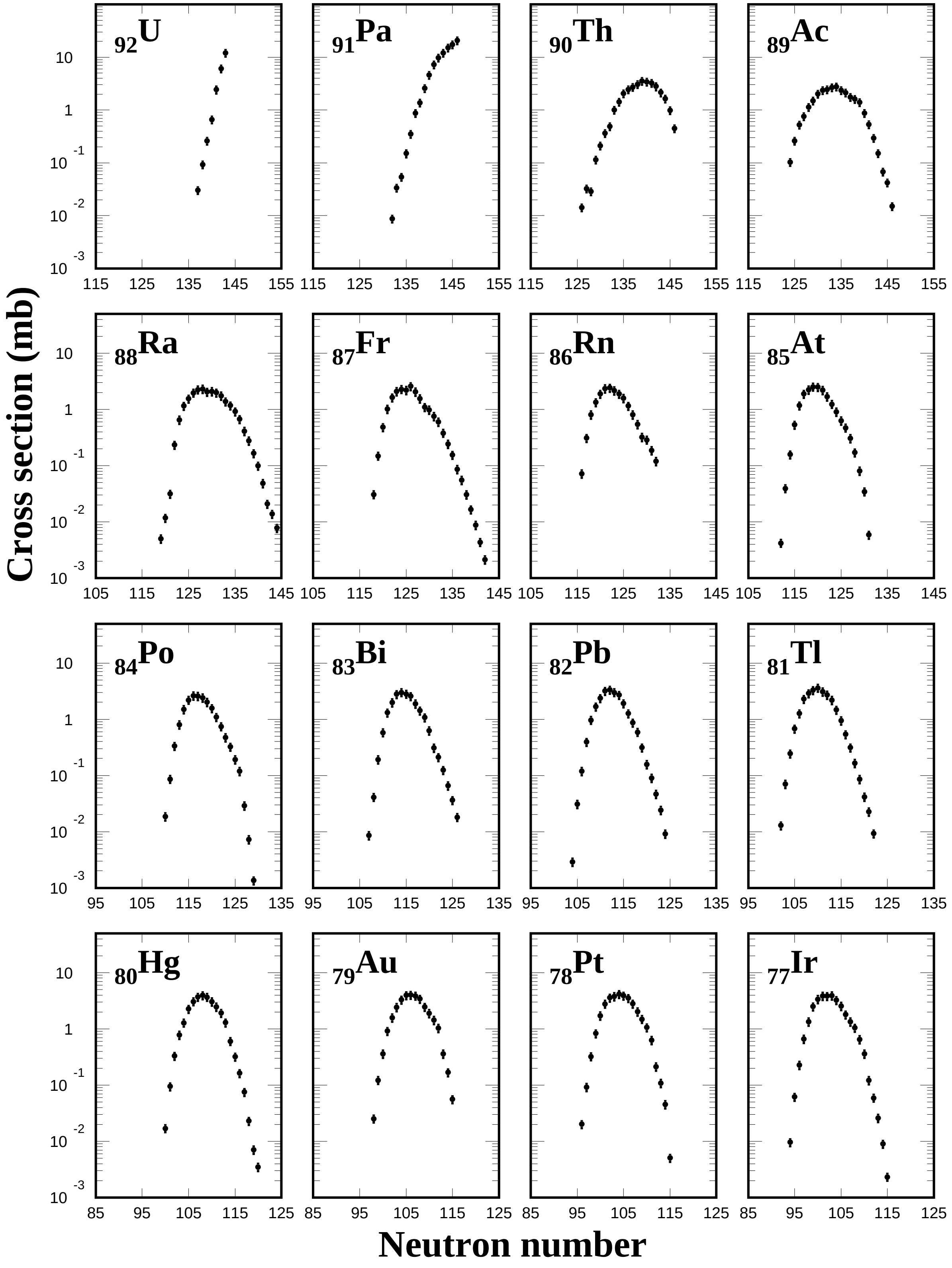

Figure 3.15: Total isotopic production cross sections measured for elements Z=65-76. Total uncertainty shown if larger than the symbol.

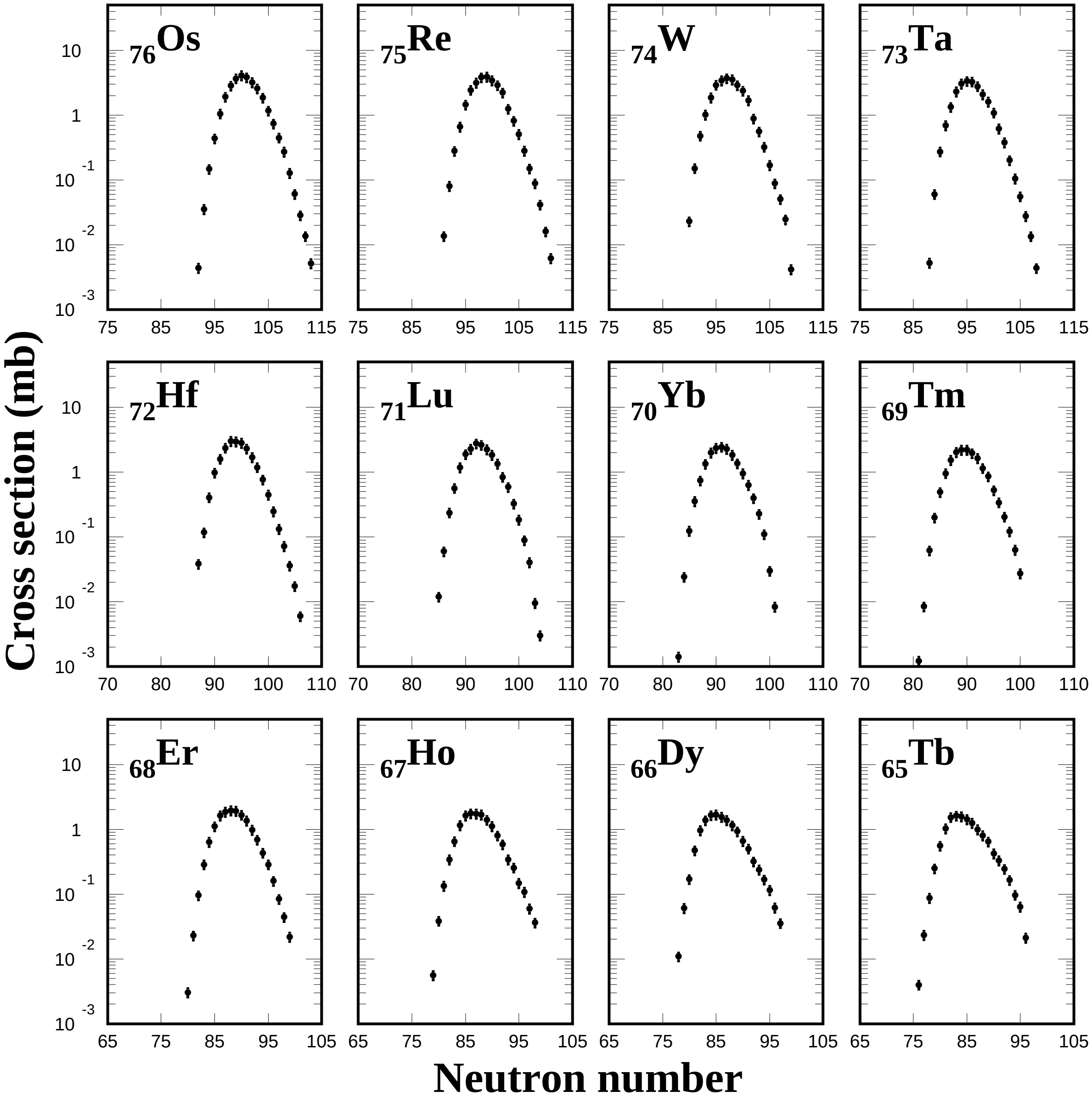

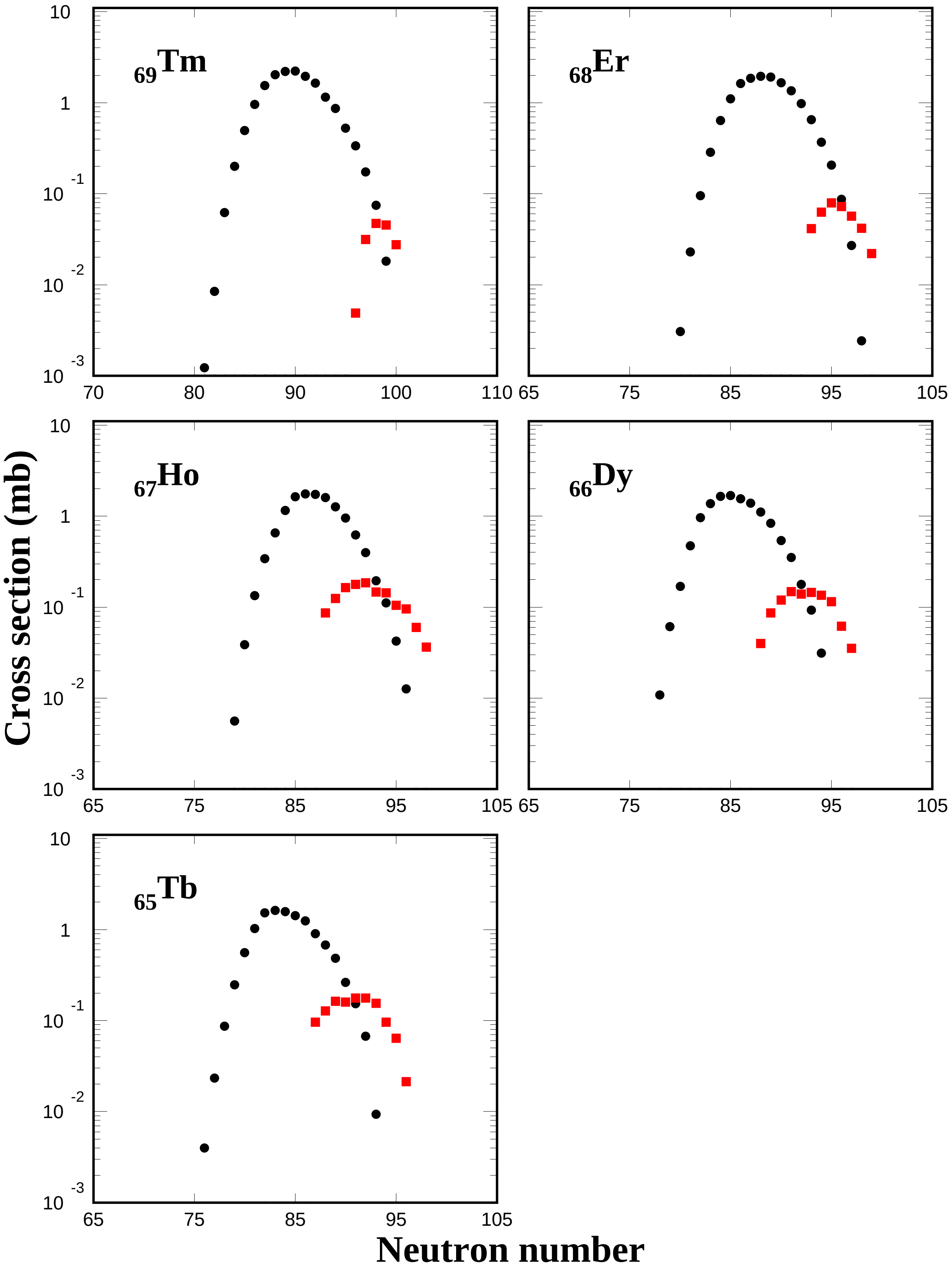

Figure 3.16: Isotopic distributions of production cross-sections measured for the reaction ^{238}U with deuteron at 1 $A{\cdot}GeV$, for elements where the fission (squares) and fragmentation (circles) contributions have been disentangled. The statistical uncertainties are shown if larger than the symbol.

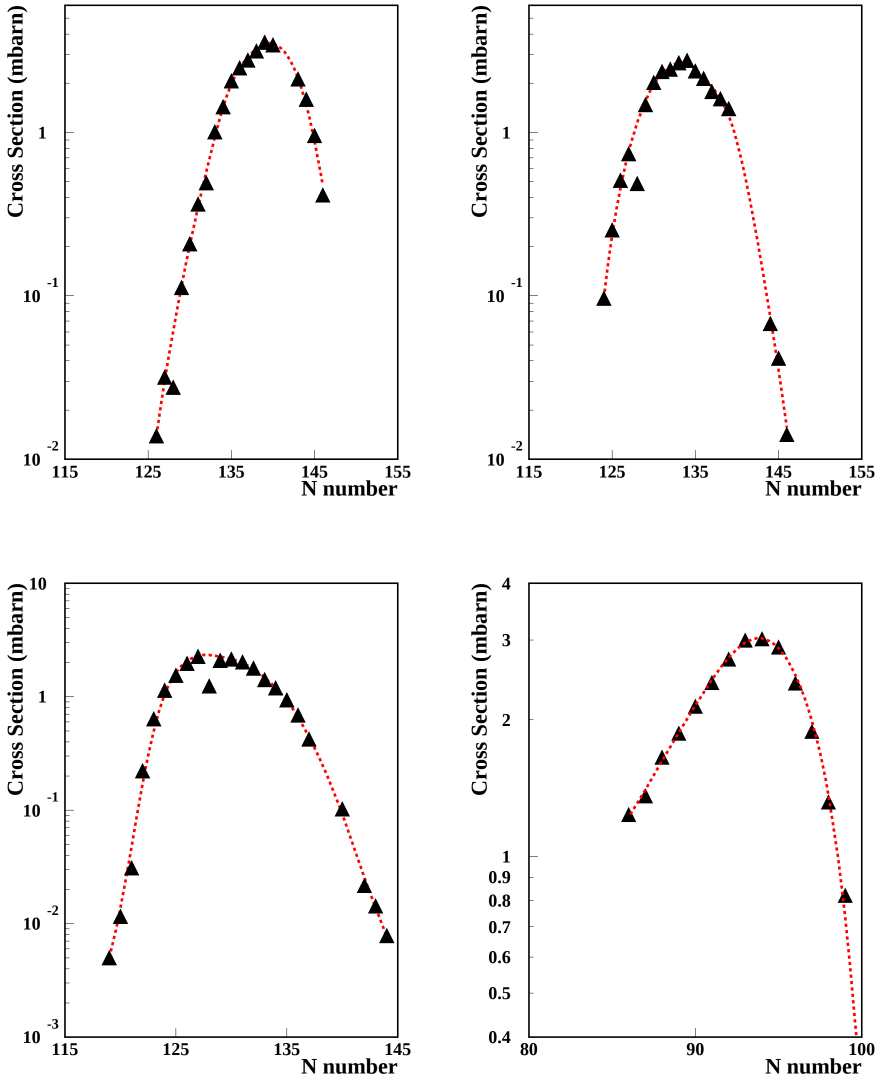

Figure 3.17: Cross sections distribution as function of the neutron number corresponding to elements ${}_{90}Th$, ${}_{89}Ac$, ${}_{88}Ra$, and for the nuclides following the relation N-Z=21, respectively. The smooth trends fitted appear as dotted lines. The missing isotopes are those which have rigidities close to the beam rigidity.

		uncertainty (%)
target thickness	T_{tar}	3
beam intensity	N_{beam}	~ 10
acquisition dead time	f_{dead}	~ 1
ionic charge-states	f^Q_{MUSIC}	~ 5
	f^Q_{FRS}	~ 5
secondary reactions	f_S	~ 10
transmission	f_{trans}	~ 1
detector efficiency	f_{eff}	< 1
dummy contribution	N_{dummy}	~ 50
fragmentation-fission separation	Γ	~ 40

Table 3.4: Contributions to the systematic error of the measured cross sections, as relative values. The uncertainty related to the fragmentation contribution Γ_{frag} does not affect to the total production cross section measured, only to the fragmentation-fission separated contributions.

production does not suffer from the uncertainty related to the separation method we applied to disentangle the two fission and fragmentation contributions. We have estimated that uncertainty to be $\sim 40\%$, resulting the values compatible with the systematics found.

The resulting quadratic addition gives a systematic uncertainty well below 20%. For the values of separated fission and fragmentation contributions, the uncertainty amounts less than 45%. The whole description of the cross section uncertainty is given below, for the sake of completness.

In the simplest approximation, see Apendix B, we obtain the cross sections as $\sigma = \frac{N}{T \cdot F_t}$ where T refers to the number of dispersion cneters in the target, per unit area, and F_1 to the beam and fragment attenuation within the target. $N = \Gamma \cdot N_{tot} = \Gamma \cdot (\frac{N_{raw}}{N_{beam}} \cdot F - N_{dumm})$ is the number of observed events N_{raw}, corrected for the losses F in the setup and analysis, normalized to the beam intensity N_{beam}, and separated the fission-fragmentation contribution by the factor Γ. The additional contributions to the deuterium in the target, are accounted by N_{dumm}. Following the previous description we obtain the relative uncertainty ϵ of the cross sections as a quadratic summ of the relative uncertainties of the different components as follows:

$$\epsilon^2(\sigma) = \epsilon^2(T) + \epsilon^2(F_t) + \epsilon^2(\Gamma) + \left(\frac{N_{tot}+N_{dumm}}{N_{tot}}\right)^2 \cdot [\epsilon^2(N_{raw}) + \epsilon^2(N_{beam}) + \epsilon^2(F)] + \left(\frac{N_{dumm}}{N_{tot}}\right)^2 \cdot \epsilon^2(N_{dumm})$$

The evaluation of $\epsilon(\sigma)$ includes already the statistical uncertainty in the term N_{raw}. All of the partial uncertainties have been described in the text and resummed in table 3.4.

3.8.3 Total uncertainty

The discussed contributions to the uncertainty of the measured data, result in a final evaluation as shown previously. The tables in Apendix A list the data together with the total uncertainty given in % of the production value. We can observe that the systematic component dominates, producing a constant uncertainty of $\sim 19\%$.

The productions for nuclei affected by fast radioactive decay and those residues lost in the setup, have been evaluated according to the measured data by comparing with the systematics of the neighbouring nuclides, as we saw in the former discussion about statistical error. We have decided to give the evaluated value, and an uncertainty similar to the neigbouring prodcution values. Nevertheless those cases have to be taken as *evaluated* and not as measured data.

Chapter 4

Discussion of the results

In this work we have measured the production cross sections and the longitudinal momentum distributions for almost all of the fragmentation residues produced in the reaction $^{238}U(1\ A \cdot GeV) + d$ above 0.01 mb. The measurement of these two magnitudes for more than 500 isotopes allows to discuss the most salient features of this reaction. In the previous chapter the measured cross sections were presented, as well as the procedure followed to define the momentum distributions. In this chapter the results are discussed. Similar results of other high-energy heavy-ion reactions have become available recently using the same experimental technique: $^{208}Pb + p$ [15], $^{208}Pb + d$ [16], and $^{238}U + p$ [37] all at $1\ A \cdot GeV$. The large amount of data we have now, helps to discuss in detail some effects and characteristics of the $^{238}U + d$ system. The comparison of the deuteron and proton systems allows to study the influence of the energy deposited in the system. The comparison with ^{208}Pb shows the influence of the fission channel in ^{238}U.

The measured and calculated total reaction cross sections available for the previous reactions are revisited. The experimental procedure described in this work allows to measure that quantity, usually separated in fission and fragmentation contributions. The fragmentation part of the reaction $^{238}U + d$ is presented in this work. When the fission contribution be analysed, the total reaction cross section value will be available. The measured value will allow to compare the existing theoretical evaluations of this magnitude. The result is also important when calculating the residue productions with simulation codes, since the values are normalized according to the total reaction cross section.

Another important feature observed in the measured isotopic distributions is the influence of fast radioactive decays of a few measured values of the residual production do not correspond to the primary production. This effect is reflected in the data in a very specific range of isotones and it affects a few nuclei. Nevertheless the radioactive decay influence is reviewed and an estimation of the real production is given. Also a few nuclei with magnetic rigidities close to high-intensity production channels were lost in the setup, due to the use of collimators to stop the hazardous intensities. Their production values are estimated from the smooth behavior of the isotopic cross sections measured.

An important topic that can be addressed with our data is the importance of the energy deposited in the first step of the reaction, outlined when comparing the ^{238}U reaction with proton and deuteron. The interaction of the latter happens at double energy. The more excited the pre-fragment the longer will be the evaporation chain, leading to lighter residues.

One of the most outstanding characteristics of the investigated system is the fission process. The influence of fission becomes clear when comparing the present data with those obtained for other heavy systems with lower fissilities. The comparison of ^{238}U and ^{208}Pb systems will show the strength of that channel in our system. Additionally, the presence of heavy fission residues, up to $Z \sim 70$, found in our data, evidences very asymmetric channels. Additionally we have measured the production of the new isotope ^{235}Ac which was also observed in the reaction $^{238}U + p(1\ A \cdot GeV)$ [37], reported first there.

On the other hand, the large spatial distribution of the deuteron, leads to similar productions when compared to proton, for a wide range of nuclides. That is an expected behaviour, since the most peripheral reactions will induce a single nucleon impact. Both, proton and deuteron projectiles behave similarly within a certain range of impact parameters, defined by the deuteron matter distribution. The result of that effect will also be discussed in the next chapter, where simulation codes are used to describe the reaction process.

Additionally the study of the fragmentation residues produced in the reaction $^{238}U(1\ A \cdot GeV) + d$ allows to discuss some topics related to the production of exotic heavy-ions. The fragmentation mechanism allows to obtain both, neutron-deficient and neutron-rich isotopes. The possibilities to produce possible *proton emitters* by using this reaction, as well as the population of the *proton-removal* channels, leading to the production of neutron-rich nuclei, are discussed using the new data. Related to the topic of production of heavy-ions, is that of the presence of ionic charge-states. The contamination can be a drawback when producing exotic neutron-rich nuclides. Here we show some example. A few data corresponding to charge pick-up was also measured. These results are compared with the existing information. The results are important also to evaluate the response of the theoretical codes.

The (longitudinal-)momentum distributions measured are presented and compared with the data available for reactions of other heavy-ions. The differences and the behaviour are discussed within some systematics and models.

4.1 Total interaction cross-section

One of the interesting results from the experimental technique we have presented, is the possibility to determine the total interaction cross-section of the reaction[1]. The reaction cross section values allow to test the theoretical models that describe the process. Additionally it helps to compare different reactions and extract estimates of each reaction mechanism contribution to the reaction, when there are only partial data available.

---

[1] When referring to *nuclear reaction* cross section, one has to consider that it includes processes with and without changes in nucleon number and/or type. Sometimes to refer to the latter processes, the term *interaction* cross-section is used. The residues we have measured do not include the projectile itself. We assume that most of the excited states the projectile reaches, lead to de-excitation by emission of nucleons. See Appendix B, and the last chapter for the discussion on de-excitation.

The main mechanisms involved in the production of residues in the reaction $^{238}U(1\ A\cdot GeV)+d$ are fission and fragmentation; other channels, as multi-fragmentation, are disregarded in a first approach. This work presents the fragmentation contribution to the residue production. The fission contribution is still under analysis [88]. Some other relativistic heavy-ion systems have been measured and reported recently: $^{238}U(1\ A\cdot GeV)+p$ [37], $^{208}Pb(1\ A\cdot GeV)+p$ [15] and $^{208}Pb(1\ A\cdot GeV)+d$ [16]. In fact, data with deuterium are very scarce. The comparison with proton becomes mandatory to understand the simplest extension from the reaction with nucleons. Also, in order to compare the expectations of the fragmentation and fission components, the comparison with the results measured for proton and deuteron reactions induced on ^{208}Pb are very useful.

In table 4.1 we show some total cross section values of measured data obtained for the reactions $^{208}Pb+p,d$ and $^{238}U+p,d$ at $1A\cdot GeV$, for both fission σ^{fiss} and fragmentation σ^{frag}. The total reaction cross section in these systems is mostly due to nuclear interaction Σ^{nuc}, being the electromagnetic dissociation (EMD) contribution Σ^{EMD} negligible, see Appendix B. We count on the results of some macroscopic and microscopic models dedicated to the evaluation of the total nuclear reaction cross sections. The formulation we have used for this study to evaluate the nuclear reaction cross section Σ^{nuc}, is the one proposed by Karol [89] and modified by Brohm [90], see Appendix B. This microscopic result is compared also in the Appendix B with some macroscopic result. The Glauber-like microscopic models are based on the nuclear-density distribution and the nucleon-nucleon interaction cross sections. A realistic deuteron description was additionally implemented in the former work to account for the deuterium. The results calculated for the EMD processes Σ^{EMD} are given also for comparison. Some systematic parameterisation for total fission cross section induced by protons (p,f), have been developed [91] over different data bases [92]. We use these results to estimate the proton induced fission component $\Sigma^{(p,f)}$.

The values presented in the table 4.1 show that the different measured total fission cross section in proton reactions with both ^{208}Pb and ^{238}U agree within their uncertainties. Using the (averaged) values of fission and fragmentation for $^{208}Pb(1\ A\cdot GeV)+p$ we obtain the total reaction cross section $\sim 1680+144=1824(223)$ mb, to be compared with the calculated value of 1800 mb (1.3% underestimation). For $^{208}Pb+d$ the only available data give $\sim 1980+175=2155(166)$ mb to be compared with the calculated value of 2321 mb (7.7% overestimation). In the case of $^{238}U(1\ AGeV)+p$ we have the measured values $\sim 398+1305=1703(175)$ mb, to be compared with the calculated value of 1964 mb. We can evaluate alternatively the cross section for $^{238}U(1\ A\cdot GeV)+p$ using the measurement of the the charge-changing processes of that reaction at $900A\cdot MeV$ [93]. The result can be completed with the U-isotopes measured for fragmentation in ref. [37] (being ~ 108 mb). The result is $\sim 1720+108=1828(181)$ mb. Both evaluations for $^{238}U(1\ A\cdot GeV)+p$ are compatible, but the result given in ref. [37] could be slightly underestimated since the fragmentation analysis was limited to elements above $_{74}W$. Considering the latter value, the calculation overestimates in 7.4% the measured cross section.

The estimations provided by the systematics presented in ref. [91] for total fission cross section in (p,f) reactions, $\Sigma^{(p,f)}$are 132 and 1281 mb for Pb and U respectively. They agree with the (averaged-)measured data, 144(36) and 1305(164) for Pb and U

	Σ^{nuc} (mb)	Σ^{EMD} (mb)	$\Sigma^{(p,f)}$ (mb)	σ^{Z} (mb)	σ^{frag} (mb)	σ^{fiss} (mb)
U+d	2514	$\leq$2			705(134) [a]	
U+p	1964	$\leq$2	1281	1720(180) [f]	398(60) [b]	1400(100) [e] 1210(130) [f]
Pb+d	2321	$\leq$1			1980(165) [c]	175(15) [c]
Pb+p	1800	$\leq$1	132		1680(220) [d]	157(31) [d] 132(13) [g] 142(14) [g]

Table 4.1: Total reaction cross sections calculated Σ and measured σ for reactions induced by protons and deuteron in ^{238}U and ^{208}Pb, with energy $\sim 1\ A \cdot GeV$. The three first columns refer to total reaction cross sections calculated by different models for total nuclear reactions Σ^{nuc}, EMD-processes Σ^{EMD},and (p,f) reactions $\Sigma^{(p,f)}$; see the text for details. The last three columns refer to measured data: total charge-changing cross section σ^{Z}, total fragmentation σ^{frag} and total fission σ^{fiss} cross sections. All values are in mb and the uncertainty is given within parentheses. The references for the measured data are: a (this work), b [37], c [16], d [15], e [94], f [93], g [95].

respectively, from refs. [15, 93, 94, 95]. Unfortunately the data cannot be extended to deuteron induced reactions. The only estimation could be done by using the systematics for protons with double energy, resulting in $\Sigma^{(p,f)}=$ 1146 and 130 mb for U and Pb for $2A \cdot GeV$ protons respectively[2]. The measured data for $^{208}Pb(1\ A \cdot GeV) + d$ show a fission component $\sigma^{fiss} = 175(15)$ mb, increasing the value relative to $^{208}Pb(1\ A \cdot GeV) + p$ about 10%. The result contradicts the estimation done by the systematics for proton at double energy, which predicts a decrease. We conclude that the parameterisation for total fission cross section does not help at all to estimate the cross sections for deuteron induced readtions.

All those comparisons allow to conclude that the evaluated Σ^{nuc} is a rather good estimation, within 10%, of the measured value. For $^{238}U(1\ A \cdot GeV) + d$ no additional data are available, neither for fission or fragmentation, to compare with our result, and the systematics used for proton systems cannot be used. The fragmentation cross section measured $\sigma^{frag} = 705(134)$ mb, and the calculated value for the total cross section $\Sigma^{nuc} \sim$ 2514 mb, allow to estimate the value for $\sigma^{fiss} = 1809$ mb with an uncertainty $\sim$ 21%. The adequacy of the estimation will be discussed when the data on the fission residue production in the reaction become available. It has been shown, see Appendix B, that simple model calculations based on the Glauber approximation, allow to obtain the total reaction cross section. Since we have no other source of information, we settle on the calculated value for $^{238}U + d$. The agreement in the case of $^{208}Pb + d$ provides confidence on the deuterium description used in the model, which otherwise would not be able to

---

[2] In that range of energy 1-3 GeV the total reaction cross section changes slightly. The fission channel is reduced at higher energies, due to dissipation effects on the fission process. While the fragmentation is enhanced, with new channels opened at higher energy, as light nuclei emission.

define an accurate value of the cross section.

4.2 Isotopic production cross sections

In figure 3.15 we can see the isotopic distributions of the measured isotopic production cross sections in the collision of ^{238}U with deuterons at 1 $A \cdot GeV$. The data are tabulated in Appendix A. The residue production below Z=65 is increasingly due to fission or double reactions within the target. In this work we have measured the fragmentation-production cross sections of more than 530 nuclides, with an average statistical uncertainty below 10%. The average systematic uncertainty is estimated to be ∼20%. One of the characteristics of the data obtained during the program developed at GSI, is the smooth evolution that the isotopic distributions show, see figure 3.15. That is the result of the success of the experimental method, which allows to unambiguously identify the residue production, and to fully reconstruct the momentum distribution, as well as the careful description of the included corrections (e.g comparing the data obtained with and without degrader).

Another well known characteristic of the data obtained in this experimental program, is the deep we observe in the measured isotopic distributions, around N=126, for elements above Z=84. This effect is not a feature of the primary production, but the result of the fast $\alpha-$decay that some isotopes close to the neutron shell N=126 undergo. Note also that some data are missing in the isotopic distributions of elements close to the projectile: the neutron-rich side of $_{89}Ac$, $_{88}Ra$ and $_{87}Fr$ mainly. Those holes correspond to nuclei with a magnetic rigidity value near to the one of the projectile, or some of its ionic charge states, or neutron-removal channels. The high intensity of those channels obliges to cut their transmission through the FRS. The cut produces also some visible effect in the isobaric distributions, see below. In order to give complete data for the measured range, the missing cross sections were evaluated. The method followed was that of the smoothing of trends, as discussed in section 3.8.

Another interesting effect observed in figure 3.15, is the different slope we notice in the neutron-deficient and the neutron-rich sides of the isotopic distributions: the neutron-deficient production is much steeper. We may understand the effect as caused by fission: the fission barriers are lower in the neutron-deficient side, and the fission channel is then enhanced, depopulating that region.

In figure 4.1 the isotopic distributions of the measured production in reactions induced by proton (squares) [37] and deuteron (dots) in ^{238}U at $1A \cdot GeV$ are shown. The same features discussed for the isotopic distributions of deuteron appear in the proton data. We notice that both distributions produce about the same result for the higher masses. The similar production cross sections can be explained as a geometrical effect: the impact of a single nucleon of the deuteron in the more peripheral collisions. This topic will be discussed in the next chapter in relation with the results obtained with simulation codes describing the reaction.

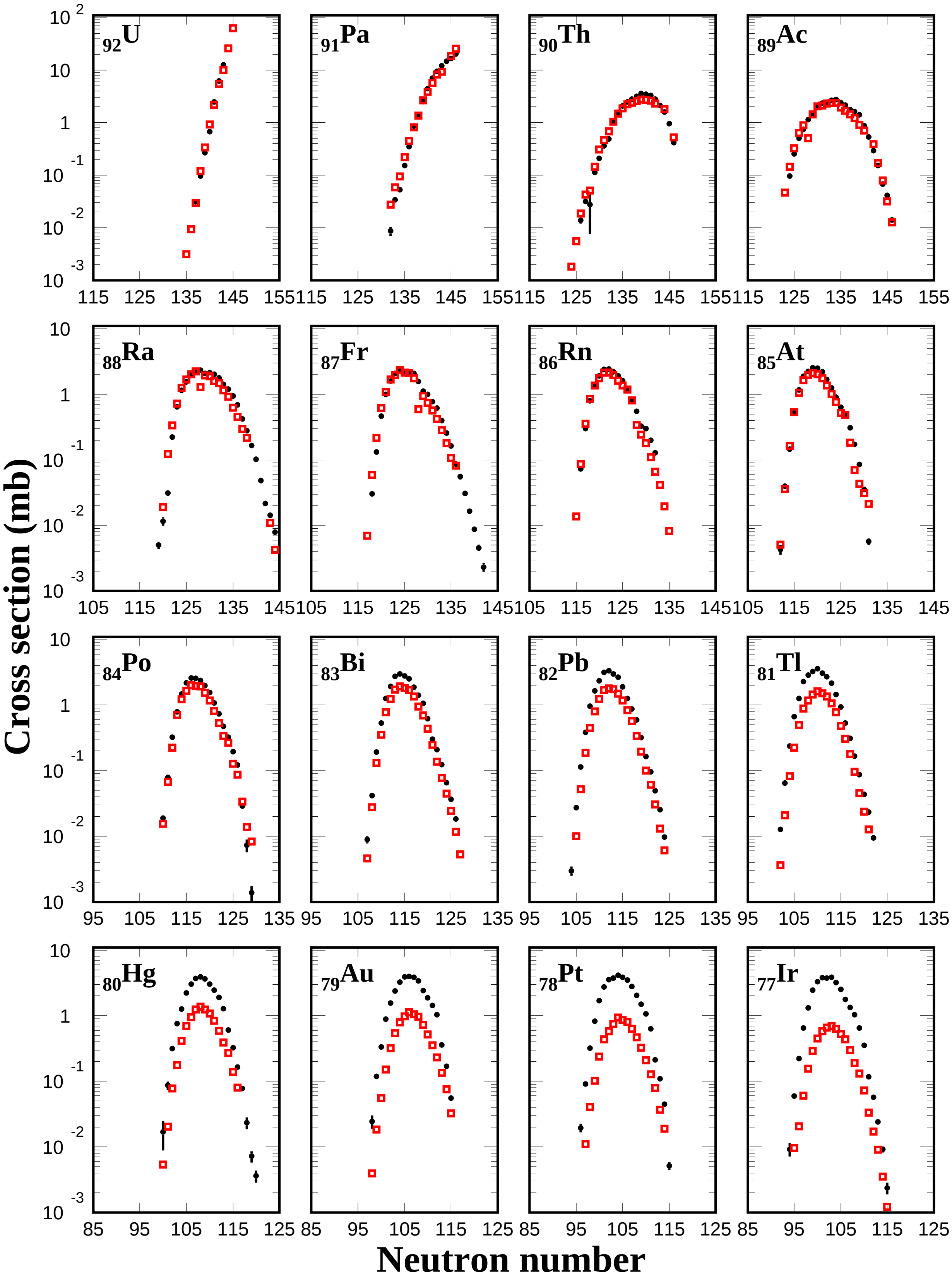

Figure 4.1: Isotopic distributions of production cross-sections measured for proton (open squares) [37] and deuteron (dots, this work) induced reactions in ^{238}U at 1 $A \cdot GeV$. The statistical errors are shown if they are bigger than the symbol.

4.2.1 The influence of fast radioactive decays

The isotopic distributions of elements with atomic numbers $Z \geq 84$, show that around the neutron number N=126 the smooth shape is disturbed, see figure 3.15. This effect is a systematic error in the measurement of the yields, that appears as a consequence of the interplay between the $\alpha-$decay and detection times involved in the identification of a certain nucleus. The time-of-flight through the FRS length (~300 ns) is the threshold we are sensible to. If a nucleus decays with a half-life of the same order of its time-of-fight, its measured yield will suffer the losses due to radioactive decay. The process will over-populate some other daughter nuclei. The measured result will reflect the radioactive decay structure and will not correspond to the fragmentation production. The nuclei in the region of $N \sim 126$ for $Z \geq 84$ decay mostly by α-emission (only ^{211}At decays $\sim 50\%$ by electron capture). In the following discussion we refer only to nuclides in the range of $Z \geq 84$.

The situation would become critical in the case of a parent nucleus highly produced and a daughter nucleus weakly produced. In that situation the decay component could be an important part of the measured yield of the daughter nucleus.

Radioactive losses within the FRS

To evaluate the effect of the radioactive decay we consider two situations. The events corresponding to a radioactive decay within the second part of the FRS will be rejected in the analysis. Since we are using the degrader for high Z elements, any change in charge within the flight-path will be discarded in the analysis, as explained previously in section 2.7. If the decay happens within the first part of the FRS, the situation is not so obvious. On the one hand, the identification will correspond to the daughter nuclei, since it depends mostly on the parameters of the second part, see section 2.2. On the other hand, with the value of the energy-loss in the degrader we define the atomic charge within the FRS; it depends on the position at the FRS central focal plane and on the A/Q value in the second FRS stage, see section 2.7. One can calculate that if the decay happens in the first FRS section the energy losses in the degrader would not be disentangled from that of the daughter nucleus. This result means that the nucleus will be identified as the daughter nuclei, not being rejected by any criteria. Of course if the decay happens before the FRS entrance, the residue will be assigned to the daughter nucleus, as if it was a primary reaction product. From this analysis we conclude that we have both, de-population (the rejected events) and over-population (the accepted, and wrongly assigned, decay events) effects, depending on the time range where the decay happens, relative to the identification time involved.

Radioactive contamination

The half-life values of isotopes with neutron number N=130-132 are of the order of ~ms [96]; that means that the isotones N=130-132 should not be influenced by de-population due to $\alpha-$decay. The half-life values of N=126-127 are higher than $120\mu s$, and then the isotones N=124-125 should not be influenced by extra-population due to $\alpha-$decay from

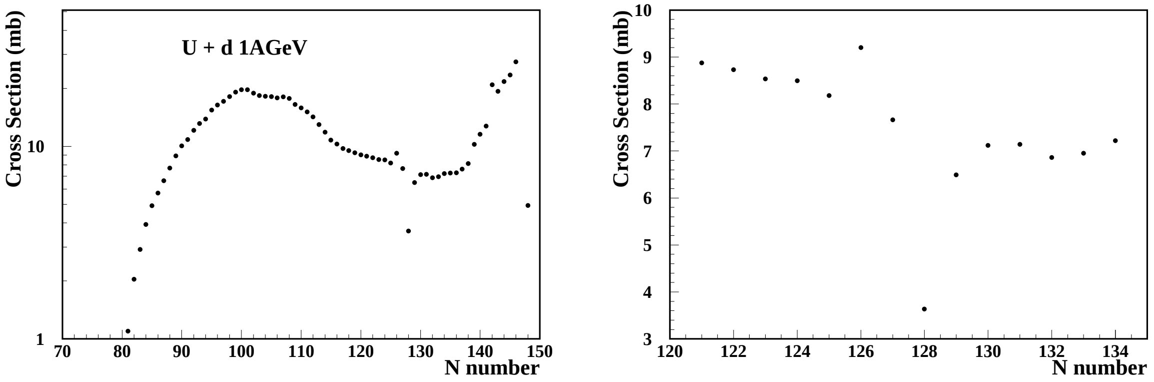

Figure 4.2: Isotonic distribution of measured production cross-sections of U+d at 1 $A \cdot GeV$. The right panel is a zoomed range of the distribution in linear scale. The statistical errors are included, and not visible as they are amaller than the symbol.

N=126-127. The group of N=126-129 is the one that one expects to be disturbed: that can be seen in the isotonic distribution of the measured cross sections shown in figure 4.2. In the table 4.2, the isotonic cross sections that are affected, N=126-129, are shown and the result of this discussion is reviewed in the last column.

We could evaluate correctly the radioactive losses of a given isotope. The value of the radioactive losses would be split additionally into the part which goes to the daughter and the part which is rejected in the analysis, as we have discussed above. Of course, the values to be added to the parent, and subtracted from the daughter, must be consistent with each other, and with the measured values of the neighbours. The whole calculation would only be possible if accurate values of half-life were available. But additionally those nuclei present isomeric states in a not well-defined proportion, which decay either by α-emission or to the ground state. The decay should also be integrated over the whole detection flight-path. All those factors make the correction quite difficult, and not worth to be done since the resulting uncertainty would be large. The cross sections affected by this fast-decay were evaluated as described in section 3.8, and they have a higher uncertainties than the neighbouring nuclides.

In table 4.2 we report the measured isotonic values σ_N, as well as the values estimated directly by the trend observed in the figure 4.2, which appear in columns two and three. We see that we can understand the observed pattern of the measured values according to the expected relationship parent-daughter and the involved times.

N	$\sigma_N^{measured}$ (mb)	$\sigma_N^{evaluated}$ (mb)	correction-expected
126	7.32	∼6.34	overpopulated by N=128
127	6.12	∼6.18	overpopulated by N=129
128	2.90	∼6.03	underpopulated towards N=126
129	5.21	∼5.87	underpopulated towards N=127

Table 4.2: Evaluated and measured cross section for different isotonic groups. The evaluated-data column shows values estimated (interplated) from the isotonic curve, as seen in figure 4.2. The correction-expected column follows directly the discussion in the text.

4.3 Energy deposition: the role of deuterons

4.3.1 The fragmentation corridor

In figure 4.3 we present the measured fragmentation cross-sections of ^{238}U with protons and deuterons at 1 $A \cdot GeV$, plotted on top of a chart of nuclides. The $^{238}U(1AGeV) + p$ data are from [37]. In both figures we observe that starting from the projectile, the reaction first populates the neutron-deficient isotopes. At higher excitation energies the excitation chains reach the so called *fragmentation corridor*. The average position of this corridor is defined by the neutron-proton emission competition. The Coulomb potentials hinders proton emission, favouring neutron emission which leads to the production of neutron-deficient isotopes. The effect is counteracted by the change in binding-energies, when the excited residue looses more and more neutrons. The result is the equilibrium at some place (that can be calulated) at the proton-rich side of the stability line, as we can see in the plot.

In figure 4.3 we observe clearly the influence of the different energy deposition induced by 1 GeV protons and by 2 GeV deuterons. The total available energy in the reaction, defines the limit for the excitation energy of the pre-fragment, and so the available energy for the evaporation-fission process. The more elongated deuteron production corridor reflects the higher energy available in that reaction, allowing the pre-fragments to de-excite by longer evaporation chains, which populate lighter nuclei.

The residue production in spallation reactions as $^{208}Pb + p, d$ decreases continuously with mass, see figure 4.5. In the reaction of ^{238}U with deuterons, we observe a merging bump in the middle of the corridor, below element 82 which is missing in the proton case. That bump is clearer in the isobaric distribution, see figure 4.4. The fission channel depopulates very fast the upper part of the production corridor, because of the higher fissility of the nuclei in that region. At higher energies the de-excitation process reaches nuclei with higher barriers, the particle evaporation competes again favorably with fission and other channels like multifragmentation. We see that competition for deuterons, resulting in the bump we observe at lower masses. In the case of proton-induced reactions, the excitation energy range covered in not sufficient to reach the region of increasing fission barriers, and favoured evaporation. The production never increases again and the bump is missing. The position of the maximum isotopic production of the fragmentation corridor is defined by the proton-neutron emission equilibrium. Nevertheless the strength of the fission channel is so important in the high mass region, that it determines the slope of the production corridor above $Z \sim 84$, as we see in figure 4.3, where the corridor follows a line of constant fissility. The different energy deposition in both ^{238}U systems will be a valuable input for the benchmarking of the simulation codes related to this topic. That will be discussed in the next chapter.

4.3.2 Isobaric distributions

In figure 4.4 we present the isobaric distribution of the measured fragmentation residues in collisions of ^{238}U with protons [37] and deuterons at $1A \cdot GeV$. The discontinuities in the initial tail are solely due to the missing cross sections close to the projectile, as commented above. The dip at about $\Delta A = 24$ is caused by fast α-decay. We observe also at the end of the $^{238}U + d$ distribution that the tail suffers a drastic change of slope around $\Delta A \sim 90$. That change is due to the contribution of lower mass residues not-included in this work [3]. The characteristics commented above, about the increase of the production observed in the deuteron but not in the proton reaction, appear from a different perspective.

The isobaric distributions obtained in ^{238}U reactions with proton and deuteron, are very similar for $\Delta A < 30$. This agreement is a signature of the impact of a single nucleon. Since the deuteron has a large spatial distribution, the probability of a single nucleon impact in peripheral reactions is quite high. We have calculated that up to 30% of the impacts correspond to one nucleon, see section 5.4.5. Despite the effects of isospin, the single impact results in a range of residual nuclei which are produced equally by deuteron and proton impacts.

The energy deposition in the fast initial stage of the reaction, i.e. the excitation energy E^* of the pre-fragment, is very different in the reactions induced by protons and deuterons. The excitation energy E^* is dissipated during the evaporation-fission step. Actually, the isobaric distribution of the residues reflects the distribution of E^* . Small excitation energies of the pre-fragments lead to the production of residues close to the projectile, while at higher excitation energies the pre-fragment evaporate more nucleons and reach lighter residues.

The kinetic energy of the projectile is twice as large for deuterons than for protons in the investigated reactions. The deuteron induced reaction populates masses till $\Delta A \sim 120$ [4] while the proton induced reaction reaches values $\Delta A \sim 65$. The proton and deuteron induced reactions with ^{208}Pb [15, 16] show a similar behavior when compared with each other, see figure 4.5. To compare the effect of higher excitation energies in figure 4.5 we show also the measured isobaric distribution of the reaction $^{238}U(950AMeV) + Cu$

---

[3] By comparing the results from deuteron and proton induced reactions in both Pb and U at 1 $A{\cdot}GeV$, see figures in this chapter, we can estimate that the fragmentation tail would arrive to $\Delta A \sim 120$ for 1 mb production. That missing production would amount for ~12% of the total fragmentation cross section, correcting the observed value ($\sim$ 693 mb) in about 100 mb.

[4] We have presented in this work the data for ΔA below 100. See previous note.

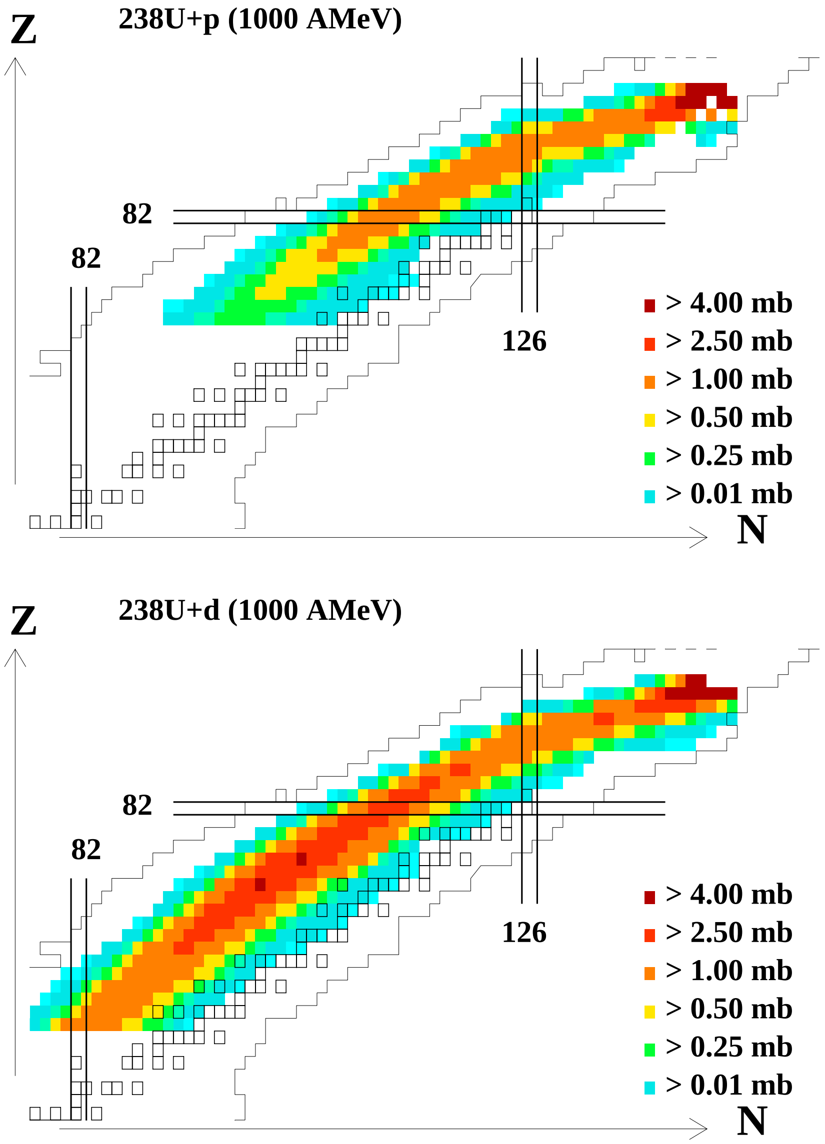

Figure 4.3: Partial view of the chart of the nuclides showing, as a two-dimensional plot, the measured production cross sections in the fragmentation reaction of ^{238}U with protons [37] (upper panel), and with deuterons (this work, lower panel), both at 1 $A \cdot GeV$. The limits of known nuclei, the stable isotopes and the N and Z shells are indicated. The colour scale, related to the production cross sections measured, is a log-scale with a fator about 2 between two adjacent colours.

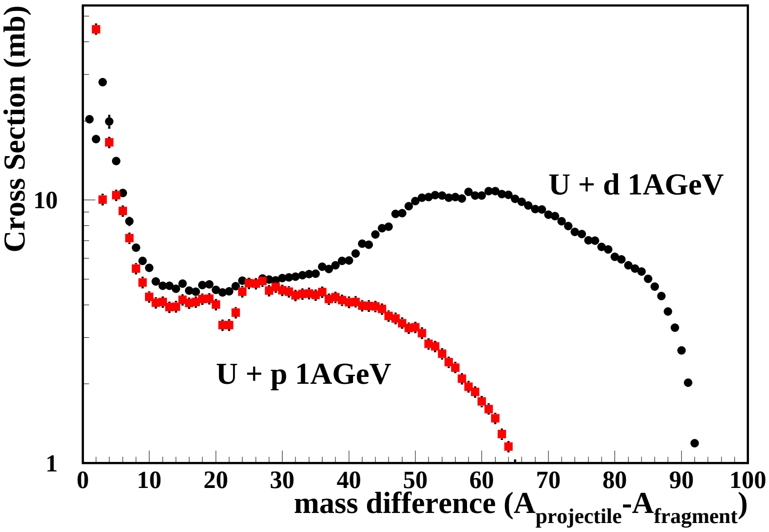

Figure 4.4: Isobaric distribution of fragmentation residues measured in collisions of ^{238}U with deuterons (this work, circles) and protons [37] (squares) at 1 $A{\cdot}GeV$. The statistical errors appear if larger than the symbol size.

from ref. [80]. The result plotted as a full line is the isobaric distribution obtained from evaluated data, since the measured isotopic distributions in ref. [80] were not complete. A smooth fit of the measured data was used to reconstruct the missing parts, and to extend slightly the range of measured elements. We can see for $^{238}U + Cu$ the high cross section values in a wide mass range, as a consequence of the higher available energy.

In proton and deuteron induced reactions in ^{238}U we also note the plateau about 4 mb for $\Delta A \sim 10 - 35$, and then the different behaviour of deuteron (increasing) and proton (decreasing) distributions. The difference is the result of the interplay between the fission strength and the fragmentation production decay with ΔA, as discussed above. In the case of ^{208}Pb reactions, the decrease is smooth and continuous with ΔA, being similar for both proton and deuteron. Of course, the reaction residues produced in deuteron induced collisions reach lower masses , and overtake the proton production.

4.4 The influence of fission

The ^{238}U and nearby nuclei are strongly fissioning systems. The fission barriers of nuclides with mass number above 200 are below 20 MeV, and decreasing very fast with atomic number. The barriers increase with the neutron number N for a given element[5]. If we

---

[5] The fission barriers, deformation, etc. can be easily connected within macroscopic models, to the *fissility* parameter $x \propto \frac{Z^2}{A}$. For $x > 0.7$, many useful expressions give an interesting approximation to different fission topics. See for instance [97].

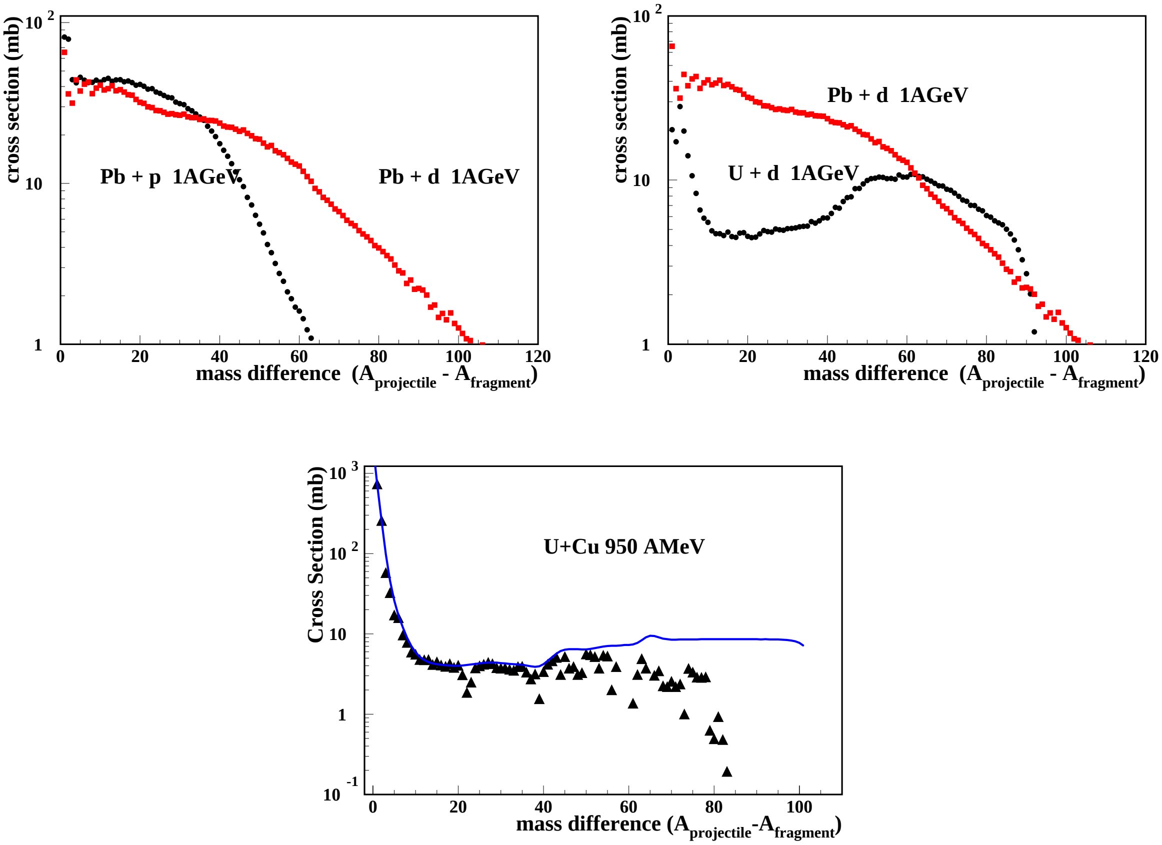

Figure 4.5: Isobaric distributions of fragmentation residues measured in collisions of $^{208}Pb(1\ A \cdot GeV)$ with deuterons and protons (upper left panel), for collisions of $^{208}Pb(1\ A \cdot GeV)$ and $^{238}U(1\ A \cdot GeV)$ with deuterons (upper right panel), and for collisions of $^{238}U + (950\ A \cdot MeV)$ with Cu (lower panel). The latter panel shows the data measured (triangles), and the evaluated fragmentation distribution (full line). See the text for details.

compare the isobaric distributions of residues from deuteron induced reactions in ^{208}Pb and ^{238}U, see figure 4.5, we notice the large difference in production for residues with a mass difference in respect to the projectile till $\Delta A \sim 65$. The same result appears in proton induced reactions, see figures 4.4-4.5. The calculated total reaction cross sections for $^{208}Pb(1\ A \cdot GeV) + d\ \ \sim 2300$ mb and $^{238}U(1\ A \cdot GeV) + d\ \ \sim 2500$ mb, differ less than 10%. We would not expect large differences for the two systems, as it is the case of $^{197}Au(0.8A \cdot GeV) + p$ and $^{208}Pb(1A \cdot GeV) + p$ [15], since these reactions are mostly characterized by the common *limiting fragmentation* regime (Appendix C), and their isotopic production only scales by a factor proportional to the total cross section. The large difference in the production of fragments between U and Pb demonstrates the influence of the strong fission channel.

At higher excitation energies of the pre-fragment, the fission process is hindered [98, 99, 100] and the nucleon emission previous to fission is then enhanced. Also the fission barriers increase for lower elements. Both effects combined make the evaporation of nucleons to compete favorably in the de-excitation process. We can see how the production from $^{238}U + d$ increases for $\Delta A > 30$, producing a bump and decreasing later when the energy is exhausted. The same fragmentation bump, but in a much smaller scale due to the reduced fission strength, is visible in the measured data of $^{208}Pb + d$ reaction. In this system the cross section shows a bump around $\Delta A = 50$. For proton reactions the behaviour is similar in ^{238}U and ^{208}Pb, but the bump is not present since the fragmentation production already for $\Delta A > 30$ starts to decrease.

Correlated with the behaviour of the isobaric distributions of the measured production cross sections, the isotopic distributions show three effects. First, the strong presence of fission produces a reduction of the isotopic cross section values in respect to similar heavy-ion systems where the particle-evaporation channels are dominant. In figure 4.7 we see the isotopic distribution of some elements measured in the reaction $^{208}Pb(1\ A \cdot GeV) + d$ compared with those from $^{238}U(1\ A \cdot GeV) + d$. The ^{238}U maximum production lies in general below that of ^{208}Pb.

Second, the neutron-deficient side of a certain isotopic distributions is more affected by fission, since the fission barriers increase with the neutron number. We observe in the figures 4.7 and 3.15, that the slope of each side of the isotopic distributions for ^{238}U are different for elements above $_{83}Bi$.

The third effect is related to the production cross sections decrease with atomic number Z. The production in the reaction $^{208}Pb(1\ A \cdot GeV) + p$ shows a continuous decrease with atomic number. The same effect appears in the production of the reaction $^{208}Pb(1\ A \cdot GeV) + d$, with a small bump as commented before. In the case of ^{238}U, fig. 4.1, the production of elements $_{84}Po - _{89}Ac$ have a common maximum about 2 mb, for both proton and deuteron induced reactions. For elements with Z number below 84, the production with proton falls , while that for deuteron raises, see figure 4.1 . In systems with reduced fission strength one expects a continuous decrease of the production with Z, cf. with the ^{208}Pb results. In the ^{238}U reactions, the production shows a quasi-constant maximum value in a wide element range. This behaviour is the result of the combined effect of fission and evaporation: while higher elements would have higher production, the fission is also enhanced, and the result is the observed quasi-constant value. Similar conclusions

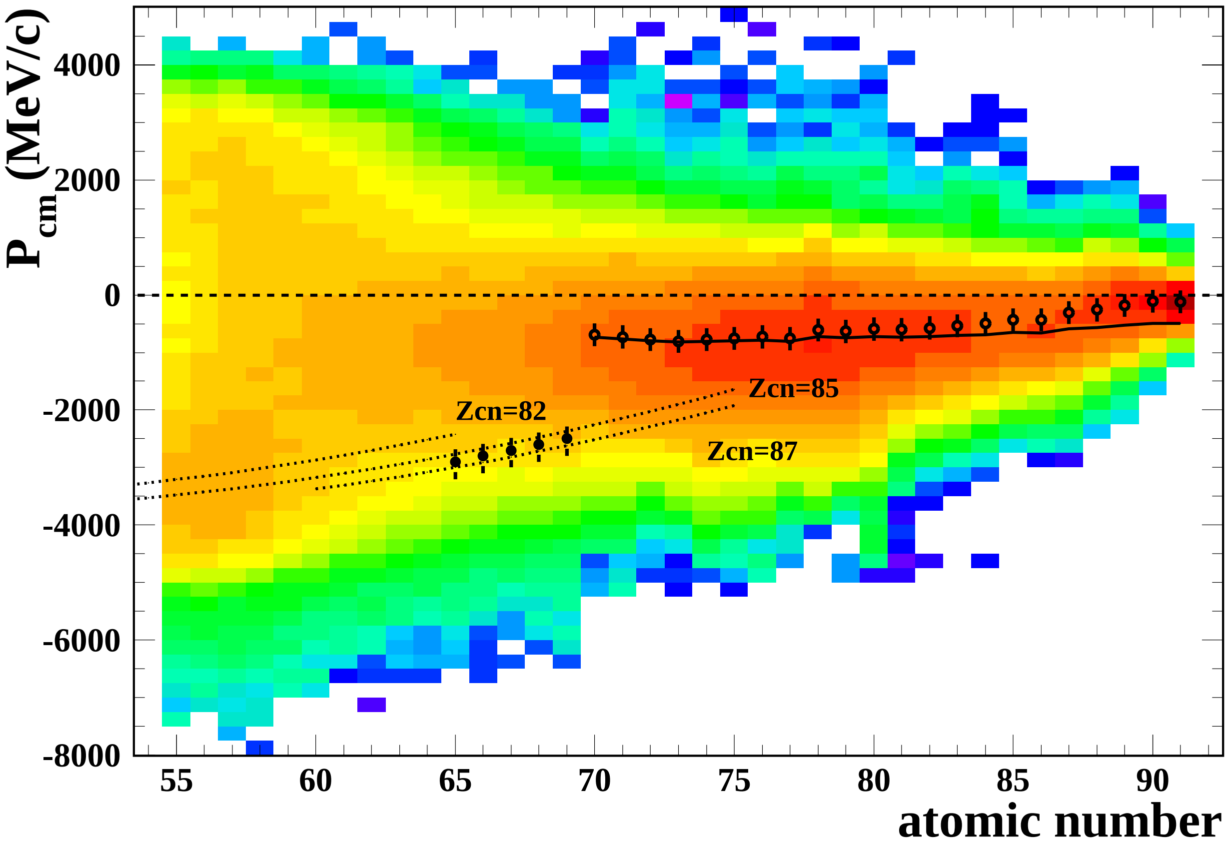

Figure 4.6: Two-dimensional histogram of the longitudinal momentum distribution of all isotopes accumulated for each element, as a function the atomic number. The colour scale is proportional to the cross section. The dashed line corresponds to the projectile velocity. The circles represent the average momentum of the measured fragmentation residues. The full line is the average momentum of fragmentation residues as estimated by Morrisey's systematics [79]. The dots correspond to the measured average momenta in fission. The dotted lines represent calculations made by using the fission TKE values, assuming that the A/Z value of the measured fragment is preserved in the fission process. Each fissioning parent nucleus assumed Z_{cn} generates a certain line; here wee plot those for Z_{cn} =87, 85 and 82. The measured data agrees with an average atomic number $Z_{cn} \approx 86$. The error of the measured data is shown if bigger than the symbol size.

are valid for proton and deuteron induced reactions.

4.4.1 Heavy fission residues

We have shown the possibility we have to disentangle the two mechanism, fragmentation and fission, leading to the production of certain isotopes, see section 3.6. For elements $_{69}Tm$, $_{68}Er$, $_{67}Ho$, $_{66}Dy$, and $_{65}Tb$ we have measured the fission production cross sections. For atomic number Z above 69 there are some indications that allow to expect the presence of fission. However, the contribution would be close to the lowest intensity limit in the present experiment. This production corresponds to very asymmetric fission channels with $Z > 65$.

In figure 4.6 we see the measured mean value of the longitudinal momentum for fragmentation (circles) and for fission (dots). Using the *total-kinetic-energy* TKE value as defined in refs. [101, 102], we can investigate the most probable parent nuclei of the observed fission fragments. The TKE depends on the charge Z_i and mass A_i of the two fission residues

$$TKE = \frac{Z_1 \cdot Z_2 \cdot e^2}{R_1 + R_2 + d} \tag{4.1}$$

where e is the charge unit, $R_i = r_o \cdot A_i^{1/3} \cdot \left(1 + \frac{2 \cdot \beta}{3}\right)$, and the parameters $r_o = 1.16$ fm, $\beta = 0.625$, $d = 2.0$ fm, are from ref. [102]. The description is given in the center-of-mass frame, and previous to evaporation processes after fission. Assuming that the A/Z value is preserved in the fission process, and $Z_{cn} = Z_1 + Z_2$, the TKE value allows to calculate the momentum of the two fission residues, considering the momentum conservation in the reference frame. Since the dependence of TKE with the mass is tiny, the result would not change noticeably even if some evaporation after fission happened. The result of the calculation is shown in figure 4.6: the dotted lines are the corresponding momenta as a function of the atomic number calculated with the TKE, according to the measured A/Z value of the fission residues observed. The measured values for elements with Z=65-69 are related to compound nuclei with values Z_{cn} =85-87. We conclude that the observed heavy fission fragments with Z=65-69 are produced in this very *asymmetric* channel, since the fissioning nucleus has an average atomic number value $Z_{cn} = 86$. The light partners of these heavy fission residues have Z values below 21. Evaporation before or after the fission process, does not change this statement. In the analysis of the reaction $^{238}U(1\ A{\cdot}GeV)+p$ the light partners of these heavy fission residues have been observed [103]. It is clear that these light fragments can be produced by fission, as claimed already earlier by some groups [104, 105], and not necessarily only due to complex break-up processes. Here we report the observation for the first time of such heavy fission production, indicated in ref. [37] for the $^{238}U(1\ A \cdot GeV) + p$ reaction before.

Additionally we can try to estimate the excitation energies involved in the process of this very asymmetric fission channels, with further assumptions. We have observed fission with mass and atomic numbers up to $Z_1 \sim 70, A_1 \sim 170$. The TKE and the measured momentum, allow to define the average charge of the fissioning nucleus. Considering that no neutron evaporation happened after the fission (i.e. a residual excitation energy below $\sim$ 10 MeV) we obtain the compound nucleus $Z_{cn} \sim 86, A_{cn} \sim 209$; and also the light partner $Z_2 \sim 16, A_2 \sim 39$. Despite the fluctuations, the average A/Z value of the initial pre-fragment distribution is about that of the projectile $A/Z|_{pf} \sim 238/92$ [6]. The deviations in the de-excitation chain from the initial pre-fragment A/Z value, are due to the evaporation. The value for the the initial pre-fragment $A/Z|_{pf}$ corresponds to a mass around 222 for $Z_{cn} = 86$, while we observe $A_{cn} \sim 209$. That means that about 13 neutrons had been evaporated before fission, corresponding to $\sim$ 130 MeV [7]. Within this scenario the excitation energy corresponding to the initial pre-fragments leading to heavy fission residues, seems to be below 150 MeV, a moderate excitation energy, which is definitely below the estimated average excitation energy of the pre-fragment distribution, $\sim$ 275 MeV, see Chapter 5.

We have considered in this energetic analysis that the evaporation after fission was negligible. We can think in a different scenario in which the observed fission residue was the result of an evaporation after fission. As an example, we can make the calculation considering that up to 10 neutrons were evaporated from the heavy fission residue[8]. We obtain similarly $Z_1 \sim 70, A_1 \sim 170 + 10$. Using again the TKE value, the compound nucleus would have got the same charge $Z \sim 86$, but now $A_{cn} \sim 221$. Since the A/Z value of the initial pre-fragment $A/Z|_{pf}$ is about that of $A/Z|_1$ it seems that almost no evaporation prior to fission had happened. The light partner would be $Z_2 \sim 16, A_2 \sim 41$. The energy available in the moment of fission is shared between the fission residues. For nuclear-induced fission the energy of the two fission residues is distributed according to their masses. The heavy fragment takes about 80% of the energy. If the heavy residue had carried $\sim$ 100 MeV it would evaporate up to 10 neutrons, while the light residues would have $\sim$ 25 MeV, evaporating up to two neutrons. The excitation of the fissioning nucleus would be that of the initial pre-fragment, $\sim 100 + 25$ MeV. Again we obtain a moderate excitation energy for the pre-fragment as possible origin of the heavy fission production.

4.4.2 Residues close to the projectile: very peripheral reactions

In figure 4.7 we see the production cross sections of the reactions of ^{238}U and ^{208}Pb with deuterons at $1A \cdot GeV$. The values are plotted for elements with atomic numbers at given distance from the projectile, and as a function of the number of lost neutrons. We can see the large loss by fission, depopulating the neutron-deficient side very close to the projectile in the ^{238}U system (circles). We can also notice the shift in the position of the maximum production close to the projectile. Six charges below from the projectile, and further down, the two systems share the same central value. The $^{208}Pb + d$ production moves faster to the fragmentation corridor. That is also due to the strong fission competition that

---

[6] In the next chapter, it will be shown that the intra-nuclear cascade models, as well as other assumptions, provide the result of the A/Z value preservation for the pre-fragment distribution.

[7] In the next chapter we will discuss that the average energy for evaporating a neutron is $\sim$ 10 MeV, while for a proton is at least $\sim$ 15 MeV. The probability of a neutron emission is al least 10 times that of a proton.

[8] According to the energies involved in the evaporation, a representative statistical ratio of evaporation of a neutron and a proton is about 10:1. So that 10 neutrons is the limit before evaporate also a proton.

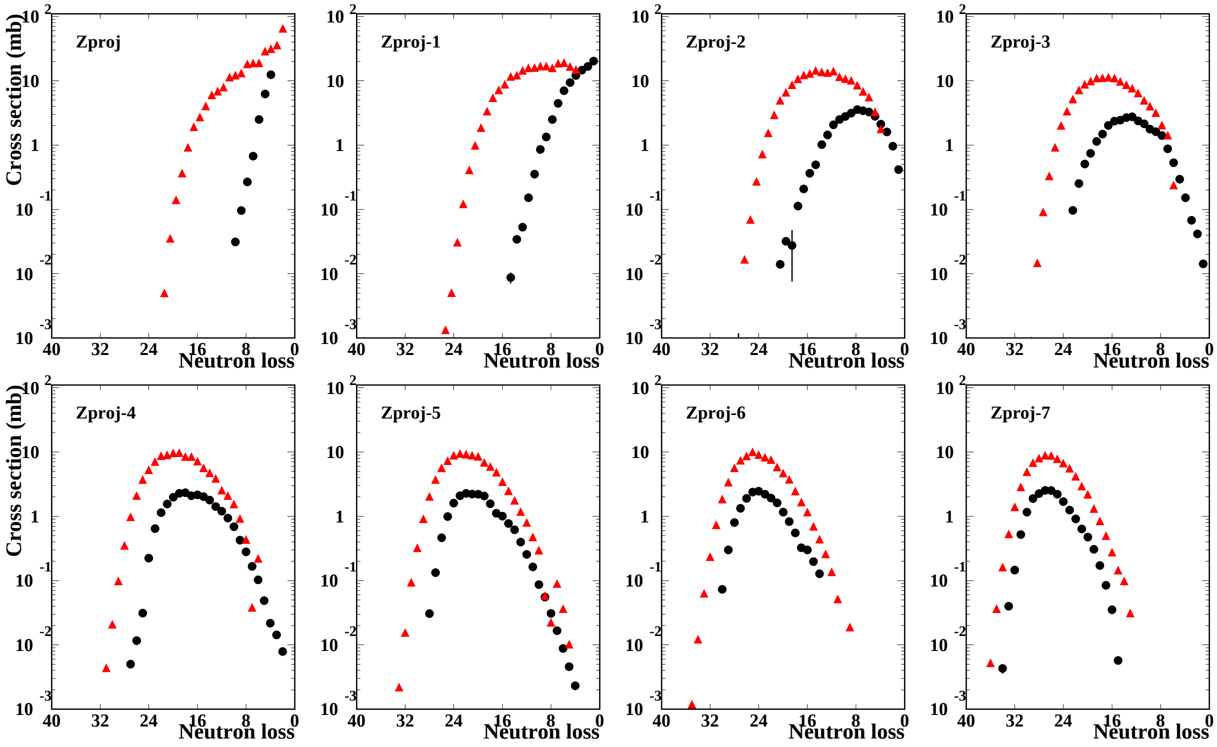

Figure 4.7: Isotopic distributions of production cross-sections measured for deuteron induced reactions in ^{208}Pb (triangles, [16]) and ^{238}U (circles , this work) at 1 $A \cdot GeV$. The cross sections correspond to the projectile (Z_{proj}) and the elements next to it (Z_{proj}-1, Z_{proj}-2, ...), as a function of the number of lost neutrons. The proton-removal channels are those data with neutron loss equal to zero.

affects the neutron-deficient side of the ^{238}U system, and shifts the maximum production to higher values.

In figure 4.1 we show the isotopic distributions of production cross-sections measured for proton (squares) [37] and deuteron (circles, this work) induced reactions in ^{238}U at 1 $A \cdot GeV$. We can see immediately that the productions for elements $_{85}At$ and above, are similar. Actually the agreement is stronger with the mass, see figure 4.4, so that for mass number $A \approx 210$ and above, the two reactions provide the same production.

4.5 Production of heavy-exotic nuclei

The use of fragmentation-fission reactions and the inverse kinematics allows the production of a large variety radioactive beams, covering both neutron-rich and neutron-deficient sides: by using fission, the medium mass neutron-rich region has been largely populated [85, 86, 87]. The fragmentation corridor reaches the neutron-deficient side down to light elements. The production of heavy-mass nuclides, with atomic number above 80, is maybe the area in which a method as that described in this work shows its strength, since there is almost no other technique available for that.

The fragmentation residues populate mainly the neutron-deficient side of the isotopic chains, around the *fragmentation corridor*, due to the inhibition of the proton evaporation induced by the Coulomb barrier. The first step of the reaction presents large fluctuations both on the A/Z ratio of the pre-fragments and excitation energy. This two effects make the process on the one hand, to produce long isotopic chains and so a great variety of nuclides. On the other hand, it reaches the neutron-rich side of elements close to the projectile, see figure 4.3.

The access to the neutron-deficient side of elements with Z>80 would open the possibility to investigate a region containing probably several *proton-emitters*. The low production rates involved limit the possibilities for the study of that region. With the results obtained in this work, some production rates can be estimated and the feasibility of the production method discussed. The fragmentation reactions also populate the *proton-removal* channels, being the most neutron-rich nuclides accessible with this process. The accumulated experience on heavy-ion reactions producing those neutron-rich nuclides has allowed to reliably predict their production, with simplified models. The data measured with ^{238}U gives us an insight into the influence of fission in the final production of those channels. The presence of ionic charge states of the produced nuclides, implies an additional effort on the techniques to unambiguously identify the fragmentation residues. That difficulty can impose strong bearings in the production of the neutron-rich region of the heavy elements. Some examples of problematic identification in that scenario are discussed in Appendix E, based on the description of the experimental method used in this work.

4.5.1 The proton-removal channels

As already mentioned, fragmentation reactions present large fluctuations in the A/Z value and excitation energies of the pre-fragments. These fluctuations can populate the *proton-removal* channels. These are reaction channels where the projectile looses only protons in the fast nucleon-nucleon interaction, whereas the excitation energy is below the particle evaporation threshold. The pre-fragment will lose its excitation energy either by γ-emission or fission. The limited energy that characterize these channels, deserves the name *cold-fragmentation* [106] for this process. These are the most neutron-rich nuclides one can observe by using the experimental procedure described in this work.

The proton-removal channels have been investigated for different target-projectile combinations. The measured cross sections for these channels seem to be independent of the reaction, see figure 4.8. We can observe that the data of the reactions with ^{238}U does not show any characteristic change in respect other heavy-ions with a smaller fissility. Actually, all the results shown are compatible within their uncertainty. The residues populating those *cold fragmentation* channels can only be produced during the fast initial step of the reaction. In low fissility systems, one can estimate the production with a calculation of the pre-fragment formation probability, with its energy being distributed below the neutron separation energy S_n. For energies above S_n the residue has an almost negligible probability to populate the *proton-removal* channels. These ideas were

nuclide	particles/hour	nuclide	particles/hour	nuclide	particles/hour
^{209}Th	300	^{208}Th	120	^{206}Th	19
^{206}Ac	1030	^{204}Ac	90	^{202}Ac	6
^{203}Ra	15	^{202}Ra	1.5	^{199}Ra	< 0.001
^{199}Fr	2	^{198}Fr	0.1	^{195}Fr	$< 10^{-4}$
^{196}Rn	14	^{195}Rn	1	^{192}Rn	$< 10^{-3}$
^{193}At	3	^{192}At	0.1	^{188}At	$< 10^{-6}$

Table 4.3: Estimated production of some neutron-deficient nuclides for a setup similar to that used in this work. The reference values used are: target thickness 200 mg/cm^2, beam intensity 10^8 Hz, efficiency depending on the charge and mass, being typically $\sim 25-35\%$, and an irradiation time of one hour. On the left column the isotopes are those next to the known nuclei, the rightmost column is the estimated threshold with half-life values above 1 μs. The decay detection of those produced nuclei is not considered. Note that details as those of parity are negleted, and the nuclides are only intended as examples of magnitudes involved. See the text for details.

proposed in ref. [3], and they succeeded in the reproduction of the available data by using an analytical model, avoiding the lengthly results by Monte-Carlo based calculations.

In highly fissioning systems, as ^{238}U, one expects that the previous model would overestimate the values in some case, since the fission channel can be opened at lower energies than those of the neutron separation energy S_n threshold. Of course the model mentioned above can be redefined to take that parameter into account. However we can investigate easily the difference between systems with very different fissilities. For the following set of nuclides ^{238}U, ^{237}Pa, ^{236}Th, ^{235}Ac, ^{234}Ra, we have the fission barrier values $B_{fiss} = 5.03,\ 5.71,\ 6.44,\ 7.21,\ 8.02\ MeV$ respectively, and the neutron separation values $S_n = 6.15,\ 5.78,\ 6.01,\ 5.57,\ 5.68\ MeV$ respectively[9]. The energy limit to observe the *cold-fragmentation*, changes rather little from one process to the other, and the induced differences are below the uncertainties in the available data. We can understand the agreement found in the measured data in systems with fissilities so different as ^{208}Pb or ^{197}Au in respect to ^{238}U.

The *cold fragmentation* offers the possibility to produce neutron-rich heavy nuclides. Studies and estimations for production of these nuclides are the starting point to design and schedule experiments with these nuclides. The data available allow both, topredict the production by improving and testing the models, and to define which kind of projectile-target system could be the most efficient for the production. In this work we conclude that the fissioning probability of the system does not influence appreciably the production of the *proton-removal* channels.

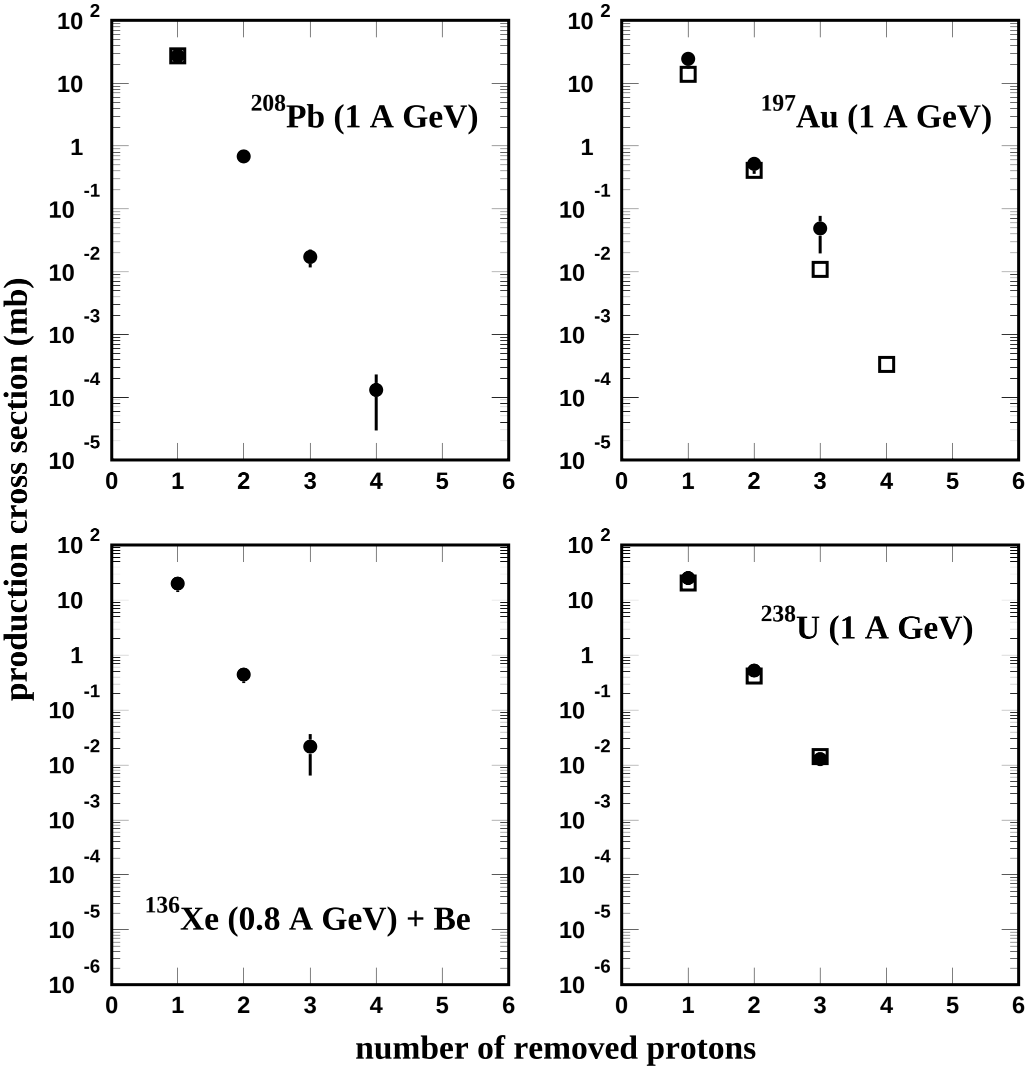

Figure 4.8: Production cross sections of the proton-removal channels measured in several heavy-ion reactions; each panel corresponds to a certain projectile: $^{197}Au(1\ A \cdot GeV) + Al$ (dots) [98], $^{197}Au(0.95\ A \cdot GeV) + Be$ (squares) [3], $^{208}Pb(1\ A \cdot GeV) + Cu$ (dots) [82], $^{208}Pb(1\ A \cdot GeV) + d$ (squares) [16] ,$^{136}Xe(0.8\ A \cdot GeV) + Be$ [3]. The $^{238}U(1\ A \cdot GeV) + p$ data (dots) is from [37] and $^{238}U(1\ A \cdot GeV) + d$ (squares) from this work. The full lines correspond to the model description given in [3].

4.5.2 Neutron-deficient residues: proton emitters

The *proton drip line*[10], has been reached for elements with atomic values below 85. Beyond that line the nuclei may be proton-unstable, but yet exist with half-life values defined by the competition of the different radioactive decay modes present.

In figure 4.9 we see a partial region of the chart of the nuclides. The known nuclei in the neutron-rich side lie on the proton drip limit for odd elements. The dashed line, corresponds to a calculation [107], showing the position of isotopes of even elements which could exist with half-life values for proton-emission above 1 μs. Up to twenty-one *proton-emitters* had been identified and studied until 1995. We can observe in figure 4.9 that for elements with Z>82, the region of possible new emitters becomes wider, with about four candidates per element. The subject opens new possibilities to study nuclear deformation and structure in an interesting region of deformation: just within that region the nuclear shapes change from spherical to deformed, and the information would be precious. The investigation of that region is also of interest in nuclear processes of interest in Astrophysics as the *rp-process*, since its production path over-passes the proton drip line at some points. The study of proton emitters is usually done by, firstly, identifiying the nucleus and, secondly studying its decay after *implantation*. It is a delicate task and typical times involved run down to μs with an efficiency below 40%. Independently of that efficiency, one has previously produced those exotic nuclei. The production rate of very neutron-deficient isotopes with atomic number above 80, is limited namely because of the very strong fission channel. We saw already in section 4.4, how the production is drastically reduced by fission.

The cross section measured in this work did not reach the proton-drip line, due to the cross section threshold imposed by the beam intensity and the beam-time available. However, the fragmentation can populate that region clearly, and our results help to estimate the cross sections of the most neutron-deficient nuclei. The estimation of the production in that region is not obvious. Some systematics as EPAX [83], succesfull in the *limiting fragmentation* regime (see Apendix C), is not adapted to fissioning systems. The models describing this type of reactions, as will be shown in Chapter 5, are good enough to define the behaviour and to reproduce the values over wide ranges of nuclides, but the description of the isotopic production tails is not completely satisfactory, and also largely time consuming.

The simple extrapolation from the available data is risky since the trend of the data is not known. Fitting an exponential function with a polynomial dependence on the neutron number, the neutron-deficient wing of the isotopic distributions we have measured can be reproduced. The result can be seen in figure 4.10. The measured data (small symbols) and the estimated values (big symbols) are plotted for Z values between 85 and 90. The full line is the result of the proposed fit. The arrows indicate the estimations for nuclides

---

[9] To evaporate a neutron, the kinetic energy has to be added, being $\sim 2-3$ MeV

[10] The proton drip line is usually defined with the condition of making the proton separation energy equal to zero. The models allowing to calculate the binding energies predict the position of the drip lines. Nevertheless the existence of nuclei beyond that limit is possible, due to the Coulomb barrier, and their half-lives defined by the limiting decay processes those nuclides can undergo. For heavy ions the competition of α emission, proton emission and fission, defines that limit.

in the edge of the drip-line. The points below the arrow (if within the range of the figure) correspond to the 1 μs half-life estimated. Nevertheless we insist in the unknown trend of the production: we extrapolate the fit with the only help of the measured data. With this crude description we can estimate the cross section for the reaction $^{238}U + d(1\ A \cdot GeV)$. In table 4.3 we see the estimated production rate of several nuclides considering a setup as that used in the experiment described in this work, with a target thickness of 200 mg/cm^2, an intensity[11] of 10^8 ions/s, a measurement efficiency[12] being typically $\sim 25 - 30\%$, and an irradiation time of one hour. The data on the left part of the table correspond to the production of the first nuclide beyond the proton drip line. The data on the rightmost column correspond to the isotope with an estimated half-life about 1 μs. It is difficult to estimate the uncertainty of the estimated yields. The trend used tends to overestimate the cross section values (up to 30% for the less produced and measured nuclei), and the results could be easily one order of magnitude overestimated. On the other hand, the rest of the parameters used to estimate the rates are conservative.

By looking to figure 4.10, we can observe the different slope for $_{89}Ac$ (circles) and $_{90}Th$ (inverted triangles), in respect to the slope of the lower Z elements. That determines that the production of the heavier elements is more feasible in terms of rates. One could increase the target thickness since the setup efficiency would not change very much, and the secondary reactions within the target are low for the higher Z nuclides. The beam intensity at GSI is some 10^8 ions/s for ^{238}U nowadays. According to this estimation the Th and Ac candidates could be studied with production rates above ~10 particles/hour. Future plans at GSI include a beam intensity increase up to 10^{11} ions/s. Those intensities would extend the possibilities to study this proton-emitter region much further. Nevertheless the 1 μs threshold is still far for the lower Z elements, as those of Rn and At.

4.6 Charge pickup processes

In this experiment we observed the production of $_{93}Np$ isotopes. The $\Delta Z = +1$ channel is not unusual in relativistic heavy ion reactions, as reported in the reaction $^{208}Pb(1A \cdot GeV) + Cu$ in ref. [108]. The process has been also been studied systematically recently, e.g. in ref. [109]. One of the interest of that production is its connection with the β-decay transition strengths, and on the nuclear structure of the nuclei [110]. Additionally the theoretical codes describing the reaction, see next chapter, include the formation of these pre-fragments. The measurement of this production, can help to cross-check the description of the reaction mechanism.

The low-energy concept of charge exchange due to proton exchange, is not longer valid for energies above 1 $A \cdot GeV$. At relativistic energies the charge pickup is solely due to π and ρ meson exchange. In fact this process competes already above 100 AMeV. The codes usually include the single-pion treatment, and here we just outline that process. The pion

---

[11] Typical intensities up to 10^9 Hz are now available at GSI, but the time structure of the spills reduce the effective intensity. Of course any improvement will go directly as a multiplicative factor to the yields.

[12] Here efficiency is used in the sense of all the setup and analysis restrictions imposed to make the identification. It depends on charge and mass.

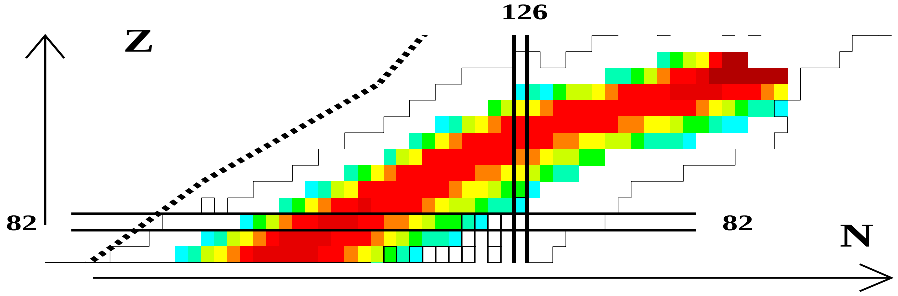

Figure 4.9: Partial region of the chart of the nuclides. The proton drip line lays on the edge of the known nuclei. On top of the chart the measured values of fragmentation production in this work are plot. The grey scale is relative to the production. The dashed line is the result of a calculation, showing the position of the isotopes which could exist with half-life for proton emission above 1 μs. See the text for details.

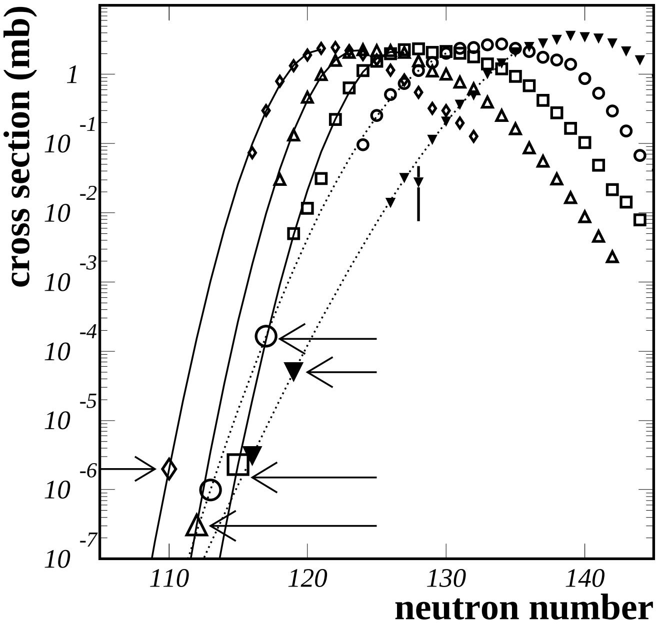

Figure 4.10: Measured and estimated production cross sections for the neutron-deficient side of elements $_{90}Th$, $_{89}Ac$, $_{88}Ra$, $_{87}Fr$, $_{86}Rn$. The lower production symbols correspond to those in the limit of the known nuclides, and to the one μs half-life limit, as shown in figure 4.9.

production happens in the Δ decay after an inelastic nucleon-nucleon NN collision:

$$NN \to N\Delta \qquad\qquad \Delta \to N\pi \tag{4.2}$$

The total charge is preserved. The absorption of the pion is described in two-steps just by reversing the process. We can see that the Δ resonances drive to different results, in which the number and type of nucleons can change. That is the origin of ${}_{93}Np$ isotopes in the case of ${}_{92}U$ fragmentation.

A systematic study of charge-pickup processes about 1 $A \cdot GeV$ is reported in ref. [111]. The parameterisation they found for the total charge pick-pickup cross section, covering a wide range of reactions, is

$$\sigma_{pickup} = 1.7 \cdot 10^{-4} \cdot \left(A_p^{1/3} + A_t^{1/3} - 1 \right) \cdot A_P^2 \qquad [mb] \tag{4.3}$$

where $A_{p/t}$ are the mass numbers of the projectile/target. They describe the available data within a factor of 2. This systematic yields $\sim$ 62 mb for ${}_{93}Np$ production by ${}_{92}U$ pickup.

The investigation by Westfall et al. [112] of ${}_{92}U$ pickup at 960 AMeV, demonstrated a upper limit of 8 mb for the production. The work of Rubehn et al. [113], investigated the ${}_{92}U$ pickup at 1 $A \cdot GeV$ with several targets, by measuring the fission production from pre-fragments with charge 93, They showed that the quadratic dependence in equation 4.3, can be reproduced by the theoretical description of heavy-ion collisions, as those described in the next chapter. The calculations show that $\sim$ 78% of the pre-fragments formed with charge 93 are depleted by fission, $\sim$ 20% evaporate some proton, and the rest, below 2% were predicted to survive as ${}_{93}Np$. According to their measured data the ${}_{93}Np$ production with a deuterium target would be $\sim$ 0.5 mb. We have observed several isotopes, ${}^{234-238}Np$, with a total cross-section of $\sim$ 0.39 mb (see Appendix A) in agreement with the work of Rubehn. We conclude that while for low fissility nuclei the description of equation 4.3 for charge-pickup production may be well adapted, for high fissility nuclei it is definitely inappropriate.

4.7 Transferred longitudinal momentum

The nuclei produced in a reaction inherit the momentum characteristics of the projectile. The reaction process induces fluctuations in the width of the momentum parallel to the projectile direction $\sigma_{||}$, as well as to the transversal direction $\sigma_{\perp}$. Also the longitudinal average momentum $< p_{||} >$ of the residues is shifted in respect to that of the projectile. The momentum distributions of the residues are measured directly in our experiment, since it is related directly with the distribution of the positions measured in the dispersive focal plane. Since the fragmentation production of high-energy heavy-ion reactions are consistent with the *limiting-fragmentation* hypothesis and *factorization*, see Appendix C, one can investigate also if those results are reflected in the momenta distributions. Extensive studies showed that irrespective of the projectile, target and beam energy, above a threshold $\sim$1 $A \cdot GeV$, the momenta distributions $p_{||}$ show certain characteristics in the projectile rest-frame [114]:

- Gaussian shape.
- average $< p_{||} >$ value negative, i.e. $p_{||} < p_{beam}$ in the laboratory frame. That shows a kind of *friction* one can expect from the fragmentation process [115].
- isotropic spread of the distribution, since $\sigma_{||} \sim \sigma_{\perp}$ within 10%, reflecting the isotropic production of fragments.

All those characteristics are consistent with the *factorization* and *limiting* hypothesis: the distributions are independent of target structure and beam energy in the projectile rest-frame. Only very light residues, H and He, were found to follow different systematics, possibly due to additional mechanisms contributing to fragmentation. The characteristic parameters of the distributions $< p_{||} >$ and $\sigma_{||}$, result independent of the target material and the beam energy, but depending on beam and fragment masses.

4.7.1 Model description of the momentum distributions

Morrisey [79] discusses the relationships found by different authors linking the induced momentum in the fast reaction step, with the induced excitation energy E^*. Under certain assumptions[13] the result is

$$p \cdot c = E^* \cdot \left. \frac{\gamma + 1}{\beta\gamma} \right|_{beam} \tag{4.4}$$

where the fragment transferred-momentum p is linked to E^* by a kinematic factor, depending the later only on the beam energy through β and γ. The excitation energy of the pre-fragment E^* is dissipated in the evaporation step. Being that an statistical process, it distributes the momentum p around its mean value. The excitation energy E^* is linked to the number of ejected nucleons in the fast reaction step, as it will seen in Chapter 5. The higher the energy available, the lighter the residues produced in the evaporation chain. Equation 4.4, and the statistically induced width, link the mean momentum and width of the residues momentum distributions, to the mass difference of the residue and projectile.

Morrisey also found a systematic linear dependence in experimental data relative to fragmentation residues, relating the mean momentum with the mass difference of the fragment and projectile

$$p_{||}^{transfer} \sim -8[MeV/c] \cdot (A_p - A_f) = -8[MeV/c] \cdot \Delta A \tag{4.5}$$

where $A_{p/f}$ refers to projectile and fragment mass numbers, and ΔA the mass difference. The kinematic factor defined in equation 4.4, takes away the energy dependence from $p_{||}$. The value that relates the mass and momentum was fitted from the available data. Note also that the result refers to the final residues, i.e., after the fast and evaporation reaction steps. The linear behaviour found is attributed to the fragmentation process, due to the relationship between ΔA and E^* given at equation 4.4. The data discussed by Morrisey extend in a wide range of masses, showing not only the linear dependence,

---

[13] See the reference [79] for a detailed discussion.

but also large fluctuations for higher ΔA values. He attributes that spreading, out of the linear behaviour, to different mechanisms than fragmentation.

Different approaches depending on simple postulates[14] predict a parabolic dependence of $\sigma_{||}$ on fragment mass [116, 117, 118]. Deviations of that parabolic-dependence, obtained with such general assumptions, are thought to indicate the importance of fragment structure and final-state-interactions. The model of Goldhaber [116] calculates the momentum width within a statistical description, and the result is that the width value of the distribution depends on the Fermi momentum p_F of the abraded nucleons

$$\sigma(p_{||}) = \frac{p_F}{\sqrt{5}} \cdot \sqrt{\frac{A_f \cdot (A_p - A_f)}{A_p - 1}} \tag{4.6}$$

where $A_{p/f}$ refers to projectile/fragment mass numbers, as before. The result in fact is the same assuming a cluster emission to be sudden or after thermal emission. Note that this is a result defined by a model describing the reaction, and it only refers to the fast initial reaction step.

Additionally the evaporation step will influence the final momentum width, and the observed values in a reaction process will differ from that of the fast-step. Since the evaporated nucleons subtract mass and add little momentum width[15], the measured values are expected to be below the width predicted by the Goldhaber's model. The Morrisey's systematics [79] accounts for many experimental results. He found an empirical relation for the measured widths according to the mass change as

$$\sigma(p_{||}) = \frac{150}{\sqrt{3}} \cdot \sqrt{A_p - A_f} \quad [MeV/c] \tag{4.7}$$

This relationship follows the trend of the residues after evaporation. The differences in between the results from equations 4.6 and 4.7 must be due to the evaporation process, providing that the model of Goldhaber is correct, and within the range of validity of the Morrisey empirical result.

4.7.2 The longitudinal momentum distributions

Together with the yields, our experiment allows to measure the longitudinal momentum $p_{||}$ distributions of the residues. The positions at the dispersive focal plane F2 of the FRS, reflects the distribution of $p_{||}$, since the position at F2 does not depend on the FRS-entrance angle. The distribution measured at F2 does not depend on selections of transverse momenta, since the angular acceptance of the FRS is wider than the angular

---

[14] The postulates relate statistically the momentum distribution of the fragments observed to those momentum distributions of the nucleons involved, e.g. Feshbach-Huang at [117], and corrected by Goldhaber [116]. Finally the Fermi momentum, and the fragment and projectile mass numbers, will describe the observed momentum. Goldhaber shows also that the momentum distribution alone does not distinguish the *sudden* hypothesis, and *thermal equilibrium* hypothesis for the reaction, since both yield the same dependence.

[15] The evaporated nucleons are expected to have momenta below the Fermi value ~ 265 MeV/c for heavy ions. Theoretical calculations support that hypothesis.

distribution of the fragmentation residues. The x-position, the central rigidity and the dispersion at F2 define the particle rigidity

$$B\rho|_{12} = B\rho|_o \cdot (1 + \frac{x_2}{D_{12}}) \tag{4.8}$$

The A and Z numbers defined after the identification of the particle determine the kinetic-energy per nucleon

$$T_1 = u \cdot \left[\sqrt{1 + \left(\frac{B\rho|_1 \cdot Z \cdot c}{A \cdot u} \right)^2} - 1 \right] \tag{4.9}$$

where c the speed-of-light and u the mass unit. Taking into account the losses at the different layers of matter [71], it is possible to recover the original kinetic energy value at the center of the target[16]. The values are finally transformed into the projectile rest-frame. The distribution of positions in F2 measured for one isotope, determines with the above description a momentum distribution.

The change in momentum, relative to the beam momentum, is due to the reaction mechanism. According to the previous discussion we assume that the momentum distribution is Gaussian. The measured distributions contain some other additional sources enhancing the width. The *location straggling*, due to the difference in energy straggling for the reaction happening at different places within the target, adds a certain width. Such distribution can be reproduced calculating the energy loss difference for the reaction happening at the entrance and exit of the target. It results in a rectangular distribution. That straggling amounts ~100(240) MeV/c for the maximum produced isotope of Z=80(70) with a typical width of ~180 MeV/c in each element. Other cumulative effects as the momentum spread of the beam itself, the straggling in the different layers of matter, the beam spot size and the position resolution achieved with the detectors[17], are estimated by measuring directly the width of the beam momentum. The distribution of the beam is observed Gaussian. The measured beam spread was $\sigma_{BEAM} = 52$ MeV/c. That width is added quadratically to the Gaussian reaction width. The momentum distributions for each nuclei are studied by unfolding the different contributions discussed (two Gaussians and one rectangular distributions). The fit parameters are the mean value $< p_{||} >$, the Gaussian width $\sigma(p_{||})$, and the normalization (this would provide the yield).

The transfer momentum, as defined by Morrisey, depends additionally on a kinematic factor

$$p_{||}^{transfer} = p_{||} \cdot \left. \frac{\gamma\beta}{\gamma + 1} \right|_{beam} \tag{4.10}$$

For ^{238}U in the middle of the target the value of that factor is 0.589 . The transfered momentum is a scaled value of the measured $< p_{||} >$. The widths are not affected by

---

[16] The value given relative to the center of the target makes sense when we have subtracted the contribution to the width from the location of the reaction. In that way we have defined a system were the reaction is considered to happen at that plane. On the other hand, that plane is the average position of reaction locations.

[17] It can be calculated that 1 mm in the position determination, amounts for ~ 28 MeV/c for the projectile momentum. For A=150 it is reduced to 18 MeV/c.

that scaling, as it was tested additionally. Some plots of the differential cross section $d\sigma/dp_{||}$ are shown in the previous chapter. In figures 4.11 and 4.12 the values measured for $< p_{||}^{transfer} >$ and $\sigma(p_{||})$ are shown.

4.7.3 Discussion of the results

The measured momentum distributions are the result of the two reactions stages: the fast nucleon-nucleus interaction and the evaporation-fission step. The parameters obtained for $< p_{||}^{transfer} >$ and $\sigma_{||}$, reflect that double process. In figure 4.11 the measured values for those magnitudes are shown as a function of the mass difference between the projectile and fragment $\Delta A = A_p - A_f$, together with the Morrisey systematics (full line), and the Goldhaber's model (dashed line). The uncertainty of the measured data was estimated from the 2 mm resolution in F2 x-position, The evaluation of the uncertainty varies constantly from $\approx$ 55 MeV/c for $A \sim 230$ till $\leq$ 25 MeV/c for $A \sim 100$, i.e. about 10 MeV/c each 50 masses. The value for the Fermi-momentum for ^{238}U, $p_F \approx 265$ MeV/c, was taken from ref. [119], where also the validity of the result is discussed.

We can see in the lower panels that for residues with $\Delta A \leq 25$, the measured widths fall below Goldhaber's prediction as expected, due to the evaporation process, and follow the Morrisey's description. However for $\Delta A \geq 30$, instead of the predicted root dependence on ΔA, we observe an almost linear dependence. That trend was also observed in the data of $^{238}U(1\ A \cdot GeV) + p$ [37], as well as in $^{238}U(1A \cdot GeV) + Pb$ [99], and proton and deuteron induced reactions on ^{208}Pb at $1\ A \cdot GeV$ [15, 16].

In very peripheral reactions, the evaporation channel can be strongly suppressed, as it is for the *proton-removal* channels. If the excitation energy of the pre-fragment is below the limit to evaporate neutrons, $\sim$ 10 MeV, the particle emission is blocked and the residue is given by the pre-fragment. The momentum widths observed in those channels followed the Fermi momenta dependence predicted by Goldhaber [116] . The interpretation of the two different behaviours observed in the widths, relate the two reaction steps to measured values [106]: whereas for *cold fragmentation* processes the widths are determined by the Fermi momenta of the abraded nucleons, it is not the case for any other channel, corresponding to higher excitation energies, dominated by the evaporation step. The process has been observed in different heavy ions reactions [98, 106, 120]. In the right panel we see the values we have measured for the momentum width $\sigma_{||}$ in a narrow ΔA range, close to the projectile. The *cold fragmentation* signature appears clearly. The three squares are the one-, two- and three-proton removal channels we have observed. These results lie definitely closer to the Goldhaber's description, while all the rest lie over the Morrisey's systematics.

In the upper panels of figure 4.11 we see the mean value of the distributions, plotted as a function of ΔA. On the left panel we observe all the measured data, together the Morrisey's description on top of it (solid line). For $\Delta A < 60$ the linear behaviour is preserved, with a dependence slightly different from that of Morrisey (7% lower). That difference was observed also in the $^{238}U(1\ A \cdot GeV) + p$ data. The slope decreases at higher values of ΔA, and the values fluctuate in a wider range. This flattening was observed in heavy ion reactions as $^{238}U(1AGeV) + Pb$ [99], and proton and deuteron induced reactions

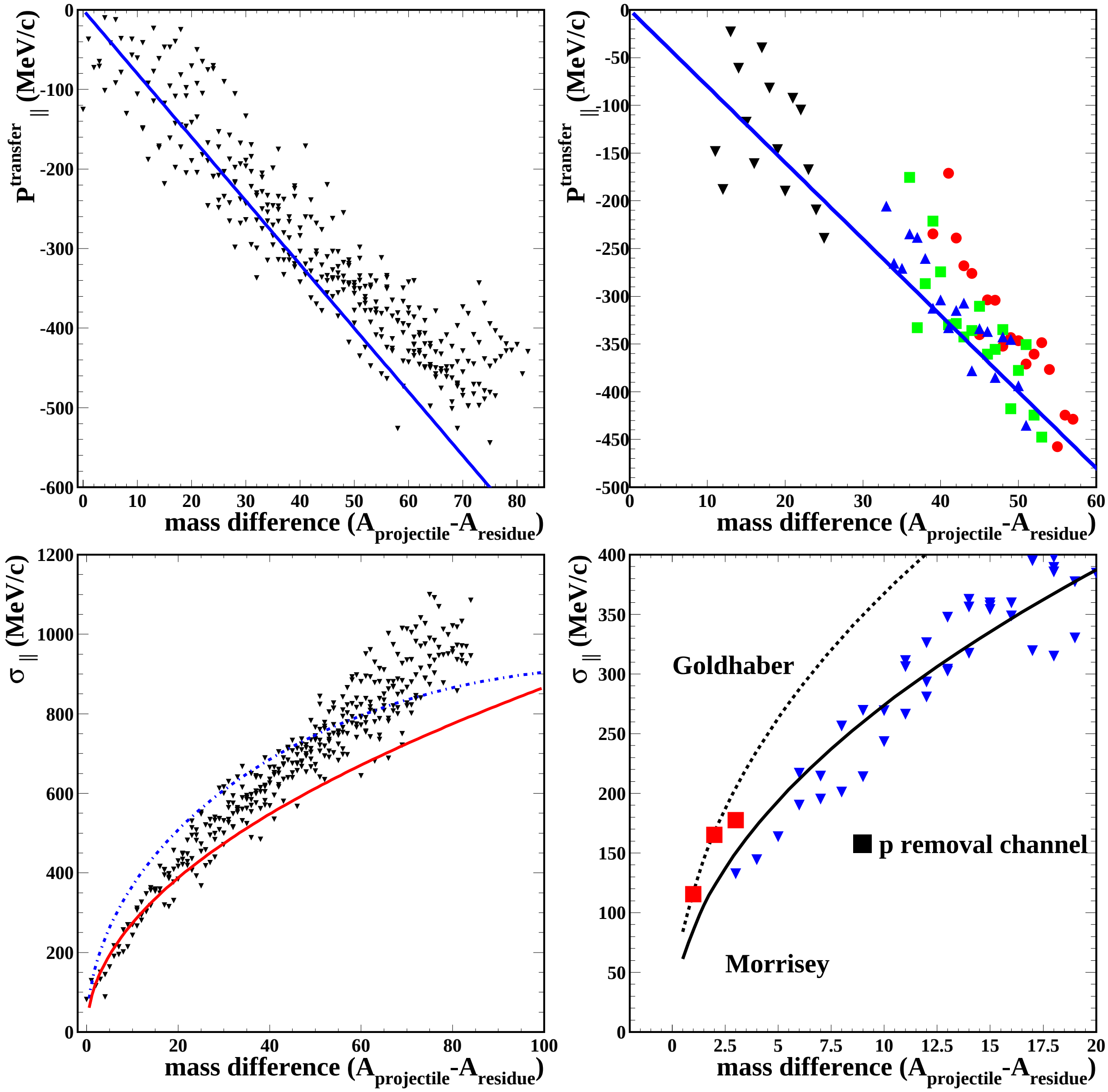

Figure 4.11: Upper panels: transferred longitudinal momentum $< p_{||}^{tarnsfer} >$ in the projectile reference system, as a function of the mass difference of the fragment respect to the projectile. In the left panel all the measured data are plotted, whereas in the right panel only a few elements appear: $_{90}Th$ (inverted triangles), $_{80}Hg$ (triangles), $_{81}Tl$ (squares) and $_{82}Pb$ (circles). The systematic estimation given by Morrisey [79] is also plotted (full line). The error bars are not included for clarity. Lower panels: width (Gaussian standard deviation) of the measured longitudinal momentum in the projectile reference system, as a function of the mass difference. In the left panel all data are plotted, together with the Goldhaber's [116] (dashed line) and Morrisey's [79] (full line) predictions. In the right panel we show a zoom of the nuclei closer to projectile. The proton removal channels are marked as squares.

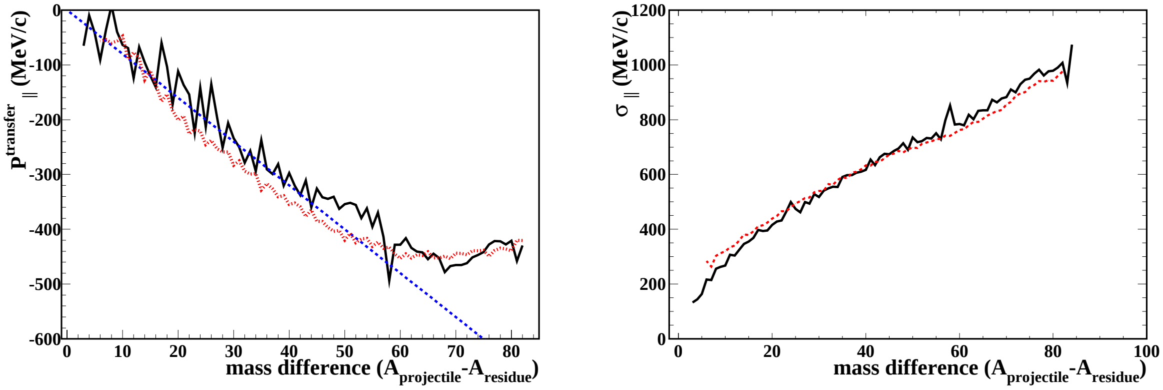

Figure 4.12: Measured $< p_{||}^{tarnsfer} >$ values (left panel) and the width (Gaussian standard deviation, right panel) of the longitudinal momentum distributions, averaged for each residue mass. The data correspond to deuteron induced reactions on ^{238}U (this work, full line) and in ^{238}Pb [16] (dotted line). The Morrisey's [79] prediction for $< p_{||}^{tarnsfer} >$ is also shown (dashed line).

on ^{208}Pb at 1 $A{\cdot}GeV$ [15, 16]. In the right panel we show the momentum of a few elements. We can see, despite the fluctuations, a certain dependence in the Z/N ratio for lighter elements ($_{80}Hg$, $_{81}Tl$, $_{82}Pb$) but not for heavier ones ($_{90}Th$). The effect is not present in the sigma value. The same effect was observed in the reaction $^{86}Kr(500A \cdot MeV) + Be$ [120]. The N/Z effect washes out for the higher ΔA values.

The data of proton [37] and deuteron (this work) induced reactions with ^{238}U, showed a common behaviour in the $< p_{||}^{transfer} >$ measured values, resulting in lower values than those predicted by Morrisey. However the data from other heavy ion reactions as $^{197}Au(950A \cdot MeV) + p$ [35], and those of ^{208}Pb at 1 $A \cdot GeV$ with proton and deuteron [15, 16], showed the opposite effect: the measured values lie below the prediction. That effect is not at all reflected in the widths. In figure 4.12 we show the averaged $< p_{||}^{transfer} >$ values (left panel) and the averaged $\sigma_{||}$ values (right panels), for each mass, weighted by the measured cross section of each nuclide. The data correspond to deuteron induced reaction with ^{238}U (full line) and ^{208}Pb [16] (dotted line). Also the Morrisey systematics (dashed line) appear on top of the left panel. We can see the effect commented, despite the fluctuations: the ^{238}U results laie above the prediction, and the ^{208}Pb data below.

Since the main difference between these two heavy ions reactions is the high fissility of the pre-fragments resulting from the ^{238}U interaction, we can relate the difference in the momenta to the fission channel. The fission barriers depend on the angular momentum of the fissioning nucleus, being lower for increasing angular momentum values. We expect that the nuclides with lower angular momenta will undergo fission with lower probability[18]. The lower momentum value carried by the nuclide is the result of a lower transfer

---

[18] The fission barriers depend on the angular momentum of the fissioning nucleus, being lower for increasing angular momentum values.

momentum in the reaction. Since the nuclides with the high momenta undergo fission, we should observe as fragmentation residues those nuclides with the lower transfered momentum. The width of the momentum distribution depends in the mechanism involved and it does not change from one reaction to another.

That is the result we can observe in figure 4.12. We conclude that the fission mechanism is biasing the production of the fragmentation residues: for a given excitation energy, the momentum of the compound nucleus influences decisively the probability of fissioning. That is a strong constraint for the models describing the process, since only if the momentum is treated realistically, the codes would reproduce this effect distinguishing the highly fissioning systems.

Chapter 5

Description of relativistic nucleon induced reactions

> *The architect F. Lloyd Wright once said that a doctor can bury his mistakes, but all an architect can do in case of failure is to hide his building in creepers. What of the theoretical physicist who is unsuccessful in constructing a complete theory? He introduces constants.*[1]

The relativistic heavy-ion reactions are typically described by combining two different models: one for the fast initial step that describes the nucleon-nucleus interaction, providing an excited pre-fragment; then a second model that describes statistically the evaporation-fission of a thermalyzed compound nucleus, which gives the final reaction residue. The identification of the pre-fragment with a compound nucleus is a delicate assumption, that was already discussed in Chapter 1. The two-step model is reflected in the treatment of an event in a calculation. One code per step, each one developed accordingly the most characteristic parameters involved in the process. The code-switching in the two-step modelization, may appear as a rather sharp and abrupt procedure. However the results are oftenly realistic and they succeed in reproducing the reactions and their general trends.

All the models that nowadays can describe the spallation residues of a high-energy reaction settle on that two-step scheme. Since the early work of Metropolis [126], different codes have been developed. All of them share a common scheme : Monte-Carlo treatment, time-like development and classical description of the nucleon-nucleon interaction. Some low-energy model succeded in the description of the so-called *pre-equilibrium* reactions, without developing a nucleon cascade in the sense described later. But these codes are not well suited for reactions induced by relativistic ions. This kind of codes are sometimes used as transition, in between a high-energy *intra-nuclear-cascade* INC and the evaporation-fission step. Since the use of this intermediate stage has not lead to decisive changes, Chapter 1, we are not going to consider it in our study.

The INC codes will show us that the initial fast interaction of the nucleons induce a rather broad distribution of excitation energies for the pre-fragment. The energy tail

---

[1] A.B.Migdal., *Nuclear Theory: the quasi-particle method*, N.A.Benjamin Inc., 1968, N.Y.

reaches values above 400 MeV. In that region we are already at temperatures ~4 MeV were different experiments mark the onset of *multifragmentation* processes. We are not going to discuss the multifragmentation channel, since the topic is well beyond the scope of this work. The energy distribution we have calculated shows also that the pre-fragments within that region of high complexity amount to ~10% of the residue production. Since most of the production is due to fission and fragmentation, we are going to discuss that part with dedicated models.

Several standard models have been used to study the reaction $^{238}U(1\ A \cdot GeV) + d$, and they are briefly outlined here. For the evaporation-fission part, we compare two models that are commonly used to describe the de-excitation of a highly-excited compound nucleus. We show that one of this models, ABLA succeeds in reproducing realistically the measured results. Then, the INC part is revisited. To further investigate some characteristics of the reaction $^{238}U(1\ A \cdot GeV) + d$ we decided to develop a simplified INC model, based on the high-energy Glauber approach. Our simple model is able to describe basically the results, and additionally it has a reduced and clear parameterisation. With the help of the code we can investigate the influence of the actual nuclear shape in the process. The model is extended in the simplest geometrical way to a double impactin order to describe the collision of two nucleons. In our reaction, the key feature is the particular mass distribution of the deuteron.

The discussions based on both the isobaric and isotopic distributions of the production cross sections allow to investigate the features of each model. The isobaric distribution reflects the excitation energy distribution of the pre-fragments E^*, since the E^* distribution depends on the number of abraded particles in the initial fast step. The isobaric distribution is very sensitive to the parameters involved. On the other hand, the isotopic distributions allow to discuss the evaporation and fission processes, since the shape, width, position of the maximum production and its depletion by fission are determined for highly excited fragments namely by the second-step of the process. Only the low-energy pre-fragments result in residues close to the projectile, and inheriting some of its features. At sufficiently high excitation energy E^*, the residues are the result of a statistical deexcitation process.

5.1 Intra-Nuclear Cascade codes

At relativistic energies the nucleon-nucleon NN sequential interactions may be considered as intra-nuclear cascade interactions rather than interactions in the mean-field[2]. This assumption is used in the INC codes briefly introduced here, which can be considered as transport codes of hadrons within the nucleus. The INC study as a two-body interaction propagated through the nucleus, was first investigated by Goldberger in 1948 by using a two-dimensional Monte-Carlo model [125]. A more realistic study was the one of Metropolis in 1958 [126], considered as the pioneering of all the later produced codes.

---

[2] Self-consistent mean field and a Pauli-blocking treatment are introduced in models of the BUU-type [121] and VUU-type [122]. QMD quantum approximations are presented e.g. in refs. [123, 124]. Nevertheless their running times are up to three orders of magnitude larger than that of the Bertini-code.

Typically there are two types of INC codes, depending on the treatment of the nuclear medium: the *Bertini-like* codes, where the nuclear density is considered continuous; and the *Cugnon-like* codes where the nucleons are treated individually from the beginning. Common to all modern codes is the semi-classical treatment: particle's (and quasiparticle's) positions and momenta are defined according to relativistic classical mechanics. The nucleon-nucleon NN interactions are defined from free-NN cross sections. The cascade is initiated by the projectile's nucleon hitting somewhere on the target sphere (only the radial density dependence is considered). The first NN impact triggers the cascade and it runs until some cutoff condition is fulfilled.

5.1.1 Bertini-like codes: ISABEL

The Bertini code [127, 128] was a successful code at its release time, and it is still a widely used option in modern implementations as the LAHET-Code-System[3]. The nuclear density used is uniform and step-like with up to 3 divisions. It includes the treatment of nucleon-nucleus interactions ($\leq$3.5 GeV) and pion-nucleon ($\leq$2.5 GeV). The collision between the initial nucleon and the nucleons in the Fermi-sea produces *cascade particles*, which continue the cascade on. Those *cascade particles* can only further interact with the Fermi-sea (which the model treats as continuum). It is a fast-code and it has been considered adequate for most of design applications during many years. Unfortunately it cannot be applied to nuclear projectiles.

Improving the original Metropolis scheme, the VEGAS code [131] was developed in 1968. A further generalization is the ISABEL code [132, 133]. The nuclear density is step-like with up to 16 divisions and includes diffuse bounaries. The target and projectile nucleons are considered within a potential well, and their momentum distributions are defined according to that of the degenerated Fermi gas. At a given time interval defined by the velocity and mean-free-path defined by free-NN cross sections, the situation is examined. In case of no interaction, the particle goes on. In case of interaction, it can be either elastic (definition of the new four-momentum vector) or inelastic ($NN \leftrightarrow N\Delta$ and $\Delta \leftrightarrow \pi N$). In the latter case the pion is propagated till it is absorbed in a recombination $N\Delta$. After each step the number of cascade nucleons increases and so the density is depleted. The density rearrangement is treated in several ways. The later versions allow the interaction among cascade-particles, in addition to collisions of cascade particles with nucleons of the Fermi-sea. Pauli blocking, the only quantum restriction, is taken into account excluding the cascade particles with an energy below the Fermi level. The cascade continues till the most energetic cascade particle falls below a certain energy level, or it has left the nucleus before. The final energy is evaluated according to the sum of the

---

[3] The original HETC code developed at Oak Ridge National Laboratory, is a transport code designed for nucleon and meson transport [129]. The HETC version from Los Alamos National Laboratory was further developed for the transport of nucleons, pions and muons [130]. It is named LAHET, and a LAHET based system of related codes is the LAHET Code System. The neutrons are treated separately within the system according to a certain energy threshold. LAHET itself may be used to calculate cross sections: the transport is avoided, and the projectile interacts directly with the target material. After the initial calculation the result goes through the evaporation or multifragmentation steps.

hole and particle energies which fall below the cutoff energy. The cutoff is selected as the Coulomb barrier plus two times the binding-energy (all above the Fermi energy).

ISABEL can treat nucleon-nucleus and nucleus-nucleus interactions. The ion-ion collisions are performed by selecting first the overlapping areas of the nuclei, and then the initial interacting nucleons. The overlapping nucleons can interact with the Fermi-sea of the partner nucleus. The running time of the code is some 5-to-10 times longer than that of the Bertini-code. ISABEL includes diffuseness, what makes it well suited for peripheral reactions studies. But the nuclear matter compressibility is not included, so it cannot deal with central collisions. This drawback does not affect our fragmentation study.

5.1.2 Cugnon's code

The Cugnon-like codes are characterized by the fact that they follow all the nucleons present in the target and projectile during all the INC process. The RELA-code (1980) described the collision of heavy relativistic ions, considering the nuclei as a free Fermi gas. The improved PNUC-code [134] was restricted to nucleon-nucleus collisions. In that code the nucleons are described as a Fermi gas within a potential well. The updated version is known as the standard INC-Liège code INCL [55]. In this version, known typially as *version 3*, all the particles are moving around, and when two of them fall below a *minimal distance*, defined as the radius of a sphere with area equal to the particle-particle cross section, the collision happens. The elastic and inelastic treatment is conceptually the same as ISABEL. For NN-collisions the free cross sections are used above 400 MeV. Below that energy in-medium correction are used. The resulting position-momenta of the interaction are calculated, and the collision is allowed only if the phase-space is not yet occupied by another particle. In that way the Pauli blocking is included. The particles leave the nucleus if they reach the bound, i.e., no refraction happens; in 2001 a new version (INCLv4) is under development to a realistic surface of the nuclear potential.

Actually, an INC-code follows till a final de-excited residue is produced, but it is stopped at a certain time before. The reason for including that halt-condition, is that the evaporation pattern depends sensitively on the level density from complicated configurations, different from the single-particle motion to which INC implicitly corresponds. So the description would not be realistic. What it is of interest is that the INC includes a clear different time development in the excitation energy: a very fast rising when the projectile triggers the cascade and the energy is released; a fast decreasing step, when the particles are thrown away from the nucleus by fast collisions; and a third slow decreasing phase, when particles leave the nucleus after many collisions. The last process may be easily identified with the evaporation stage. The stopping time is defined by the point where the decreasing slopes change: some 18 fm/c for 1.2 GeV p+Fe or 25 fm/c for 1.2 p+U. The evaporation is better described by a statistical treatment, but it is interesting to recognize a process that appears naturally in the model.

The energy of the pre-fragment is the difference between the final kinetic energies sum, referred to the potential well, and that of the ground state; i.e., the kinetic energy of a Fermi gas with the final number of nucleons, again referred to the potential well.

5.2 Particle emission and fission

The second part of the reaction, the de-excitation of the pre-fragment, is based on the statistical model. Assuming that the pre-fragment resulting from the INC is thermalized, one deals with a compound nucleus, as proposed initially by Weisskopf [45]. The excitation energy is dissipated by either particle emission (*evaporation*) or fission. In the study we will neglect multi-fragmentation channels, having a minor role in the population of the residual production we have measured. The nucleus may evaporate single nucleons as well as α-particles, and light-nuclei (deuterium, ^3He, ^4He, ...). The de-excitation chain continues while there is available excitation energy, assuming that at each step the residue is a compound nucleus. This method, sampling the channels according to their probabilities, was applied first by Rudstam [135]. The probability $P(\omega)$ of a certain de-excitation channel ω in each de-excitation step n, is evaluated as the ratio of its width Γ_ω^n over the sum of the widths of all present channels

$$P(\omega)^n = \frac{\Gamma_\omega^n}{\sum_\Omega \Gamma_\Omega^n} \tag{5.1}$$

Here we will refer to results of the ABLA code [47, 80], but the basic concepts are general to most of the evaporation codes[4].

The particle decay widths are obtained in the basis of the statistical model, as proposed initially by Weisskopf. The original description only preserves the energy of the compound nucleus, while the conservation of the angular momentum was added latter by Wolfstein [140] and Hauser-Feshbach [48]. All those results are reviewed e.g. by Ericsson [49] and Darrah-Thomas [141, 142]. Following the description of the later we can write the width of a certain channel by integrating in energy the probability of emission from a certain initial compound nucleus with energy E_i and momentum J_i to a final compound nucleus characterized by E_f and J_f

$$\Gamma_\nu = \int_{S_\nu - B_\nu}^{E_i - B_\nu} \left[\sum_{J_f} \frac{1}{2\pi} \cdot \frac{\rho(E_f, J_f)}{\rho(E_i, J_i)} \cdot \sum_{S=|J_f - s|}^{|J_f + s|} \sum_{l=|J_i - S|}^{|J_i + S|} \tau_l(u) \right] du \tag{5.2}$$

where $\rho_{i/f}$ is the level densities of the initial/final states respectively, s the spin of the emitted particle, and l the angular momentum between the residue and the emitted particle; B, S refer to the Coulomb barrier and the separation energies respectively; τ is the transmission coefficient, given by the penetration through the potential barrier for the inverse-emission process, i.e. particle capture. This coefficient is usually calculated using the capture cross sections. The energy limits may be clearer considering the value $u = E_i - B_\nu - E_f$.

The possibility to evaluate Γ_ν depends on the simplifications we can apply to equation 5.2. Considering the sharp cut-off approximation in the evaluation of the capture cross sections, and the effective interaction radius R of the residue ($\sigma \approx 2\pi R^2$), we can

---

[4] The evaporation built-in code in the LAHET-code-system is EVAP [136] . The code is developed after the work of Dostrovsky [137]. The fission used in the system can be selected within two models: The RAL model [138], allowing fission for Z≥71; and the ORNL model [139] for Z≥91.

reduce the calculation of the transmission coefficient τ_l . If the level density is described as $\rho(U) \propto e^{(aU)^{1/2}}$ and additionally the nuclear temperature as $U = aT^2$, where a is the *level density parameter*, we can integrate equation 5.2, resulting in [143]

$$\Gamma_\nu \approx \frac{2m_\nu R_f^2 g_\nu T_f^2}{\hbar^2} \frac{\rho_f(E^* - S_\nu - B_\nu)}{\rho_i(E^*)} \tag{5.3}$$

where ν refers to the particle type, being S its separation energy, m its mass, g its spin degeneracy, B the Coulomb barrier; E^* is the excitation energy of the initial compound nucleus and R its radius; T is the temperature of the residual nucleus, and $\rho_{i/f}$ is the level density which describes the residual and the initial compound nuclei, respectively.

Note that this expression is obtained by neglecting the energy/momentum dependence of the τ coefficients. The full treatment of the total angular momentum may be quite cumbersome. Fortunately the angular momentum values involved in relativistic ion-ion reactions are low as demonstrated in refs. [47, 108, 144] and the simplification justified. However, the evaluation of the level densities in equation 5.3 can include all the dependencies on the momentum, i.e. $\rho(E, J)$ as described in ref. [144].

The Coulomb barrier in the evaporation of protons and α particles are parameterised as

$$B_\nu = \frac{e^2}{r_o} \cdot \frac{Z_\nu \cdot (Z - Z_\nu)}{(A - A_\nu)^{1/3}} \tag{5.4}$$

where $A(Z)_\nu$ refers to the particle mass (charge), e is the charge unit, and $r_o = 2.08$ fm; the barriers are lower than the usual barriers to effectively include the tunnelling effect, see ref. [145].

The fission width is described by using the Bohr-Wheeler model [50] according to the Moretto formulation [51]

$$\Gamma_f = \frac{1}{2\pi} \frac{1}{\rho(E_i, J_i)} \int_0^{E_i - B_{sad}} \rho_{sad}(E_i - B_{sad} - u, J_i) du \tag{5.5}$$

where *sad* refers now to the saddle point, and B_{sad} is the fission barrier with rotational energy included. The same description of the level density as given above, allows to obtain the result [143]

$$\Gamma_f \approx \frac{T_f}{2\pi} \frac{\rho_f(E^* - B_f)}{\rho_i(E^*)} \tag{5.6}$$

where $E^* - B_f$ is the energy above the saddle point, B_f the fission barrier as described in ref. [146], and again the level density ρ refers to the residue and to the compound nucleus as before. Additionally the barrier may be influenced by the temperature T_f of the residue.

The ABLA code includes additionally the microscopic effects of shells and pairing in the level density description, as described in ref. [47]. Also the nuclear collective effects, both vibrational and rotational, are described in ABLA, according to ref. [80]. All those effects are parameterised within the description of the *level density parameter*, that relates the nuclear temperature T and energy.

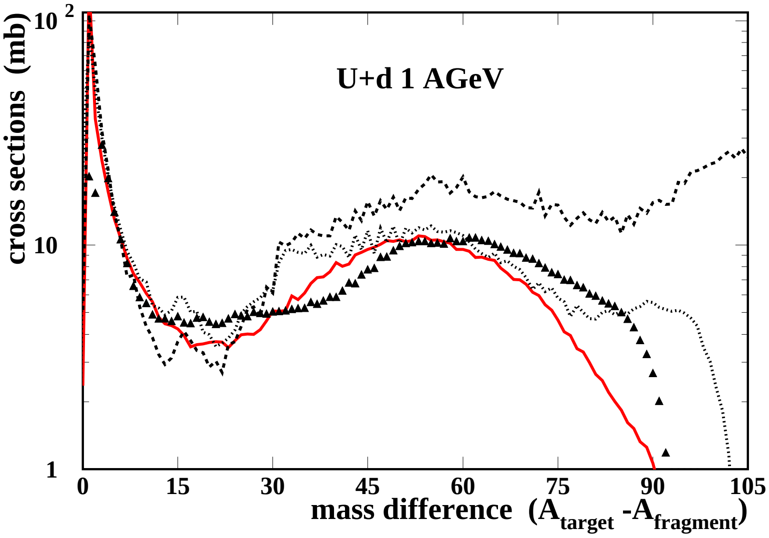

Figure 5.1: Isobaric distribution of the production cross sections of the reaction $^{238}U(1\ A\cdot GeV)+d$, measured in this work. The lines corresponds to the calculations done with the codes ISABEL+ABLA (full line), ISABEL+EVAP (thick-dotted line) and INCL+EVAP (thin-dotted line). The INCL code was modified to include the matter distribution of the deuteron. See the text for details. The fluctuations in the curves are only due to statistics of the number of events.

The nuclear dissipative effects during the fission process are accounted for in the code as described in refs. [98, 99, 100]. The result of this *nuclear friction* is a *transient-time* for fission after the formation of the compound nucleus. In that way the particle emission prior to fission is enhanced.

Also γ-ray emission is possible, and its parameterisation is similar, see ref. [145]. The channel is always open if no transitional restrictions appear. Usually only giant resonances are of importance, and the electric dipole resonance E1 (GDR) gives the largest contribution. For nuclei with masses A∼100-200 the $\gamma-$emission is known to exceed the neutron-emission only for excitation energies below 20 KeV above the neutron-threshold [147]. It results also that the neutron to γ-ray emission is dominated by particle emission. Only below the nucleon binding energies or in case of strongly momentum-restricted available states (nearly the reaction energy threshold), the γ-ray emission competes appreciably with particle emission.

5.3 Comparison with standard codes

The measured data for the reaction $^{238}U(1\ A\cdot GeV)+d$ can be compared with the result of the standard codes describing relativistic heavy-ion reactions. The calculated values are the result of a complex processing by using a two-step model. Typically one code developed for each reactions step. Any discrepancy of the results of the codes with the measured data can be argued as due to one or the other reaction step description. Due to the inter-playing of the codes, it is not obvious to decide that a certain code partner is working realistically while the problems come from the second partner. By using the results from different code calculations and data from different heavy-ions reactions, one can review the performances of the available theoretical descriptions and decide about the most realistic. The first part in our discussion will be the selection of the evaporation-fission code. We are going to show how the results from one of this codes, ABLA, is realistic and well suited for our study. Then we will settle on that code, and we will discuss about the INC performance.

The aim of this comparison is not to obtain a numerically-compatible reproduction of the results, but to discuss about the effects that characterize best the ^{238}U-deuterium system. Since the deuterium is already a nucleus-nucleus collision and for the sake of simplicity, here we will refer to the results of the $^{238}U(1\ A\cdot GeV)+p$, whose fragmentation has been measured recently [37], and for which several INC-codes can be applied.

5.3.1 Evaporation step

In figure 5.1 we show the isobaric distribution of the measured cross sections in the reaction $^{238}U(A \cdot GeV) + d$. The results of the calculations performed by different combinations of the INC codes and evaporation-fission codes are plotted: ISABEL+ABLA (full line), ISABEL+EVAP (thick-dotted line) and INCL+EVAP (thin-dotted line). In the case of deuteron reactions only the ISABEL code allows to obtain a result, since INC-L can only deal with nucleon-nucleus collisions. Nevertheless, the original INC-L was modified to include the deuterium matter distribution [148]. We observe immediately that the two descriptions using EVAP show strong differences respect to the measured distribution. In figure 5.2 we show the results for the reaction of $^{238}U(A \cdot GeV) + p$ with measured data from ref. [37]. The lines correspond to calculations done with the codes ISABEL+ABLA (full line) and ISABEL+EVAP (dotted line). In this case we observe the strong differences of the two calculated results, being ABLA much more realistic.

In figure 5.3 we show isotopic production cross sections of $_{91}Pa$, $_{84}Po$ and $_{74}W$ from the reaction $^{238}U(1\ A \cdot GeV) + d$. Also the results of the calculation with the codes ISABEL+ABLA (thick-full line), ISABEL+EVAP(dotted line) and INC-L+EVAP (thin-full line). The different behaviour of the two evaporation codes is clearly seen. Close to the projectile the different descriptions are rather good. But for lower masses, when the excitation energy is higher and the evaporation is strongly defining the result, the ABLA description performs much better. The shape, width and the maximum-production position of the isotopic distributions are realistically reproduced. However EVAP is not able to accomplish for those characteristics. We have also studied the less complex system $^{238}U + p$, and comparing with the measure data we found that the results from the codes behave as seen for the deuteron.

We observe that independently of the INC-code used, the overall performance of the code results depends strongly on the evaporation-fission step. Our conclusion from these

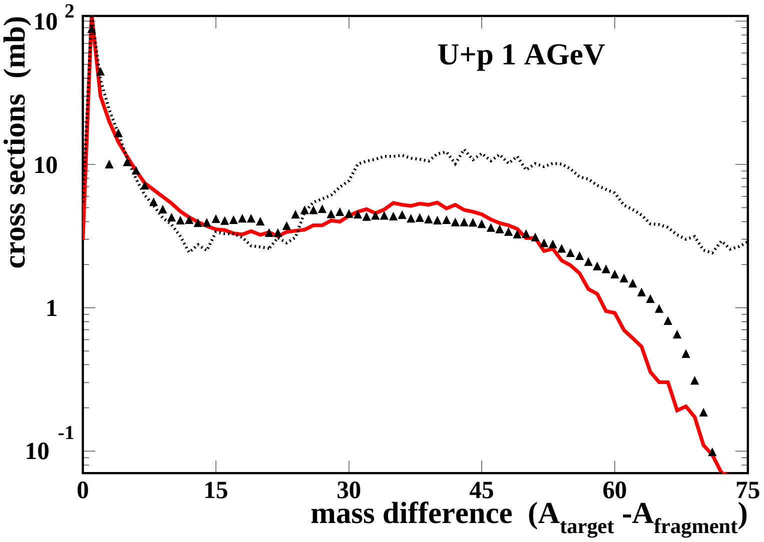

Figure 5.2: Isobaric distribution of the production cross sections of the reaction $^{238}U(1\ A\cdot GeV) + p$, measured in ref. [37]. The lines corresponds to the calculations done with the codes ISABEL+ABLA (full line), ISABEL+EVAP (dotted line). The fluctuations in the curves are only due to statistics.

comparisons is that the ABLA code is able to provide a realistic description of the second reaction step. In this work we do not investigate further the details of the evaporation step, and we use the ABLA description which has been used successfully to describe the results of other heavy-ion reactions [80, 149]. In the following sections we will concentrate in a detailed description of the first reaction step.

5.4 A simple INC model

Any realistic model includes many correlated parameters. The complexity depends on the type of physics described and it is reflected in the time needed to provide event-outputs. the complexity is also reflected in the difficulty to extract information of the influence of simple parameters. We propose the following basic questions to be investigated

- the geometrical image of the impact as description of the deuteron collision, based on a realistic deuteron matter distribution
- the excitation energy deposited in the interaction
- the influence of the nuclear shape
- the influence of the free-NN cross sections values

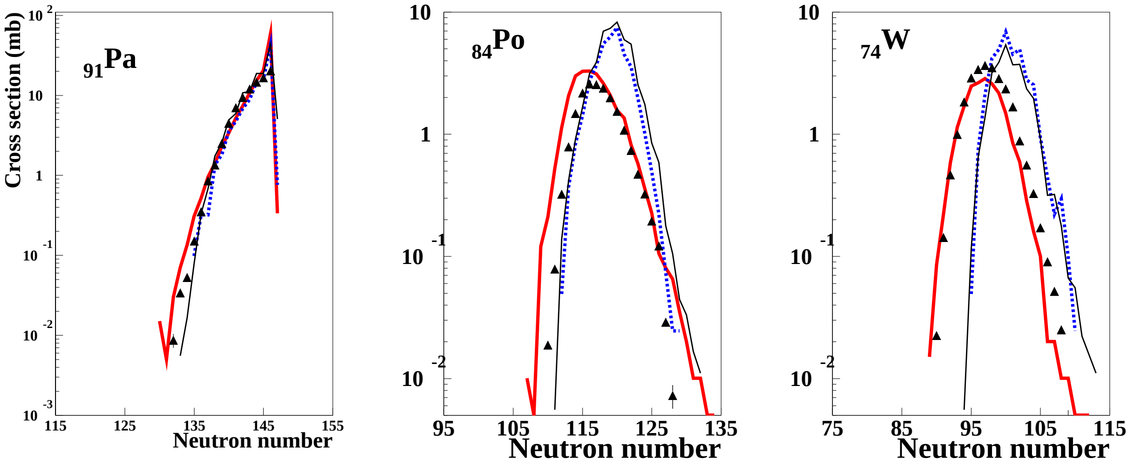

Figure 5.3: Isotopic distributions of the production cross sections of elements $_{91}Pa$, $_{84}Po$, and $_{74}W$ in the reaction $^{238}U(1\ A\cdot GeV)+d$, as measured in this work. The lines corresponds to the calculations done with the codes ISABEL+ABLA (thick-full line), ISABEL+EVAP (dotted line) and INCL+EVAP (thin-full line). The INCL was modified to include the matter distribution of the deuteron. The fluctuations in the curves are only due to statistics. See the text for details.

Only the ISABEL code allows to include ion-ion reactions[5], in particular collisions induced by deuterons. Unfortunately, as in most of the codes, the parameterisation of the matter distribution is based on general trends and does not include dedicated cases, as the deuterium which presents a low density of mater-distribution. On the other hand, a point which is never found implemented in these codes, is the actual shape of the nucleus. That discussion is of importance in order to compare reactions with ions as ^{238}U and ^{208}Pb, where the shapes are very different. Since the available standard codes are difficult to modify, in order to treat these alternative questions, we have developed a simplified INC code.

We propose to use the Glauber ideas [150] in the high energy domain. The collision of the projectile is described in a semi-classical frame. The path length through the target nucleus and the mean free path define the number of nucleons hit by the projectile. Relating the number of abraded particles to the NN collisions we can define both the pre-fragment mass and atomic numbers and the pre-equilibrium emission. However, we do not describe the kinematic properties of that pre-equilibrium emission. With the model we only want to describe the pre-fragment and its excitation energy. In principle this is a very crude model, and we do not expect to describe the cascade process in detail. The advantage of such a model is that some general aspects of the collisions can be studied within a frame where all the inputs and their interplay are described on a simple basis.

---

[5] The code admits ion-ion reactions but its capabilities are limited and difficulties arise when two heavy ions are involved, see e.g. [82].

We describe first the nucleon induced reactions with our model. The comparison with the data measured for the reaction $^{238}U(1A \cdot GeV) + p$ [37] will allow to determine the performance of the model. The model will be extended to a geometrical impact of two nucleons, in order to describe the deuteron collision.

5.4.1 Abraded nucleons: pre-equilibrium emission

Our model describes the pre-fragment resulting from the collision of a nucleon in a target nucleus. We propose to describe the collision by relating the number of abraded particles to the number of nucleons seen by the projectile in its path through the target nucleus. The model assumes that a nucleon traversing the target will abrade all the particles it encounters. The projectile trajectory within the nucleus is approximated as linear. It has been tested in full INC calculations, that the average number of abraded particles η is maximum for the smaller impact parameters. Actually it is consistent with the dependence of η with the length of a rectilinear path of the nucleon through the nucleus [134, 151] [6].

The definition of the energy deposition into the target, i.e. the excitation energy of the resulting pre-fragment, is based on the particle-hole excitations as proposed in ref. [47]. Using that result as reference, we have modified it in order to better represent the measured data. We will see how this simple model describes approximately the measured isobaric and isotopic cross section distributions.

To define the number of abraded particles in our model, we will study the number of possible NN-collisions for a nucleon traversing the target nucleus, n_o. The quantity n_o contains two dependences: the length of the path followed by the projectile l; and the mean-free-path of the nucleon within the target medium λ. The mean-free-path λ is calculated according to $\lambda^{-1} = \rho \cdot \sigma_{NN}$, where $\rho = 0.17\ fm^{-3}$ is the nuclear density value and σ_{NN} is the averaged NN interaction cross section. In realistic INC calculations it was found that n_o is below the value obtained by the approximation of ρ given here [134]. The reasons are the change of σ_{NN} with the kinetic energy, the Pauli blocking effect, and also the Δ production which has a lower total cross section.

The averaged NN interaction cross section σ_{NN} was adapted to the nuclear medium to account for Pauli-blocking effects and nuclear field as proposed in ref. [152]. The free-NN cross sections are corrected to in-medium values, based on a zero-temperature Fermi gas, and depending on the energy of the nucleon. The particular correction used for the energy dependence is demonstrated to influence little the result little [153, 154]. The more realistic calculation by using anisotropic NN cross sections instead of isotropic ones, introduces a difference below 5% in the results [155]. The temperature can also be included in the Fermi gas model, and it results that for ~ 30 MeV above the Fermi level the temperature dependence vanishes [155]. For a comprehensive review see ref. [54]. The free-NN cross sections were taken from ref. [156]. Other references for the free-NN cross sections are [157, 158, 159]. We have found some discrepancy among the values. We will

---

[6] Actually most of the codes assume rectilinear paths in between two collisions. That is the same as disregarding the potential gradient within the nucleus. Some codes, by dividing the potential in zones, include refraction in between two zones to model that effect.

discuss the possible influence of those differences later on this chapter. The values from different isospin combinations are averaged as follows

$$\sigma_{NN} = \Gamma \cdot \frac{Z \cdot \sigma_{ip} + N \cdot \sigma_{in}}{A} \tag{5.7}$$

where n/p stands for target neutron/proton respectively, and $i = n, p$ for the nucleon projectile type. This average is the particular case of the general target-projectile average[7] proposed by Glauber [150]. Γ is the in-medium correction factor, as defined in the references above. The average free-NN cross section for nucleons at 1 $A \cdot GeV$ (kinetic energy) is 44.0 mb, and the in-medium factor 0.96 [54]. The resulting mean-free-path is $\lambda \sim 1.34$ fm.

The path length l is calculated by considering the impact-parameter dependence of the trajectory of the projectile nucleon traversing the target. To introduce the diffuseness in the treatment, the length is folded with a Fermi-like distribution and integrated along the collision path

$$l = \int \frac{1}{1 + e^{\frac{r(z)-R}{d}}} dz \tag{5.9}$$

where $R = r_o \cdot A_T^{1/3}$, $r_o = 1.16$ fm, and $d = 0.57$ fm, from ref. [160]. This procedure extends the interaction radius of the target to the diffuseness region, but weighting the *density*, and preserving the volume of the nucleus.

The ratio $n_o = l/\lambda$ provides the average number of collisions for a given impact parameter. To obtain the number of actual collisions η, and the number of abraded nucleons within our model, we introduce fluctuations by folding the result n_o with a Poisson distribution, being the former result n_o the distribution parameter. The Poisson distribution was found to be well reproduced by the collisions observed within realistic INC calculations [134].

The N/Z ratio of the abraded nucleons is defined according to the *hyper-geometrical* model [46]. No isospin difference is included is our model considering that the nucleons are fully uncorrelated[8]. This approximation has demonstrated to perform better than other approximated evaluations[9]. Any additional interaction of the hit particles, producing the so called *final state interactions*, are neglected, and the projectile absorption possibility disregarded. Also the inelastic channels, with the formation of Δ resonances and the possible formation of different nucleons, are not considered (see section 4.6).

The result of the calculation obtained for the reaction $^{238}U(1\ A \cdot GeV) + p$ can be seen in figure 5.4-(a), where the mass distribution of the pre-fragments is plotted. It can be

---

[7] The average NN cross section for a given target T and projectile P is defined as

$$\sigma = [(Z/A)|_T \cdot (Z/A)|_P + (N/A)|_T \cdot (N/A)|_P] \cdot \sigma_{ii} + [(Z/A)|_T \cdot (N/A)|_P + (N/A)|_T \cdot (Z/A)|_P] \cdot \sigma_{ij} \tag{5.8}$$

where σ_{ii} refers to the proton-proton or neutron-neutron collision, and σ_{ij} refers to the proton-neutron collision.

[8] Only the N and Z numbers of the target are considered, as well as the number of abraded nucleons. The ratio Z/N is chosen randomly within that combinatorial distribution.

[9] Other possibilities are the conservation of the Z/N ratio of the compound nucleus or the estimation from the giant-dipole resonance zero-point oscillations. See the discussion in ref. [47].

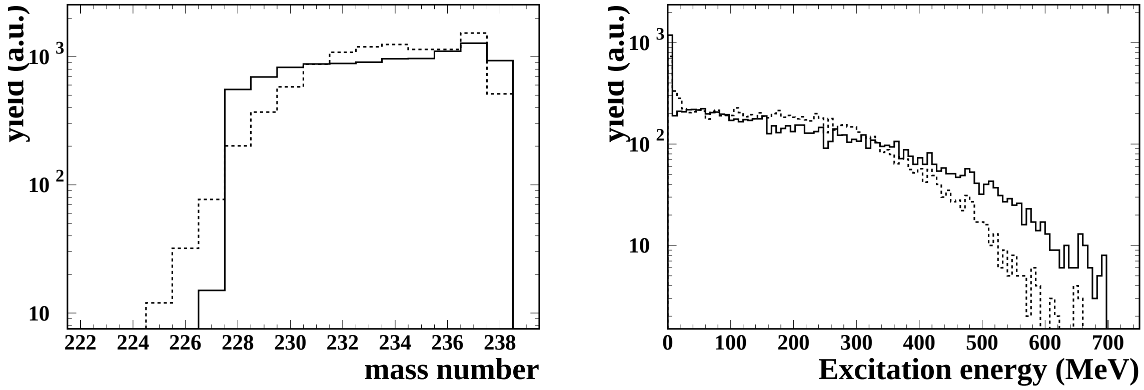

Figure 5.4: Distribution of mass (left) and energy (right) for the pre-fragments as resulting from the calculations by using the ISABEL code (dashed line) and the model we propose in this work (full line) for the $^{238}U(1\ A \cdot GeV) + p$ reaction.

seen that for the more central collisions, our model (full line) overestimates the number of abraded particle when compared with the ISABEL result for the same reaction (dashed line). On the other hand the pre-fragment mass distribution of ISABEL is wider, what is probably due to the final-state interactions included in the code.

5.4.2 Excitation energy

The evaluation of the excitation energy distribution used in this model is similar to that presented in ref. [47]. The single particle-hole excitation energies in a Woods-Saxon potential, provides a simple relation for the distribution of the excitation energy of a nucleus, in the case of a nucleon was removed. The result can be extended to n-particles by convoluting the single-nucleon distribution. Using this model we disregard the inelastic channels. It was found [149] that the average value of the energy-per-abraded-nucleon necessary to describe the data from ion-ion reactions, was ~ 2 times the value resulting directly from the model, i.e. $\sim 2 \cdot 13.5$ MeV. The difference was related to the lack of *final-state-interactions* within the model. That description was demonstrated to be well suited in the study of several relativistic ion-ion reactions [47, 81, 80, 98, 106, 120, 149, 161] .

Using the mentioned model as starting point, E^* was adapted additionally to better fit the measured data. The distribution is modified by a certain *enhacement factor*. We found that only making this enhacement factor, always bigger than 2.5, dependent on the number of abraded particles, the results of the calculation can reproduce the measured data. (see the discussion in section 5.4.7). The result of the pre-fragment excitation energy distribution obtained for the reaction $^{238}U(1\ A \cdot GeV) + p$ can be seen in figure 5.4 resulting from this INC model (full line) and from the ISABEL code (dashed line). We see that our model underestimates the range 100-300 MeV, while it populates more the high energy tail.

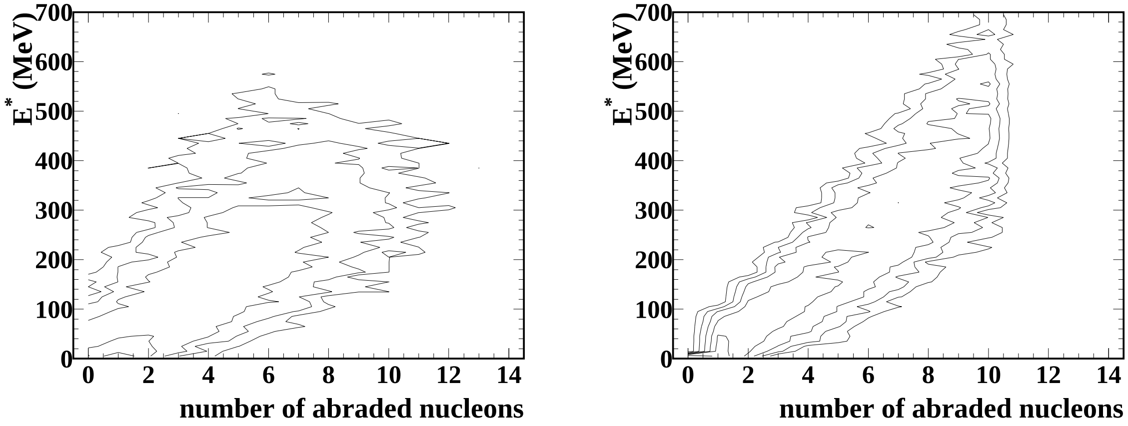

Figure 5.5: Pre-fragment distribution of the excitation energy as function of the number of abraded nucleons for the reaction $^{238}U(1\ A \cdot GeV) + p$. The contour lines join equal yield points, in logarithmic scale. The left panel shows the result from the ISABEL-code. The right panel shows the result from the model proposed in this work.

5.4.3 Nucleon-nucleus collision description

In figure 5.5 the contour plots corresponding to the excitation energy E^* as a function of the number of abraded particles η are shown, as calculated with the ISABEL code (a) and our model (b), for the reaction $^{238}U(1\ A \cdot GeV) + p$. The ISABEL description always produces wider distributions of E^* for a given number of abraded particles. Also, ISABEL limits more the energy E^* for high number of abraded particles: we see that for $\eta = 9$ ISABEL gives E^* values 200-450 MeV, while our model reaches 600 MeV. We can see also that for $\eta < 4$, the excitation energy in our model changes too fast, compared to ISABEL. All the differences found between the two INC codes will be reflected in the final distribution of the residues, since the space E^*-η determines the next step in the description of the reaction.

To describe the residual production resulting from the pre-fragment distributions obtained with the different INCs, we apply the evaporation code ABLA. An additional ingredient we have to add in the description of the pre-fragments is the angular momentum of the nucleus, resulting from the collision. We have evaluated the total angular momentum according to the description for heavy-ion collisions as given in ref. [144], depending on the number of abraded particles.

The isobaric distributions of the production cross sections for the residues resulting from the calculation with ISABEL and our model can be seen in figure 5.6, for the reaction $^{238}U(1\ A \cdot GeV) + p$. The overall result from ISABEL (full line) is rather good. However the tail of the distribution, the production of lighter masses, decays too early.

That can indicate either a small energy deposition for the smaller impact parametes

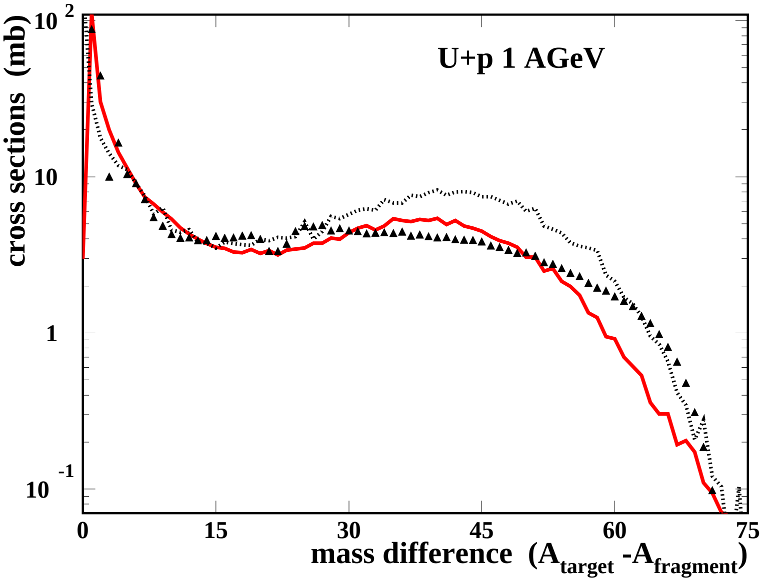

Figure 5.6: Isobaric distribution of the production cross sections for the reaction ${}^{238}U(1\ A\cdot GeV)+p$. The data from ref. [37], are compared with the ISABEL based calculation (full line), and also the result based on the model proposed in this work (dotted line).

in ISABEL, or an inadequate description of the second part of the reaction[10]. ISABEL gives about 41 MeV as average excitation energy per abraded nucleon.

The result from our model (dotted line) is satisfactory, considering the simplicity of the assumptions. The initial slope $\Delta A < 10$ shows smaller cross sections than the measured ones, indicating a too high energy deposition for the most peripheral collisions. It was carefully tested that small modifications in the enhacement factor applied to the excitation energy, drive to drastic changes in the distribution. If the energy per abraded nucleon is increased slightly, the initial decay is faster and produces a big deep around $\Delta A = 11$, while the bump around $\Delta A = 45$ is displaced to higher values, and the tail elongates to much lower masses. The reduction of the energy, produces the opposite effect. Whereas the initial decay of the isobaric production changes slightly, the bump observed at lighter values moves much faster with changes in the enhacement factor. The present result is the best compromise found to represent the overall trend.

The differences found in the INC excitation energy E^* distributions between the models determine the results we obtain. The higher range of values covered in our model helps to reproduce the whole mass range of the observed fragments. On the other hand the narrower energy distribution for a given pre-fragment (η value) is probably responsible for the bump observed around $\Delta A \sim 40$, since the energy is not enough to deplete that region.

---

[10] We insist in the not explored possibility of different reaction mechanisms present in the higher energy regimes.

5.4.4 Nuclear shape: deformation

With the present model we can investigate some feature of our system that cannot be extracted from the standard codes. The ^{238}U is a deformed nucleus, and we could expect some influence of the shape in the final pre-fragment distribution.

The ^{238}U nucleus is axially symmetric, prolate-type (cigar-like shaped), with two equal radii (~ 6.7 fm) shorter than the third one (~ 8.8 fm), the later being the symmetry axis. By using the simple description of the surface by spherical harmonics Y_{lm}, the nuclear shape can be described with dipole β_2 and quadrupole β_4 components. The nuclear radius R is parameterised as

$$R = R_\beta \cdot \left(1 + \sum_l \beta_l \cdot Y_{l0}(cos\theta)\right) \tag{5.10}$$

where θ is chosen relative to the the symmetry axis. Additionally, to preserve the volume, the next condition must be fulfilled

$$R_o^3 \approx R_\beta^3 \cdot \left(1 + \frac{3}{4\pi} \sum_l |\beta_l|^2\right) \tag{5.11}$$

The parameter $R_o = r_o \cdot A_T^{1/3}$ corresponds to the sharp-sphere radius, with $r_o = 1.16$ fm [160], with a value $R_o = 7.2$ fm for ^{238}U. The values of the deformation parameters are $\beta_2 = 0.2150$ and $\beta_4 = 0.0930$, as given in ref. [162].

The impact of a nucleon in a deformed shape has to be carefully described in order to fully cover all the possible relative orientations of the nucleus and the projectile. We have parameterised the impacts as follows[11]. First we select a random direction in space, in the frame of the nucleus, which defines a plane Π perpendicular to that direction . The intersection of the plane Π with the nucleus gives all the possible impact trajectories parallel to the selected direction, which are also perpendicular to the plane Π. The procedure to select the impact trajectory is firstly to define a plane Π and then a point in that plane, to determine the trajectory that passes through it. By a Monte-Carlo procedure the whole range of impact trajectories are scanned. In the case of a pure spherical nucleus this method is strictly equivalent to the usual impact in two dimensions, when the path only depends on the radius. The nuclear diffuseness is included by the same procedure described in equation 5.9.

The expected difference resulting from the calculation when using either the spherical or the deformed shapes is the possible enhancement of the number of collisions for the most peripheral impact parameters. That is possible due to the wider low-density region that defines the random orientation of the deformed nucleus, in the nuclear difuseness region.

In figure 5.7 we compare the path-length l distribution of the projectile nucleon inside the target nucleus, for the reaction $^{238}U(1\ A \cdot GeV) + p$, for spherical (full line) and a deformed geometry (dashed line) of ^{238}U. The result including the deformation (dashed line) differs slightly from the spherical case (full line). In particular there are no large

---

[11] This impact model was carefully discussed and coded together with J.Pereira (at USC-Santiago in 2001).

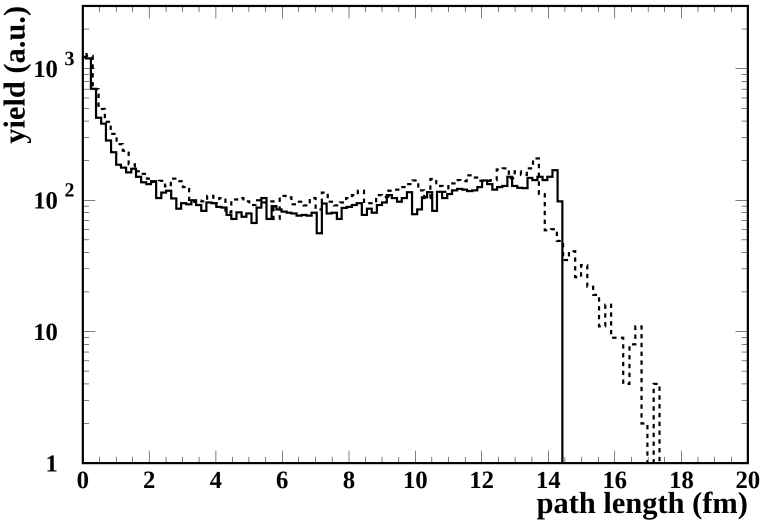

Figure 5.7: Distribution of the path length traversed by the projectile through the target including the shape deformation (dashed line) or not (full line), for the $^{238}U(1A \cdot GeV)+p$ reaction.

differences in peripheral collisions, $l < 2$ fm. The range of the path length values shows a maximum $l \leq 14$ fm, and a tail (till $l \sim 17$) in the deformed geometry. The values in the tail are given by the two radii in the elliptical case. Since the spherical radius has a value in between the two elliptical radii values, the maximum path of the spherical geometry lies in the tail of the deformed nucleus.

The prefragments calculated with the new parameterisation of the nuclear shape present a mass and energy distributions very similar to the one of the spherical case. The differences observed in the residual production are negligible. It means that the introduction of the actual shape of the nucleus will not change the distribution of the production cross sections of the reaction. This result can be understood if we consider that the mean-free-path is $\lambda \sim 1.3$ fm, and the average radius of the deformed shape is ~ 8.1 fm, according to the two radii mentioned above. The difference to the spherical radius ($\sim$7.2 fm) amounts ~ 0.7 times the value of the mean-free-path λ. This difference induces a similar number of abraded particles for both descriptions.

Since the INC models develop the nuclear processes within the target matter density, the distribution of that density is a parameter that, in principle, would induce differences between two nuclei with very different shapes. The difference were expected to modify the distribution of abraded particles and energy deposition in the most peripheral collisions. With our study we conclude that the deformation of the nuclear shape does not play a major role in the description, since it induces negligible differences in the pre-fragment distribution. Despite the result we have found, the question how deformation enters and changes a calculation of this type is not a commonly addressed topic. We have probed

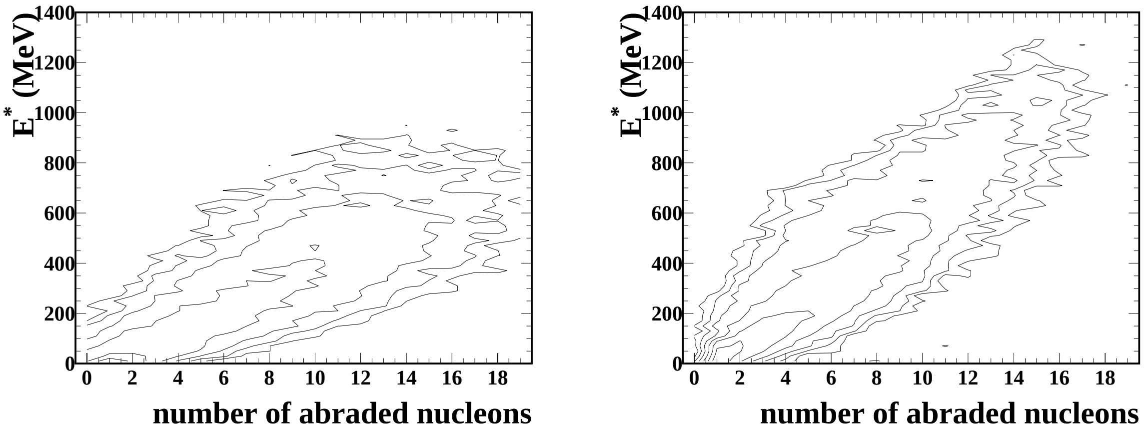

Figure 5.8: Excitation-energy vs number of abraded-nucleons for the reaction $^{238}U(1A \cdot GeV) + d$. The contour lines join the equal yield points, in logarithmic scale. The left panel is the result from ISABEL. The right panel is the result of the model presented in this work, with the description of the deuterium geometry as explained in the text.

that the shape is not decisive to describe this stage of the reaction.

5.4.5 The deuterium case: double impact of nucleons

The results from proton and deuteron interactions with ^{238}U at $(1\ A \cdot GeV)$ are similar in a wide range of masses, see figure 4.4. That can be understood because of the wide spatial distribution of the deuteron nucleus, consequently many events produce a single nucleon impact in the target. To investigate that effect we decided to parameterize the impact of the deuteron in a pure geometrical way, shooting the two nucleons successively. In each nucleon impact, the INC model proposed in this work for nucleon-nucleus interaction determines the resulting pre-equilibrium emission and the excitation energy deposited. The two sequential impacts add up their results into a unique excited pre-fragment.

To describe the impact, one starts by shooting the deuteron into the target, isotropically. The impact parameter defines the collision of the center-of-mass of the deuteron. Then, according to the mass distribution of the deuteron, one samples the position of one of the nucleons and its isospin. The impact point of the second is automatically defined by the center-of-mass constrain. To describe the deuteron matter-distribution one can select different models [163]: a Hulthén wave function, a repulsive-core wave function or a Gaussian-like distribution. Since we want to reproduce the trend of the interaction and not to make a detailed study among the different possibilities to define the matter distribution, we decide to use the Gaussian option, rather general and well adapted to parameterise. The main parameter of the distribution is the root-mean-square value of the nuclear radius. The measured charge-density distribution, model independent, in ref. [164] gives the value 2.10 fm from electron scattering data. The inter-play between the charged and neutral matter distributions is discussed in ref. [160]. For our purpose we use the former value within a three-dimensional Gaussian distribution to sample the impact positions of the two nucleons when hitting the target. This description determines completely the geometrical impact of the two nucleons of the deuterium.

Unfortunately the treatment is not completely self-consistent, since one has to allow the first nucleon to interact with the target, producing a whole cascade event; then the second nucleon triggers a second cascade. The tricky point in the model is to decide what is actually seen by the second nucleon: either the full target nucleus, or the pre-fragment resulting from the first cascade. We have chosen the second option to somehow include the perturbation that the nucleons cause to each other.

The resulting pre-fragment distributions from the calculation for the reaction $^{238}U(1\ A{\cdot}GeV) + d$ is shown in figure 5.8 (b), where the distribution of the excitation energy as function of the the number of abraded particles is represented. The contour lines join points with equal yield. The result from the ISABEL code is also shown in figure. 5.8 (a). We observe that ISABEL restricts the upper energy value to ~ 900 MeV, compared to the ~ 1200 MeV in our model. The energy distribution for a given number of abraded nucleons η is narrower in our model, particularly for $\eta > 10$.

The isobaric distribution of the production cross sections for the residues after the evaporation are shown in figure 5.9 for both INC cascades, ISABEL (full line) and our model (dotted line). The measured data are from this work. The defects of our model in the U+p description are inherited in the U+d result. The initial slope, underestimated, is the same for proton, and deuteron. The low energy deposition at lower impact parameters is reflected is the fast increase resulting in the bump around $\Delta A = 50$, and the shift in the maximum-production position. This trend is similar for ISABEL.

If the proton result could be reproduced more accurately, the bump would not appear; and the initial slope would be more realistic. But the model is limited to this result. The interesting discussion is that the simplest modelization of a double impact, i.e. the extension of the nucleon-nucleus impact, can be reproduced in its general trend, by geometrical considerations. The peculiarities in matter distribution are shown to be important in the INC description, and some cases like deuterium need a dedicated parameterisation. That dependence was also the result observed in the calculation of the total-cross section, see Appendix B.

The models reflect very realistically the mass range in which very peripheral collisions induce a single nucleon impact. We have measured with our model that up to 30% of the impacts involve a single nucleon of the deuteron. The common range of residual production from proton and deuteron induced reactions, results slightly longer in ISABEL ($\Delta A < 32$) than in our model ($\Delta A < 27$). The difference is thought to be due to the general mass density parameterisation that ISABEL uses, not reflecting exactly the deuteron distribution.

In figure 5.10 we show the isotopic distribution of the production cross sections of several elements measured in the reaction $^{238}U(1\ A{\cdot}GeV) + d$ (this work). The predictions made with ISABEL (thin-full line) are shown, together with the results obtained with the INC-model proposed (dotted line). We observe an overall good agreement of both codes with the measured data.

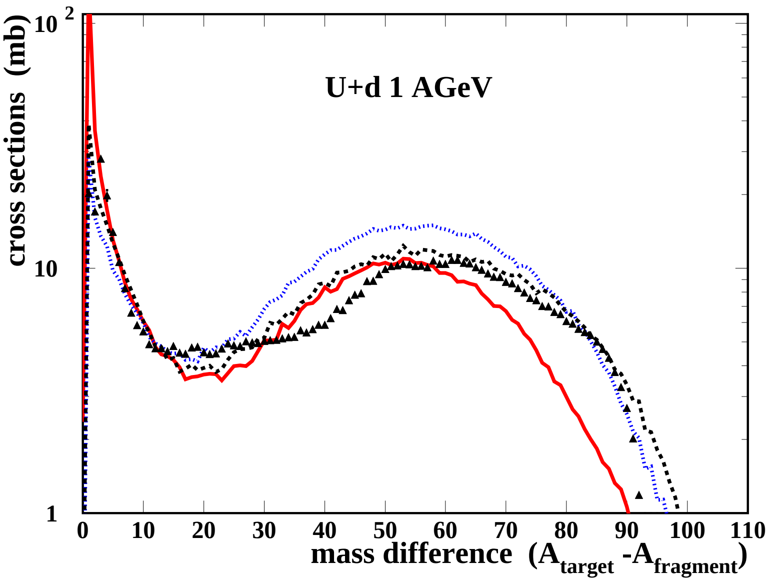

Figure 5.9: Isobaric distribution of the production cross sections of the residues of the reaction $^{238}U(1\ A \cdot GeV) + d$. The data were measured in this work. The result from a ISABEL-code based calculation (full line) and from the model proposed in this work (dotted line) are shown. The dashed-line corresponds to the same model than that of the dotted-line, but the energy of the second nucleon impact has been modified, see the text for details.

The production of residues close to the projectile is similar in both INC-models, showing the same shortcomings for Z=89-88, under-predicting the neutron-deficient side values. For elements with Z∼82-86 our model shows an extended tail (despite the statistical fluctuations) on the neutron-rich side, probably coming from low-energy excited pre-fragments that cannot evaporate that contribution. For elements with Z below 77, ISABEL underestimates the maximum and the neutron-rich side production, while our code keeps the description.

5.4.6 The influence of NN cross sections

An additional possible investigation with the model proposed, is the influence of the values used as NN cross sections, σ_{NN}. In the model this parameter determines the value of the mean-free-path λ. If σ_{NN} is reduced, λ increases and the excitation energy decreases, since we reduce the number of abraded particles. The increment in the σ_{NN} value produces the opposite effect.

Using the simplified model, we introduce a factor in the NN cross sections, to study the influence of that parameter in the final production. In figure 5.11 we show the results of calculations with σ_{NN} modified by an increment of 10% (dotted line) and a decrement of 20% (dashed line). We observe first that the influence of the change works as expected.

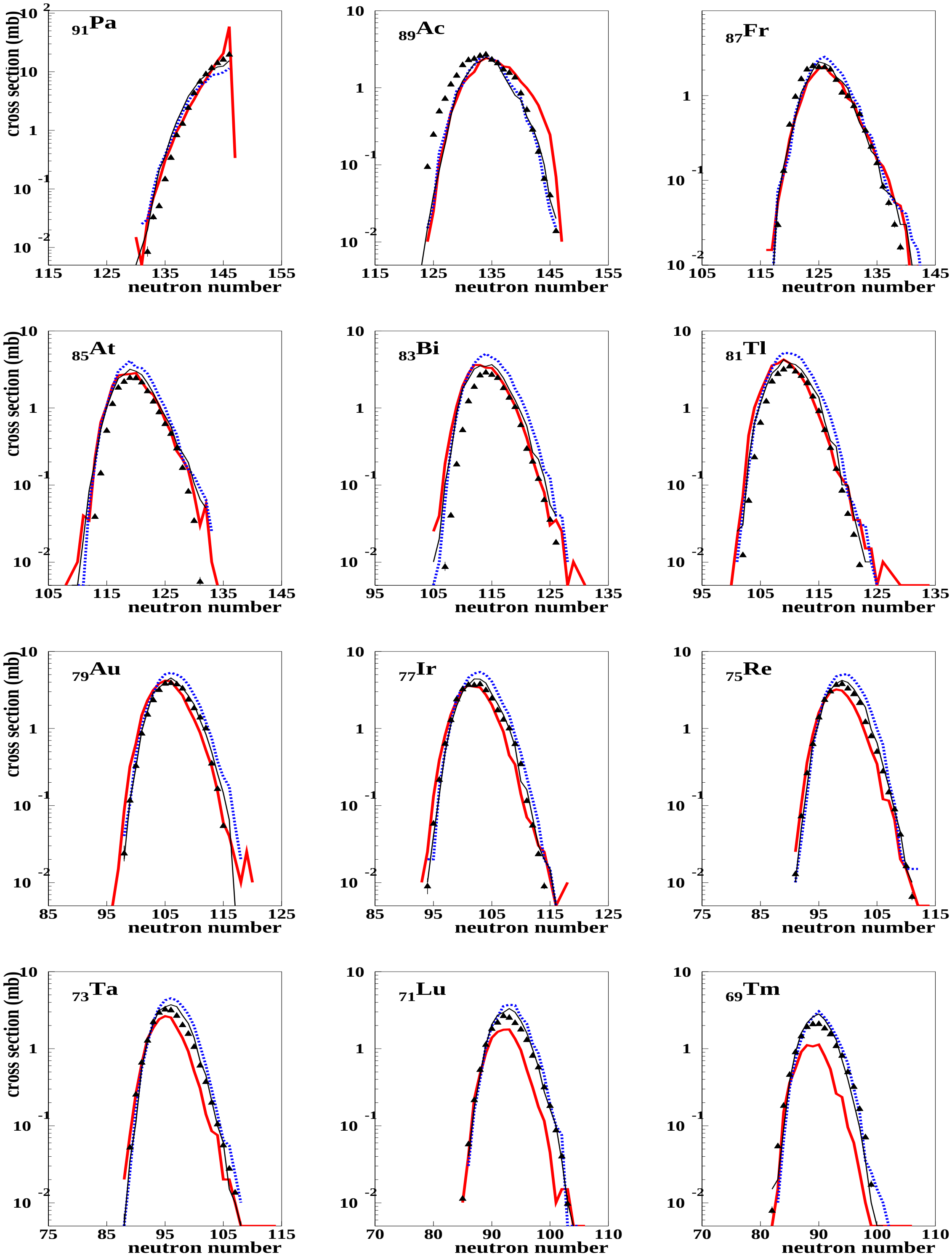

Figure 5.10: Isotopic production cross sections for some elements, of the reaction $^{238}U(1\ A{\cdot}GeV) + d$ as measured in this work. The lines are calculated with different INC-codes but the same ABLA-code for evaporation-fission: ISABEL-based calculations (thick-full line) and calculations based on the model presented in this work (dotted line). Within the latter model, a modification in the energy of the second nucleon impact produces the result plotted as thin-full line. See the text for details.

Second, a change of $\sim 10\%$ is not visible in the final result, what agrees with the discussion on the total reaction cross sections in refs. [165, 166] and commented in Appendix B. Third, a change in σ_{NN} leads to modifications only for the lower impact parameters. The result can be easily understood, since the number of collisions is higher and small changes in σ_{NN}, cumulate small differences.

On the other hand, the same σ_{NN} values are used also to evaluate the total reaction cross section σ_R, see Appendix B. Using a similar description of the mean-free-path as the one we have employed in our INC model, Ernst [167] calculates σ_R for nucleon induced reactions as

$$\sigma_R = 2\pi \cdot \int \left(1 - e^{\frac{-r}{\lambda}}\right) b \cdot db \tag{5.12}$$

where b is the impact parameter and r is the path-coordinate depending on b. The procedure is very similar to the description of the INC model above, but with a different aim. It is a result strongly based on Glauber's results [150], since the description in equation 5.12 is based on the definition of the transparency function with the mean-free-path depending on the σ_{NN} values. A more sophisticated method is the one described in Appendix B, also Glauber type. The results obtained for σ_R are realistic, as discussed in Chapter 4. To preserve the consistency with those results we took the same σ_{NN} values used to calculate the total reaction cross section.

5.4.7 The energy deposition and the abrasion models

In the model proposed the excitation energy E^* of the pre-fragment is made dependent on the number of abraded particles η. Following ref. [47], the excitation energy distribution associated to one hole after a particle ejection $P(E^*)$, is calculated within a diabatic model, considering that the spectator trajectories are not disturbed in the process, and the energy excess being caused by the presence of the hole. This assumption gives a linear relation for $P(E^*)$, depending on E^*. The result can be extended to η holes. The model provides an average value of E^* per nucleon ~ 13.6 MeV. This result was applied to the description of ion-ion interactions [80, 149]. It was found that the final-state-interactions, not accounted for in the model, make the value of E^* to double. With that increase, the particle-hole model for the excitation energy allows to describe the experimental results, within statistical reaction models.

We have used for our INC model the same prescription to define the excitation energy in the description of the interaction of ^{238}U with protons and deuterons at $1A \cdot GeV$. We found that the energy deposition had to be enhanced by a factor larger than in the former results about ion-ion collisions. Our model is very sensitive to the excitation energy parameterisation, and the best result was by applying an enhancement factor of the excitation energy E^* as function of η, varying from 2.5-to-3.75 for η=1-to-10 . That parameterisation produces the results discussed above for the reactions $^{238}U + p$ and the extension to $^{238}U + d$, see figures 5.6 and 5.9. The correction factor increases for more central collisions. Evidently the excitation energy model used, being well suited for more peripheral collisions, has to be corrected for lower impact parameters. Thais is connected to final-state-interactions, making the energy deposition higher for central collisions. On

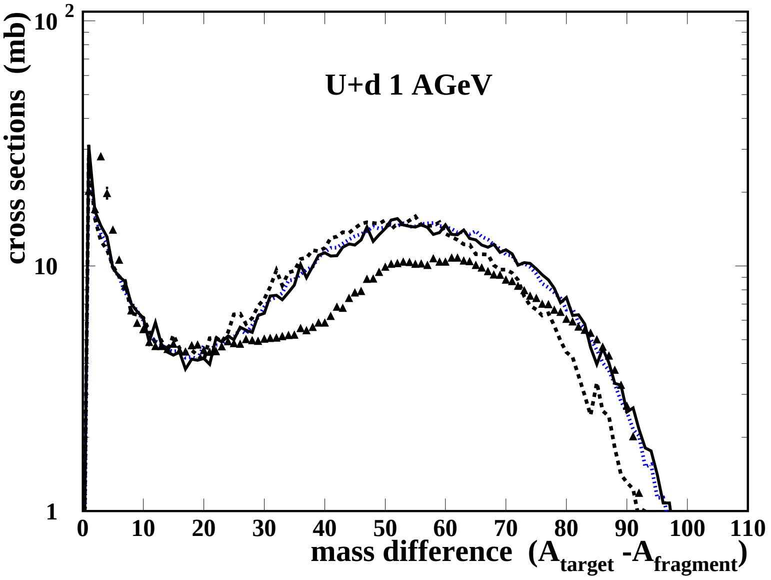

Figure 5.11: Isobaric production cross sections from the reaction $^{238}U(1A \cdot GeV) + d$. The model proposed in this work includes a nucleon-nucleon cross section correction factor of 1.10 (doted line) and 0.80 (dashed line). The fluctuations in the curve are only due to statistics.

the other hand, since the enhancement factor is always greater than in ion-ion collisions, it seems that the energy is more effectively deposited by single nucleons than by the emsemble of nucleons in a heavy nucleus.

We investigated further the difference between the two nucleons of the deuteron. We observed a poor description of the excitation energy distribution, i.e. the isobaric distribution, figure 5.9. For residues with a mass difference $\Delta A > 25$ the calculated distribution rises too fast. Apparently the excitation energy E^* is too low. By adding an extra factor 2 to the second collision in the double impact case, the model gives the results plotted as isobaric distribution in figure 5.9(dashed line), and isotopic distributions at figure 5.10(thin full line). The performance in this case is much better, the isobaric and isotopic distributions resulting rather realistic. The extra factor increases even more the excitation energy E^* deposited by two nucleons, as compared to the particle-hole energy of the original model.

5.5 Conclusions

We have compared the data measured with calculations done with standard codes. The description is done by combining the results from an intra-nuclear cascade and a de-excitation code based on the statistical model.

Firstly, we could determine that the ABLA evaporation-fission code is able to describe realistically the measured data. We have seen that the description of the reaction $^{238}U+p$ is satisfactory with the INC-code ISABEL. However, the code fails in the overall description of the result of the $^{238}U+d$ reaction, underestimating the lighter fragmentation production.

To further investigate some topics related to the ^{238}U system, we have developed a simple model. The description of the pre-fragment and excitation energy is based on the number of abraded particles, and those are evaluated from the number of collisions of the projectile with the target nucleons.

We found that the energy distribution had to be enhanced in respect to former results involving ion-ion collisions, in order to reproduce the proton induced reaction. The enhancement also depended on the impact parameter. This result is interpreted as a consequence of the excitation energy parameterisation we used, being better suited for the most peripheral collisions. With these corrections the model was found to perform correctly in the nucleon-nucleus collision of $^{238}U(1\ A\cdot GeV)+p$, reproducing the general trends and results.

We additionally could investigate with our model the influence of a realistic nuclear shape, instead of the widely assumed spherical description in realistic INC codes. A possible influence for the most peripheral collisions could not be shown. We conclude that the nuclear shape is not a decisive parameter in the description of the INC step and a spherical symmetric description is adequate. We also investigated the influence of the modifications of the nucleon-nucleon interaction cross section. Changes up to 10% did not modify appreciably the results.

We extended further our model to investigate the influence of the deuterium geometry and the energy deposition in the deuterium induced reactions. A semi-classical impact model was proposed, with a geometrical sequential impact of the two nucleons. The results showed a good response, and reproduced the characteristics of the production measured in this work for $^{238}U(1\ A\cdot GeV)+d$. The common range of production of proton and deuteron induced reactions is immediately reproduced within our simplified model. We found also that by enhancing additionally the excitation energy, in the case of double impact, the results were more realistic. That implies that the energy for an impact parameter given had to be additionally modified.

The possibility to describe such complex processes with simplified assumptions is already a success, where we could test the adequacy of the Glauber-like descriptions in the high-energy domain. Since the standard codes are long-time consuming and cannot reproduce with equal accuracy the whole range of the reaction production, the capabilities of these simplified models open the possibility of using fast and reliable code results for dedicated applications.

Resumen

Introducción

El objetivo de esta tesis es el estudio experimental de los núcleos residuales producidos en la reacción de fragmentación del ^{238}U con deuterio, a una energía cinética de 1 GeV por nucleón. Para caracterizar la producción de dichos residuos se midieron sus secciones eficaces de producción y sus velocidades de retroceso. Este sistema pertence al grupo de reacciones de iones pesados a energías relativistas, que permiten el estudio de los núcleos bajo condiciones extremas de densidad y temperatura. El impacto a alta energía de un núcleo pesado contra otro ligero se interpreta como un proceso en dos fases: una rápida, en que una cascada intranuclear produce un *núcleo compuesto* excitado; y una segunda parte en que los núcleos residuales de la reacción se forman por la emisión de partículas (evaporación) o fisión del núcleo compuesto. La mayor parte de la produción de residuos pesados es debida la fragmentación, y ese estudio constituye el tema de este trabajo.

El interés en las reacciones de espalación[12] parte de muy diversos campos. Las reacciones de espalación permiten estudiar la materia nuclear excitada, con una desidad normal y con un bajo momento angular. Esas condiciones son óptimas para investigar los orígenes de la multifragmentación térmica. Además, la espalación ha cobrado un mayor interés debido a sus nuevas aplicaciones. Los blancos de espalación pueden usarse como *fuentes de neutrones*. Algunas tecnologías, como los *sistemas asistidos por aceleradores* ADS utilizados para transmutar residuos nucleares, se relacionan muy estrechamente con los estudios de la espalación. Estas reacciones también hacen possible la producción de haces de núcleos radiactivos, que se han convertido en un instrumento muy interesante para investigar nuevas regiones de la carta de núcleos. Los estudios de *estructura nuclear* se han visto renovados con esta técnica, al permitir la producción y uso de muchos núcleos hasta ahora no accesibles experimentalmente. La *Astrofísica nuclear* también precisa del estudio de la espalación. Primero por los propios fenómenos en que la reacción interviene: en la nucleosínteis, el denominado *proceso-l* determina las abundancias de elementos observadas, ya que los procesos de espalación en el medio interestelar modifican las abundancias producidas originalmente en el interior de las estrellas. Y además, porque el estudio de algunos procesos fundamentales (*proceso-rp, proceso-r*) requiere la producción de núcleos más o menos exoticos, pero siempre cercanos a los límites de existencia;

---

[12] Espalación y fragmentación son términos que se refieren la misma reacción pero estudiadas en condiciones cinemáticas inversas. La primera se refiere a la colisión de una partícula ligera rápida contra un blanco pesado. La fragmentación es el proceso inverso.

y la fragmentación lo permite en muchos casos.

Esos temas implican el estudio de reacciones cubriendo un rango muy amplio de combinaciones proyectil-blanco y energías diferentes, y hace no viable el estudio de todas las que serían requeridas. Por otra parte, las aplicaciones citadas requieren datos muy precisos para poder diseñar correctamente los experimentos (en el caso de producción de núcleos exóticos), comprender mecanismos básicos como el proceso de núcleosínteis estelar, o planificar sistemas alternativos de producción de energía (ADS). Diferentes códigos de cálculo, basados en modelos teóricos, simulan estos procesos de espalación. La comparación con los datos disponibles permite mejorar los modelos, al mismo tiempo que comprender los fenómenos físicos que caracterizan la reacción. Algunas comparaciones especializadas, concluyen que la capacidad predictiva de los modelos actuales no está bien adaptada a las exigencias que son requiridas. La falta de datos en grandes rangos de energías y regiones de núcleos, ha impedido en muchos casos que los modelos puedan contrastarse con medidas experimentales.

La combinación proyectil blanco presentada en este trabajo es parte de un estudio sistemático iniciado en el *Gesellschaft für Schwerionenforschung* GSI (Darmstadt, Alemania) en 1996, en el marco de una colaboración europea entre diferente instituciones. Su propósito es el estudio de un grupo de reacciones nucleares para obtener una perspectiva sistemática y representativa del proceso de espalación, y definir además un catálogo de datos que sirvan de referencia para comparar los resultados obtenidos con modelos de simulación de estas reacciones. Los institutos de la colaboración, además del GSI, son el *Institute de Physique Nucleaire* IPN (Orsay, Francia), SphN-CEA (Saclay, Francia), CENBG (Bordeaux, Francia) y la *Universidad de Santiago de Compostela* (Spain). El programa experimental incluye, entro otros, los sistemas $^{238}U(1.0AGeV)$ y $^{208}Pb(1.0, 0.5AGeV)$ ambos en colisión con protones y deuterio. El trabajo experimental del programa se completó en octubre de 2000. Los resultados han sido parcialmente analizados y publicados.

El estudio hecho en este trabajo se corresponde con una de las piezas necesarias para comprender las características de los cuatro sistemas ^{238}U y ^{208}Pb con protones y deuterio. Estos sistemas son representativos de las reacciones de iones pesados, pero con fisilidad muy diferente en cada caso. Además, el deuterio se compara con el protón para definir las diferencias que aporta a la reacción, el nucleón y la energía extras añadidos en al sistema. La reacción nucleón-núcleo es la que la mayoría de modelos teóricos describen. El estudio del deuterio pone de manifiesto las diferencias entre los procesos inducidos por uno y dos nucleones, y los datos permiten comparar la respuesta de los modelos en su extensión mas sencilla al sistema dinuclear.

Técnica experimental y secciones eficaces

El experimento que describe este trabajo fue realizado en el GSI-Darmstadt, haciendo incidir un haz de ^{238}U a una energía de 1AGeV, sobre un blanco criogénico de deuterio líquido. Los núcleos residuales salen del blanco a energías comparables a las del haz, debido a la cinemática de la reacción. Ese caraterística permite que sean analizados e identificados en carga y masa durante su vuelo, mediante un espectrómetro magnético.

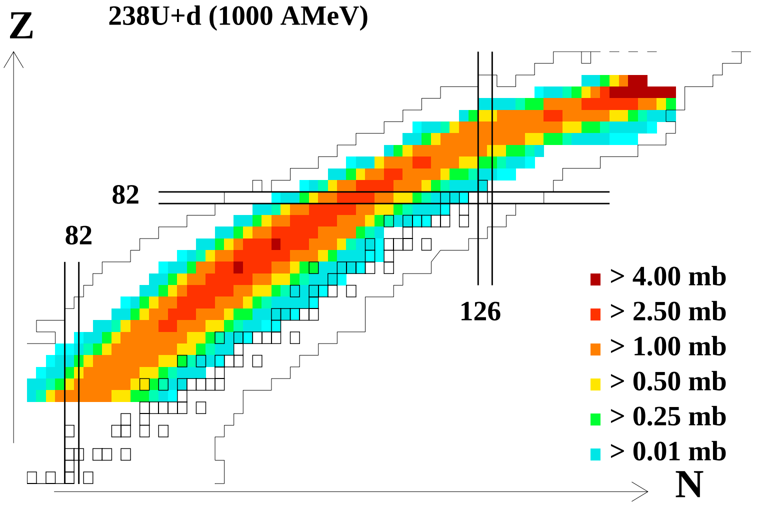

Figura 5.12: Vista parcial de la carta de núcleos sobre la que se representan, en escala de grises, las secciones eficaces medidas. Más de 500 isótopos que fueron identificados como residuos de espalación en la reacción $^{238}U + d(1\ AGeV)$.

Esta es una técnica nueva, denominada de *cinemática inversa*, que supone un gran avance respecto a técnicas más convencionales empleadas en los estudios de espalación. La posibilidad de acelerar iones tan pesados como el ^{238}U hasta energías relativistas, y poder identificar los núcleos residuales de la reacción, solo es factible actualmente en el GSI, gracias a su sincrotrón SIS y el espectrómetro de 70 m de longitud FRS. Esta es una técnica muy exigente, y cualquiera de los experimentos realizados constituye un logro en sí mismo. La peculiaridad añadida de este experimento fue el uso de un blanco criogénico de hidrógeno y deuterio. Un repaso a las instalaciones del GSI permite reconocer los requisitos tan exigentes que esta técnica supone. Pese a su complejidad, los experimentos han demostrado su compatibilidad con los resultados existentes previamente, que eran escasos. El mayor éxito de la nueva técnica, es la enorme cantidad de resultados de alta calidad que son producidos en un solo experimento.

Puesto que el objetivo del trabajo descrito es la medida de las secciones eficaces de producción, se han medido independientemente la tasa de producción de cada núcleo, la intensidad del haz incidente y el espesor del blanco, que son necesarios para normalizar la producción. Para monitorizar el haz, se empleó una cámara interpuesta en su trayectoria, que por la emisión electrónica inducida por el flujo de partículas, permite determinar la intensidad del haz. Su calibración con una cámara independiente, permite extender el límite de contaje a rangos donde este monitor no se satura. El espesor real del blanco depende de la diferencia de presión con el medio que lo rodea. Para determinarlo con la debida precisión se realizó un pequeño experimento, en el que el blanco se escaneó con un haz cuya rigidez magnética era muy sensible a las variaciónes de espesor. De ese modo fue posible hacer un mapa preciso del espesor del blanco, y además definir la influencia de pequeñas variaciones en la precisión final. La tarea más compleja es la definición de la tasa de producción. Primero porque la técnica de identificación de cada núcleo es muy exigente. Y segundo por las correciones que son necesarias para evaluar todas las influencias que el método induce en la medida de las tasas de producción. El espectrómetro empleado es el único que existe capaz de separar iones a tales energías con resolución suficiente. La identificación de la partícula depende de la determinación de su rigidez magnética:

$$B\rho = \frac{p}{Q} = \frac{A}{Q} \cdot \beta\gamma \cdot \frac{u}{c} \tag{5.13}$$

donde B es el campo de deflexión (uniforme y transversal a la trayectoria de la partícula), ρ el radio de deflexion, p el momento, Q la carga atómica, c la velocidad de la luz, u la unidad de masa y $\beta\gamma$ el momento reducido sugún los parametros relativistas. Un grupo de detectores diferentes (cámaras multihilos, plásticos centelleadores, ...) son empleados para definir la rigidez magnética $B\rho$ y el tiempo de vuelo de la partícula, i.e. $\beta\gamma$. Mediante cámaras de ionización se mide la carga nuclear de cada residuo producido, de modo que se identifica la partícula en carga y masa. El método en sí mismo permite determinar la secciones eficaces como función del momento longitudinal del nucleo. Eso permite la medida de la distribución de esa magnitud. Las distribuciones de momento son también una información muy valiosa para ayudar a comparar los modelos teóricos, y en la determinación de parámetros técnicos necesarios para aplicaciones de estas reacciones, como los daños inducidos en materiales irradiados.

La propuesta inicial del proyecto iniciado en le GSI, incluía la obtencion de datos con un alto grado de calidad. El límite de precisión se fijó en un 10% para los valores de sección eficaz superiores a 0.1 mb. Eso significaba, junto con el desarrollo de la nueva técnica experimental, un estudio muy detallado de todas las correciones que se incluyen en el cálculo de las secciones eficaces. Esas correcciones afectan a los estados de carga ionicos presentes y que son seleccionados durante la identificación. También a las reacciones secundarias que atenúan los flujos producidos al atravesar diferentes materiales en el sistema de medida, la transmisión de iones en el espetrómetro, ...

Una de las dificultades principales a la hora de trabajar con iones pesados en este régimen de energías, es que no se presentan completamente ionizados, y la distribución de sus estados iónicos cambia al atravesar un material. La posibilidad de identificar de manera completamente no ambigua cada núcleo, suceso a suceso, fue posible mediante el uso de un *degrader* acromático situado en la trayectoria de vuelo de las partículas y dentro del espectrómetro. La selección en rigidez magnética que induce ese sistema, junto con la medida añadida de pérdida de energía que supone su presencia, permiten identificar los estados de carga dentro del espectrómetro. Para definir la carga nuclear, mediante cámaras de ionización, surge la misma dificultad. La combinación de la medida con dos cámaras independientes y los resultados obtenidos con el degrader,nos permite diferenciar todos los las combinaciones de estados de carga posibles. De ese modo, la identificaión es completa. Por debajo de la carga Z=70, desaparece esa dificultad y el uso del degrader ya no es necesario. La comparación de las medidas hechas con y sin ese elemento permitió además evaluar el grado de precisión de las correcciones efectuadas. Más de 500 secciones eficaces de producción, y sus momentos, han sido medidos en la fragmentación de $^{238}U + d$, ver figura 5.12. El resultado es en sí mismo una colección de datos importante para los

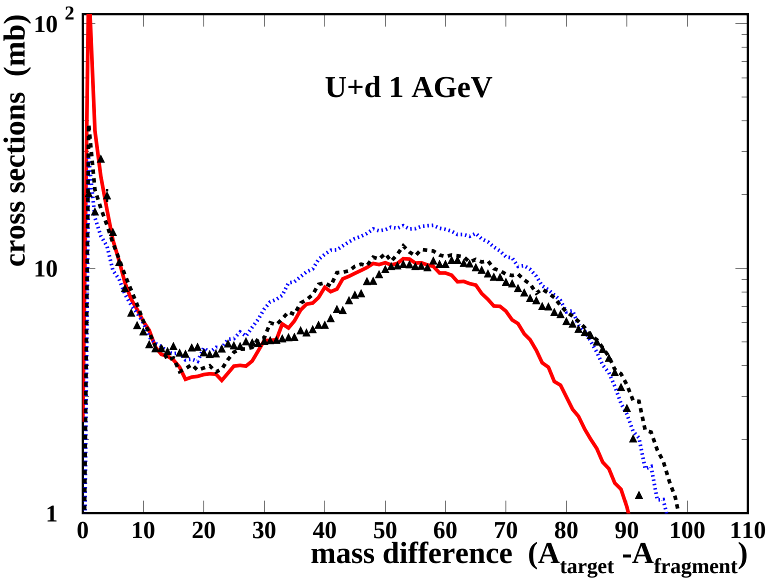

Figura 5.13: Distribución isobárica de las secciones eficaces medidas. Tambien aparece el resultados de dos cálculos: uno basado en el código ISABEL (línea continua) y el segundo basado en el modelo propuesto en este trabajo, con dos parametrizaciones de la energía de excitación diferentes (línea discontinuas). Ver el texto para los detalles.

estudios de las reacciones de espalación.

Discusión de resultados y modelos

Los datos obtenidos con esta técnica permiten tambien determinar la sección eficaz total de reacción. En la producción de núcleos residuales se distinguen las dos contribuciones que provienen de los dos mecanismos de reacción presentes: fisión y fragmentación. Los datos disponibles nos han permitido discutir la idoneidad de alguna descripción microscópica de la sección eficaz d reación, como la basada en el modelo de Karol y modificada por Brohm. La escasez de datos no permite una conclusión respecto al sistema $^{238}U + d(1\ AGeV)$ que nos ocupa, y los resultados futuros del analisis de la parte de fisión serán de gran ayuda para ello.

La gran cantidad y la calidad de los datos obtenidos se refleja en las distribuciones isotópicas de las secciones eficaces, que resultan suaves y continuas. Así mísmo, ese comportamiento permite estimar con gran precisión aquellos datos que por razones del dispositivo experimental, no se han podido medir. También se ha podido reconstruir la distribución isobárica de los fragmentos residuales, que es interesante porque refleja la distribución de la energía depositada en la primera parte de la reacción. Esa es una información muy importante en la comparación con modelos teóricos. La comparación de los datos obtenidos con otros resultados de fragmentación de iones pesados, nos permite definir las caracteristicas principales del sistema estudiado. La comparación con la reacción de $^{238}U+p$, permite estudiar la influencia de la mayor energía añadida al sistema en el caso del deuterio. En este caso se observa que la produccion de residuos se extiende a masas mucho menores que en el caso de protón, debido a que la energía disponible hace los procesos de emisión de partículas mucho mas largos. Por otra parte en un rango de masas muy amplio $\sim A > 205$, ambas producciones son muy similares. Eso se interpreta como el resultado de la colisión de un único nucleón. En el caso del deuterio eso es posible en las interacciones más periféricas, debido a la ditribución de materia tan extensa que presenta el deuterio. La comparación de los resultados de los sistemas $^{208}Pb+d$ y $^{238}U+d$, permite poner en evidencia la forma drástica el papel del canal de fisión en el segundo sistema. Ese efectooriginа la caida rápida de producción y recuperación posterior, que se observan en la distribución isobárica en la figura 5.13. Dicho efecto es debido al papel combinado del debilitamiento del canal de fisión a altas energías y el aumento de las barreras de fissión en nucleos más ligeros.

Además en este trabajo se ha puesto de manifiesto la producción de residuos de fisión en elementos con $Z \sim> 70$. El análisis de las características de estos residuos permite establecer que los núcleos complemetarios producidos en estos procesos de fisión tan asimétricos, deben tener un valor de número atómico igual o inferior a 20. Esa producción por fissión asimétrica, no había sido observada hasta ahora en residuos de fisión pesados, y abre una posibilidad para producir núcleos ricos en neutrones tanto ligeros como pesados. Estos resultados deben ser considerados en la discusión sobre la producción de haces radioactivos.

La técnica de fragmentación permite producir tanto núcleos muy deficientes en neutrones (típicos de los procesos de evaporación, poblando el *corredor de fragmentación*, ver figura 5.12), como explorar la producción de núcleos pesados ricos en neutrones. Esto último se debe a las grandes fluctuaciones en A/Z que ocurren en la parte inicial de la reacción, y que se reflejan en los residuos más cercanos al proyectil, donde se producen núcleos a la derecha del valle de estabilidad, ver figura 5.12. En este último caso, la producción mas exótica accesible es la denominada *fragmentación fria*, gracias a los canales de pérdida de protones. Los resultados obtenidos en este trabajo son comparables con los observados en otros experimentos, y su modelización ayuda a la planificacion precisa de experimentos relacionados con su producción. La producción de núcleos deficientes en neutrones, típicos de la reacciones de fragmentación, permite acceder a la región de los núcleos *emisores de protones*. Para elementos superiores al Pb, se ha definido una región amplia en la que prodrían existir emisores con vidas medias al alcance de las técnicas actuales. Su producción es la clave para estudiar la estructura de estos núcleos. Debido a su baja tasa de producción una estimación precisa se hace necesaria para diseñar experimentos que incluyan su estudio. Tanto para un tipo de producción como la otra, los resultados de este trabajo ayudan a definir el tipo de reacción más adecuada, y a estimar de manera precisa las tasas d producción involucradas.

Los resultados obtenidos sirvieron además para comparar las predicciones de modelos teóricos. Debido a que ahora existe una gran cantidad de datos disponibles, las comparaciones detalladas son posibles. Así como algunos efectos sutiles no se reflejan en las distribuciones isotópicas, las distibuciones isobáricas ponen de manifiesto muy exigentemente la capacidad descriptiva de un código. Estos códigos suelen describir la reación a partir de dos modelos, referidos cada uno a un parte de la reacción: una cascada intra nuclear, primer proceso de la reacción, muy rápido, que genera un núcleo compuesto excitado; y una parte de fisión y/o emisión de nucleones en el proceso de desexcitación. La comparación de los resultados de diversos códigos y los datos medidos, nos ha permitido condiderar como correcto el funcionamiento de uno de los modelos que describen la evaporación y fisión, el código ABLA. En cambio otros códigos como EVAP, ampliamente usados, describen de manera muy pobre los resultados medidos es éste y otros experimentos. Una vez que hemos podido definir un modelo que describe la fissión-evaporación de manera realista, hemos dedicado una mayor atención a la parte the formación del núcleo compuesto. El código ISABEL proporciona una descripción adecuada en el caso de las reacciones nucleón-núcleo, e.g. $^{208}Pb + p$ y $^{238}U + p$. Además este código permite el estudio de la interacción núcleo-núcleo, como en el caso del $^{238}U + d$. En este último caso se observó que el resultado dado por el modelo no describe completamente la producción observada. El resultado subestima la producción de los residuos de fragmentación para los componentes más ligeros, lo que nos indica que la distribución de la energía de excitación resultante de la cascada no es correcta. En la figura 5.13 se muestra la distribución isobárica de los residuos medidos en la reacción $^{238}U + d$, comparados con el resultado de del código ISABEL (línea continua).

Para extender el estudio de algunas características del sistema $^{238}U+d$, en este trabajo hemos propuesto un nuevo modelo sencillo, que simula una colisión nucleón-núcleo. Las cascadas realistas no pueden modificarse fácilmente para incluir otros efectos adicionales a los que presentan. Así, por ejemplo, estos modelos siempre describen los procesos de interacción nucleón-nucleón dentro de la distribución de materia del nucleo. Eso, en pricipio, puede causar diferentes resultados para dos núcleos cuyas formas difieran, como es el caso de ^{208}Pb y ^{238}U, ya que este último no es esférico. Así mismo decidimos investigar si la similitud de los resultados entre la colisión con protón y deuterio, podía explicarse como debido, fundamentalmente, a la geometría del sistema.

Este modelo se basa en las ideas más sencillas de la aproximación de Glauber. La descripción microscópica de la formación del nucleo compuesto la hemos obtenido a partir de la evaluacion del número de nucleones abradidos y de la energía depositada por cada uno de ellos. Para evaluar el número de nucleones abradidos, se define el número medio de colisiones del nucleón incidente con los nucleones del núcleo blanco. Para ello se calculan el recorrido del nucleón, pesado por la densidad nuclear para incluir el contorno difuso del núcleo; y el recorrido libre medio del nucleón, a partir de las secciones eficaces de interacción nucleón-nucleón. Ese número medio de colisiones se distribuye despues de manera poissoniana, y se asume que todas la colisiones inducen la abrasión de un nucleón. Para determinar la proporción de protones y neutones, se considera una correlacción nula entre nucleones, hipotesis que ya ha sido utilizada con éxito en otros modelos. La energía depositada se parametriza a partir de la distribución resultante de la creación de un hueco en el núcleo blanco. Se ha observado que dicha distribución de energía debe escalarse para reproducir los resultados experimentales en el caso de colisiones ion-ion pesados. En este trabajo se ha puesto de manifiesto que dicho factor depende del número de nucleones abradidos. Eso se puede interpretar como debido a que el modelo de distribución de energía es solo adecuado para la colisiones más periféricas. El resultado es aceptable cuando se compara con los datos de $^{238}U + p$ o $^{208}Pb + p$, demostrandose la validez de las simplificaciones *a la Glauber*.

Con este modelo como punto de partida, se ha estudiado también la posible influencia de la forma exacta del núcleo blanco, ya que el ^{238}U es un nucleo deformado. En principio, se puede esperar que la variación de densidad observada en los bordes de las distribuciones, haga variar las distribución de las colisiones más periféricas. La comparación de los resultados obtenidos incluyendo o no esta parametrización, no muestra diferencias apreciables. Este resultado se interpreta debido a que la variación del recorrido del nucleón en una distribución deformada o no, es muy pequeña comparada con el recorrido libre medio, que constitye la dimensión de referencia.

El modelo también se ha extendido para estudiar colisiónes núcleo-núcleo en el caso más sencillo que es la colisión de un sistema dinuclear. Ese es el caso del deuterio, con la peculiaridad de su distribución de densidad. La descripción se hizo también dentro de un esquema sencillo: un impacto geométrico y secuencial de los dos nucleones sobre el núcleo blanco, donde el parámetro de impacto lo definía la distribución de densidad del deuterio. El resultado es en general bueno, mostrando de manera natural la zona de producción común del deuterio y el protón. Adicionalmente el modelo se mejoró notablemente al aumentar la energía depositada en el caso de una doble colisión. Eso lo interpretamos una vez más como el resultado de la descripción inadecuada de la distribución de energía. Esos resultados abren la posibilidad de parametrizar de manera sencilla y efectiva los calculos para usos concretos, que de otro modo son tremendamente lentos y de difícil aplicación.

Conclusiones y perspectivas

En este trabajo se ha discutido en detalle un nuevo procedimiento experimental para estudiar las reacciones de fragmentación-espalación y solucionar las dificultades que surgen en el estudio de nucleos pesados a la energía de 1 AGeV. Este método permite obtener una cantidad muy grande de datos, además con gran precisión, lo que supone un avance importante en este tipo de estudios.

Estos resultados permiten de manera inmediata discutir algunas implicaciones en la producción de isotopos exóticos. La comparación de los resultados de la fragmentación en $^{238}U + d$ con otros sistemas de iones pesados y con reacciones con protónes, han permitido discutir además las caracterísicas de nuestro sistema en cuanto los efectos de la fisión y de la energía, en este sistema.

La cantidad de datos experimentales, más de 500 secciones eficaces medidas en este trabajo, y de otros resultados recientemente disponibles, ha permitido la comparación con modelos teóricos existentes. Además hemos propuesto un modelo basado en ideas muy sencillas que reproduce básicamente los resultados y permite discutir la influencia de parámetros fundamentales, como la energía de excitación promedio, la forma exacta de las distribuciones de materia nuclear, la caracterización geométrica del impacto en el caso del deuterio, ... Esos modelos sencillos suponen la posibilidad de obtener calculos rápidos y correctos en estudios concretos donde los modelos realistas, muy complejos, se muestran lentos y, a veces, inexactos.

Los resultados futuros del analisis de la parte de fisión de la reacción de ^{238}U con protón y deuterio, son de gran importancia, ya que estonces se dispondrá del conjunto de datos completos de la producción de residuos en estas reacciones. Eso ayudará en la discusión y comprensión del proceso completo, y tambien en la comparación con los modelos capaces de estimar tanto las secciones eficaces totales de reacción, como las parciales de fisión y fragmentación. El programa experimental concluido recientemente ha estudiado los sistemas ^{238}U, ^{208}Pb, ^{179}Au, ^{56}Fe con protón y deuterio, a 1 AGeV. Esos resultados constituyen una cantidad enorme de datos de alta calidad en el estudio de las reacciones de espalación. Un estudio de la reacción incluyendo un haz con masa $A \sim 100$, sería de gran ayuda para describir la producción en sistemas con masas intermedias a las ya estudiadas. Una posibilidad muy interesante es la de un haz de ^{136}Xe, que es, además de un núcleo estable, un núcleo rico en neutrones. Eso permitiría estudiar la producción de núcleos ricos en neutrones en esa región por fragmentación fría. Actualmente ya existen proyectos y están programados experimentos para el estudio de esa vía de producción, por fragmentación fría. Los sistemas pesados ^{238}U, ^{208}Pb, ^{186}W con blancos de Be van a ser investigados proximamente en el GSI-Darmstadt.

Appendix A

Table of cross sections

Tables A.1-A.4 show the data corresponding to **total production cross sections**, for $Z > 69$ being related to fragmentation. Tables A.5-A.6 show the data for $Z < 70$, corresponding to the disentangled fragmentation and fission contributions. The evaluated data appear in **bold**. The uncertainty (statistical and systematic) is within parentheses and corresponds to the % of the cross section value, see section 3.8. For the separated fragmentation contribution, the estimated uncertainty of the separation is added.

nucleus	σ(mb)	nucleus	σ(mb)	nucleus	σ(mb)	nucleus	σ(mb)
^{234}Np	0.036(19)	^{230}Th	3.406(19)	^{218}Ra	2.103(19)	^{203}Rn	0.310(19)
^{235}Np	0.068(19)	^{231}Th	**3.263(19)**	^{219}Ra	1.991(19)	^{204}Rn	0.810(19)
^{236}Np	0.099(19)	^{232}Th	**2.796(19)**	^{220}Ra	1.754(19)	^{205}Rn	1.343(19)
^{237}Np	0.116(19)	^{233}Th	2.149(19)	^{221}Ra	1.389(19)	^{206}Rn	1.903(19)
^{238}Np	0.068(19)	^{234}Th	1.625(19)	^{222}Ra	1.176(19)	^{207}Rn	2.370(19)
^{229}U	0.030(19)	^{235}Th	0.994(19)	^{223}Ra	0.917(19)	^{208}Rn	2.424(19)
^{230}U	0.094(19)	^{236}Th	0.452(19)	^{224}Ra	0.672(19)	^{209}Rn	2.170(19)
^{231}U	0.262(19)	^{213}Ac	0.103(19)	^{225}Ra	0.413(19)	^{210}Rn	1.900(19)
^{232}U	0.656(19)	^{214}Ac	0.262(19)	^{226}Ra	**0.279(19)**	^{211}Rn	1.587(19)
^{233}U	2.430(19)	^{215}Ac	0.522(19)	^{227}Ra	**0.166(19)**	^{212}Rn	**1.154(19)**
^{234}U	6.118(19)	^{216}Ac	0.759(19)	^{228}Ra	0.100(19)	^{213}Rn	0.812(19)
^{235}U	12.058(19)	^{217}Ac	**1.136(19)**	^{229}Ra	**0.049(19)**	^{214}Rn	**0.547(19)**
^{223}Pa	0.009(19)	^{218}Ac	1.503(19)	^{230}Ra	0.021(19)	^{215}Rn	0.323(19)
^{224}Pa	0.034(19)	^{219}Ac	2.037(19)	^{231}Ra	0.014(19)	^{216}Rn	0.290(19)
^{225}Pa	0.054(19)	^{220}Ac	2.367(19)	^{232}Ra	0.008(19)	^{217}Rn	0.187(19)
^{226}Pa	0.150(19)	^{221}Ac	2.448(19)	^{205}Fr	0.031(19)	^{218}Rn	0.121(19)
^{227}Pa	0.352(19)	^{222}Ac	2.657(19)	^{206}Fr	0.150(19)	^{197}At	0.004(19)
^{228}Pa	0.866(19)	^{223}Ac	2.750(19)	^{207}Fr	0.485(19)	^{198}At	0.040(19)
^{229}Pa	1.376(19)	^{224}Ac	2.362(19)	^{208}Fr	1.020(19)	^{199}At	0.158(19)
^{230}Pa	2.573(19)	^{225}Ac	2.120(19)	^{209}Fr	1.635(19)	^{200}At	0.536(19)
^{231}Pa	4.617(19)	^{226}Ac	1.765(19)	^{210}Fr	2.108(19)	^{201}At	1.174(19)
^{232}Pa	7.258(19)	^{227}Ac	1.601(19)	^{211}Fr	2.296(19)	^{202}At	1.895(19)
^{233}Pa	9.762(19)	^{228}Ac	1.397(19)	^{212}Fr	2.220(19)	^{203}At	2.252(19)
^{234}Pa	**12.022(19)**	^{229}Ac	**0.872(19)**	^{213}Fr	**2.595(19)**	^{204}At	2.541(19)
^{235}Pa	15.183(19)	^{230}Ac	**0.532(19)**	^{214}Fr	2.066(19)	^{205}At	2.516(19)
^{236}Pa	17.307(19)	^{231}Ac	**0.295(19)**	^{215}Fr	**1.570(19)**	^{206}At	2.215(19)
^{237}Pa	20.885(19)	^{232}Ac	**0.152(19)**	^{216}Fr	1.100(19)	^{207}At	1.703(19)
^{216}Th	0.014(19)	^{233}Ac	0.068(19)	^{217}Fr	0.989(19)	^{208}At	1.252(19)
^{217}Th	0.033(19)	^{234}Ac	0.042(19)	^{218}Fr	0.759(19)	^{209}At	0.908(19)
^{218}Th	0.029(19)	^{235}Ac	0.015(19)	^{219}Fr	0.603(19)	^{210}At	0.634(19)
^{219}Th	0.114(19)	^{207}Ra	0.005(19)	^{220}Fr	0.383(19)	^{211}At	**0.475(19)**
^{220}Th	0.211(19)	^{208}Ra	0.012(19)	^{221}Fr	0.245(19)	^{212}At	**0.307(19)**
^{221}Th	0.366(19)	^{209}Ra	0.032(19)	^{222}Fr	0.155(19)	^{213}At	**0.172(19)**
^{222}Th	0.493(19)	^{210}Ra	0.235(19)	^{223}Fr	**0.087(19)**	^{214}At	0.081(19)
^{223}Th	1.006(19)	^{211}Ra	0.654(19)	^{224}Fr	**0.055(19)**	^{215}At	0.035(19)
^{224}Th	1.425(19)	^{212}Ra	1.155(19)	^{225}Fr	**0.031(19)**	^{216}At	0.006(19)
^{225}Th	2.050(19)	^{213}Ra	1.562(19)	^{226}Fr	**0.017(19)**	^{194}Po	0.019(19)
^{226}Th	2.466(19)	^{214}Ra	1.981(19)	^{227}Fr	0.009(19)	^{195}Po	0.086(19)
^{227}Th	2.739(19)	^{215}Ra	2.262(19)	^{228}Fr	**0.004(19)**	^{196}Po	0.334(19)
^{228}Th	3.101(19)	^{216}Ra	**2.326(19)**	^{229}Fr	0.002(19)	^{197}Po	0.805(19)
^{229}Th	3.527(19)	^{217}Ra	2.056(19)	^{202}Rn	0.072(19)	^{198}Po	1.496(19)

Table A.1: Total production cross section. The number in parentheses is the value of the uncertainty given as % of the cross section value. Part-I/IV.

nucleus	σ(mb)	nucleus	σ(mb)	nucleus	σ(mb)	nucleus	σ(mb)
^{199}Po	2.196(19)	^{192}Pb	2.353(19)	^{185}Hg	2.257(19)	^{181}Pt	3.796(19)
^{200}Po	2.619(19)	^{193}Pb	3.164(19)	^{186}Hg	3.068(19)	^{182}Pt	4.148(19)
^{201}Po	2.586(19)	^{194}Pb	3.342(19)	^{187}Hg	3.706(19)	^{183}Pt	3.879(19)
^{202}Po	2.416(19)	^{195}Pb	3.005(19)	^{188}Hg	3.952(19)	^{184}Pt	3.511(19)
^{203}Po	2.020(19)	^{196}Pb	2.698(19)	^{189}Hg	3.686(19)	^{185}Pt	2.792(19)
^{204}Po	1.568(19)	^{197}Pb	1.911(19)	^{190}Hg	3.050(19)	^{186}Pt	2.030(19)
^{205}Po	1.093(19)	^{198}Pb	1.267(19)	^{191}Hg	2.475(19)	^{187}Pt	1.491(19)
^{206}Po	0.743(19)	^{199}Pb	0.864(19)	^{192}Hg	1.919(19)	^{188}Pt	1.060(19)
^{207}Po	0.473(19)	^{200}Pb	0.591(19)	^{193}Hg	1.290(19)	^{189}Pt	0.632(19)
^{208}Po	0.323(19)	^{201}Pb	0.313(19)	^{194}Hg	0.603(19)	^{190}Pt	0.213(19)
^{209}Po	0.192(19)	^{202}Pb	0.157(19)	^{195}Hg	0.319(19)	^{191}Pt	0.109(19)
^{210}Po	0.119(19)	^{203}Pb	0.091(19)	^{196}Hg	0.162(19)	^{192}Pt	0.045(19)
^{211}Po	**0.029(19)**	^{204}Pb	0.046(19)	^{197}Hg	0.075(19)	^{193}Pt	0.005(19)
^{212}Po	**0.007(19)**	^{205}Pb	0.024(19)	^{198}Hg	0.023(19)	^{171}Ir	0.010(19)
^{213}Po	0.001(19)	^{206}Pb	0.009(19)	^{199}Hg	0.007(19)	^{172}Ir	0.062(19)
^{190}Bi	0.009(19)	^{183}Tl	0.013(19)	^{200}Hg	0.003(19)	^{173}Ir	0.227(19)
^{191}Bi	0.041(19)	^{184}Tl	0.070(19)	^{177}Au	0.025(19)	^{174}Ir	0.664(19)
^{192}Bi	0.192(19)	^{185}Tl	0.245(19)	^{178}Au	0.122(19)	^{175}Ir	1.342(19)
^{193}Bi	0.579(19)	^{186}Tl	0.675(19)	^{179}Au	0.360(19)	^{176}Ir	2.497(19)
^{194}Bi	1.306(19)	^{187}Tl	1.267(19)	^{180}Au	0.915(19)	^{177}Ir	3.367(19)
^{195}Bi	1.988(19)	^{188}Tl	2.284(19)	^{181}Au	1.586(19)	^{178}Ir	3.849(19)
^{196}Bi	2.777(19)	^{189}Tl	2.866(19)	^{182}Au	2.424(19)	^{179}Ir	3.818(19)
^{197}Bi	3.008(19)	^{190}Tl	3.272(19)	^{183}Au	3.286(19)	^{180}Ir	3.902(19)
^{198}Bi	2.814(19)	^{191}Tl	3.597(19)	^{184}Au	3.950(19)	^{181}Ir	3.255(19)
^{199}Bi	2.560(19)	^{192}Tl	3.098(19)	^{185}Au	4.019(19)	^{182}Ir	2.544(19)
^{200}Bi	1.891(19)	^{193}Tl	2.713(19)	^{186}Au	3.861(19)	^{183}Ir	1.789(19)
^{201}Bi	1.419(19)	^{194}Tl	2.184(19)	^{187}Au	3.399(19)	^{184}Ir	1.346(19)
^{202}Bi	1.071(19)	^{195}Tl	1.466(19)	^{188}Au	2.446(19)	^{185}Ir	1.042(19)
^{203}Bi	0.625(19)	^{196}Tl	0.946(19)	^{189}Au	1.894(19)	^{186}Ir	0.652(19)
^{204}Bi	0.309(19)	^{197}Tl	0.538(19)	^{190}Au	1.436(19)	^{187}Ir	0.359(19)
^{205}Bi	0.210(19)	^{198}Tl	0.312(19)	^{191}Au	1.035(19)	^{188}Ir	0.122(19)
^{206}Bi	0.124(19)	^{199}Tl	0.166(19)	^{192}Au	0.361(19)	^{189}Ir	0.059(19)
^{207}Bi	0.066(19)	^{200}Tl	0.086(19)	^{193}Au	0.168(19)	^{190}Ir	0.026(19)
^{208}Bi	0.036(19)	^{201}Tl	0.042(19)	^{194}Au	0.056(19)	^{191}Ir	0.009(19)
^{209}Bi	0.018(19)	^{202}Tl	0.023(19)	^{174}Pt	0.020(19)	^{192}Ir	0.002(19)
^{186}Pb	0.003(19)	^{203}Tl	0.009(19)	^{175}Pt	0.092(19)	^{168}Os	0.004(19)
^{187}Pb	0.031(19)	^{180}Hg	0.017(19)	^{176}Pt	0.323(19)	^{169}Os	0.036(19)
^{188}Pb	0.119(19)	^{181}Hg	0.095(19)	^{177}Pt	0.829(19)	^{170}Os	0.147(19)
^{189}Pb	0.393(19)	^{182}Hg	0.329(19)	^{178}Pt	1.724(19)	^{171}Os	0.437(19)
^{190}Pb	0.967(19)	^{183}Hg	0.781(19)	^{179}Pt	2.781(19)	^{172}Os	1.056(19)
^{191}Pb	1.670(19)	^{184}Hg	1.282(19)	^{180}Pt	3.569(19)	^{173}Os	1.919(19)

Table A.2: Total production cross section. The number in parentheses is the value of the uncertainty given as % of the cross section value. Part-II/IV.

nucleus	σ(mb)	nucleus	σ(mb)	nucleus	σ(mb)	nucleus	σ(mb)
^{174}Os	2.851(19)	^{168}W	1.867(19)	^{163}Hf	1.600(19)	^{158}Yb	1.342(19)
^{175}Os	3.688(19)	^{169}W	2.930(19)	^{164}Hf	2.373(19)	^{159}Yb	2.006(19)
^{176}Os	4.118(19)	^{170}W	3.426(19)	^{165}Hf	3.029(19)	^{160}Yb	2.359(19)
^{177}Os	3.833(19)	^{171}W	3.701(19)	^{166}Hf	2.971(19)	^{161}Yb	2.456(19)
^{178}Os	3.212(19)	^{172}W	3.548(19)	^{167}Hf	2.832(19)	^{162}Yb	2.290(19)
^{179}Os	2.583(19)	^{173}W	2.887(19)	^{168}Hf	2.312(19)	^{163}Yb	1.845(19)
^{180}Os	1.853(19)	^{174}W	2.379(19)	^{169}Hf	1.699(19)	^{164}Yb	1.364(19)
^{181}Os	1.169(19)	^{175}W	1.689(19)	^{170}Hf	1.189(19)	^{165}Yb	0.960(19)
^{182}Os	0.737(19)	^{176}W	0.888(19)	^{171}Hf	0.766(19)	^{166}Yb	0.632(19)
^{183}Os	0.449(19)	^{177}W	0.558(19)	^{172}Hf	0.449(19)	^{167}Yb	0.397(19)
^{184}Os	0.273(19)	^{178}W	0.323(19)	^{173}Hf	0.248(19)	^{168}Yb	0.227(19)
^{185}Os	0.128(19)	^{179}W	0.169(19)	^{174}Hf	0.133(19)	^{169}Yb	0.110(19)
^{186}Os	0.061(19)	^{180}W	0.089(19)	^{175}Hf	0.072(19)	^{170}Yb	0.030(19)
^{187}Os	0.028(19)	^{181}W	0.050(19)	^{176}Hf	0.036(19)	^{171}Yb	0.008(19)
^{188}Os	0.014(19)	^{182}W	0.024(19)	^{177}Hf	0.017(19)	^{150}Tm	0.001(19)
^{189}Os	0.005(19)	^{183}W	0.004(19)	^{178}Hf	0.006(19)	^{151}Tm	0.008(19)
^{166}Re	0.014(19)	^{161}Ta	0.005(19)	^{156}Lu	0.012(19)	^{152}Tm	0.062(19)
^{167}Re	0.081(19)	^{162}Ta	0.060(19)	^{157}Lu	0.060(19)	^{153}Tm	0.200(19)
^{168}Re	0.281(19)	^{163}Ta	0.274(19)	^{158}Lu	0.238(19)	^{154}Tm	0.494(19)
^{169}Re	0.664(19)	^{164}Ta	0.697(19)	^{159}Lu	0.569(19)	^{155}Tm	0.962(19)
^{170}Re	1.455(19)	^{165}Ta	1.335(19)	^{160}Lu	1.185(19)	^{156}Tm	1.540(19)
^{171}Re	2.444(19)	^{166}Ta	2.310(19)	^{161}Lu	1.895(19)	^{157}Tm	2.036(19)
^{172}Re	3.155(19)	^{167}Ta	3.058(19)	^{162}Lu	2.283(19)	^{158}Tm	2.214(19)
^{173}Re	3.821(19)	^{168}Ta	3.363(19)	^{163}Lu	2.768(19)	^{159}Tm	2.221(19)
^{174}Re	3.912(19)	^{169}Ta	3.284(19)	^{164}Lu	2.640(19)	^{160}Tm	1.953(19)
^{175}Re	3.424(19)	^{170}Ta	2.785(19)	^{165}Lu	2.250(19)	^{161}Tm	1.643(19)
^{176}Re	2.899(19)	^{171}Ta	2.101(19)	^{166}Lu	1.852(19)	^{162}Tm	1.153(19)
^{177}Re	2.222(19)	^{172}Ta	1.616(19)	^{167}Lu	1.351(19)	^{163}Tm	0.862(19)
^{178}Re	1.252(19)	^{173}Ta	1.090(19)	^{168}Lu	0.843(19)	^{164}Tm	0.526(19)
^{179}Re	0.817(19)	^{174}Ta	0.620(19)	^{169}Lu	0.591(19)	^{165}Tm	0.341(19)
^{180}Re	0.509(19)	^{175}Ta	0.378(19)	^{170}Lu	0.326(19)	^{166}Tm	0.205(19)
^{181}Re	0.282(19)	^{176}Ta	0.201(19)	^{171}Lu	0.185(19)	^{167}Tm	0.122(19)
^{182}Re	0.150(19)	^{177}Ta	0.105(19)	^{172}Lu	0.089(19)	^{168}Tm	0.063(19)
^{183}Re	0.089(19)	^{178}Ta	0.056(19)	^{173}Lu	0.041(19)	^{169}Tm	0.027(19)
^{184}Re	0.042(19)	^{179}Ta	0.028(19)	^{174}Lu	0.010(19)	^{148}Er	0.003(19)
^{185}Re	0.016(19)	^{180}Ta	0.014(19)	^{175}Lu	0.003(19)	^{149}Er	0.023(19)
^{186}Re	0.006(19)	^{181}Ta	0.004(19)	^{153}Yb	0.001(19)	^{150}Er	0.096(19)
^{164}W	0.023(19)	^{159}Hf	0.039(19)	^{154}Yb	0.024(19)	^{151}Er	0.287(19)
^{165}W	0.151(19)	^{160}Hf	0.118(19)	^{155}Yb	0.124(19)	^{152}Er	0.638(19)
^{166}W	0.480(19)	^{161}Hf	0.408(19)	^{156}Yb	0.357(19)	^{153}Er	1.109(19)
^{167}W	1.018(19)	^{162}Hf	0.985(19)	^{157}Yb	0.743(19)	^{154}Er	1.629(19)

Table A.3: Total production cross section. The number in parentheses is the value of the uncertainty given as % of the cross section value. Part-III/IV.

nucleus	σ(mb)	nucleus	σ(mb)	nucleus	σ(mb)	nucleus	σ(mb)
^{155}Er	1.856(19)	^{152}Ho	1.631(19)	^{149}Dy	1.367(19)	^{145}Tb	0.556(19)
^{156}Er	1.949(19)	^{153}Ho	1.750(19)	^{150}Dy	1.646(19)	^{146}Tb	1.026(19)
^{157}Er	1.920(19)	^{154}Ho	1.741(19)	^{151}Dy	1.677(19)	^{147}Tb	1.532(19)
^{158}Er	1.664(19)	^{155}Ho	1.687(19)	^{152}Dy	1.550(19)	^{148}Tb	1.618(19)
^{159}Er	1.360(19)	^{156}Ho	1.397(19)	^{153}Dy	1.384(19)	^{149}Tb	1.578(19)
^{160}Er	0.978(19)	^{157}Ho	1.116(19)	^{154}Dy	1.145(19)	^{150}Tb	1.430(19)
^{161}Er	0.689(19)	^{158}Ho	0.797(19)	^{155}Dy	0.923(19)	^{151}Tb	1.250(19)
^{162}Er	0.431(19)	^{159}Ho	0.582(19)	^{156}Dy	0.661(19)	^{152}Tb	0.997(19)
^{163}Er	0.287(19)	^{160}Ho	0.341(19)	^{157}Dy	0.500(19)	^{153}Tb	0.803(19)
^{164}Er	0.159(19)	^{161}Ho	0.255(19)	^{158}Dy	0.317(19)	^{154}Tb	0.645(19)
^{165}Er	0.084(19)	^{162}Ho	0.148(19)	^{159}Dy	0.238(19)	^{155}Tb	0.422(19)
^{166}Er	0.044(19)	^{163}Ho	0.108(19)	^{160}Dy	0.167(19)	^{156}Tb	0.330(19)
^{167}Er	0.022(19)	^{164}Ho	0.060(19)	^{161}Dy	0.115(19)	^{157}Tb	0.244(19)
^{146}Ho	0.006(19)	^{165}Ho	0.036(19)	^{162}Dy	0.062(19)	^{158}Tb	0.165(19)
^{147}Ho	0.038(19)	^{144}Dy	0.011(19)	^{163}Dy	0.035(19)	^{159}Tb	0.097(19)
^{148}Ho	0.133(19)	^{145}Dy	0.061(19)	^{141}Tb	0.004(19)	^{160}Tb	0.064(19)
^{149}Ho	0.342(19)	^{146}Dy	0.170(19)	^{142}Tb	0.023(19)	^{161}Tb	0.021(19)
^{150}Ho	0.651(19)	^{147}Dy	0.470(19)	^{143}Tb	0.087(19)		
^{151}Ho	1.157(19)	^{148}Dy	0.961(19)	^{144}Tb	0.248(19)		

Table A.4: Total production cross section. The number in parentheses is the value of the uncertainty given as % of the cross section value. Part-IV/IV.

nucleus	σ^{FRAG}(mb)	σ^{FISS}(mb)	nucleus	σ^{FRAG} (mb)	σ^{FISS}(mb)
^{150}Tm	0.001(19)	0.000(0)	^{158}Er	1.664(19)	0.000(0)
^{151}Tm	0.008(19)	0.000(0)	^{159}Er	1.360(19)	0.000(0)
^{152}Tm	0.062(19)	0.000(0)	^{160}Er	0.978(19)	0.000(0)
^{153}Tm	0.200(19)	0.000(0)	^{161}Er	0.648(44)	0.041(44)
^{154}Tm	0.494(19)	0.000(0)	^{162}Er	0.369(44)	0.063(44)
^{155}Tm	0.962(19)	0.000(0)	^{163}Er	0.207(44)	0.079(44)
^{156}Tm	1.540(19)	0.000(0)	^{164}Er	0.087(44)	0.072(44)
^{157}Tm	2.036(19)	0.000(0)	^{165}Er	0.027(44)	0.057(44)
^{158}Tm	2.214(19)	0.000(0)	^{166}Er	0.002(44)	0.042(44)
^{159}Tm	2.221(19)	0.000(0)	^{167}Er	0.000(0)	0.022(44)
^{160}Tm	1.953(19)	0.000(0)	^{146}Ho	0.006(19)	0.000(0)
^{161}Tm	1.643(19)	0.000(0)	^{147}Ho	0.038(19)	0.000(0)
^{162}Tm	1.153(19)	0.000(0)	^{148}Ho	0.133(19)	0.000(0)
^{163}Tm	0.862(19)	0.000(0)	^{149}Ho	0.342(19)	0.000(0)
^{164}Tm	0.526(19)	0.000(0)	^{150}Ho	0.651(19)	0.000(0)
^{165}Tm	0.337(44)	0.005(44)	^{151}Ho	1.157(19)	0.000(0)
^{166}Tm	0.173(44)	0.031(44)	^{152}Ho	1.631(19)	0.000(0)
^{167}Tm	0.075(44)	0.047(44)	^{153}Ho	1.750(19)	0.000(0)
^{168}Tm	0.018(44)	0.045(44)	^{154}Ho	1.741(19)	0.000(0)
^{169}Tm	0.000(0)	0.027(44)	^{155}Ho	1.600(44)	0.086(44)
^{148}Er	0.003(19)	0.000(0)	^{156}Ho	1.272(44)	0.125(44)
^{149}Er	0.023(19)	0.000(0)	^{157}Ho	0.952(44)	0.164(44)
^{150}Er	0.096(19)	0.000(0)	^{158}Ho	0.620(44)	0.177(44)
^{151}Er	0.287(19)	0.000(0)	^{159}Ho	0.397(44)	0.184(44)
^{152}Er	0.638(19)	0.000(0)	^{160}Ho	0.194(44)	0.147(44)
^{153}Er	1.109(19)	0.000(0)	^{161}Ho	0.111(44)	0.143(44)
^{154}Er	1.629(19)	0.000(0)	^{162}Ho	0.042(44)	0.105(44)
^{155}Er	1.856(19)	0.000(0)	^{163}Ho	0.013(44)	0.095(44)
^{156}Er	1.949(19)	0.000(0)	^{164}Ho	0.000(0)	0.060(44)
^{157}Er	1.920(19)	0.000(0)	^{165}Ho	0.000(0)	0.036(44)

Table A.5: Fragmentation and fission production cross section. Only those isotopes where the two contributions, fission σ^{FISS} and fragmentation σ^{FRAG} , have been separated are shown. The number in parentheses is the value of the uncertainty given as % of the cross section value. Part-I/II.

nucleus	σ^{FRAG}(mb)	σ^{FISS}(mb)	nucleus	σ^{FRAG} (mb)	σ^{FISS}(mb)
^{144}Dy	0.011(19)	0.000(0)	^{142}Tb	0.023(19)	0.000(0)
^{145}Dy	0.061(19)	0.000(0)	^{143}Tb	0.087(19)	0.000(0)
^{146}Dy	0.170(19)	0.000(0)	^{144}Tb	0.248(19)	0.000(0)
^{147}Dy	0.470(19)	0.000(0)	^{145}Tb	0.556(19)	0.000(0)
^{148}Dy	0.961(19)	0.000(0)	^{146}Tb	1.026(19)	0.000(0)
^{149}Dy	1.367(19)	0.000(0)	^{147}Tb	1.532(19)	0.000(0)
^{150}Dy	1.646(19)	0.000(0)	^{148}Tb	1.618(19)	0.000(0)
^{151}Dy	1.677(19)	0.000(0)	^{149}Tb	1.578(19)	0.000(0)
^{152}Dy	1.550(19)	0.000(0)	^{150}Tb	1.430(19)	0.000(0)
^{153}Dy	1.384(19)	0.000(0)	^{151}Tb	1.250(19)	0.000(0)
^{154}Dy	1.105(44)	0.040(44)	^{152}Tb	0.901(44)	0.096(44)
^{155}Dy	0.836(44)	0.086(44)	^{153}Tb	0.676(44)	0.127(44)
^{156}Dy	0.541(44)	0.119(44)	^{154}Tb	0.482(44)	0.163(44)
^{157}Dy	0.352(44)	0.148(44)	^{155}Tb	0.262(44)	0.159(44)
^{158}Dy	0.178(44)	0.139(44)	^{156}Tb	0.153(44)	0.176(44)
^{159}Dy	0.092(44)	0.145(44)	^{157}Tb	0.068(44)	0.177(44)
^{160}Dy	0.031(44)	0.135(44)	^{158}Tb	0.009(44)	0.156(44)
^{161}Dy	0.000(0)	0.115(44)	^{159}Tb	0.000(0)	0.097(44)
^{162}Dy	0.000(0)	0.062(44)	^{160}Tb	0.000(0)	0.064(44)
^{163}Dy	0.000(0)	0.035(44)	^{161}Tb	0.000(0)	0.021(44)
^{141}Tb	0.004(19)	0.000(0)			

Table A.6: Fragmentation and fission production cross section. Only those isotopes where the two contributions, fission σ^{FISS} and fragmentation σ^{FRAG} , have been separated are shown. The number in parentheses is the value of the uncertainty given as % of the cross section value. Part-II/II.

Appendix B

Total cross sections and related topics

In order to evaluate either the reaction or the survival probabilities of a certain pair projectile-target, two processes are of interest: nuclear and electro-magnetic EMD interactions. Using dedicated models one can estimate the related cross sections σ^{EMD} and σ^{nuc} for a given target-projectile combination, and energy. The total reaction cross sections is the sum of both. The reaction P_r and the survival P_s probabilities after traversing a certain thickness d of material are defined immediately as

$$P_r = 1 - P_s = 1 - e^{\frac{n_o}{A_t} \cdot d \cdot \sigma^{tot}} \tag{B.1}$$

where A_t is the target mass number and n_o the Avogadro's number.

B.1 Nuclear cross section

In a nuclear interaction one usually distinguishes the *scattering* and *absorption* contributions to $\sigma_{tot} = \sigma_{abs} + \sigma_{scatt}$. Additionally the absorption part includes processes in which the number or type of nucleons have changed or not. Sometimes they are referred to as *interaction* and *reaction* cross sections, the latter including also the nuclear excitation channels. In experiments to measure the absorption cross sections usually the measured quantity is the interaction cross section, using the transmission technique see ref. [168]. A more accessible quantity is the charge changing cross section $\sigma_{\Delta z}$. That value is used often as an estimation of σ where any neutron-loss channel is neglected, e.g. see ref. [93].

B.1.1 Microscopic models

A common model to describe the interaction is the *optical model*, using a complex interaction potential. Describing the quantum particle current for a given state, one can see that its divergence is null for the case of a real potential, and that the (negative) imaginary part of the potential is related to absorption. Using the partial-wave expansion of the nuclear wave function and potential, the strong absorption models were used first to describe low energy nuclear reactions. In order to obtain some general trend of the data some approximation is generally done. For instance the *sharp-cutoff* approximation

$$\sigma = \pi \cdot (\lambda/2\pi)^2 \cdot \sum_l (2l+1) \cdot T_l = 2 \cdot \pi \cdot R_s^2 \cdot \left(1 - \frac{D}{E_{cm}}\right) \tag{B.2}$$

where R_s is the strong absorption radius, D the potential barrier height and E_{cm} the kinetic energy; T_l are the *transmission coefficients.* The saturation value for increasing energies has a pure geometrical interpretation of the interaction radius. Different parameterisation have been done, but the descriptions are not well suited above $\sim 20-30$ MeV, when they do not describe the measured data any more.

The evaluation of the *phase-shift* values included in the former model in the T_l coefficients, requires the numerical evaluation of certain differential equations. Additionally, when the energy increases the number of terms needed to evaluate the series increases rather quickly, up to ∼40. In a high energy regime, when the excitation energies of the nucleus are much smaller than the energies involved in the reaction, and the nucleons move in almost forward direction, the so called *Eikonal approximation*, strongly generalized by Glauber, provides a very simplified description of the problem by using the total *eikonal phase*

$$\chi(b,z) = \frac{-1}{\hbar v} \cdot \int_{-\infty}^{z} V(b,\nu) d\nu \tag{B.3}$$

where the impact parameter b and the coordinate z define a three-dimensional position, and V is the interaction potential.

Within this approximation the different components of the cross section may be described as

$$\sigma_{tot} = 2 \cdot \int \left(1 - \Re e^{i\chi(b)}\right) db \tag{B.4}$$

$$\sigma_{abs} = 2 \cdot \int \left(1 - \left|e^{i\chi(b)}\right|^2\right) db \tag{B.5}$$

Note again that χ is real if the potential is real, the absorption part being zero. We can write alternatively the very familiar expression

$$\sigma = \int [1 - T(b)] d^2 b \tag{B.6}$$

where we define the *transparency function* T, being (1-T) interpreted as the probability of interaction, a function of the impact parameter. The eikonal approximation is generally valid when the momentum-energy transfer in the reaction is small compared to the kinetic energies of the projectile.

A microscopic description is needed in order to define the potential involved in the reaction, and to obtain the cross section value. One of the possible solution is that described in ref. [169], considering that the nucleus-nucleus potential depends on the nucleon densities. For a review of the method see ref. [170]. Concepts like Pauli-blocking and Fermi motion are not included. We can relate the nucleon-nucleon interaction potential and cross sections and the nuclear densities of the interacting nuclides, resulting in

$$LnT(b) = -\sigma_{NN} \int_{-\infty}^{\infty} dz \int \rho_1(r) \rho_2(R+r) d^3 r \tag{B.7}$$

where we recognise easily T(b) from the equations above. An additional interpretation shows up: being T the survival probability of NN collisions, the mean-free-path for a NN collision λ_{NN} is defined straightforward, and we re-write the transparency as

$$T(b) = exp\left[\int \frac{dz}{\lambda_{NN}(R)}\right] \tag{B.8}$$

The usual description of the σ_{NN} is using an average NN cross-section, as defined e.g. at [89]. The extension of the model to sub-relativistic energies has to account for the possible deflection of the projectile: that influences the impact parameters. A typical solution is substituting b by a value reflecting the maximum classical approach within the Coulomb+nuclear potential, as described in ref. [171]. That is worthless at relativistic energies.

The starting point of the Karol's model [89] we have used within our work, are the equations above and the averaged σ_{NN} values. He demonstrates that the $T(b)$ value depends mostly on the tail of the nuclear density. The central part contributes geometrically, and independently of the parameterisation, being normalised, it gives the same result. The peripheral part is the most sensitive. He shows that by using either a realistic Fermi-like distribution or a Gaussian-like distribution he obtains the same results. The only conditions is the definition of the Gaussian parameters so that the tail of the nuclear distributions are about the same for both descriptions. The success of the description relies on the analytic solution to σ_{abs} showing a rather satisfactory agreement with the measured trends versus geometrical parameters as $A^{1/3}$ and energy.

A further refinement of the model was done by Brohm [90]. The description of the cross-section lies in a statistical description of the fast initial interaction of the nucleons. Their argumentation is shown equivalent to that of Karol. They introduce a separate description of the neutron and proton densities and diffuseness, as described in the spherical droplet-model [172, 173]. Also the finite range of the nuclear force is considered, since the product of nuclear densities reproduce the zero-range limit.

An additional improvement to that description was done during this work to describe properly the deuteron as well as other lower mass projectiles, with realistic density distributions. The parameters used were taken from muonic-states and electron-scattering experiments and selected model independent when possible according to ref. [164].

B.1.2 Macroscopic models

The measured values of σ_{abs} are usually represented by some macroscopic parameterisation. All the models rely in the definition of an effective radius R_{eff} so that the interaction is described geometrically as $\sigma_{abs} = \pi \cdot R_{eff}^2$. The classical overlapping depending on the target t and projectile p radii needs an additional term to describe a transparency-like trend observed in experiments at higher energies

$$R_{eff} = r_o \cdot (A_t^{1/3} + A_t^{1/3} - c) \tag{B.9}$$

with fitted values r_o=1.75 fm and c=1.7 fm in ref. [174]. Its use is revisited to describe different ranges of energy and-or masses as in ref. [175] with updated parameters 1.35 and

0.83 respectively or in ref. [176] with values 1.4 fm and 1.0 fm respectively, the later for heavy-ion induced reactions and $A_T = 12 - 56$.

The features discussed with the microscopic models (transparency, mass asymmetry effects, ...) are used to improve the macroscopic descriptions. That is the case of the Kox description [177] where the parameterisation of R_{eff} is given as

$$R_{eff} = r_o \cdot \left[A_p^{1/3} + A_t^{1/3} + a \cdot \left(\frac{A_p^{1/3} \cdot A_t^{1/3}}{A_p^{1/3} + A_t^{1/3}} - c \right) + \Gamma \right] \tag{B.10}$$

The correction $\Gamma = \frac{5 \cdot (A_t - 2Z_t) Z_p}{r_o \cdot A_p \cdot A_t}$ is only used below 200 $A \cdot MeV$; above that value $\Gamma = 0$. The values they give are $r_o = 1.1$ fm, $a = 1.85$, and c depends on the kinetic energy, being c=1.9 in the range 900-1200 $A \cdot MeV$. They claim to fit the results in a broad range as $A < 208$ and $T < 2.1$ AGeV.

Also is common the Benesh description [178]

$$R_{eff} = r_o \cdot [A_t^{1/3} + A_p^{1/3} - x \cdot (A_t^{-1/3} + A_p^{-1/3})] \tag{B.11}$$

The values $r_o = 1.34$ fm and $x = 0.75$ were obtained by fitting the trend of values from microscopic Glauber-like calculations. The results were compared with data at $\sim 1A \cdot GeV$, being quite satisfactory. Note that the result is energy-independent. It is worth to remark that the interest of the paper was mostly to define a realistic interaction radius R_{eff}, in order to explore the description of the (p n) reactions, and not to define a total reaction cross-section. Recent measured nuclear cross-sections of ^{238}U on Be and Pb [179] confirmed the validity of the description in that energy range, within 10%.

The microscopic results, mostly Karol-like, combined with measurements is sometimes are used to define microscopic parameters. Nevertheless that is a difficult task since, as pointed out in refs. [165, 166], the variation in σ_{NN} is sometimes hardly reflected in σ. Greiner [93] used a Karol-like description for ^{238}U reactions in different targets, by fitting the σ_{NN} values. The difference obtained from measured charge-changing data was interpreted as due to the lost neutron-removal channels. On the other way around, they used the calculated values to estimate the contribution of the missing channels to the total reaction cross section.

B.2 Electro-magnetic dissociation

In relativistic heavy-ions collisions, electromagnetic processes have an important contribution to the reaction cross section. The excitation energy distribution may be calculated by the equivalent (virtual-)photon spectrum that the projectile sees, created by the target, and the photo-absorption cross section of the projectile. The electromagnetic field of the target nucleus seen by the projectile may be formulated as a flux of equivalent photons. By using several empirical systematics it is possible to define the photon absorption for the main components of the electromagnetic field. The two magnitudes allow to estimate the σ^{EM} value. For a review of the calculation method see e.g. refs. [180, 181].

If the absorption of a (virtual-)photon excites the nucleus above the particle or fission threshold, those channels will be open, i.e. the dissociation is possible. The values of σ^{EM} of light particles are small and usually negligible.

B.3 Single reaction approximation

Once a certain primary product coming out of a certain reaction is formed within the target, it may undergo sequentially new reactions. The distribution of products coming out from a target is actually the result of such complex phenomena. Of course, the probability of the sequential processes decays very fast, since the probability of a secondary reaction is that of the primary times the probability for that product undergoing a new reaction, and so on.

In very thin targets the probability of two sequential processes may be already negligible. Under that conditions the yield and cross section of the reaction are related easily by

$$\frac{\partial N_p}{\partial d} = -\lambda_p^{tot} \cdot N_p \tag{B.12}$$

$$\frac{\partial N_r}{\partial d} = -\lambda_r^{tot} \cdot N_r + \lambda_r^{p+t} \cdot N_p \tag{B.13}$$

where p, r, t refer to the projectile, residue and target respectively, N is the number of nuclides (and also the yield for a given projectile intensity); $\lambda^{tot} = (n_o/A_t) \cdot \sigma^{tot}$ refers to the total reaction production either for the projectile p or the residue r, within the target t; d the target thickness, n_o the Avogadro's number and A_t the target mass number. The λ_r^{p+t} is the same parameter but referred to the production cross section of the residue r by the projectile p on target t. The solution to that system is

$$N_r = N_p^o \cdot \lambda_r^{p+t} \cdot \frac{e^{-\lambda_p^{tot} \cdot d} - e^{-\lambda_r^{tot} \cdot d}}{\lambda_r^{tot} - \lambda_p^{tot}} \tag{B.14}$$

The yield, normalised to the beam intensity N_p^o is

$$y_r = \frac{N_r}{N_p^o} = \frac{n_o}{A_t} \cdot \sigma_r^{p+t} \cdot \Gamma \tag{B.15}$$

The Γ factor is defined straightforward according the former equation, and contains the correction for the attenuation of the beam and the residue fluxes within the target. Note that the approximation relies on the assumption of the whole production of r is only due to the projectile-target reactions, i.e. no other reaction is present, but attenuation. We have used this description in the definition of the reaction cross sections presented in this work, when mentioned that the *single reaction approximation* is used.

A further approximation is by considering that the beam is so intense that its attenuation is negligible, i.e. $N_p = N_p^o$. An even further approximation is additionally neglecting the attenuation of the residue, and the result is simply $y_r = \frac{n_o}{A_t} \cdot \sigma_r^{p+t} \cdot d$.

Appendix C

Limiting fragmentation and factorization

One important concept inherited from high-energy Physics is that of the *scaling* [182] or *limiting fragmentation* [183]. The invariant cross-section for the fragment F production in the reaction of a projectile P with the target T

$$E\frac{d^3\sigma^F_{PT}(s,p_{||},p\perp)}{d^3p} = f(s,p_{||},p\perp) \tag{C.1}$$

where $s^2 = p^2_{||} + p\perp^2$ becomes energy independent when $s \to \infty$ or

$$lim_{p\to\infty} f(s,p_{||},p\perp) = f(p_{||},p\perp) \tag{C.2}$$

This means that the single-particle inclusive spectrum and cross section become energy independent above certain threshold.

The hypothesis was tested e.g. by Lindstrom et al. [184]. They show that for a wide range of fragments the production cross sections were independent of the energy $\sigma^f_{PT}(2,1AGeV)/\sigma^f_{PT}(1,05AGeV) = 1.01 \pm 0.01$. Also the momentum distributions were similar for the two energies. Depending on the reaction the threshold that defines the limiting regime has to be studied. A typical value of $\sim 500A \cdot MeV$ may be used as reference.

A second concept in relativistic heavy-ion reactions is that of the *factorization* [185]: the production cross sections can be split into a term depending in the target T and a term depending in both projectile P and fragment F

$$\sigma(P+T;F) = \sigma^T_{PF} = \gamma^T \cdot \Gamma_{PF} \tag{C.3}$$

The target term scales like $\gamma^T \sim A^{.25}$. Such a geometrical dependence is a typical fragmentation pattern that corresponds to peripheral reactions. Of course central collisions will contribute to the mass distribution since all impact parameters produce spallation residues. Nevertheless a central impact does not follow factorization and the yield will depend on the target mass.

Those two concepts, limiting fragmentation and factorization are related to the decay of a compound nucleus, and are extensively reported in ref. [114] for relativistic heavy-ion reactions. The Glauber description of interactions also contains these ideas. The Glauber description, above $\sim 1A \cdot GeV$, gives limiting fragmentation so far the nucleon-nucleon cross-sections are rather constant. Some kind of factorization is also natural for light-projectiles: the contact of the nucleons happens in a localized region, and so not being influenced by the shape of the nucleus.

Appendix D

List of layers in the experiment

List of the layers of matter used in the experiment described in this work. The different materials are placed on the path through the FRS spectrometer and beyond, in S4. See figure D.1 for some detail of placement at S4. The layers are ordered downstream in table D.1. See the text for the purpose and placement of each layer.

Some values are calculated for the beam of ^{238}U with a initial energy of 1 $A \cdot GeV$: the mass thickness, the nuclear reaction probability $Prob_{reac}^{nuc}$ (i.e. no EMD contribution included), and the energy at the exit of the layer E_{kin}. The probability of the ion to be fully stripped at the exit of the layers used as strippers and also the thick degrader is $Prob_{bare}$. The evaluation was done supossing that the input ion was also bare. The *three state method* was used. If the charge *equilibrium* is achieved, the value is marked with *. See the text for details.

The two inputs (6) refer to the degraders used in our experiment. The values below that point belong to the thicker option.

1. vacuum window
2. SEETRAM
3. cryogenic container. The mylar itself is$C_5H_4O_2$, and the thickness given corresponds to the aluminized part of it, being the rest almost negligible.
4. ionic strippers
5. scintillator plastic: 5.6 mm at S2 and 3.0 mm at S4. Value for H and C together.
6. degraders. Either one or the other was used. The energy of the rest of the layers are for the thicker degrader.
7. MUSIC chamber
8. Air gap

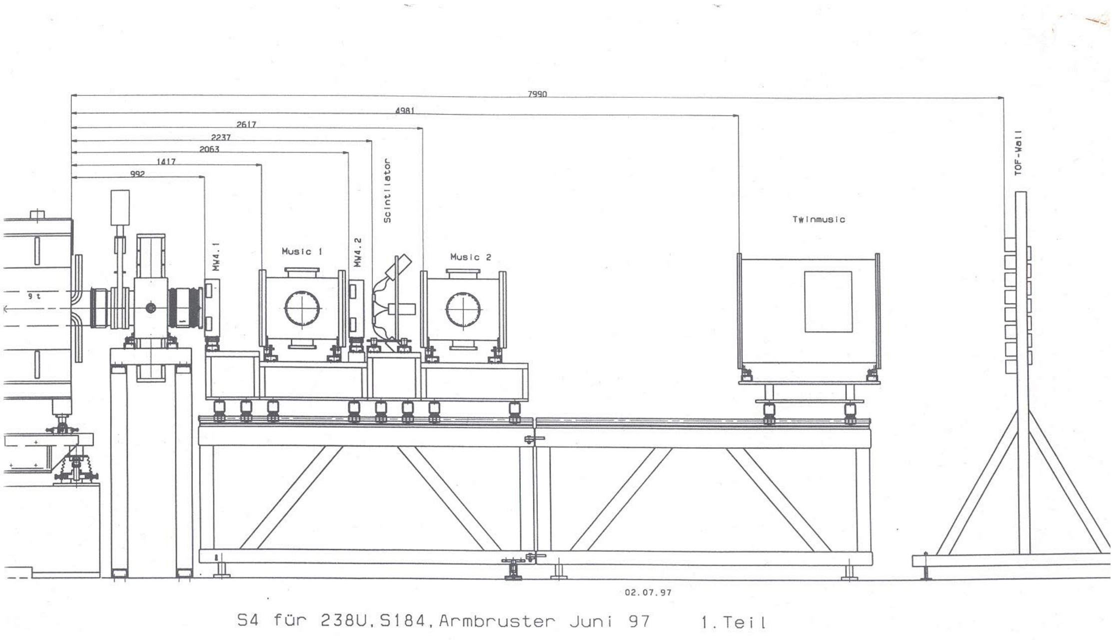

Figure D.1: Scheme of the detector positions at the area S4. The FRS magnets ends are on the leftmost side. The vacuum pipe follows till the entrance of the first multi-wire chamber. In between the two MUSIC ionisation chambers we see the second multi-wire chamber and the plastic scintillator. The larger ionisation chamber and the ToF-wall detectors on the right, were not used in the measurement described in this work.

place	material		thickness	^{238}U		
			mg/cm^2	$Prob^{nuc}_{reac}(\%)$	$E_{kin}(A \cdot MeV)$	$Prob_{bare}$
S0	Al	(1)	4.07	< 0.1	999.722	
	Al	(2)	8.90	< 0.1	999.114	
	Ti	(3)	18.16	0.1	997.992	
	deuterium		201.0	14.3	982.108	
	Al-mylar	(3)	9.7	< 0.1	981.442	
	Ti	(3)	18.16	0.1	980.315	
	Nb	(4)	60.0	0.2	976.851	0.89
S2	H	(5)	49.3	6.43	969.008	
	C	(5)	532.5	9.27	927.937	
	Al	(6)	4085.	33.0	629.779	0.57 *
	Al	(6)	4488.	35.6	598.316	0.55 *
	Nb	(4)	100.	0.4	591.836	0.67
S4	Al	(1)	4.07	< 0.1	591.514	
	N	(8)	50.	0.8	587.082	
	O	(8)	15.	0.2	585.754	
	Ar	(7)	107.0	0.8	578.072	
	Nb	(4)	230.	0.9	562.995	0.63 *
	H	(5)	26.4	3.5	558.025	
	C	(5)	285.3	5.1	532.000	
	N	(8)	39.	0.6	528.419	
	O	(8)	12.	0.2	527.317	
	Ar	(7)	107.0	0.8	519.369	

Table D.1: List of the layers of matter used in the experiment. See the text for details.

Appendix E

Contamination due to ionic-charge states

The presence of ionic charge states of the produced nuclides, implies an additional effort on the techniques to unambiguously identify the fragmentation residues. That difficulty can impose strong bearings in the production of the neuton-rich region of the heavy elements. Some examples of problematic identification in that scenario are dicussed, based on the description of the experimental method used in this work.

That difficulty increases with lower energies. Several projects schedule the use of ^{238}U fragmentation for radioactive beams production, with energies below $1A \cdot GeV$: the RIA project [6] includes beams from protons till U, below 400 $A \cdot MeV$; also at RIKEN a RIB project is designed with U beams below 150 AMeV [186]. Some examples of problematic identification in that scenario are given, based on the discussion done previously about the experimental method.

In this study we discussed in Chapter 2 the presence of ionic charge-states of the produced nuclides. The distribution of those states depends on the atomic and mass numbers of the nucleus and its energy. The higher the atomic number Z of the nuclides, the lower the probability to be fully stripped. Any selection based on the measurement of the atomic charge, will suffer from a certain contamination due to ionic charge-states. In the case of using a spectrometer the ratio mass-to-charge is measured. Even if the nuclear charge were correctly assigned independently, the ionic charge-states would contaminate the identification[1]. It is the same difficulty if ionisation chambers are used to define the nuclear charge, since the response is sensitive to the atomic charge. In this study we used the uncorrelated signals from two chambers with a stripper in between them, to determine Z. Nevertheless only by additionally comparing with a third energy loss measurement, that from the degrader, it was possible to fully disentangle the ionic charges, see 2.7.

The presence of the ionic charge states can make the identification of neutron-rich isotopes difficult, due to the production rates involved. When moving into the neutron-rich side the cross sections values decrease very fast with proton number. Since the contaminants have less neutrons their production can be easily some order of magnitude

---

[1] We can see easily that the A/Q ratio of certain nuclide (Z,A) is about the same of the ionic charge-state with one electron of the nucleus (Z-1,A-5). See Chapter 2.

higher than the production of the nucleus of interest. The presence of high intensity contaminants is a problem since they cannot be suppressed on line, and so they limit the conditions of production of the nucleus of interest.

To make some estimation of the effect of that contamination, we can think in using the same experimental setup and procedure as that used in this work. Supposing the nuclear charge being clearly identified after the spectrometer, the right identification of a nucleus would depend on the A/Q definition. A nuclide as ^{233}Fr could be contaminated by the one and two electron ions of ^{228}Rn and ^{225}Rn respectively. Using the cold-fragmentation model of ref. [3] commented above, and the ionic probability distributions within the FRS, we can estimate the relative importance in production of the bare nuclide and its contaminants. The result is that the contaminating and nuclide production will be 3:1. In the case of ^{232}Rn production, the contaminants would be ^{227}At and ^{224}At, and they would produced in proportion 10:1.

Here we are considering that the degrader is used, see section 2.7, and the intensities are not limiting the production. However the disentangling proposed in this work, relies in the fact that the two spots corresponding to the main production and the contamination can be separated with low overlapping. Since the productions predicted for neutron-rich isotopes are so unequal, the ions of interest will be rather contaminated unless the selection is made by restricting crudely the region of interest in a histogram as that shown in figure 2.10.

Supposing that the degrader procedure was not used, the contamination of ^{233}Fr and ^{232}Rn would be increased enormously. We conclude that the use of the degrader is mandatory to deal with those ionic charge-states contamination. The limits of the procedure are those cases in which the ratio between the cross section values and the ionic transmission, becomes extremely favorable to the contaminant. That could arise in very exotic regions, making largely in-efficient the production.

We have been considering all the time a 1 $A \cdot GeV$ ^{238}U beam. The increment of the energy will be a help to overcome the charge states problem. For a 2 $A \cdot GeV$ beam, the ionic distribution would become such that for the production of ^{233}Fr, the contaminants would be produced 1:1. The ionic charge-states impose severe restrictions on the identification of the nuclides, and that has to be take into account if the energy of the beam is reduced as some projects plan to do, with ^{238}U beams up to 400 MeV in the RIA projects in the US [6].

Appendix F

Simulation

F.1 Beam profile and target thickness

The deuterium target is kind of *sandwich* where the walls are deformed outwards due to the pressure gradient. As a first approximation, the deformed shape can be considered as spherical. This shape causes a change in the target thickness due to the distribution of impinging positions of the projectiles. Additionally, the beam, perpendicular to the target walls[1], passed through the target walls off its symmetric axis. Since now I will refer to the *beam axis lattice* to describe the effect.

The shape of the target walls is described as the surface vectors (x,y) following $x^2 + (y - y_o)^2 < R$, where y_o is the axis offset, and R limits the target walls, so R about 14 mm. It was found that the target and beam were shifted by $y_o = -2$ mm.

The beam distribution is Gaussian around its own axis, and so described as

$$\frac{1}{\sigma \cdot \sqrt{2\pi}} \cdot e^{-\frac{r^2}{2\sigma^2}} \tag{F.1}$$

where $r^2 = x^2 + y^2$. The beam spot has a size of 2.7 mm for a $\sqrt{6}\sigma$ criterium (97% of he 1D population included), so that $\sigma = 1.102$ mm.

The projection of the beam profile onto the spherical shape is

$$\left(\frac{1}{\sigma \cdot \sqrt{2\pi}}\right)^2 \cdot \int_{Y_{min}}^{Y_{max}} e^{-\frac{y^2}{2\sigma^2}} \cdot \int_{X_{min}}^{X_{max}} e^{-\frac{x^2}{2\sigma^2}} dxdy \tag{F.2}$$

where $X_{max} = -X_{min} = \sqrt{R^2 - (y - y_o)^2}$, and $Y_{min/max}$ are determined by the thickness change considered. In our target we found that a change of 1% in thickness corresponds to $Y_{min} = -5$ mm and $Y_{max} = 1$ mm.

The former description allows to evaluate the part of the beam passing through a target length with a thickness variation below a certain limit. We calculated that 82% of the projectiles sees a thickness variation below 1%; and all the projectiles suffer a variation below 2%.

---

[1] The uncertainty due to the target-beam orientation is within the more important contribution considered here.

F.2 Model of a $3 \cdot D$ random collision into an axial-symmetric volume

To emulate a random impact into a given volume one has to take care in the parameterisation to be sure to include the whole geometry. In the case of a nucleus, one uses the symmetry conditions to simplify the problem.

The ^{238}U nucleus is axially symmetric, prolate-type (cigar-like shaped), with two equal radii (~ 6.7 fm) shorter than the third one (~ 8.8 fm), which is the symmetry axis. Using the simple description of the surface by spherical harmonics Y_{lm}, the nuclear shape can be described with dipole β_2 and quadrupole β_4 components. We remark that the reference system used in the following, is that of centered in the nucleus, the Z-axis the axis of symmetry, and the spherical coordinates defined as usual, with θ defined from the Z-axis.

(1) First we consider a reference sphere around the nucleus, with radius R_T, about two times the maximum radius of the nucleus. We select a random direction in space, given by random angles (θ_Y, ϕ_T). Those angles define a plane Π_T perpendicular to that direction, with the a normal unitary vector $N_T = (A, B, C)$ given by

$A = sin\theta_T cos\phi_T; \quad B = sin\theta_T sin\phi_T; \quad C = cos\theta_T$

The intersection of the plane with the reference sphere, defines the point P_T.

(2) If we define a point P_3 lying in the plane Π_T, we can define a trajectory (x,y,z) parallel to the initial direction N_T, passing by P_3, as

$x = x_3 + A \cdot t; \quad y = y_3 + B \cdot t; \quad z = z_3 + C \cdot t$

The t parameter range (t_1, t_2) is defined by the intersection of the reference sphere and the plane Π_T:

$t_{1,2} = \frac{-\beta \pm \sqrt(\beta^2 - 4\alpha\beta)}{2 \cdot \alpha}$

for $\alpha = R_T = 1, \beta = 2 \cdot (Ax_3 + By_3 + Cz_3), \gamma = R_3^2 - R_T^2$ where R is the module. For a null or negative discriminant, the trajectory does not impact neither the sphere nor the nucleus.

(3) To define a point as P_3, we need a pair of auxiliary points P_1, P_2, belonging to the plane Π_T, and defining with P_T a normal base. Supposing we have the three points we obtain $P_3 = P_1 + P_2 - P_T$, since all the vectors are referred to the main frame. The algorithm to define the auxiliary points [2]:

$P_1:$

$\phi_1 = \phi_T;$

$\theta_1 = \theta_T + arctan(d_1/R_T);$

$R_1 = \sqrt(R_T^2 + d_1^2)$

$P_2:$

$\phi_2 = \phi_T + arctan(\frac{d_2}{R_T sin\theta_2});$

$R_2 = \sqrt(z_T^2 + R_T^2 sin^2(\theta_2))$

---

[2] This algorithm was proposed by J.Pereira (at USC-Santiago in 2001).

$\theta_2 = arcsin\left(\frac{d_2^2+R_T^2 sin^2(\theta_2)}{R_2^2}\right)$

The values $d_{1,2}$ are randomly defined in the range $(-R_T, +R_T)$ so that they allow to intercept the whole sphere. The only restrictions to this algorithm are d_1, d_2 and θ_t not null.

(4) Once we have the impact trajectory, the path l through the nucleus is defined according the Fermi-like density distribution

$l = \int \frac{1}{1+e^{(\frac{r-r_o}{d})}} dr$

where r_o is the nuclear radius (defined by the θ angle of the impact trajectory, in the lattice defined), $d \sim 0.57$ parameterices the nuclear surface, and r is defined along the trajectory.

By a Monte-Carlo procedure all possibilities of impact trajectories are scanned. In the case of a pure spherical nucleus this method is strictly equivalent to the usual impact in two dimensions, when the path only depends on the radius.

F.3 Simulation of the the identification pattern within the FRS

In order to identify the measured nuclides we count, on the one hand, with the evaluation of the A/Q ratio, and in the other, with the independent charge Q measure. Despite the ambiguity due to the presence of ionic charge states, both measurements allow to define the identity of each nucleus. Both magnitudes, A/Q and Q are calibrated. The later with the help of the beam. The former with the independent calibrations of position detectors, time-of-flight, and ion-optic parameters of the FRS.

Nevertheless the resolution and unambiguity pursued in this kind of experiments make the former procedure not to be sufficient. In the text it is discussed the whole procedure to finally define the identity of any observed nucleus. Additionally we count on different cross-checking procedures to reveal any fail of the method: independent identifications, characteristics radioactive decays, ... The atomic number Z and mass A assignation is made in two independent steps. First, the energy loss in the two MUSIC chambers combined, and the energy loss in the degrader allow to define the atomic number Z the nucleus. Then, the projection of each Z selection into the A/Q versus position at S2, allow to define the mass. The help of an independent realistic calculation of the detection-measurement components is a powerful tool in order to define the identification, as well as to understand the observed patterns. One of the main goals was the definition of the one-neutron removal, and the one-electron charge state positions within the FRS.

These kind of calculations have been used and built by several members of the collaboration and contributors, after some years. The code we propose inherit the features of our appreciated *AMADEUS* and *LIESCHEN* codes, which have allow the preparation of a bunch of experiments and helped in the analysis in many cases. Additionally, the Monte-Carlo like description and detection conditions, made of this code a tool extremely useful in the analysis of the present reaction.

In the following we describe the characteristic parts of the code.

(1) Since the FRS is tuned with given dipole fields (despite higher order corrections), and it has certain bending radii, the spectrometer can be tuned to match the magnetic rigidity $B\rho$ of a given nucleus. The definition of the main orbit, that of the selected nucleus, is equivalent to the definition of the central rigidity $B\rho|_o$. The possibility to evaluate with enough accuracy the energy loss in the different layers of matter traversed by an ion, as well the reaction energy, allow the definition of the rigidity. Additionally, we input the different energy stragglings to randomly distribute the mean results. An effect as that of the *location straggling*, appears easily by allowing the reaction to happen randomly within the target length. The list of layers used is that of the experiment, see Appendix D.

(2) The achromaticity of the whole FRS, has to be simulated with the evaluation of the position dependent thickness of the degrader, or *slope*. A numerical evaluation of the slope, for the selected fragment is done. The concept is to preserve the rigidity change in between the two FRS sections, by modifying the dispersion with a position dependent slope.

(3) The ion-optical relations, as those appearing in Chapter 2, allow to define the positions of the different nuclides at S2 and S4. Note that only the energy of each nucleus, i.e. the rigidity, and the relation to the central orbit rigidity, are necessary to define the detection parameters. At this point one can think in the possibility to include the transmission conditions into the FRS to make a full evaluation of the transport. Since the aim of our calculation is the identification matrix, we did not introduce that step. Nevertheless it is feasible. As we discussed in the text, the transmission for fragmentation is close to 100%, and border effects are overcome by overlapping of few magnetic settings.

(4) Additional ingredients are the definition of relative intensities for production, random distribution of ionic charge states after the layers of matter, neutron or proton removal channels, ... In fact, with the help of those options we studied the identification features of the ions of our interest.

The result of this code calculations are shown in few examples in Chapter 2. The comparison of measured and evaluated magnitudes if largely satisfactory, and the help in the identification probed. It also allowed the further investigation of special channels patterns (one-neutron removal, hydrogen-like charge states, ...)

Bibliography

[1] Rossi et al., Zeit. Phys. 82 (1933) 151

[2] E.M.Friedlander et al., Phys. Rev. 129(1963) 1809

[3] J.Benlliure et al., Nucl. Phys. A 660 (1999) 87

[4] Study Group on Radioactive Nuclear Beams, OECD Megasciece Forum, Feb. 1999

[5] cosult e.g. http://www.nupecc.org/nupecc/working_groups/rbf/

[6] See the ANL and MSU projecs e.g. at www.phy.anl.gov/ria/index.html and www.nscl.msu.edu/research/ria/home.html

[7] Proc. of the Int. Workshop on Research with Fission Fragments, Germany, Oct. 1996. Eds. T. von Edigy et al., World Scientific, 1997.

[8] Concept for an advanced exotic beam facility based on ATLAS, Physics Division, Argonne National Laboratory, Feb. 1995

[9] cosult e.g. http://www.ganil.fr/spiral/

[10] E.O. Lawrence, E.M. McMillan and L.W. Alvarez, Electronuclear Reactor, US Patent No.2-933-442, 1960

[11] Status of the MTA process, report LRL-102, Livermore Research Laboratory, USA, Feb. 195

[12] J.Benlliure et al., Nucl. Phys. A 628 (1998) 458

[13] G.Münzenberg, Experimental techniques in Nuclear Physics, ed. D.N Poenaru and W.Greiner, Walter de Cruiter & Co., 1997.

[14] K.-H.Schmidt et al., Nucl. Phys. A 664 (2000) 221

[15] T.Enqvist et al., Nucl. Phys. A 686 (2001) 481

[16] T.Enqvist, private communication. Soon to be sent to Nucl. Phys. A

[17] J.M.Carpenter, Nucl. Inst. Meth. 145 (1977) 91

[18] G.S.Bauer, IAEA Vienna-Austria, TECDOC 836 (1995)

[19] European Spallation Source available at www.isis.rl.ac.uk/ESS/ (1999) and ESS (The ESS Technical Study, report ESS-96-53-M (1996))

[20] Spallation Neutron Source, status report, Oak Ridge National Laboratory, USA. Available at www.ornl.gov/sns/ (1999)

[21] J.C.Browne et al., 2nd. Int. Conf. on Acc. Driven Transmutation Technologies, Kalmar, Sweden, June 1996 101

[22] J.L.Flament, Proc. of the 2nd. Int. Workshop on Spallation Materials and Technology, Ancona, Italy, 1997, F.Carsughi et al., editors., KFA Julich, Julich, 1997.

[23] C.Rubbia et al., Rep. CERN-AT/95-44(ET), 1995

[24] C.D.Bowman, Annu. Nucl. Part. Sci., 1999, 505-556

[25] M.Blann et al., International Code Comparison for Intermediate Nuclear Data, OECD/NEA (1994)

[26] D.Filges et al., OECD thick target benchmark, repot NCS/DOC 95 2 (1995)

[27] C.E.Rolfs, W.S.Rodney, *C*auldrons in the Cosmos, The University of Chicago Press, 1988

[28] M.M.Saphiro and R.Silberberg, Ann. Rev. Nucl. Sci. 20 (1970)

[29] R. Michel et al.,Nucl. Ins. Meth. B 103 (1995) 183 and B 129 (1997) 153

[30] Y.T.Titarenko et al., Nucl. Inst. Meth. A 414 (1998) 73

[31] L.N.Andronenko et al., Z. Phys. A 318 (1984) 97

[32] J.R.Cummings et al., Phys. Rev C 42 (1990) 2508 and 2530

[33] C.J.Waddington et al., Phys. Rev. C 61 (2000) 24910

[34] W.R.Webber et al., Phys. Rev C 41 (1990) 520 and 547

[35] J.Benlliure et al., Nucl. Phys. A 683 (2001) 513

[36] F.Rejmund et al., Nucl. Phys. A 683 (2001) 540

[37] J.Taieb, Ph.D. Thesis presented at Universite de Paris Sud and U.F.R. Scientifique d'Orsay, France, Sep. 2000. IPN report IPNO-T-00-10.

[38] Analysis in progress during 2001.

[39] B.B.Cunningham et al., Phys. Rev. 72 (1947) 739

[40] R.Serber, Phys. Rev. 72 (1947) 1114

[41] J.D.Bowman et al., Lawrence Berkeley Lab. Report LBL-2908 (1973)

[42] N.Bohr, Nature 137 (1936) 344

[43] G.F.Bertsch, Z. Phys. A 289 (1978) 103

[44] D.Brink, Nucl. Phys. A 519 (1990) 3c

[45] V.Weisskopf, Phys. Rev. 52 (1937) 295-303

[46] Hüfner et al., Phys. Rev. C 12 (1975) 1888

[47] J.J. Gaimard and K.-H Schmidt, Nucl. Phys. A 531 (1991) 709

[48] W.Hauser, H.Feshbach, Phys. Rev. 87 2 (1952) 366

[49] T.Ericson, Adv. Phys. 9 (1960) 425-511

[50] N.Bohr and J.A.Wheeler, Phys. Rev. 56 (1939) 426-450

[51] L.G.Moretto, Nucl. Phys. A 247 (1975) 211

[52] W.J.Swiatecki, Aus. J. Phys. 36 (1983) 641

[53] R.G. Stokstad at Tretatise on heavy-ion science, vol 3, D.A.Bromley ed., Plenum Press, New York, 1986

[54] E.Gadioli, P.E.Hodgson, Pre-equilibrium Nuclear Reactions, Claredon, Oxford, 1992

[55] J.Cugnon et al., Nucl. Phys. A 620 (1997) 475.

[56] D.Ridikas and W. Mittig, Prodeedings of ENAM'98, ed. B.M.Sherril, Am. Ins. Phys. (1998) 1003

[57] K.Blasche, SIS beam development 1989-91, GSI report GSI-INT-/86-2

[58] A.Magel et al., Nucl. Inst. Meth. B 94 (1994) 548

[59] A.Junghans et al., Nucl. Inst. Meth. A 370 (1996) 312

[60] B. Jurado, K.-H. Schmidt and K.-H Behr, submitted to Nucl. Ins. Meth. (2001)

[61] K.-H.Schmidt et al., Nucl. Inst. Meth. A 260 (1987) 287

[62] P.Chesny et al., submitted to Nucl. Inst. Meth. A (1993); also preprint LNS/SSGD/93-73

[63] G.Münzenberg, Nucl. Ins. Meth. B 70 (1992) 265

[64] J.Pereira et al., Nucl. Inst. Meth. A, accepted for publication (2001)

[65] H.Geissel et al., Nucl. Inst. Meth. B 70 (1992) 286

[66] see e.g. D.C.Carey *The optics of charged particle beams*, Harwood Academic Publishers, 1987, Switzeland

[67] H.Stelzer, Nucl. Ins. Meth. A 310 (1991) 103

[68] M.Steiner et al., Nucl. Ins. Meth. A 312 (1992) 420

[69] B.Voss et al., Nucl. Inst. Meth. A 364 (1995) 150-158

[70] B.Mustapha, Ph.D. Thesis presented at Universite de Paris Sud and U.F.R. Scientifique d'Orsay, France, Sep. 1999. Published as IPN report IPNO-T-99-05.

[71] E.Hanelt, Ph.D. Thesis presented at TH-Darmstadt (Germany), 1992. Published also as GSI report GSI-92-05, 1992.

[72] Ch.Scheidenberger et al., Nucl. Inst. Meth. B 142 (1998) 441

[73] S.K.Allison, Rev. Mod. Phys. 30 4 (1958) 1137

[74] T.Brohm, Ph.D. thesis at Technische Hochschule Darmstadt, Germany, 1994

[75] M.Pfützner et al., Nucl. Inst. Meth. B 86 (1994) 213

[76] J.P.Dufour et al., Nucl. Inst. Meth. A 248 (1986) 267

[77] H.Geissel et al., Nucl. Ins. Meth. A 282 (1989) 247

[78] W.Mittig and P.Roussel-Chomaz, accepted for publication in Nucl. Phys. A, 2001.

[79] D.J.Morrisey, Phys. Rev. C 39 2 (1989) 460

[80] A.R.Junghans et al., Nucl. Phys. A 629 (1998) 635

[81] H.-G.Clerc et al., Nucl. Phys. A 590 (1995) 785

[82] M.deJong et al., Nucl. Phys. A 628 (1998) 479

[83] K.Suemmerer, B.Blank, Phys. Rev. C 61 (2000)

[84] E.Casarejos et al., 5th Int.Conf. on RNB, April, 2000 Divonne, France. Proceedings to be published in Nucl. Phys. A, in preparation.

[85] P.Armbruster et al., Z. Phys. A 355 (1996) 191

[86] M.Bernas et al., Phys. Lett. B 331 (1994) 19-24

[87] M.Bernas et al., Phys. Lett. B 415 (1997) 111-116

[88] Analysis in progress in 2001, by J. Pereira at the University of Santiago de Compostela (Spain)

[89] P.J.Karol, Phys. Rev. C 11 (1975) 1203

[90] T.Brohm, K.-H. Schmidt, Nucl. Phys. A 569 (1994) 821

[91] A.V.Prokofiev, Nucl. Inst. Meth. A 463 (2001) 557

[92] Nuclear Data Centers Network IAEA(NDS)-324 (1995). Consult also http://iaeaand.iaea.org.at or http://www.nea.fr/html

[93] D.E.Greiner et al., Phys. Rev. C 31 (1985) 416

[94] B.A.Bochagov et al., Sov. J. Nucl. Phys. 28 (1978) 291

[95] L.A.Vaishnene, Z. Phys. A 302 (1981) 143

[96] Karlsruher Nuklidkarte, G.Pfenning et al., Forschungszentrum Karlsruhe GmbH (1995)

[97] S.G.Nilsson, I.Ragnarsson, *Shapes and shells in nuclear structure*, Cambridge University Press, 1995

[98] K.-H.Schmidt et al., Nucl. Phys. A 452 (1992) 699

[99] T.Enqvist et al., Nucl. Phys. A 658 (1999) 47; GSI-preprint-99-11 (1999)

[100] A.Heinz et al., Annual Report GSI 1998, GSI-1-99, GSI, Darmstadt.

[101] B.D.Wilkins et al., Phys. Rev. C 14 (1976) 1832

[102] C.Bockstiegel et al., Phys. Lett. B 398 (1997) 259

[103] V.Ricciardi et al., 5th Intern. Conf. on RNB, France, 2000.

[104] W.AFriedman, W.G.Lynch, Phys. Rev. C 28 (1983) 10 and W.friedman, Phys. Rev. Lett. 60 (1988) 2125

[105] L.G.Moretto, G.J.Wozniak, Nucl. Phys. A488 (1988) 337

[106] E.Hanelt et al., Z. Phys. A 346 (1993) 43

[107] S.Hofmann, Radiochim. Acta 70/71 (1995) 93

[108] M.deJong, Ph.D. dissertation, Technische Hochschule Darmstadt, Germany , 1998; also at GSI-DISS-98-02

[109] H.dekhissi et al., CERN-preprint DFUB 98-19, 1998

[110] C.A.Bertulani, D.S.Dolci, Nucl. Phys. A 674 (2000) 527

[111] R.Guoxiao et al., Phys. Rev. C 39 (1989) 1351

[112] G.D.Westfall et al., Phys. Rev. C 45 (1992) 2423

[113] Th.Rubehn et al., Phys. Rev. C 53 (1996) 993

[114] A.S.Goldhaber and H.H.Heckman, Ann. Rev. Part. Sci. 28 (1978) 161

[115] C.K.Gelbke et al., Phys. Rep. 42 312 (1978)

[116] A.S.Goldhaber, Phys. Lett. 53 B 4 (1974) 306

[117] H.Feshbach and K.Huang, Phys. Lett. B 47 (1973) 300

[118] J.V.Lepore and R.J.Riddell, LBL Rep. 3086 (1974)

[119] E.J.Moniz et al., Phys. Rev. Lett. 26 (1971) 445

[120] M.Weber et al., Nucl. Phys. A 578 (1994) 659

[121] J.Aichelin et al., Phys. Rev. C13 (1985) 1730

[122] H.Kruse et al., Phys. Rev. Lett. 54 (1985) 289

[123] K.Niita et al., Phys. Rev. C 52 (1995) 2620

[124] M.B.Chadwick et al., Phys. Rev. C 52 (1995) 2800

[125] M.L.Goldberger, Phys. Rev. 74 (1948) 1269

[126] N.Metropolis et al., Phys. Rev 110 (1958) 185 and 204

[127] H.W.Bertini, Phys. Rev. 131 (1963) 1801

[128] H.W.Bertini, Phys. Rev. 188 (1969) 1711

[129] T.W.Armstrong and K.C.Chandler, Nucl. Sci. Eng. 49 (1972) 110; report CCC-178, ORNL (1977)

[130] R.E.Prael and H.Lichtenstein, LAHET code system 2.7d, Los Alamos National Laboratory Report LA-UR-89-3014 (1989).

[131] K.Chen et al., Phys. Rev. 166 (1968) 949

[132] Y.Yariv and Z.Fraenkel, Phy. Rev. C 20 (1979) 2227

[133] Y.Yariv and Z.Fraenkel, Phy. Rev. C 24 (1981) 488

[134] J.Cugnon, Nucl. Phys. A 462 (1987) 751

[135] S.G.Rudstam, *Spallation of medium weight elements*, Uppsala (1956).

[136] L.Dresner, Oak Ridge report ORNL-TM-196 (1962)

[137] Dostrovsky et al., Phys. Rev. 118 (1960) 781

[138] F.Atchison, Jul-Conf-34, Kernforschungsanlage Julich GmbH, january 1980.

[139] J.Barish et al., ORNL-TM-7882 (1981)

[140] I.Wolfstein, Phys. Rev. 82-5 (1951) 690

[141] T.Darrah-Thomas, Nucl. Phys. 53 (1964) 558

[142] T.Darrah-Thomas, Review (1968) 343-406

[143] L.G.Moretto, Proc. 3rd. IAEA Symp. Phys. Chem. of fission, Rochester, NY, Aug. 1973 vol 1 IAEA 1974, p.329

[144] M.deJong et al., Nucl. Phys. A 613 (1997) 435

[145] K.-H.Schmidt, W.Morawek, Rep. Prog. Phys. 54 (1991) 949

[146] A.J.Sierk, Phys. Rev. C 33 (1986) 2039

[147] B.L.Cohen, *Conceps of nuclear physics*, ed. T.McGraw-Hill, McGraw-Hill, New Delhi (1975) p238.

[148] S.Leray, C.Volant and A.Boudard (CEN-Saclay, France) kindly performed those calculations with the INC-L and the LAHET codes for this work. Private comunication.

[149] K.-H.Schmidt et al., Phys. Lett. B 300 (1993) 313

[150] R.J.Glauber et al., Nucl. Phys. B 21 (1970) 135 and *L*ectures in theoretical Physics, vol. 1, W.E.Britting and L.G.Duchan ed., Intersecience Publishers New York, 1958

[151] J.Cugnon et al., Nucl. Phys. A 625 (1997) 729.

[152] K.Kikuchi, M.Kaway, *Nuclear matter and nuclear reactions*, North-Holland, Amsterdam (1968)

[153] E.Clementel, C.Villi, Nuovo Cim. 12 (1955) 176

[154] S.Hayakawa et al., Prog. Theor. Phys. 13 (1955) 415

[155] M.T.Collins, J.J. Griffin, Nucl. Phys. A 348 (1980) 63

[156] Lock, Measday, *Intermediate energy, nuclear physics*, Methuen, London 1970 pp 180-ff

[157] D.Bugg et al., Phys. Rev. 146 (1966) 980

[158] Particle Data Group, Rev. Mod. Phys. 45 S1 (1973)

[159] W.Hess, Rev. Mod. Phys. 30 (1958) 365

[160] W.D.Myers, Nucl. Phys. A 204 (1973) 46

[161] A.V.Ignatyuk et al., Nucl. Phys. A 593 (1995) 519

[162] P.Moller,J.R.Nix, Atom. Data Nucl. Data Tab. 59 2 (1995) 185

[163] L.Durand, Phys. Rev. 123 (1961) 1393

[164] H. deVries et al, Atm. Data Nucl. Data Tables 36 (1987)

[165] G.Yekutieli et al., Nuovo Cim. 19 and 20 (1961)

[166] H.Aizu et al., Prog. Theor. Phys. Suppl. 16 (1961) 54

[167] D.Ernst, Phys. Rev. C 19 (1979) 896

[168] U.Amaldi et al., Nuo. Cim. 34 (1964) 825, T.J.Gooding, Nucl. Phys.12 (1959) 241

[169] A.K.Kerman et al., Ann. Phys. 8 (1959) 551

[170] M.S.Husein et al., Phys. Rep 201 (1991) 279

[171] R.M.DeVries, J.C.Peng, Phys. Rev. C 22 (1980) 1055

[172] W.D.Myers, W.J.Swiatecki, Ann. Phys. 84 (1974) 186

[173] W.D.Myers, H.vonGrotte, Phys. Lett. B 61 (1976) 125

[174] H.L.Brad, B.Peters, Phys. Rev. 77 (1950) 54

[175] W.R.Binns et al., Phys. Rev. C 36 (1987) 1870

[176] G.D.Westfall et al., Phys. Rev. C 19 (1979) 1309

[177] S.Kox etal., Phys. Rev. C 35 (1987) 1678

[178] C.J.Benesh et al., Phys. Rev. C 40 (1989) 1198

[179] M.Hesse et al., Z. Phys. A 355 (1996) 69

[180] Th.Rubehn et al., Z. Phys. A 353 (1995) 197

[181] K.-H.Schmidt et al., Nucl. Phys. A 665 (2000) 221

[182] R.P.Feinman, Phys. Rev. Lett. 23 (1969) 1415

[183] J.Benecke et al., Phys. Rev. 188 (1969) 2159

[184] P.J.Lindstrom et al., Lawrence Berkeley Lab. rep., LBL-3650 (1975)

[185] M.Gell-Mann, Phys. Rev. Lett. 8 (1962) 263

[186] T.Kubo et al., at the 5th. Int. Conf. on RNB, France, 2000. Accepted for publication at Nucl. Phys. A .